High-Resolution Imaging of Chemistry in Extreme Interstellar Environments

Thesis by
Olivia Harper Wilkins

In Partial Fulfillment of the Requirements for the
Degree of
Doctor of Philosophy

CALIFORNIA INSTITUTE OF TECHNOLOGY
Pasadena, California

2022
Defended December 13, 2021

ACKNOWLEDGEMENTS

Something I learned multiple times throughout my time working on the Ph.D. is that graduate school is a marathon, not a race. There were many times when I felt like I was sprinting, fueled by the high of my code working for more than a day or going several days without being disrupted by software crashes when using CASA (the software every radio astronomer loves to hate). Many other times, I felt exhausted and out of breath, wondering if I really could reach the finish line.

Well, I have completed this marathon, and it would not have been possible without having a supportive group of people who have trained me, cheered for me, or provided water (read: coffee) breaks along the way. Fortunately for me, I have had a lot of people cheering me on. Perhaps not so fortunate for you, that means reading these acknowledgements is a marathon of its own.

First, I thank my research advisor, Geoff Blake, for providing an environment in which I could thrive as an independent researcher. You have fostered a community in your group that attracts kind, generous, and hardworking people, and I am so glad to have been a part of that. I appreciate your support of my own professional endeavors, especially those outside of astrochemistry research. I was not interested in coming to Caltech before I met you in Cologne when you visited while I was in Germany as a Fulbrighter. I was only planning to apply because the Fulbright got me an automatic application fee waiver. However, during that visit, I asked you whether you were open to me pursuing my interests in teaching even though at the time teaching was not required of chemistry Ph.D. students. My first impression of you was that you were someone who wanted your students to be their own people in their professional development, and I have not been disappointed in that. I have grown so much as a researcher over these last five years, but I have also grown in many other ways, all with your enthusiastic support. Thank you for giving me a place at Caltech to become not just a well-rounded scientist but a more well-rounded person.

Next, I thank the rest of my committee for their conversations and advice. You have all added meaning to my Ph.D. experience in different ways. One of my fondest memories of my Ph.D. experience comes from my first year when I was in Mitchio Okumura's quantum chemistry class. The midterm exam was a take-home exam that had to be completed in a continuous 3-hour period. As a mother with an infant, I asked if I could break up my 3-hour time to nurse my son if he woke up while I took my exam. I had heard horror stories of the experiences of grad-parents and grad-mothers in particular, so I was terrified to ask you that question. Not only did you agree to that, you lifted the time limit for me, acknowledging that if I was called away from the exam, it might take me some time to get back into the mindset of quantum chemistry. That experience made me feel like I belong in academia as a mother and removed much of the fear I had that I would not be seen as a serious researcher.

Scott Cushing, you have been an amazing advocate for mental health, and I am so thankful to have connected with you. Thank you for addressing mental health concerns on campus and working with me to set up the mental wellness community-building lunches. I especially appreciate you speaking up, especially as a new faculty member, at town halls to validate students' concerns about their mental and general well-being.

Katherine de Kleer, I appreciate the candid advice you have given me about collaborations and professional development. Even more than that, I am thankful for the confidence you have given me in data analysis. At my first committee meeting that included you, you mentioned me being a resource to some of the Planetary Science students with respect to working with data in CASA. In one sentence, you made me realize how much I had learned and made me feel empowered in my ability to learn independently.

Throughout my Ph.D., I think I have learned the most from my fellow group mates, not just in terms of science, but in terms of friendship and advocacy. Thank you to everyone who I have connected with in the group: Marco Allodi, Ian Finneran, Danielle Piskorz, Brandon Carroll, Masha Kleshcheva, Dana Anderson, Griffin Mead, Cam Buzard, Alex Froebel, Kyle Virgil, Haw-Wei Lin, Sadie Dutton, and Albert Hsieh. Special thanks to Brandon, for getting me started with ALMA data and always encouraging me. Thank you to Dana for being my ALMA proposal dinner buddy and an ongoing resource. Kyle, I am so grateful for our coffee dates; thank you for your amazing pep talks. Griffin, thank you for swapping rides to the airport and for the chats that came with them. And to Cam, my first friend at Caltech, thank you for being a part of my family in California and being with me for every milestone along the way.

I have been fortunate to have not one but two divisions to call home during my time at Caltech. Officially, on the Chemistry side, I thank Alison Ross, graduate program coordinator extraordinaire, for being an amazing source of support for chemistry graduate students and for making my family feel welcome on campus. I also thank Elisha Jung Okawa for helping with the planning of mental health lunches.

Many thanks to the Chemistry Graduate Studies Committee, especially those who have worked on projects with me: Sadie Dutton, Joey Messinger, Krystal Vasquez, Karli Holman, Reina Buenconsejo, and Marta Gonzalvo. Chemistry is a better place because of all of you.

In Planetary Science, I thank the wonderful P. S. office staff for making South Mudd home: Irma Black, Margaret Carlos, Ulrike Terrones, Stephanie Petty, and Loreta Young. Gracias a Martín Cruz por mantener a South Mudd cómodo.

The Planetary Science grads are consistently found to be the happiest group of grad students on campus through campus climate surveys, and after having spent most of my time on campus with them, I can understand why. They are amazing. Thank you for welcoming me as an unofficial Planetary Science grad student. Special thanks to Aida Behmard, Maria Camarca, Ellen Leask, Henry Ngo, Shreyas Vissapragada, Nicole Wallack, and Mike Wong. Nicole, thank you for being not only my friend but Güni's too and for helping me use my voice. Maria, I am so glad to have found another person who will drive around and belt out "Take Me Home, Country Roads" by John Denver.

I also want to thank my fellow grad student-parents for working to make Caltech and academia in general a more friendly and supportive place for early-career folks with children.

During my time at Caltech, I have also seized opportunities to learn about and practice effective teaching pedagogy, especially through the Center for Teaching, Learning, and Outreach. Thank you to the wonderful people in that office who have supported me along the way: Jenn Weaver, Cassandra Volpe Horii, Kitty Cahalan, Mitch Aiken, Leslie Rico, and Ellie Race-Moore. Special thanks to Jenn for advising the Caltech Project for Effective Teaching and giving me the opportunity to work with you as graduate director. Thank you to my co-directors over the years: Kelsey Boyle, Rebekah Silva, Daniel Martin, and Harrison Parker. Whether we overlapped for a couple of months or for a year, I'm glad to have been your colleague.

Also related to teaching, thank you to Prof. Carl Parker for being the best co-instructor I could have asked for. In case it was not obvious by my voluntarily teaching Scientific Writing for 11 terms, teaching the class with you has been one of the highlights of my graduate school experience. Thank you for making me feel valued and for giving me the agency to develop my own teaching practices in the class.

I want to acknowledge the amazing work done by the Center for Inclusion and Diversity on campus to make Caltech a better place for everyone. I am especially thankful for the mentorship and friendship I received from Erin-Kate Escobar.

Thank you to Kate McAnulty for being a friend and advocate. I always enjoyed our interactions, from working on graduate orientation to swapping mom stories.

The last people I want to thank on campus are the librarians. Research cannot be done without librarians, and I am so thankful for having the Caltech library as a resource. I especially want to thank Donna Wrublewski for being a friend, but also for believing in my dream of writing and illustrating a book.

My growth as a scientist and person has also been fostered by many people outside Caltech. Thank you to my Dickinson College professors and mentors: Amy Witter, my forever-mentor; Sarah St. Angelo, for encouraging my enthusiasm; Rebecca Connor, for orienting me to Pasadena from afar; Jennifer Schaefer, for sharing your candid perspectives on academic culture.

I would not be an astrochemist if Green Bank Observatory (then part of the National Radio Astronomy Observatory) in West Virginia had not offered me a summer research experience despite me never having taken an astronomy course. I also do not know if I would have found my passion for public outreach without Green Bank. Thanks to the folks there who helped me then and as a Ph.D. candidate, especially Toney Mintor, Dave Frayer, Will Armentrout, and Wilson Skipper.

Thank you to Karin Öberg for giving me my first real research experience in observational astrochemistry at the Center for Astrophysics. Thank you to Edith Fayolle for being an astrochemistry research and life mentor at CfA and then in Pasadena.

To Stephan Schlemmer, Nadine Wehres, Holger Müller, Marius Hermanns, and all of the Cologne Laboratory Astrophysics Group, thank you for hosting me during my Fulbright year, but also for making me feel like family.

Thanks to the fantastic folks at the National Radio Astronomy Observatory (NRAO) and the North American ALMA Science Center (NAASC), especially Sarah Wood. Your patience and knowledge have made me a better radio astronomer. I know that when I'm having problems with my ALMA data, all I have to do is NAASC.

My academic friends on social media have also been an important part of my graduate school experience. Thank you to Gaius Augustus, Richard Hendricks, Briley Lewis, Sarah Mojarad, Erin Ryan, Susan Walden, and Ashley Walker. Extra thanks to Veronica Allen and Ilsa Cooke for sharing your astrochemistry wisdom. Finally, to Hannah Toru, thank you for being a wonderful friend and hype-person, and thank you for introducing me to many other amazing science folks, especially Sommer Johansen, who gives me strength when I want to share my vulnerabilities to let other people know they are not alone in their struggles.

Outside of academia, there are plenty of people around Pasadena who have helped me on this journey. Thank you to my therapist for helping me find myself and become a mentally healthier version of myself. Thank you to the various coffee establishments around Southern California and beyond, especially the Coffee Bean and Tea Leaf on South Lake Avenue. I know I paid for the coffee, but the friendliness and change of scenery that came with it were the true fuel. Thank you to Ransom Eaves, my frequent table neighbor at the Starbucks on South Lake. And, on the other side of the country, thank you to the folks at Denim for fueling my year of finishing my Ph.D. in a pandemic about 2,600 miles away from campus.

Most of my gratitude is reserved for my family. Rachel and Luke, thanks for being awesome younger siblings and rooting for me (even if you both own houses and have cats and Luke got a first-author research publication before me). Mom, thank you for being my best friend and filling our lives with laughter. There is so much you do for me, but as I am writing this and preparing to move, I am especially grateful for you for helping us with so many of our moves, whether it was from Germany or in California. Dad, thanks for always being proud of me and responding with "So what? You'll still have a Ph.D." when I said I was worried it would take me ten years to finish. I hope you're still proud of me even though I have not found any aliens (yet).

Finally, thank you, Güni, for making sure I take plenty of time to play. Being a student-parent comes with its challenges, but you made this experience much more fun and helped me balance work and life.

Thank you to my husband, my partner, and my best friend, Alex, for supporting me in every way possible, especially by being my personal barista and for feeding my obsession with traveling to obscure places to visit radio telescopes. Thank you for listening to every practice talk and reading just about every piece of writing. Alex, I truly could not have done this without you.

ABSTRACT

Advancements in imaging technologies have changed the ways in which we see and understand our chemical universe. Given the extreme distances between Earth, from which we observe the wider chemical universe, and the molecular clouds where stars are born, we cannot resolve the chemical structure of these interstellar laboratories on the same scales as we can with samples on Earth. Nevertheless, with the advent of larger and more sophisticated telescopes, such as the Atacama Large Millimeter/submillimeter Array (ALMA) in Chile, we can now look at interstellar chemistry on scales much smaller than the solar system. The research presented here uses ALMA to investigate the chemistry in (massive) star-forming regions in different parts of the Milky Way with high spatial resolution.

This thesis first focuses on the nearby Orion Kleinmann-Low nebula (Orion KL), the closest (at about 400 parsecs away) massive star-forming region to us, at spatial scales smaller than those of typical planetary systems. Using methanol and methyl cyanide as molecular probes, we provide new insight into the physical structure—especially the thermal structure—of the nebula by mapping physical parameters derived from observed spectra. We also use different isotopologues of methanol to understand its chemistry, specifically after it forms on the surfaces of icy dust grains. This work provides a new view of Orion KL by providing high-angular-resolution maps of parameters such as abundance and temperature, whereas much of the existing literature provides a single set of parameters for a region.

However, Orion KL is only one interstellar laboratory, and it is part of a cohort of star-forming regions that are the targets of repeated astrochemical observations. The second part of this thesis ventures into the so-called molecular ring, a region 4-8 kiloparsecs from the galactic center that has remained relatively unexplored in the context of astrochemistry. Using the Atacama Compact Array (ACA) component of ALMA, we observed a slew of millimeter-emitting objects across 11 giant molecular clouds at higher angular resolutions than most previous observations of our sample, and we characterize their chemistry for the first time. This pilot survey establishes a catalogue of interstellar laboratories for future higher-angular-resolution observations. Over time, this catalogue will drive a better understanding of the chemistry in molecular-ring young stellar objects, allowing us to see whether (and if so, how) chemistry varies across distance from the galactic center and significantly increasing the number of targets for astrochemical observations.

PUBLISHED CONTENT AND CONTRIBUTIONS

Research

Wilkins, O. H., Carroll, P. B., and Blake, G. A. Mapping Physical Parameters in Orion KL at High Spatial Resolution. *Astrophys. J.*, Accepted, 2021.

O. H. W. was the P. I. on the telescope proposal, carried out data reduction and analysis, and prepared the manuscript.

Wilkins, O. H. and Blake, G. A. *Astrochemistry*. American Chemical Society, Washington, DC, USA, 2021. DOI: `10.1021/acsinfocus.7e5004`.

O. H. W. prepared the book proposal, wrote the text, and created multiple illustrations, including the cover image.

Buzard, C., Finnerty, L., Piskorz, D., Pelletier, S., Benneke, B., Bender, C. F., Lockwood, A. C., Wallack, N. L., **Wilkins, O. H.**, and Blake, G. A. Simulating the Multi-epoch Direct Detection Technique to Isolate the Thermal Emission of the Non-transiting Hot Jupiter HD187123b. *Astron. J.*, 160(1):1, 2020. DOI: `10.3847/1538-3881/ab8f9c`.

O. H. W. assisted with observations and provided feedback on the prepared manuscript.

Teaching

Athnos, A., Kou-Herrema, T., Langley, M., Oshima, E., Parker, H., Rawal, H., **Wilkins, O. H.**, Lee, A., Hunt, S., Searle, E., and Marinho, N. "Graduate Teaching Communities of Practice: Fostering a Sense of Belonging and Professional Development for Graduate Students, by Graduate Students." *Exploring How We Teach*. Book edited by Sam Clem, 2022.

O. H. W contributed to discussions about manuscript preparation, especially about content related to the Caltech Project for Effective Teaching (CPET), and made extensive edits to the prepared manuscript.

Wilkins, O. H. and Buzard, C. F. Integrating course material and application: A progressive writing assignment applied to an astrochemistry tutorial. *Prompt: A Journal of Academic Writing Assignments*, 2(1), 2018. DOI: `10.31719/pjaw.v2i1.18`.

O. H. W. designed the writing assignment, developed surveys to collect data, and drafted the manuscript.

TABLE OF CONTENTS

LIST OF ILLUSTRATIONS

LIST OF TABLES

NOMENCLATURE

Adsorption. The process by which a molecule is held onto a solid, such as a dust grain, as a thin film.

Amino acids. Organic compounds containing an amino (-NH_2) group, a carboxyl (-COOH) group, and a side chain or functional group that are the basic units of proteins.

Arcsecond. Equivalent to 1/3600 of a degree; a measure of angular distance in celestial coordinates.

Astronomy. The scientific study of celestial objects.

Chemistry. The scientific study of the properties and behavior of matter.

Column density. The number of particles—such as molecules or atoms—per unit area, typically given in unites of cm^{-2}; this measurement is commonly used for interstellar clouds for which the depth is unknown.

Complex organic molecule (COM). A molecule found in interstellar or circumstellar space that has six or more atoms, including at least one carbon atom and one hydrogen atom.

Critical density. The density where the probability of collisional de-excitation for an excited particle is equal to the probability of radiative de-excitation.

Desorption. The process by which an adsorbed molecule is released from the surface of a solid, such as a dust grain.

Deuterium. Hydrogen isotope whose nucleus has one proton and one nucleus, making it heavier than the primary isotope of hydrogen, which has only a proton for its nucleus; heavy hydrogen; represented as ‘D’.

Emission. Electromagnetic radiation expelled due to an atom or molecule making a transition from a higher energy state to a lower energy state.

Flux density. In radio astronomy, the amount of electromagnetic radiation arriving at a telescope per second per unit area.

H II region. A region of interstellar space composed of ionized atomic hydrogen (H II).

High-mass star. A star with a mass at least 10 times that of the Sun (i.e., $\geq 10\ M_\odot$).

Hydrocarbon. An organic compound consisting of only carbon and hydrogen.

Interstellar medium (ISM). The matter and radiation between stars in a galaxy.

Isotopologues. Molecules that are chemically identical but have slightly different masses due to substitutions of heavier atoms.

Isotopomers. Variants of the same isotopologue in which the inventory of constituent isotopes is identical except for their placement.

Light-year. A unit of astronomical distance equivalent to the distance traveled by light in one year.

Low-mass star. A star with a mass of no more than four times that of the Sun (i.e., $\leq 4\ M_{\odot}$).

main sequence. The most numerous stars in the universe, used to describe “true” stars; the continuous band of stars that appears on plots of temperature (or stellar color) versus stellar brightness.

Maser. In astrophysics, a source of stimulated spectral line emission, typically at radio or microwave frequencies.

Molecular cloud. An interstellar cloud in which molecules, mostly molecular hydrogen (H_2), reside; sometimes referred to as a “stellar nursery” when it contains active star-forming regions.

Molecular ring. Term used to describe radii between about 4 and 8 kpc from the galactic center where the bulk of molecular matter in the Milky Way is thought to reside.

Molecule. A group of atoms bonded together; the fundamental unit of a chemical compound.

Nebula. A body of interstellar clouds of dust and gas.

Number density. The number of particles—such as molecules or atoms—per unit volume, typically given in units of cm^{-3}.

Protostar. A very young star still gathering mass from its parent molecular cloud; the earliest stage in stellar evolution.

Radical. An atom or molecule with at least one unpaired valence electron; these types of chemical species are highly reactive.

Radio astronomy. The subfield of astronomy that studies celestial objects at radio and microwave frequencies, or frequencies of <300 GHz; this term is often used to describe the astronomy targeting celestial objects at (sub)millimeter wavelengths as well, which includes frequencies up to ~1 THz.

Radio telescope. An antenna and radio receiver used to collect radio waves from space. At lower frequencies, radio telescopes somewhat resemble television antennas; at higher frequencies, radio telescopes look like satellite dishes.

Raman scattering. The inelastic scattering of photons by matter in which the direction of light changes and energy is transferred, typically from visible light photons to the lower-energy vibrational modes of molecules.

Scanning electron microscopy (SEM). A type of imaging in which a focused beam of electrons scans the surface of a sample and interacts with atoms on the surface to produce signals that carry information about the sample's composition and topography.

Spectroscopy. The study of interactions between matter and electromagnetic radiation as a function of radiation wavelength or frequency; a tool used to characterize matter through emitted and absorbed light.

Transmission electron miscroscopy (TEM). A type of imaging in which a beam of electrons is transmitted through an ultra thin sample, producing an image resulting from the electrons interacting with the sample.

van der Waals forces. Weak electrostatic attractive forces between neutral molecules arising from electric dipole moments.

Young stellar object (YSO). A star in the early stages of its evolution, typically classified as either a protostar or a pre-main-sequence star.

PREFACE

Over the last century, evolving instrumentation has equipped scientists to catch a glimpse of a previously hidden universe. The structures of cells, particles in the air, and synthetic materials are all far too small to be viewed with the unaided eye. However, continually evolving techniques enable us to view the microscopic aspects of our world.

Recent examples of high-resolution imaging in the chemical sciences are abundant on Caltech's own campus. For example, Miao & Wei (2020) introduced a method for viewing live cells with subcellular resolution by coupling stimulated Raman scattering microscopy with deuterium-labeled amino acids. Lakshmanan et al. (2020) developed acoustic biosensors which are molecules that show up in ultrasound images as a response to enzyme activity.

High-resolution imaging is also prevalent for non-biological systems. Transmission electron microscopy can be used to study the structures of aerosols (e.g., Zangmeister et al., 2018), and scanning electron microscopy can be used to study pores in responsive polymers that undergo physical changes instigated by their environment (Zhou et al., 2017). Jones et al. (2018) developed a technique using electron cryo-microscopy and microcrystal electron diffraction as a way to routinely and unambiguously image the structures of small organic molecules.

Evidently, these advances in imaging have been paramount to understanding our chemical and physical world on microscopic scales. This thesis is also concerned with high-resolution imaging of chemical systems. However, instead of revealing the hidden chemical universe on extremely small scales, it is concerned with astronomically large scales.

In 1933, just a few years before the first high-resolution scanning electron microscope was developed (McMullan, 1995), a radio engineer named Karl Guthe Jansky reported his accidental discovery of radio waves coming from the center of the galaxy (Jansky, 1933). Jansky's "merry-go-round" antenna (Figure 0.1) was a far cry from the radio telescopes of today. Nevertheless, it was crucial in initiating the field of radio astronomy. Antennas evolved into single-dish radio telescopes, and single-dish telescopes were connected to build interferometers, or arrays of individual radio antennas that act as one large telescope with lots of holes in it.

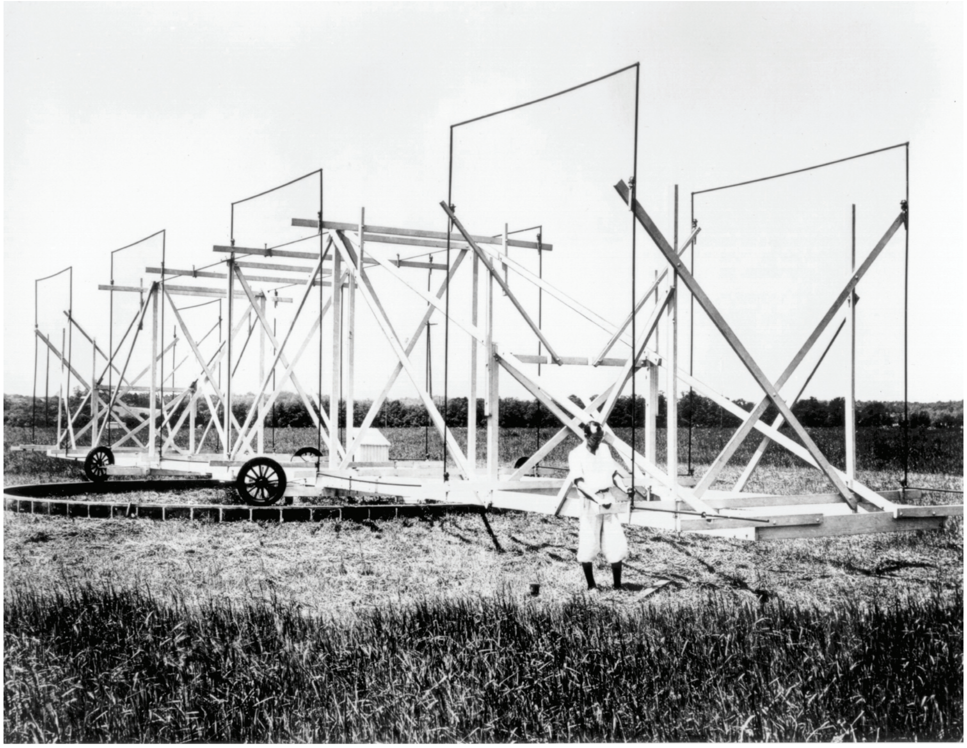

Figure 0.1: Karl Jansky and his “merry-go-round” antenna. Jansky, who was a radio engineer at Bell Telephone Laboratories, constructed this antenna to identify sources of stating that would interfere with transatlantic radio telephone communications. It was with this antenna that he discovered a steady hiss coming from the galactic center. *Credit: NRAO/AUI/NSF.*

The *soul* of this thesis is an interferometer called the Atacama Large Millimeter/submillimeter Array, or ALMA. In this thesis, ALMA is used to image the wider molecular universe with high spatial resolution. While ALMA cannot resolve individual dust grains in the interstellar medium, it can show how chemical patterns change across molecular clouds, which serve as interstellar laboratories that host some of the most extreme chemical conditions in our universe, at unprecedented angular resolution.

Because the environments studied in this thesis are at least 1,300 light-years away, we cannot make in situ measurements or collect samples of icy dust grains to bring back to Earth. Instead, we observe interstellar space from afar, specifically from the Atacama Desert at an elevation of 5,000 meters (16,000 feet) on the Chajnantor Plateau in northern Chile. ALMA (Figure 0.2) dots the plateau with 66 antennas: 50 movable dishes that are 12 meters in diameter, twelve fixed 7-meter antennas, and 4 fixed 12-meter antennas.

Figure 0.2: Illustration of some of the ALMA antennas in the Atacama Desert in Chile. *Colored pencil on paper.*

The movable aspect of the telescope allows ALMA to observe the invisible radio universe with extremely high resolution. Each of the 115-metric-tonne (127-U.S.-ton) antennas can be moved by giant transporter, giving ALMA the flexibility to be as much as 16 kilometers (10 miles) across. At its highest angular resolution (0.004″, or 0.004 arcseconds), ALMA has the equivalent resolving power of being able to photograph a U.S. dime from 575 miles away. While such high angular resolutions are not used in this thesis specifically, this nonetheless demonstrates ALMA's incredible power when it comes to synthesizing images of our broader universe.

Since achieving first light in 2011 and becoming fully operational in 2013 (Ghosh, 2011), ALMA has been used to make a number of chemical discoveries. Some of the first ALMA observations revealed chemical signatures of iso-propyl cyanide (i-C_3H_7CN), the first branched compound detected in interstellar space, near the galactic center (Belloche et al., 2014), and the simple sugar glycolaldehyde, which was detected in close proximity to an infant star for the first time (Jørgensen et al., 2012). ALMA has also been used to intimately study the distribution of different chemical compounds, such as hydrocarbon chain molecules around protostellar cores (Sakai et al., 2014).

In this thesis, molecular signatures observed with ALMA act as probes of the physical and chemical conditions of interstellar environments. A brief introduction to astrochemistry, the field comprising this work, is given in Chapter 1. Chapters 2-4 discuss observational work focused on the Orion Kleinmann-Low nebula, and Chapters 5-6 focus on observations of giant molecular clouds in the molecular ring of the Milky Way. A summary of the thesis and outlook are given in Chapter 7. Appendices A-I provide supplemental information to the aforementioned chapters.

In addition to the research that constitutes this thesis, teaching and service have been important aspects of my graduate experience. Activities and accomplishments in these areas are summarized in Appendices J and K, respectively.

References

Belloche, A., Garrod, R. T., Müller, H. S. P., & Menten, K. M. 2014, *Science*, 345, 1584, doi: `10.1126/science.1256678`

Ghosh, P. 2011, Alma telescope begins study of cosmic dawn. `https://www.bbc.com/news/science-environment-15107254`

Jansky, K. G. 1933, *Nature*, 132, 66, doi: `10.1038/132066a0`

Jones, C. G., Martynowycz, M. W., Hattne, J., et al. 2018, *ACS Cent. Sci.*, 4, 1587, doi: `10.1021/acscentsci.8b00760`

Jørgensen, J. K., Favre, C., Bisschop, S. E., et al. 2012, *Astrophys. J. Lett.*, 757, L4, doi: `10.1088/2041-8205/757/1/L4`

Lakshmanan, A., Jin, Z., Nety, S. P., et al. 2020, *Nat. Chem. Biol.*, 16, doi: `10.1038/s41589-020-0630-x`

McMullan, D. 1995, *Scanning*, 17, 175

Miao, K., & Wei, L. 2020, *ACS Cent. Sci.*, 6, 478, doi: `10.1021/acscentsci.9b01196`

Sakai, N., Sakai, T., Hirota, T., et al. 2014, *Nature*, 507, 78, doi: `10.1038/nature13000`

Zangmeister, C. D., You, R., Lunny, E. M., et al. 2018, *Carbon*, 136, 85, doi: `10.1016/j.carbon.2018.04.057`

Zhou, Y., Huang, J., Sun, W., et al. 2017, *ACS Appl. Mater. Interfaces*, 9, 4177, doi: `10.1021/acsami.6b13525`

Chapter 1

INTRODUCTION

The content in this chapter is discussed more fully in the following text:

Wilkins, O. H. and Blake, G. A. *Astrochemistry*. American Chemical Society, Washington, DC, USA, 2021. DOI: `10.1021/acsinfocus.7e5004`.

Astrochemistry is an interdisciplinary field that addresses matter in space, from what types of molecular compounds are out there to how these molecules form and interact with each other and with stellar radiation. Despite being rooted in two fields that have ancient origins in proto- and pseudo-scientific fields, namely alchemy and astrology, astrochemistry has emerged only relatively recently.

Astrochemistry relies on spectroscopy in both its observational astronomy and laboratory chemistry branches. The modern field of spectroscopy emerged in the 17th century, but it was not until two centuries later that spectroscopy truly laid the foundation for astrochemical research. In the 1800s, William and Margaret Lindsay Huggins used spectroscopy to reveal for the first time that hazy nebulae dotting the night sky were not clusters of distant stars but a "luminous gas" (Huggins, 1897, 1898). This gas was composed of some mysterious element dubbed *nebulum* or *nebulium* that was later identified, in 1927, as doubly ionized atomic oxygen emission (Bowen, 1927).

The first *molecule* discovered in space was the methylidyne radical, or CH, in 1937 (Dunham, Jr., 1937; Swings & Rosenfeld, 1937). Since then, nearly 250 compounds have been detected in interstellar and circumstellar space. These molecules provide us with an interesting perspective of chemistry because interstellar space contains some of the most extreme conditions in the universe.

Interstellar space is extremely cold and diffuse by terrestrial standards. Stars form in the coldest regions of space, which have temperatures of about 10 K (−263 °C, −442 °F) (Evans et al., 2009). Stars also form from the densest gas with number densities of around 10^4–10^6 molecules cm^{-3}. Whereas this is dense in the interstellar medium

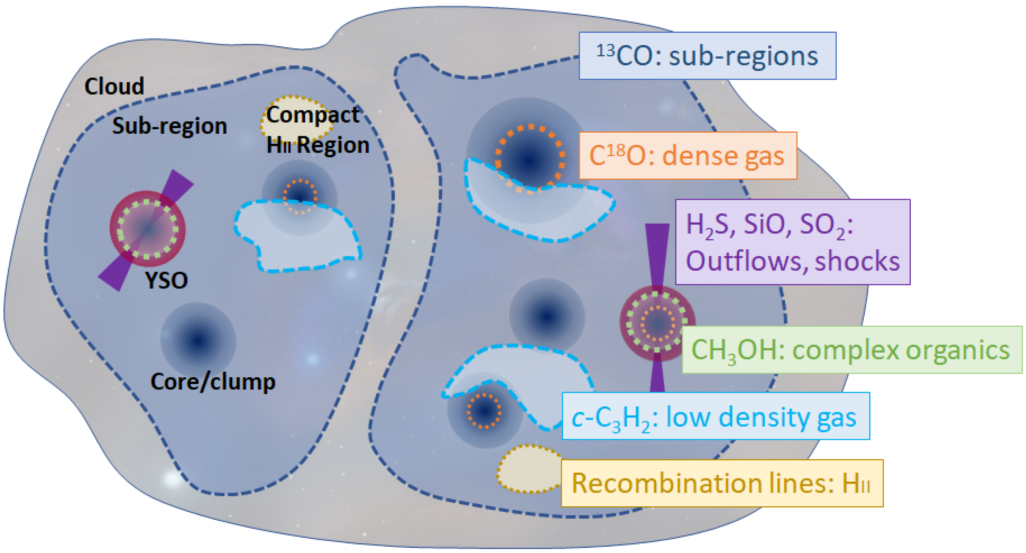

Figure 1.1: Schematic of a molecular cloud and examples of molecular tracers that can tell us about different interstellar environments.

(ISM) , it is sparse by terrestrial standards; even the air we breathe has about 10^{19} molecules cm^{-3}.

Molecules can also be used as probes of the physical environments in space. The spectra, or chemical fingerprints, of interstellar molecules carry important information about the velocity, temperature, and abundance of gas. The types of molecules seen can also reveal much about the physical conditions of an environment (Figure 1.1). Besides molecular hydrogen (H_2), carbon monoxide (CO) is the most abundant chemical compound produced in molecular clouds. The isotopologues—or molecules that are chemically identical but have slightly different masses due to substitutions of heavier atoms—of CO can be used to identify regions of higher density than the ambient molecular cloud. For instance, ^{13}CO can be used to locate subregions within a cloud, and $C^{18}O$ traces dense gas, typically associated with the cores of infant stars. Such cores have also been found to host complex organic molecules (COMs), which have six or more atoms; methanol (CH_3OH) is often used to search for places likely to be rich in COMs. Simple molecules containing sulphur and silicon, such as H_2S, SiO, and SO_2, reveal the location of molecular outflows or jets emanating from evolving young stellar objects (YSOs). Other molecules, such as cyclopropenylidene (c-C_3H_2), instead trace low-density gas in the outer regions of YSOs.

In this thesis, methanol is the primary chemical targeted in astronomical observations. Methanol is used—along with some other compounds, namely methyl cyanide (CH_3CN) and $C^{18}O$—to reveal new information about massive star-forming regions, from the already well-studied but still-enigmatic Orion KL (Chapter 2) to new chemical stockrooms in a region of the galaxy called the molecular ring (Chapter 6). This thesis also studies the chemistry of methanol, specifically addressing questions previously unanswered about what happens to this molecule *after* it forms (Chapter 3).

Before learning about the research culminating in this thesis, we must first understand, broadly, how astrochemical research is conducted as well as the types of big picture questions about our wider chemical universe that can be answered by this field.

1.1 Approaches to Astrochemical Research

Astrochemistry research integrates observational astronomy, laboratory astrophysics, and computational modeling and theory. Early observations of interstellar molecules were made using optical and ultraviolet (UV) telescopes, which target electronic transitions of atoms and molecules. This includes the detection of CH using the 100-inch telescope at Mount Wilson Observatory (Figure 1.2). However, such transitions require high amounts of energy found in stellar atmospheres or nebulae energized by the light from stars. Instead, much of observational astrochemistry, specifically that of molecular clouds and YSOs, comes from IR and radio astronomy.

Most observational astrochemistry uses radio telescopes, which are tuned to collect the signals from distant molecules tumbling and rotating in interstellar gas. Radio telescopes are able to "see" through Earth's atmosphere without much interference except for some water emission. For this reason, many radio telescopes are built in deserts or at high altitudes to circumvent much of the atmosphere's water vapor. For example, the Atacama Large Millimeter/submillimeter Array (ALMA) sits high up in the Chilean Desert at an elevation of 5 kilometers (16,400 feet).

IR astronomy is also important, but instead of capturing the signals from molecular rotations, IR telescopes detect molecular vibrations. This is useful for observing compounds in the gas that are nonpolar (or whose electrons are shared equally across all bonds, meaning their movements do not produce any changes in rotational state), such as methane (CH_4). IR is also used to study molecules locked up in ices on interstellar dust grains. Unlike radio astronomy, however, IR astronomy is quite

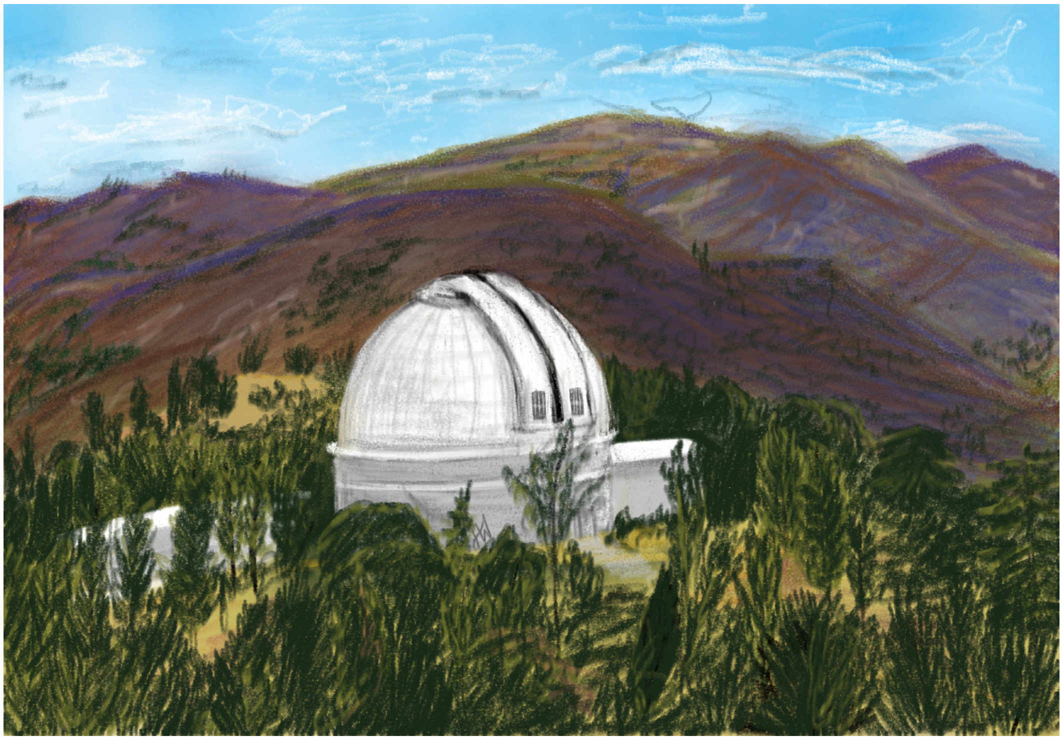

Figure 1.2: Illustration showing the dome of the 100-inch Hooker telescope atop Mount Wilson in southern California. The observatory is visible from Caltech's campus. This illustration was digitally hand-drawn in Microsoft Paint by O. H. W.

sensitive to molecules in Earth's atmosphere. As such, IR telescopes are built at high elevations or, when budgets allow, as space telescopes.

There is also plenty of astrochemistry conducted in terrestrial laboratories. Some laboratory work measures the spectra of molecules under (ultra-)high vacuum conditions to compile spectroscopic databases which allow astronomers to identify what molecules are detected with their telescopes. Other experimental work looks at the kinetics of gas-phase chemistry or watches to see what products form on irradiated interstellar ice analogues.

Finally, computational modeling is used to contextualize what is observed in space or what is seen in the lab. Theorists make assumptions about the initial conditions in star-forming regions and try to extrapolate what led to the molecular abundances observed in the present. Theory can also make use of molecular emission as a sort of chemical clock to determine the age or evolutionary state of a YSO. Computational work also helps when making predictions about what chemistry will be observable.

All of these pieces are needed to assemble the astronomical puzzle that is astrochemistry. Although this thesis is centered on observational work, results from experiments and theory are incorporated into the discussion throughout.

1.2 Differences between Chemistry and Astronomy

Although this is a chemistry dissertation, the research included in it falls within the realm of astronomy. There are some key differences between the conventions of both fields, and some of these conventions will make any true chemist squirm. For instance, to the astronomer, every element heavier than helium is a “metal.” This means that carbon, oxygen, and nitrogen—non-metals to the terrestrial chemist—are all considered metals. Similarly, the pressures and temperatures of interstellar space are too low for liquid phases of matter, which means astronomers sometimes use the term “evaporate” to mean going from a solid to a gas (i.e., sublimation) instead of going from a liquid to a gas (which is the definition used by chemists).

Other differences between the two fields come from a physical frame of reference. On a celestial map, the east and west directions are swapped; if north is up, west is right and east is left. This is because we think of the sky, and its coordinates, as a sphere that envelops our world. Because we observe the cosmos from inside that sphere, east and west are swapped from our vantage point.

Temperatures are also quite different from what a terrestrial chemist is accustomed to. Both chemistry and astronomy can agree that 10 K is “cold,” but in the interstellar medium, temperatures of 100 K or more are considered “warm.” Room temperature on Earth is 300 K, so 100 K is much colder at -173 °C or -280 °F.

Finally, timescales are quite different. To the terrestrial chemist, long timescales may mean experiments take a few days or even weeks. But such timescales in the interstellar medium, where stars evolve over millions of years, are considered fast. For example, molecular hydrogen (H_2) forms as quickly as hydrogen atoms can arrive to the surfaces of dust grains, which happens about once per Earth-day. The observed abundances of methanol described throughout the thesis are the product of $\sim 10^5$ years of chemical reactions that proceed alongside star formation.

1.3 Star Formation

Much of astrochemistry addresses the evolution of chemical complexity alongside star formation. Much of what we know about star formation comes from observations of nearby, low-mass stars. The star formation sequence gleaned from such observations is outlined below. A similar model of star formation is applied to high-mass stars. However, there are some uncertainties for high-mass star formation, specifically at the beginning of the evolutionary sequence (e.g., Motte et al., 2018).

Stars are seeded in molecular clouds when dense clumps of gas form. Cold cores form at the center of these clumps, and gravity pulls material inward while gas pressure pushes material out, keeping the core in hydrostatic balance. As the core rotates, it begins to flatten out, forming a disk.

Material continues to accrete onto the core. At some point, enough material has been accreted that the force of gravity overcomes the gas pressure. The core collapses, and a protostar is born. This protostar is composed of dense gas and dust in a ratio of 100:1; this material is gradually warmed to temperatures of $>$100 K as the infant star grows. The protostar is enveloped in a cooler envelope, and it is also flanked by bipolar outflows or jets. To conserve angular momentum as it rotates, the protostar flattens even more to produce a circumstellar disk.

After about 10^5-10^6 years, the envelope dissipates, leaving the infant star in the protoplanetary disk stage. The protoplanetary disk continues to feed material into the infant star. This disk is also where planets and other bodies form. After another 10^4-10^5 years, planets form and the remaining gas in the disk dissipates, leaving behind a debris disk of protoplanets, dust grains, and other rubble.

1.4 Interstellar Chemical Processes

The molecules detected alongside every stage of stellar evolution are part of a complicated chemical network. Disentangling the reactions in this network is the primary goal of astrochemistry. Gas-phase and grain-surface chemistries are often treated as competing categories of molecule formation, but the bulk of the chemistry in the ISM relies on a coupled gas-grain chemistry. This is perhaps best exemplified by water (van Dishoeck et al., 2021), as illustrated in Figure 1.3. There are indeed separate processes that are carried out on the grains versus in the gas, and there are more reactions still that connect these two camps.

Coupled gas-grain chemistry is also imperative for complex organic chemistry, specifically. Molecular hydrogen (H_2), which forms on grains, is a key aspect of chemical evolution because H_2 not only reacts with other species but it helps to regulate the physical environment, for example by cooling the gas through collisions. Other molecules that form on grains or are frozen out onto grains also provide the chemical backbone of more complex species. The cold conditions of early star

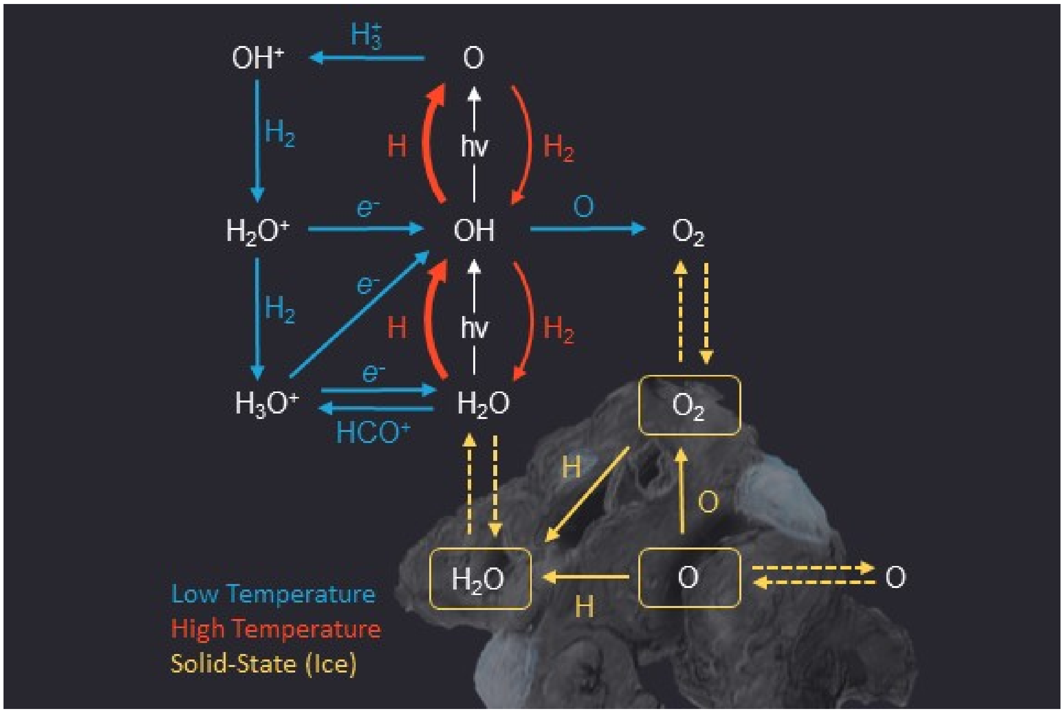

Figure 1.3: In coupled gas-grain networks, like the reaction network for water, some compounds form and reaction on the surface of icy grain mantles (yellow arrows). In the gas phase, the reactions that proceed depend on whether the gas is at a low temperature (blue) or a high temperature (red). In this figure, dashed arrows represent a phase change, either sublimation off the grains and into the gas, or freeze-out of the gas onto the grains. The illustration of the dust grain was digitally hand-drawn in Microsoft Paint by O. H. W.

formation also require energetic input from cosmic rays and photons, which break apart molecules and atoms to produce ionic species.

These conditions provide a chemical stockroom by which a wide range of different types of chemical reactions can proceed. The types of chemical reactions that take place in the ISM include neutral-neutral reactions (typically at higher temperatures), ion-neutral reactions, and electron-molecule reactions. There are also radiation-induced processes in which photons break apart chemical constituents.

In addition to reactions, chemistry is also facilitated by adsorption onto and desorption off of the surfaces of grains. Adsorption can be either a physical phenomenon (called physisorption) or involve a chemical bond (chemisorption). Physisorption involves weak van der Waals forces at low temperatures, which allows adsorbed atoms to be highly mobile on the grain surface. Chemisorption is much stronger and keeps an atom bonded long enough that other atom can collide with it to react.

1.5 Astronomical Questions

With all of this in mind, this thesis addresses several questions related to (massive) star formation and the accompanying chemical processes.

What are the sources of heating that facilitate the chemistry in the Orion Kleinmann-Low nebula?

What molecular emission can reveal about sources of heating is discussed in Chapter 2. The Orion Kleinmann-Low nebula (Orion KL) is notoriously complex and exhibits a range of physical and chemical components. We conducted high-angular-resolution (subarcsecond) observations of $^{13}CH_3OH$ $\nu = 0$ (~$0\farcs3$ and ~$0\farcs7$) and CH_3CN $\nu_8 = 1$ (~$0\farcs2$ and ~$0\farcs9$) line emission with ALMA to investigate Orion KL's structure on small spatial scales ($\leq$350 au). Gas kinematics, excitation temperatures, and column densities were derived from the molecular emission via a pixel-by-pixel spectral line fitting of the image cubes, enabling us to examine the small-scale variation of these parameters. Subregions of the Hot Core—one of Orion KL's components—have a higher excitation temperature in a $0\farcs2$ beam than in a $0\farcs9$ beam, indicative of possible internal sources of heating. Furthermore, the velocity field includes a bipolar ~7-8 km s^{-1} feature with a southeast-northwest orientation against the surrounding ~4-5 km s^{-1} velocity field, which may be due to an outflow. We also find evidence of a possible source of internal heating in the Northwest Clump, since the excitation temperature there is higher in a smaller beam versus a larger beam. Finally, the region southwest of the Hot Core (Hot Core-SW) presents itself as a particularly heterogeneous region bridging the Hot Core and Compact Ridge. Additional studies to identify the (hidden) sources of luminosity and heating within Orion KL are necessary to better understand the nebula and its chemistry.

Methanol after it forms on the surfaces of icy grains, but how does it get injected into the gas phase?

While methanol is widely accepted to form on the surfaces of icy dust grains through successive hydrogenation of carbon monoxide (CO), how this molecule is injected into the gas phase where it is observed by radio telescopes is less understood. Chapter 3 provides insights into this question. ALMA observations of $^{13}CH_3OH$ at high angular resolution were used to investigate the desorption of methanol in Orion KL. We conclude that thermal desorption is the primary driver of methanol desorption in Orion KL, specifically in the Compact Ridge and the Hot Core-SW.

This conclusion is based on plots showing that the abundance of $^{13}CH_3OH$ rises with temperature, only moderate enhancements in abundance across the nebula (whereas shocks would be marked by large enhancements), and narrow line widths. Chapter 3 discusses thermal desorption being driven by young stellar objects, and it also discusses non-thermal desorption mechanisms that may be at play at colder temperatures. While this does not universally answer the question of how methanol transitions from being a solid on icy grains to being incorporated into the molecular gas, it addresses this question in Orion KL.

Why are singly-deuterated methanol abundances not what we expect?

In high-mass star-forming regions, the abundance of CH_3OD relative to CH_2DOH is enhanced compared to the statistical ratio. The deviation of the $[CH_2DOH]/[CH_3OD]$, which is $\sim$1 in Orion KL, from the expected value of 3 has been attributed to both grain-surface and gas-phase processes. In Chapter 4, we investigate the relationship between CH_3OD abundance and temperature observed in Orion KL. We find evidence of a jump in abundance between 100 and 125 K, which we attribute to rapid D/H exchange between the CH_3OH hydroxyl (-OH) group and deuterated water in the ices. In some regions of Orion KL, we see a sharp decrease in the abundance of CH_3OD around 200 K, which we suspect is the result of gas-phase processes in which deuterated methanol is protonated before undergoing dissociative recombination, converting CH_3OD into the primary isotopologue (CH_3OH). This work provides a unique perspective by mapping changes in CH_3OD abundance with respect to temperature, where as most existing work centers on single sets of parameters. Future investigations of CH_3OD, specifically through experiments and computational models, and CH_2DOH, through observations, are needed to further constrain the peculiar deuterated methanol chemistry in Orion KL and other sources. In particular, the work presented in this chapter calls for investigations of D/H exchange across a range of temperatures between methanol and water in ices and of methanol in the gas.

How can we make the current sample of interstellar laboratories more representative of chemistry throughout the galaxy?

Chapter 5 provides an overview of a survey of molecular-ring objects to find new YSOs for astrochemical observations. Much of our understanding of the chemistry that evolves alongside star formation comes from studies of nearby low-mass star-forming regions. Detailed astrochemical imaging of high-mass star formation has been limited to a few well-known, typically complex sources. Giant molecular clouds (GMCs) are prime hunting grounds for additional high- and intermediate-mass young stellar objects (YSOs) toward which we can constrain chemical abundances and possible formation mechanisms in these environments. We conducted a survey of 11 compact, millimeter-bright GMCs in the molecular ring with the Atacama Compact Array (ACA) component of the Atacama Large Millimeter/submillimeter Array (ALMA). In Chapter 5, we present the 1.2 mm dust continuum images of these GMCs, which reveal 96 millimeter-emitting sources. We also conducted an extensive literature search to see what is known about the detected millimeter-emitting sources and identified 41 objects that are associated with known YSO or YSO candidates from previous surveys. Of these, 14 of the 1.2 mm continuum sources also coincide with 70 μm emission, a signature perhaps of either icy dust grains or warm dust close-in to a YSO, as seen by Herschel. From this pilot survey, we identify candidate sources for follow-up high-spatial-resolution observations to further our understanding of gas (e.g., with ALMA) and grain (e.g., with JWST) chemistry in high-mass star-forming regions.

What does chemistry look like in the so-called molecular ring?

Several YSOs are characterized in terms of their chemistry for the first time in Chapter 6. The so-called molecular ring at galactic radii of 4-8 kpc is thought to house the majority of molecular matter in the galaxy. Nevertheless, it is notably absent from the existing astrochemical literature. We conducted a spectral line survey simultaneously with the continuum emission survey presented in Chapter 5. We report on the distribution of a variety of chemical tracers in he sample of 11 molecular-ring GMCs. We also fit CH_3OH molecular emission to get a first look at the column densities and temperatures in these objects. This work provides a roster of new interstellar laboratories to be observed at high angular resolution.

Finally, all of this is summarized in Chapter 7, which also provides an outlook on the work presented herein.

References

Bowen, I. S. 1927, *Nature*, 120, 473, doi: `10.10388/120473a0`

Dunham, Jr., T. 1937, *Publ. Astron. Soc. Pac.*, 49, 26, doi: `10.1086/124759`

Evans, Neal J., I., Dunham, M. M., Jørgensen, J. K., et al. 2009, *Astrophys. J. Supp.*, 181, 321, doi: `10.1088/0067-0049/181/2/321`

Huggins, M. L. 1898, *Astrophys. J.*, 8, 54, doi: `10.1086/140540`

Huggins, W. 1897, *Ninet. Century*, 41, 907

Motte, F., Bontemps, S., & Louvet, F. 2018, *Annu. Rev. Astron. Astrophys.*, 56, 41, doi: `10.1146/annurev-astro-091916-055235`

Swings, P., & Rosenfeld, L. 1937, *Astrophys. J.*, 86, 483, doi: `10.1086/143880`

van Dishoeck, E. F., Kristensen, L. E., Mottram, J. C., et al. 2021, *Astron. Astrophys.*, 648, A24, doi: `10.1051/0004-6361/202039084`

Chapter 2

MAPPING PHYSICAL PARAMETERS IN ORION KL AT HIGH SPATIAL RESOLUTION

The content in this chapter is adapted from the following article:

Wilkins, O. H., Carroll, P. B., and Blake, G. A. Mapping Physical Parameters in Orion KL at High Spatial Resolution. *Astrophys. J.*, accepted 18 October 2021.

2.1 Introduction

Molecules are useful tools for characterizing the physical structure of dense interstellar environments (e.g., Herbst & van Dishoeck, 2009; Ginsburg et al., 2017; Moscadelli et al., 2018; Gieser et al., 2019; Law et al., 2021). As has been illustrated repeatedly with the Orion Kleinmann-Low nebula (Orion KL; $d \sim 388$ pc)—the closest region of high-mass star formation to the Earth (Kounkel et al., 2017)—different types of molecules can be used to trace different types of environments and conditions in interstellar material. In Orion KL, the complex interplay of dense molecular gas and star formation is traced by several components, such as the Hot Core, the Compact Ridge, the Extended Ridge, and the Plateau regions, each of which has varying chemical and physical properties (e.g., Blake et al., 1987; Friedel & Widicus Weaver, 2011; Feng et al., 2015; Tercero et al., 2018; Luo et al., 2019; Cortes et al., 2021). Figure 2.1 shows a schematic representation of Orion KL illustrating regions discussed in this work. The variety of chemical and physical properties, as well as the readily detectable emission lines from isotopologues (e.g., Neill et al., 2013), observed toward Orion KL, make it an excellent laboratory for studying the formation and subsequent chemistry of molecules in high-mass star-forming regions.

Generally, the two dominant subregions of Orion KL that harbor complex chemistry are the so-called "Hot Core," which contains denser and warmer gas ($n_{\mathrm{H}_2} \sim 10^7$ cm^{-3}, $T_{kin} \sim 200$ K), and the "Compact Ridge" that lies to the southwest of the Hot Core, and which is both cooler and less dense ($n_{\mathrm{H}_2} \lesssim 10^6$ cm^{-3}, $T_{kin} \sim 100{-}150$ K; Blake et al., 1987; Genzel & Stutzki, 1989). The regional variation in physical

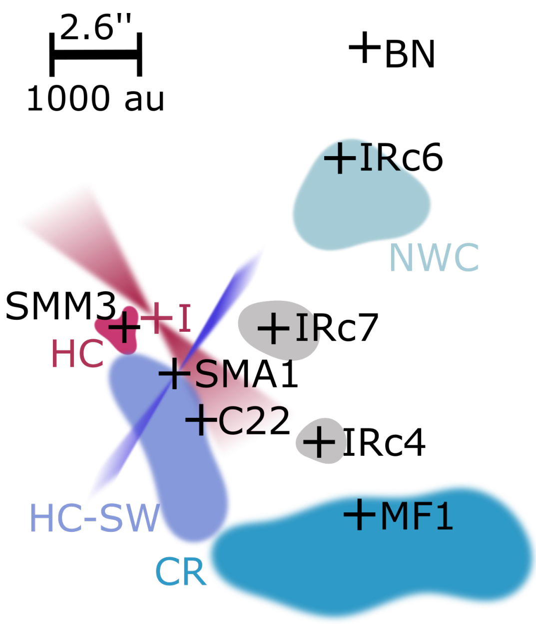

Figure 2.1: Illustration of Orion KL's morphology, as seen in the plane of the sky. Regions of interest include Source I (I), the Hot Core (HC), the Hot Core-Southwest (HC-SW), the Compact Ridge (CR), and the Northwest Clump (NWC). The crosses indicate specific emission regions that are discussed in the text. The scale bar in the top left corresponds to a linear scale of ∼1000 au (2.6″) at Orion KL's distance of 388 pc.

conditions has also resulted in large-scale variation in the chemistry, with the Hot Core and Compact Ridge being the sites of prominent emission from nitrogen-bearing and oxygen-bearing species, respectively (e.g., Blake et al., 1987; Friedel & Widicus Weaver, 2011).

The variation in both the physical conditions and chemistry of Orion KL has been well documented across various spatial scales, e.g., ∼20″-43″ with Herschel/HIFI by Wang et al. (2011); ∼0.″5−5.″0 with CARMA by Friedel and Widicus Weaver (Friedel & Widicus Weaver, 2011); and ∼2.″6−3.″7 with combined SMA and IRAM 30m data by Feng et al. (2015). There has also been high-angular-resolution millimeter continuum imaging of the nebula, e.g., by Hirota et al. (2015) at ∼0.″5 with ALMA. Ginsburg et al. (2018) and Wright et al. (2020) imaged continuum and line emission specifically toward the disk and outflow of Source I alone down to 0.″03.

Observations of molecular line emission have shed light on both the velocity structure and sources of heating within Orion KL. Ammonia (NH_3) and methyl formate ($HCOOCH_3$), for example, have been used to trace the velocity fields throughout the nebula at subarcsecond angular scales (e.g., Goddi et al., 2011; Pagani et al., 2017).

CH_3OH, $HCOOCH_3$, thioformaldehyde (H_2CS), and cyanoacetylene (HC_3N) are included in the suite of molecules used to probe whether Orion KL's different components are internally or externally heated, a question that remains the subject of debate toward the Hot Core specifically (de Vicente et al., 2002; Goddi et al., 2011; Zapata et al., 2011; Crockett et al., 2014b; Orozco-Aguilera et al., 2017; Peng et al., 2017; Li et al., 2020).

Even with these studies, many questions remain about the nature of Orion KL. Investigations of the nebula's three-dimensional (3D) structure, for example, have mostly looked at the so-called high-energy "fingers" and "bullets" emanating on arcminute scales from an explosion that took place in the nebula about 500 years ago (Nissen et al., 2007; Bally et al., 2015; Youngblood et al., 2016; Bally et al., 2017). However, a more small-scale view of the 3D structure of the dense molecular gas in Orion KL is largely absent in the literature, despite continuum and molecular line emission imaging showing that both the physical and chemical complexity of Orion KL are not simply regional but are manifest on more localized scales as well. That is, while the physical and chemical aspects of Orion KL can be divided into large areas such as the dense, nitrogen-rich Hot Core and the less dense, oxygen-rich Compact Ridge, there is growing evidence suggesting that this heterogeneity extends to within these subregions of the nebula as well (e.g., Friedel & Widicus Weaver, 2011; Crockett et al., 2014b).

Thus far, the results of high-angular-resolution imaging of Orion KL have generally focused on distinct regions or line emission peaks. Such observations at various spatial scales are imperative to understanding the physical and chemical conditions of star-forming regions, and they reveal that there is still much to uncover in Orion KL.

Here we present a more localized ($\sim 0.''9$-$0.''2$) view of Orion KL using a combination of ground-state $^{13}CH_3OH$ and vibrationally excited CH_3CN line emission with the Atacama Large Millimeter/submillimeter Array (ALMA). These compounds are both complex (i.e., have at least six atoms) and (near) symmetric top molecules, which means they have spectra that are both abundant in lines and relatively simple, such that deriving their abundances and temperatures is rather straightforward. We specifically target methanol to trace colder, less dense gas; the carbon-13 methanol isotopologue was specifically targeted because it serves as an optically thin proxy for the primary carbon-12 isotopologue, which is optically thick toward Orion KL. Similarly, CH_3CN $\nu_8 = 1$ was selected to trace hotter and denser gas, to probe high-energy emission excited by massive embedded protostars, and because ground-state CH_3CN is optically thick toward the Orion KL Hot Core.

The observations presented here complement previous studies of Orion KL to further elucidate the small-scale physical structure of the nebula. The angular resolutions (from $0.''9$ down to $0.''2$) were deliberately chosen to enable observations of disk-like scales at the expense of resolving out extended emission that is already widespread in the existing literature. Combining both molecular tracers in a single analysis is needed to characterize the wide range of environments in Orion KL, especially in light of the longstanding observations that nitrile and oxygen-bearing organic emission lines are kinematically and spatially distinct, even at 10-30″ spatial resolution (e.g., Blake et al., 1987; Crockett et al., 2014b). We find that our observations agree overall with previous studies toward Orion KL; however, we resolve spatial structure at scales on the order of protoplanetary disks, which lie within radii typically associated with molecular abundance enhancements caused by heating from embedded protostars (Boonman et al., 2001; Schöier et al., 2002). Furthermore, our results provide new insights to the kinematics and thermal profile of the nebula.

The ALMA observations and an overview of the data analysis are described in Sections 2.2 and 2.3, respectively. The chemical distribution, including column density measurements, is discussed in Section 2.4. A discussion of the physical and chemical structure in Orion KL, including line width and velocity field maps, is presented in Section 2.5. Section 2.6 provides a discussion of derived temperature maps and possible sources of heating. The results of this work are summarized in Section 2.7.

2.2 Observations

Observations of Orion KL were taken in ALMA Cycles 4 and 5 with a pointing center of $\alpha_{\rm J2000} = 05^{\rm h}35^{\rm m}14.^{\rm s}50$, $\delta_{\rm J2000} = -05^\circ22'30.''9$. All observations were carried out with the 12-meter array.

The Cycle 4 observations (project code #2016.1.01019, PI: Carroll) include the CH_3CN $v_8 = 1$ lines used in these analyses. These observations comprised two epochs, each with one execution block and and one spectral window covering a frequency range of 146.83-147.77 GHz in Band 4 at a spectral resolution of 488.28 kHz ($\sim$1.0 km s^{-1}). The Cycle 4 data taken on 2016 October 2 used 44 antennas with projected baselines between 18.6 and 3.2 km (9.3kλ and 1600kλ) and a primary beam (field of view) of 39.8″. The on-source integration time was 455 s. The precipitable water vapor was 2.1 mm, and typical system temperatures were around 50-100 K. The observations taken on 2016 November 28 used 47 antennas with projected baselines between 15.1 and 704.1 m (7.6kλ and 350kλ) and a primary beam of 39.8″. The on-source integration time was 151 s. The precipitable water vapor was 1.9 mm, and typical system temperatures were around 50-100 K.

The Cycle 5 observations (project code #2017.1.01149, PI: Wilkins) include the $^{13}CH_3OH$ $v = 0$ lines used in these analyses. These observations comprised one execution block and 10 spectral windows, three of which contained the targeted $^{13}CH_3OH$ lines. These three windows covered frequency ranges of 155.13-155.37, 155.57-155.80, and 156.06-156.29 GHz in Band 4 at spectral resolutions of 244 kHz (~0.5 km s^{-1}). These observations were carried out on 2017 December 14 and used 49 antennas with projected baselines between 15.1 m and 3.3 km (7.6kλ and 1650kλ) and a primary beam of 39.1″. The on-source integration time was 2062 s. The precipitable water vapor was 3.7 mm, and typical system temperatures were around 75-125 K.

The spectra for each molecular probe analyzed here were confined to a single correlator subband; as such, the uncertainties for quantities derived from for these molecular probes are dominated by the thermal and phase noise and are mostly unaffected by systemic calibration uncertainties. Calibration was completed using standard CASA calibration pipeline scripts using CASA 4.7.0 for Cycle 4 data and CASA 5.1.1-5 for Cycle 5 data. The source J0423−0120 was used as a calibrator for amplitude, atmosphere, bandpass, pointing, and water vapor radiometer (WVR) variations, while J0541−0211 was used as a phase and WVR calibrator.

The image cubes presented here were created with continuum emission estimated from line-free channels subtracted in the UV-plane using the `uvcontsub` task in CASA.

Cycle 4 Data Reduction

The Cycle 4 data were processed in CASA 4.7.0 using the Cycle 4 ALMA data processing pipeline[1], which used the `tclean` algorithm with Briggs weighting and and a pipeline-generated mask. A robust parameter of 0.5 was used for deconvolution. The resulting continuum and line images are primary beam corrected and have a noise level of $\sigma_{\rm RMS} \sim 1.2$ mJy beam^{-1}. Comprising two epochs, which yield images of CH_3CN $v_8 = 1$ at two angular resolutions, the Cycle 4 data taken on

---

[1] Pipeline-Cycle4-R2-B, r38377 (ALMA Pipeline Team, 2016).

2016 October 2 have a $0\farcs23\times0\farcs21$ synthesized beam (hereafter identified using the shorthand $0\farcs2$), which corresponds to linear scales of ~90 au in Orion KL, with a position angle of PA = -8°. Images from observations on 2016 November 28 have a synthesized beam of $1\farcs13\times0\farcs72$ (hereafter $0\farcs9$), which corresponds to linear scales of ~350 au in Orion KL, with PA = -71°.

The targeted CH_3CN $v_8 = 1$ lines in these data were also detected in Cycle 2 observations (project #2013.1.01034, PI: Crockett; (Carroll, 2018)) toward Orion KL but at an angular resolution of ~$2\farcs0$ (~800 au). Comparing the integrated intensities for the CH_3CN lines listed in Table 2.1, we find that we recover ~28% and ~16% of the flux integrated over the whole Orion KL region in the $0\farcs2$ and $0\farcs7$ images, respectively, compared to what is recovered in the $2\farcs0$ observations.

Cycle 5 Data Reduction

The Cycle 5 data were similarly processed in CASA 5.1.1-5 using the `tclean` algorithm (interactive) with Briggs weighting and the 'auto-multithresh' masking algorithm (Kepley et al., 2020). A robust parameter of 1.5 (i.e., seminatural weighting) was used for deconvolution to overcome significant artifacts that obstructed analysis of the images when using a robust parameter of 0.5. One possible explanation for these artifacts is that the $^{13}CH_3OH$ emission is extended such that it is difficult to image at longer baselines, thus requiring a robust parameter that gave higher weights to shorter baselines. The images are primary beam corrected and have a noise level of $\sigma_{\rm RMS} \sim 1.0$ mJy beam^{-1}.

There was only one set of observations taken, on 14 December 2017, toward Orion KL during the Cycle 5 program. These images have a synthesized beam of $0\farcs34\times0\farcs20$ (hereafter $0\farcs3$), which corresponds to linear scales of ~110 au in Orion KL, with PA = -56°. To compare the $^{13}CH_3OH$ emission on multiple spatial scales, we reimaged these data splitting the measurement set to include only baselines of ≤500 m, resulting in a synthesized beam of $0\farcs74\times0\farcs63$ (hereafter $0\farcs7$), which corresponds to linear scales of ~270 au in Orion KL, with PA = -72°. The image cube generation was otherwise done in the same fashion as that used for the full $^{13}CH_3OH$ data set.

The $J = 5$ transition of $^{13}CH_3OH$ at 156.3 GHz in these data was also detected in the aforementioned Cycle 2 observations toward Orion KL but at ~$2\farcs0$ angular resolution (~800 au). Comparing the integrated intensities for this line, we find that we recover ~9% and ~14% of the $^{13}CH_3OH$ flux integrated over the whole Orion

KL region in the $0\farcs3$ and $0\farcs7$ images, respectively, compared to what is recovered in the $2\farcs0$ observations. Moreover, we estimate that we recover about 4% and 6% of the total $^{13}CH_3OH$ $J = 5$ flux based on rough estimates of the flux derived from abundances and rotation temperature measurements made using Herschel (Crockett et al., 2014b). We attribute this to extended emission being resolved out in our observations, which have maximum recoverable scales equivalent to about 930-2400 au in Orion KL. In this work, however, we focus on probing the small-scale structure rather than large-scale features of the nebula. Thus we emphasize that these observations complement the existing lower-angular-resolution studies of Orion KL and that observations at multiple spatial scales are imperative for a holistic picture of star-forming regions such as Orion KL.

2.3 Methods

As noted in Section 1, different molecular tracers can be used as probes of different conditions in star-forming regions. The spectra from the ten spectral windows in the ALMA Cycle 5 observations, which are shown in Figure 2.2, illustrate this, with distinct profiles observed in the Hot Core (red) and the Compact Ridge (blue). While some transitions emit with similar intensities across the nebula, some lines show up in either the Hot Core or the Compact Ridge, but not both, while others have lines in both regions but at substantially different intensities. Using three transitions of $^{13}CH_3OH$ and eight transitions of CH_3CN $v_8 = 1$, which we list in Table 2.1, we resolve detailed profiles of velocity, temperature, and line widths of these tracers toward Orion KL. As discussed in Section 2.2, these lines were chosen because they were observed within a single correlator setup (across three spectral windows for $^{13}CH_3OH$ and in one spectral window for CH_3CN $v_8 = 1$), hence minimizing the uncertainties for the derived parameters. While there were additional lines present in the data, the selected lines represent a subset of consistently strong and unblended emission lines across the nebula.

Line width, velocity, excitation temperature, and column density of $^{13}CH_3OH$ $v = 0$ and CH_3CN $v_8 = 1$ as a function of position were derived by a pixel-by-pixel fit of the data.[2] Because all lines used in the fit for each molecule were observed simultaneously, the uncertainties in excitation temperature, which are derived from relative fluxes, should be dominated by thermal noise rather than by multiple sources of calibration uncertainty. For the column density estimates, the relative differences across the images should again be dominated by thermal (and phase) noise, while

---

[2] Python script available at https://github.com/oliviaharperwilkins/LTE-fit.

the overall calibration error budget does impact the total column densities derived but by ≤5% in Band 4 (Andreani et al., 2018).

The pixel-by-pixel fit of the data was achieved by extracting spectra in a single synthesized beam centered on each pixel, in succession. To avoid erroneous fits, only lines with peak amplitudes of $\geq 3\sigma_{\rm RMS}$ were considered. Line parameters—namely line width, velocity shift, excitation temperature, and column density—were determined simultaneously by least-squares fitting with `LMFIT`[3] (version 0.9.15) to

---

[3] `LMFIT` (Newville et al., 2019) is a nonlinear least-squares minimization and curve-fitting algorithm for Python that can be accessed at https://doi.org/10.5281/zenodo.598352.

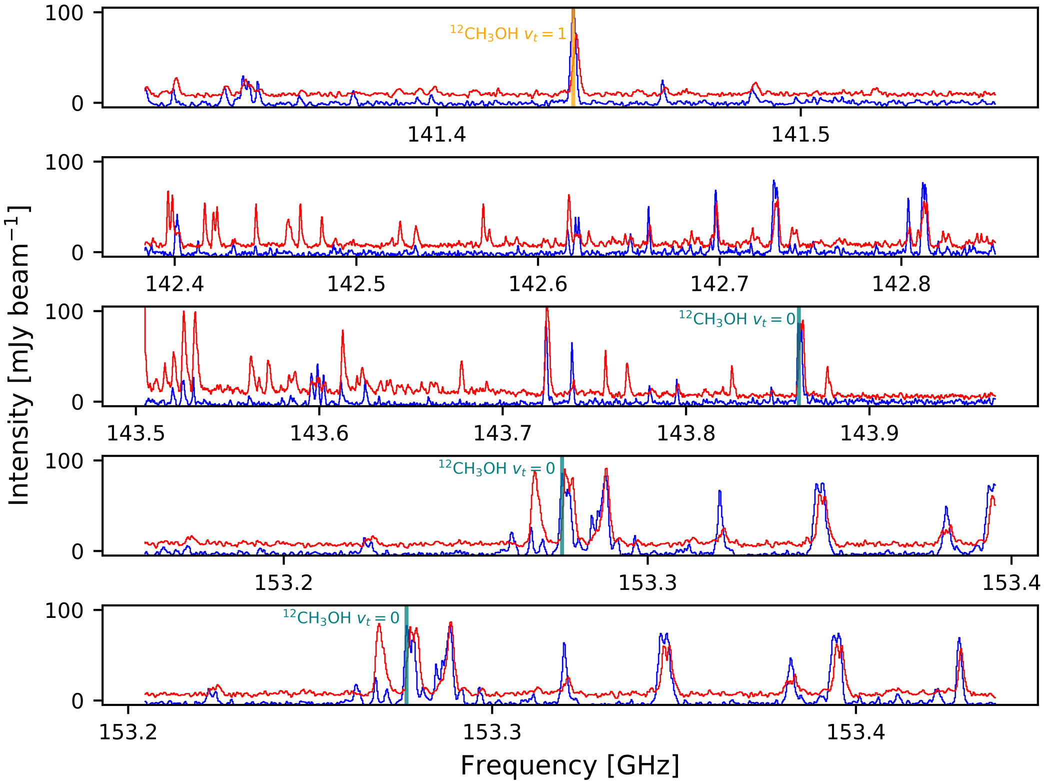

Figure 2.2: Spectra from 10 ALMA Cycle 5 Band 4 spectral windows toward Orion KL, displaying the plethora of molecular line emission toward the Compact Ridge (blue) and the Hot Core (red, offset by 10 mJy beam^{-1} for better visibility). Solid lines show transitions of ^{13}CH$_3$OH (black), ^{12}CH$_3$OH $v_t = 0$ (teal), and ^{12}CH$_3$OH $v_t = 1$ (orange). All tick marks are separated by 0.1 GHz. *Continued on next page.*

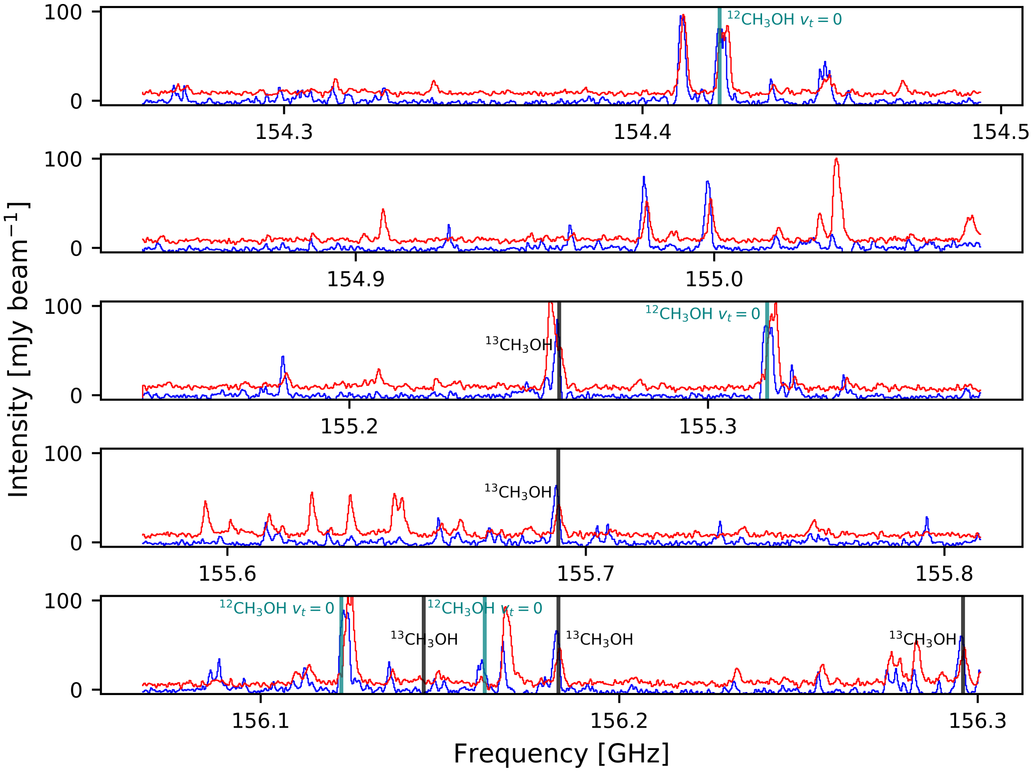

Figure 2.2: *Continued from previous page.*

model the spectra assuming optically thin lines at local thermodynamic equilibrium (LTE)[4] using Equation 2.1 (adapted from Remijan et al., 2003):

$$N_{\text{tot}} = 2.04 \times 10^{20} C_\tau \frac{1}{\Omega_S(\Omega_S + \Omega_B)} \frac{\int I_\nu dv}{\theta_a \theta_b} \frac{Q(T_{\text{ex}}) e^{E_u/T_{\text{ex}}}}{\nu^3 S_{ij} \mu^2} \text{ cm}^{-2} \tag{2.1}$$

where N_{tot} is the total column density [cm^{-2}] and T_{ex} is the excitation temperature [K]. Line width and velocity were extracted from the Gaussian fits used in the $\int I_\nu dv$ term, which is the integrated intensity of the line [Jy beam^{-1} km s^{-1}]. The optical depth correction factor $C_\tau = \tau/(1 - e^{-\tau})$ was assumed to be unity, since the optical depth τ is known to be small for the isotopologue transitions selected (see Appendix A). The Ω_S and Ω_B terms are the solid angles of the source and beam, respectively; we assume that the source completely fills the beam at all positions and that $\Omega \approx \pi\theta^2$ since θ is small. The remaining terms are known: θ_a and θ_b are the full-width-at-half-maximum beam sizes [$''$], Q is the partition function, E_u is the upper-state energy level [K], ν is the rest frequency of the transition [GHz],

---

[4] For the rationale behind the assumption of optically thin lines at LTE, see Appendix A.

Table 2.1: Transitions used for line fits.

Transition	ν (GHz)	E_u (K)	$S_{ij}\mu^2$ (Debye^2)	A_{ul} ($\times10^{-5}$ s^{-1})	g_u
^{13}CH$_3$OH[a]					
$8_{(0,8)} - 8_{(-1,8)}$	155.6958	94.59	6.86	1.77	17
$6_{(0,6)} - 6_{(-1,6)}$	156.1866	60.66	5.70	1.94	13
$5_{(0,5)} - 5_{(-1,5)}$	156.2994	47.08	4.98	2.01	11
CH$_3$CN $\nu_8 = 1$[b]					
$J = 8_{-5} - 7_{-5}$	147.5123	802.03	278.88	15.32	68
$J = 8_{-4} - 7_{-4}$	147.5439	724.50	171.63	18.87	34
$J = 8_{-3} - 7_{-3}$	147.5698	661.23	196.67	21.64	34
$J = 8_5 - 7_5$	147.5756	668.87	139.43	15.34	34
$J = 8_{-2} - 7_{-2}$	147.5899	612.23	429.03	23.61	68
$J = 8_4 - 7_4$	147.5954	618.01	343.26	18.89	68
$J = 8_{-1} - 7_{-1}$	147.6040	577.50	225.29	24.80	34
$J = 8_2 - 7_2$	147.6199	559.01	214.52	23.62	34

[a] Spectroscopic data for ^{13}CH$_3$OH comes from CDMS.
[b] Spectroscopic data for CH$_3$CN $\nu_8 = 1$ comes from the JPL spectroscopic database.

and $S_{ij}\mu^2$ is the product of the transition line strength and the square of the electric dipole moment [Debye^2].

The transitions of ^{13}CH$_3$OH and CH$_3$CN used for the fits are summarized in Table 2.1. One other ^{13}CH$_3$OH transition is present in our observations at 155.262 GHz but was not included in the fits due to line blending. The ^{13}CH$_3$OH lines are ground vibrational state *c*-type transitions with upper-state energies E_u between 47 and 95 K and $J = 5, 6, 8$. The $J = 7$ line at $\nu_{\text{rest}} = 155.994$ GHz is expected to be unblended but was excluded in our observations to optimize the spectral setup. Three other ^{13}CH$_3$OH transitions fall within our spectral setup at $\nu_{\text{rest}} = 141.381$, 155.262, and 156.149 GHz. The 141.381 and 155.262 GHz lines appear to be blended: with CH$_3$OH $v_t = 1$ at 141 GHz and an unknown contaminant at 155 GHz. The line at 156.149 GHz is high J ($J = 26 - 25$) with $E_u = 988$ K and thus a strong detection of this transition would not be expected especially toward the Compact Ridge. An example spectrum of the ^{13}CH$_3$OH lines fitted in our analyses is shown in Figure 2.3.

The CH$_3$CN lines analyzed are all strong, vibrationally excited ($\nu_8 = 1$) $J = 8 - 7$ transitions. Their upper-state energies between 559 K and 803 K make these lines appropriate tracers of high-energy (or radiatively pumped) emission, in and near the

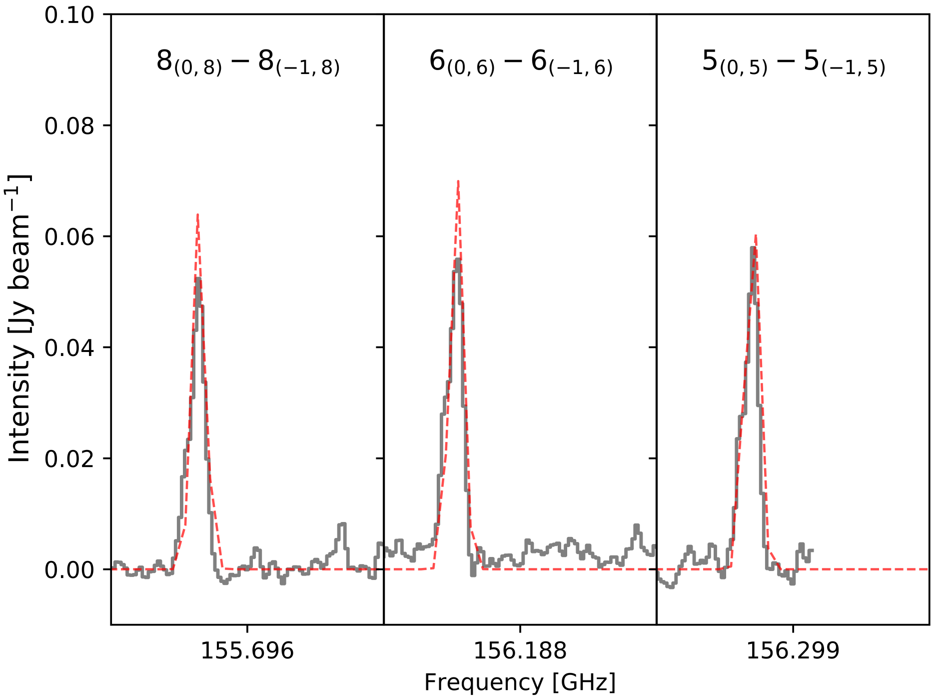

Figure 2.3: Example spectrum of $^{13}CH_3OH$ $v = 0$ toward the center of the Compact Ridge, showing the Gaussian fits to the unblended transitions by the red dashed line over the data in black.

Hot Core. There are other, weaker CH_3CN $v_8 = 1$ lines in Figure 2.4; however, these lines were excluded from the fits because they are blended, which prevented good line fits. Nevertheless, the fitted parameters characterizing the CH_3CN emission come with reasonable propagated uncertainties of ≤20% for much of the Hot Core (and up to ~30% near the region's edges where emission drops off).

Because the synthesized beams are small compared to the extent of molecular emission toward Orion KL, we assume the sources completely fill the beam at all positions. The E_u, ν, $S_{ij}\mu^2$, and $Q(T_{\rm ex})$ values for $^{13}CH_3OH$ and CH_3CN $v_8 = 1$ were obtained from the Cologne Database for Molecular Spectroscopy (CDMS; Müller et al., 2001) and the JPL molecular spectroscopy database (Pickett et al., 1998), respectively, via the Splatalogue[5] database for astronomical spectroscopy. Values and uncertainties (standard errors calculated using `LMFIT`) for $N_{\rm tot}$, $T_{\rm ex}$, and local standard of rest velocity $V_{\rm LSR}$ were extracted from the line fits using Equation 2.1 and are presented throughout the rest of the paper.

---

[5] http://splatalogue.online

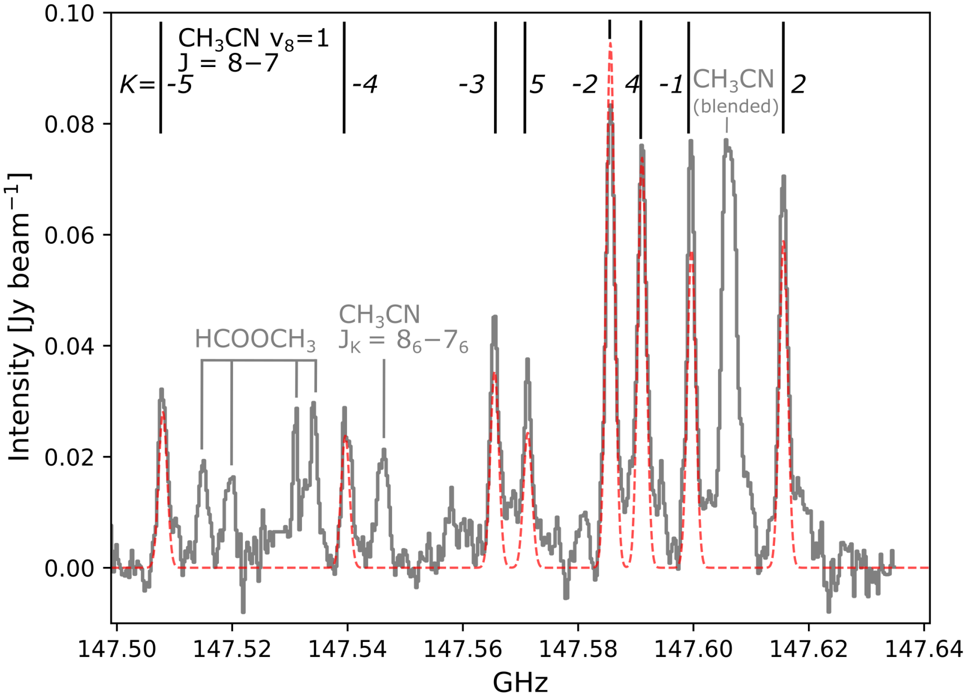

Figure 2.4: Example spectrum of CH$_3$CN ν_8 = 1 toward the center of the Hot Core showing the Gaussian fits to the included transitions by the red dashed line over the data in black.

The figures presented herein show color maps of the derived parameters from CH$_3$CN ν_8 = 1 and ^{13}CH$_3$OH ν = 0 line emission with contours of the continuum at both the full and tapered angular resolution (Figures 2.6-2.9). In general, the estimated uncertainty is <30% for the column density and excitation temperature and <5% for the velocity and width fields. Maps of the propagated uncertainty are given in Appendix B. The continuum contours are the same as those plotted over the Cycle 5 Band 4 (~150 GHz) continuum images in Figure 2.5. The continuum images obtained from the Cycle 4 data exhibit similar profiles and are not shown here.

2.4 Chemical Distributions

The bottom-most panels of Figures 2.6-2.9 show the integrated intensities of ^{13}CH$_3$OH and CH$_3$CN ν_8 = 1 throughout Orion KL. While ^{13}CH$_3$OH emission is present throughout the nebula, most of the emission arises from the region extending southwest from the Hot Core and toward the Compact Ridge, which fits

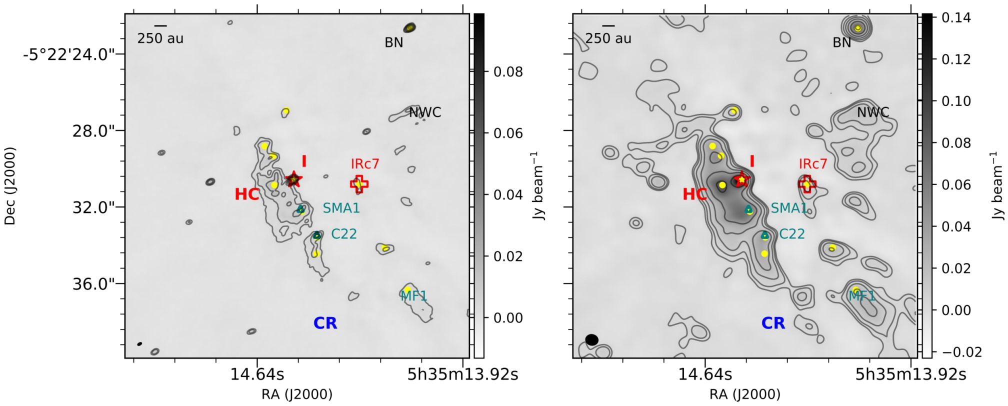

Figure 2.5: ALMA Cycle 5 continuum in Band 4 ($\nu \sim 150$ GHz, $\lambda \sim 2$ mm) toward Orion KL at full (left) and tapered (right) angular resolution. The synthesized beam is shown by the black oval in the bottom left. The warmer, denser Hot Core region is shown by **HC**, and the cooler, less dense Compact Ridge region is indicated by **CR**. The locations of source I and IRc7 are shown by the red star and red plus, respectively. The yellow circles correspond to millimeter/submillimeter continuum sources identified by Hirota et al. (2015). The embedded millimeter source C22 (Friedel & Widicus Weaver, 2011) and the protostar SMA1 (Beuther et al., 2006) are shown by the teal triangles. Both the greyscale and contours plot the continuum with contours at $3\sigma_{\rm RMS}, 6\sigma_{\rm RMS}, 12\sigma_{\rm RMS}, 24\sigma_{\rm RMS}, \ldots$ where $\sigma_{\rm RMS} = 1.3$ mJy beam^{-1} is the noise level for the full resolution image, and $\sigma_{\rm RMS} = 1.0$ mJy beam^{-1} is the noise level for the tapered resolution image.

the profile of this region being the site of oxygen-bearing chemistry (e.g., Blake et al., 1987; Favre et al., 2017; Tercero et al., 2018). CH_3CN $v_8 = 1$ is found predominantly in the region surrounding the Hot Core and Source I, as well as IRc7.

In our analyses, $^{13}CH_3OH$ $v = 0$ was selected to trace colder, less dense gas such as that in the Compact Ridge, a component that is also rich in oxygen-bearing chemistry (Blake et al., 1987; Friedel & Widicus Weaver, 2011). Furthermore, $^{13}CH_3OH$ serves as an optically thin proxy for the primary carbon-12 isotopologue of methanol, which is often optically thick in star-forming regions and which is known to be optically thick toward the Hot Core and Compact Ridge in Orion KL specifically, from Herschel Space Telescope observations (Crockett et al., 2014b). Compared to lower-angular-resolution images (e.g., CARMA images by Friedel & Widicus Weaver, 2011), the methanol emission in our observations is much more compact. We attribute this to the extended emission of the nebula being resolved out in our images. As stated in Section 2.2, we recover ~9% and ~14% of the $^{13}CH_3OH$ flux in the 0.″3 and 0.″7 images compared to observations at 2.″0. Even between

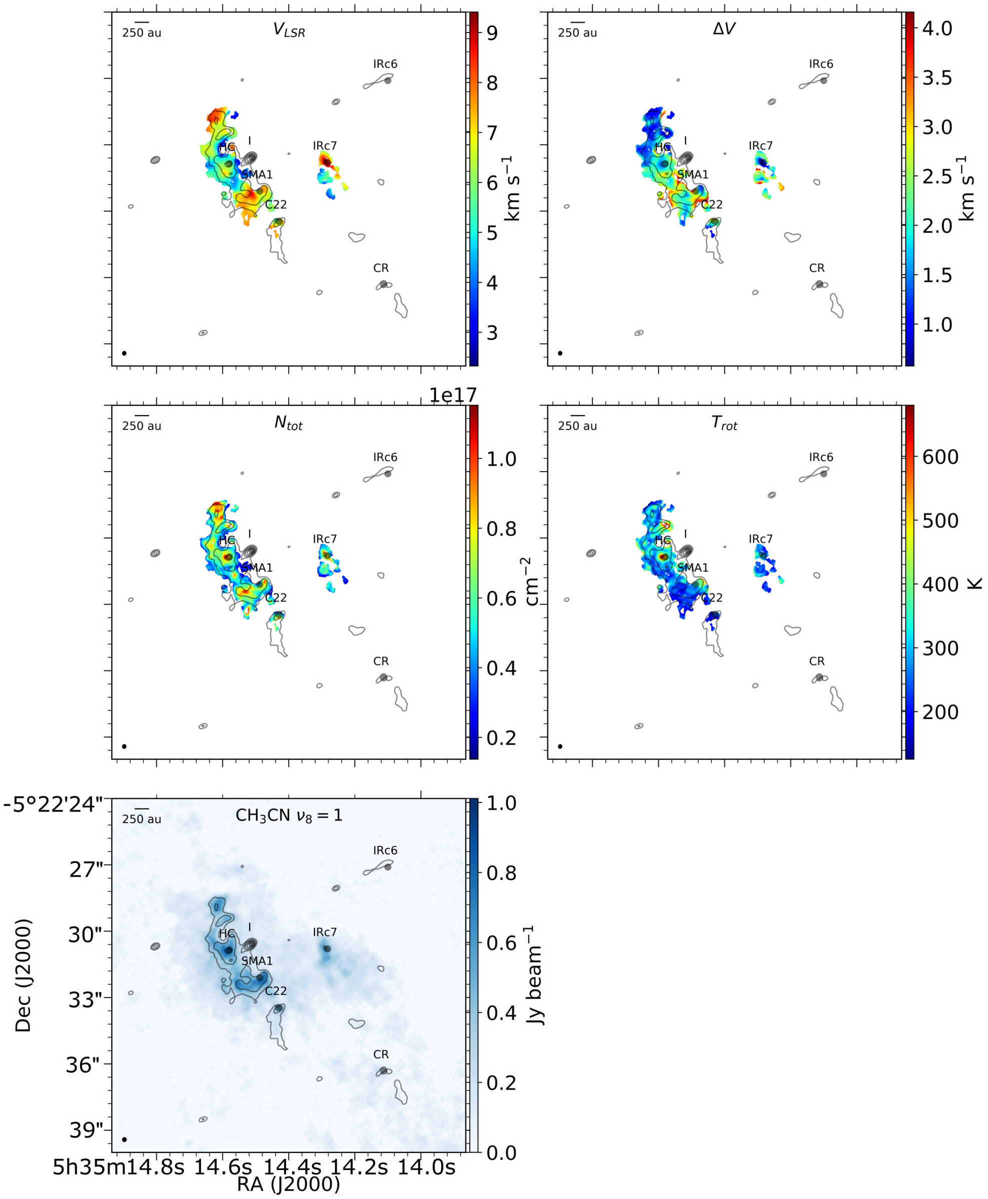

Figure 2.6: Parameter maps for the full angular resolution images of CH$_3$CN $v_8 = 1$. Contours show the 2 mm (~150 GHz) continuum from the left panel of Figure 2.5. The color plots show, from left to right: (top row) velocity field, line width field; (middle row) total column density, excitation temperature, and (bottom row) integrated intensity (moment-0). All panels have the same field of view.

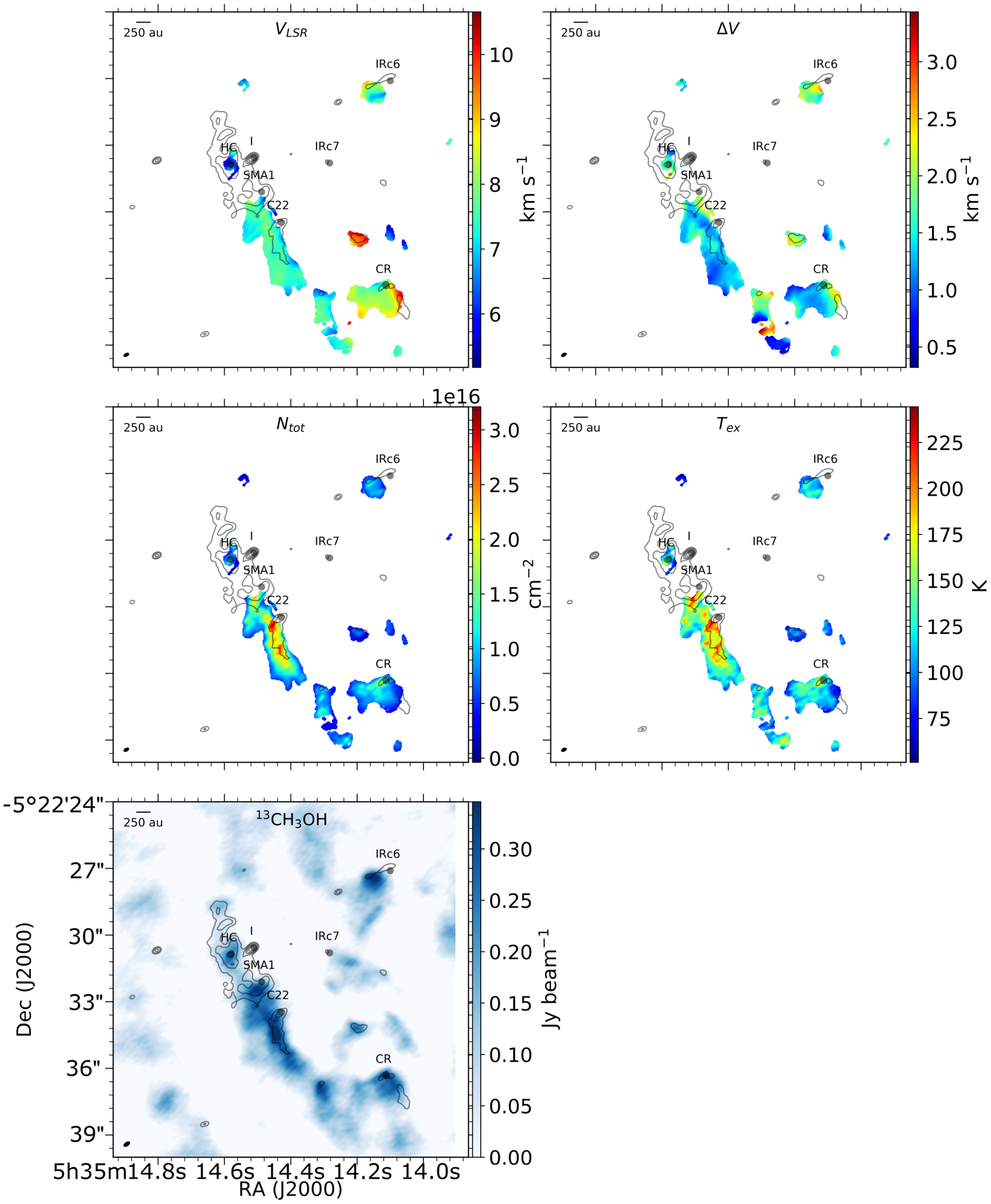

Figure 2.7: Parameter maps for the full angular resolution images of $^{13}CH_3OH$ $v = 0$. Contours show the 2 mm (~150 GHz) continuum from the left panel of Figure 2.5. The color plots show, from left to right: (top row) velocity field, line width field; (middle row) total column density, excitation temperature; and (bottom row) integrated intensity (moment-0). All panels have the same field of view.

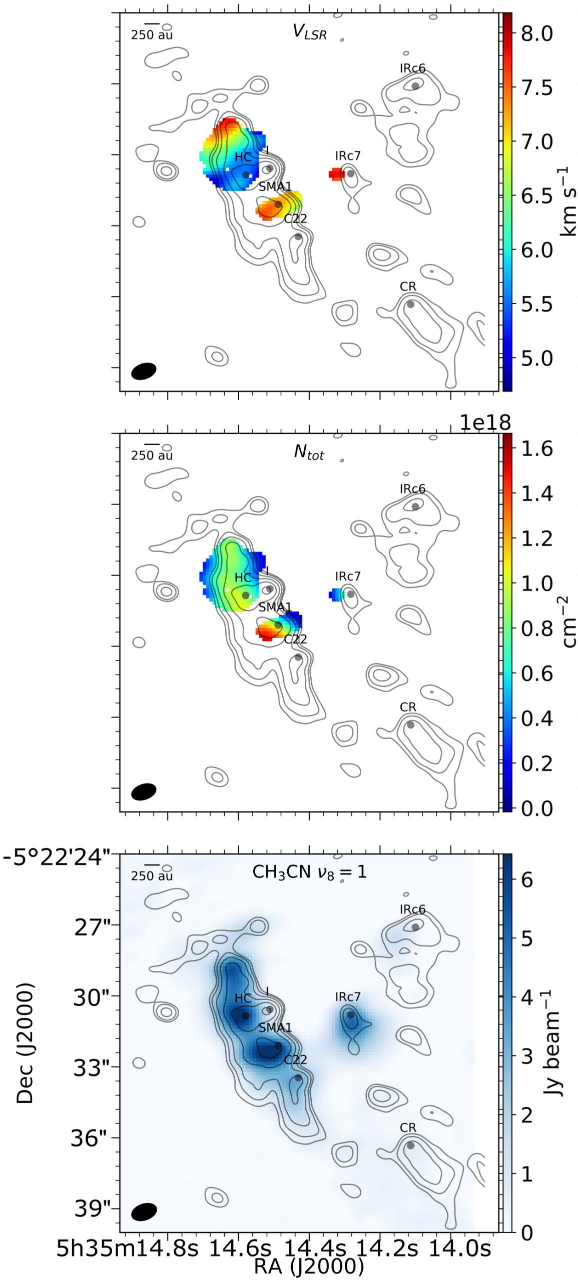

Figure 2.8: Parameter maps for the tapered angular resolution images of CH$_3$CN $\nu_8 = 1$. Contours show the 2 mm (~150 GHz) continuum from the right panel of Figure 2.5. The color plots show, from left to right: (top row) velocity field, line width field; (middle row) total column density, excitation temperature; and (bottom row) integrated intensity (moment-0). All panels have the same field of view.

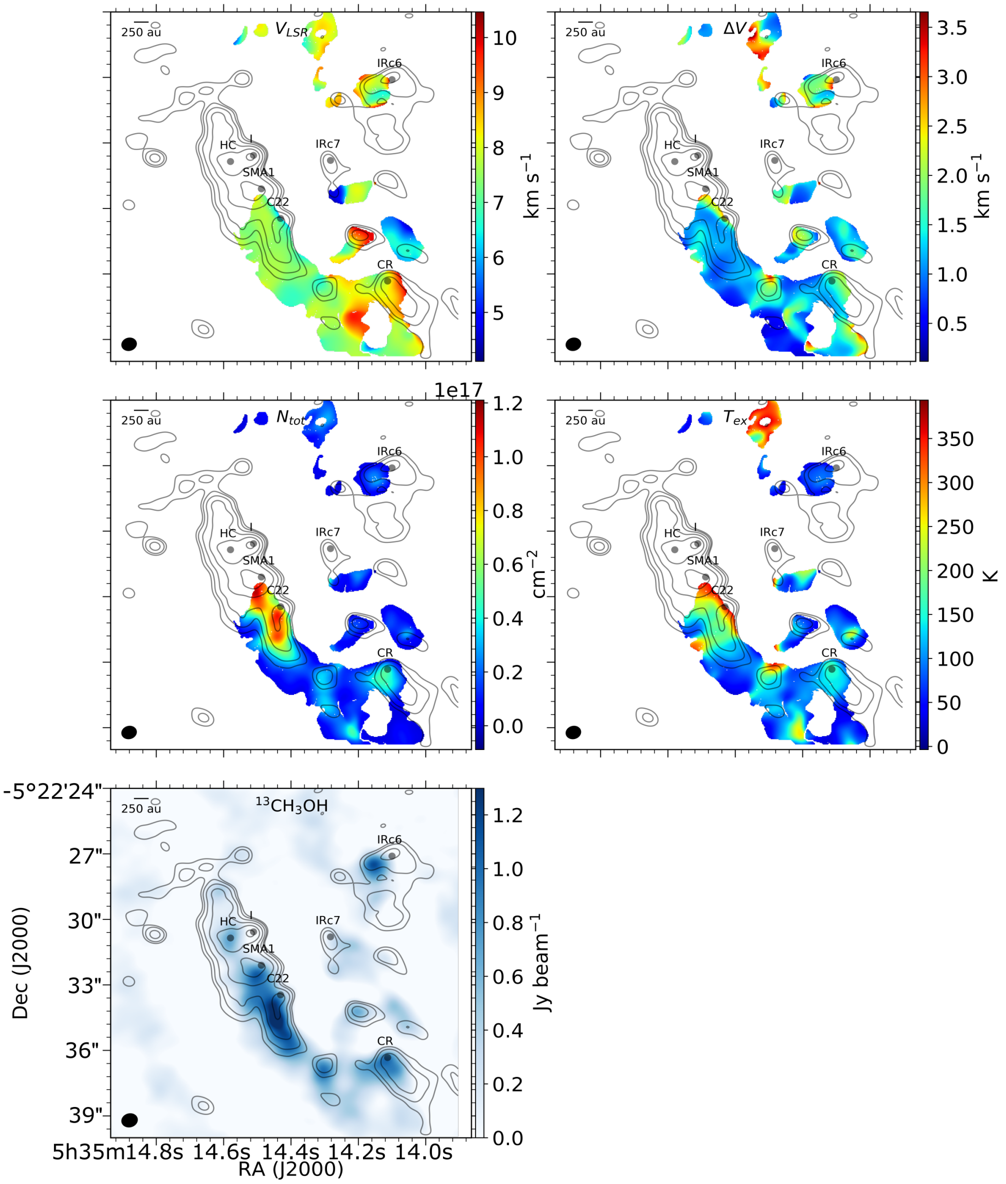

Figure 2.9: Parameter maps for the tapered angular resolution images of ^{13}CH$_3$OH $\nu = 0$ (bottom cluster). Contours show the 2 mm (∼150 GHz) continuum from the right panel of Figure 2.5. The color plots show, from left to right: (top row) velocity field, line width field; (middle row) total column density, excitation temperature; and (bottom row) integrated intensity (moment-0). All panels have the same field of view.

Figures 2.7 and 2.9, the (fittable) $^{13}CH_3OH$ emission is generally more compact in the full angular resolution images (Figure 2.7) than in the tapered angular resolution images (Figure 2.9).

The derived $^{13}CH_3OH$ column densities are shown in the middle left panel Figures 2.7 and 2.9. We derive $^{13}CH_3OH$ column densities on the order of 10^{16} cm^{-2} throughout the Compact Ridge and the region southwest of the Hot Core (Hot Core-SW) at $0\farcs3$, which is in agreement with the $^{13}CH_3OH$ column densities reported by Crockett et al. (2014b). In the Compact Ridge and the edges of the Hot Core-SW, the column density is $\sim 1.0 \times 10^{16}$ cm^{-2}; toward the center of the Hot Core-SW, there are pockets of higher column density, as much as $\sim 3.0 \times 10^{16}$ cm^{-2}. At $0\farcs7$ angular resolution, the derived column density is as much as four times higher, particularly in elongated structures extending south from SMA1 and C22. This is perhaps due to emission, which is resolved out in the $0\farcs3$ images, from material that is being blown southward by the explosive event that took place north of Source I 500 years ago (e.g., Bally et al., 2015).

CH_3CN $\nu_8 = 1$ was selected for similar reasons, but to trace the hotter and denser gas toward the Hot Core region, which is also rich in nitrogen-bearing molecules (Blake et al., 1987; Friedel & Widicus Weaver, 2011). The vibrationally excited lines were specifically targeted to probe high-energy emission excited by far-IR pumping associated with particularly dense gas from massive embedded protostars (e.g., Genzel & Stutzki, 1989) while also overcoming the fact that CH_3CN $\nu = 0$ has been observed to be optically thick toward the Hot Core, Compact Ridge, and Plateau regions in Orion KL (Crockett et al., 2014b).

The column density of CH_3CN $\nu_8 = 1$ is on the order of 10^{16}–10^{18} cm^{-2} in the Hot Core and Source I region, with the column density derived from the $0\farcs9$ data being about an order of magnitude greater than that derived from the $0\farcs\,2$ data. Crockett et al. (2014b) report CH_3CN $\nu_8 = 1$ column densities of 3.7×10^{15} cm^{-2}, which is almost two orders of magnitude less than what we generally find in our fits, toward the Hot Core in a $\geq 9''$ beam. The discrepancy may be the result of probing vastly different spatial scales ($\geq 9''$ versus subarcsecond angular scales) or because Crockett et al. use a different analytical method, including a wideband survey, whereas our analyses includes $J = 8$ transitions of CH_3CN $\nu_8 = 1$ only. We suspect that the former is the likely source of the difference between the two sets of measurements because CH_3CN $\nu_8 = 1$ traces dense gas, in particular gas affected by far-IR pumping associated with massive embedded protostars. In other words, we can expect the CH_3CN $v_8 = 1$ to be more compact such that its emission was perhaps diluted in a much larger beam.

Alternatively, the $v_8 = 1$ mode is not necessarily in thermal equilibrium with the CH_3CN ground state at the same effective rotational temperature (i.e., $T_{\rm vib} \neq T_{\rm rot}$). However, Crockett et al. (2014b) report that the $v = 0$ and $v_8 = 1$ models are consistent toward the Hot Core, or that $T_{\rm rot} = T_{\rm vib}$, and we find that the rotational LTE models employed in this work fit the data well (see Appendix A). Thus we proceed under the assumption of thermal equilibrium, with the caveat that the derived excitation temperatures for the $v_8 = 1$ lines do not necessarily reflect the actual kinetic temperature. However, previous measurements for ground-state CH_3CN at $0\farcs33 \times 0\farcs35$ (Carroll, 2018) yield similar temperature values as what we see in our $0\farcs9$ data. These values are also similar to the temperature measurements in our $0\farcs2$ data cube except at the very center of the Hot Core over an area presumably resolved out in the larger beam.

2.5 Physical Properties

The (sub)millimeter continuum of Orion KL is mostly dominated by thermal dust emission (e.g., Masson et al., 1985; Wright & Vogel, 1985; Wright & Plambeck, 2017); however, some regions—namely Source I—may have significant contributions from free-free emission (Beuther et al., 2006). It is well established that the Hot Core region is denser than the Compact Ridge, and this is evident by the greater thermal dust emission toward the Hot Core in our continuum images as well, as seen in Figure 2.5. The velocity maps derived here, consistent with previous results, show that the Hot Core and Source I regions have a lower LSR velocity than the Compact Ridge, one that is blue shifted with respect to the large scale molecular cloud complex, perhaps showing a profile resulting from the recent Orion KL explosive event.

The top left panel of each set of Figures 2.6-2.9 show the velocity fields derived from $^{13}CH_3OH$ $v = 0$ and CH_3CN $v_8 = 1$ line emission. The velocity fields for each tracer were derived from the frequency offset in the pixel-by-pixel fits of the lines. Deriving the velocity offsets from a fixed frequency offset results in only a modest level of uncertainty because of Orion KL's low $V_{\rm LSR}$, the high frequency of these observations, and the close proximity of the included lines (Table 2.1): within 0.6 GHz for $^{13}CH_3OH$ and 0.1 GHz for CH_3CN. This adds negligible uncertainty ($\ll 1\%$) to the derived frequency offsets. This is confirmed by consistently low

Table 2.2: Velocity profiles traced by molecular emission in Orion KL.

Molecule	$V_{\rm LSR}$ (km s^{-1})	Reference
Compact Ridge		
^{13}CH$_3$OH	~7−9	This work
^{13}CH$_3$OH	7.8	(Crockett et al., 2014b)
CH$_3$OH	8.6	(Wang et al., 2011)
CH$_3$OH	7.6	(Wilson et al., 1989)
Hot Core		
^{13}CH$_3$OH	~6	This work
^{13}CH$_3$OH	7.5	(Crockett et al., 2014b)
CH$_3$OH	6−9	(Wang et al., 2011)
CH$_3$OH	~7	(Wilson et al., 1989)
CH$_3$CN ν_8 = 1	~6−8	This work
CH$_3$CN ν_8 = 1	6−9	(Wang et al., 2011)

velocity uncertainties: the uncertainty on these measurements is ≤3.5%, except for a few regions in the 0.″2 CH$_3$CN map, in which some regions near the edges of the emission region have uncertainties as high as ~8%. Generally, the uncertainty is <0.5% in all maps, and places with higher uncertainties often occur at the edges of emission regions and thus may be the result of the flux dropping off, giving rise to weak or noisy lines.

The velocity gradients mapped by ^{13}CH$_3$OH in this work agree well with past methanol observations, as summarized in Table 2.2. In brief, our derived velocity field in the Compact Ridge spans ~7-9 km s^{-1}, and previous measurements have yielded an LSR velocity of 7.6−8.6 km s^{-1}.

Our derived velocity toward the Hot Core region is slightly lower at ~6 km s^{-1} in the ^{13}CH$_3$OH images. Likewise, the LSR velocity derived from CH$_3$CN ν_8 = 1 spans ~6-8 km s^{-1}, which agrees with Wang et al. (2011), who report a $V_{\rm LSR}$ of 6-9 km s^{-1} toward the Hot Core.

The velocity field provides insight into the physical structure of Orion KL at spatial scales of ≤350 au. Specifically, we find possible evidence of a molecular outflow in the Hot Core and a velocity gradient in the Hot Core-SW.

Hot Core

In our CH$_3$CN 0.″2 velocity map, the Hot Core millimeter/submillimeter emission peak (alternatively designated SMM3 by Zapata et al., 2011) is characterized by a radial velocity gradient that runs from ~5 km s^{-1} (the LSR velocity of Source I) around the edge of its signature heart shape to values closer to 7-8 km $s^{-1}$to both the north and south of Source I. This velocity gradient is centered about $0.45''$ to the south of the Hot Core's 865 μm emission peak, as seen by the light orange region near the center of Figure 2.10. This contrasts with the location of the peak excitation temperature and column density of CH_3CN, which are centered approximately at the location of the 865 μm emission peak. Opposite the Hot Core millimeter/submillimeter peak, to the north, the velocity approaches ~8 km s^{-1}.

Restated in terms of 3D structure, the velocity field in the north is close to the systemic velocity of Orion KL (9 km s^{-1}, e.g., Hall et al., 1978), but becomes more blue-shifted for the emission to the south associated with the Hot Core and Source I. With increasing blue shift, the velocity width also increases, as is seen in the top right panel of Figure 2.6. The combination of the relative blue shift of the gas and the broader line widths may indicate that this dense gas is being pushed away from the putative explosive event. Areas throughout the Hot Core and Source I region where the velocity is closer to the systemic velocity, then, may be acting as a buffer to slow the gas, whereas a lower LSR velocity shows where that gas is pushed outward with fewer obstacles.

Another explanation for the elongated velocity structure is that it may be the result of a low-velocity outflow emanating from a source east of Source I. The millimeter/submillimeter peak at the center of this purported outflow is also reported to be the site of an embedded edge-on disk (Otter et al., 2021) that is perpendicular to the elongated velocity structure. Goddi et al. (2011) detect a similar elongated velocity structure toward IRc7 in Expanded Very Large Array (EVLA) observations of high-excitation NH_3 lines in a $0\farcs8$ beam. They conclude that the elongated velocity structure, coupled with line width enlargements, is evidence of a low-velocity outflow. As seen in the bottom right panel of Figure 2.6, CH_3CN $v_8 = 1$ has narrower line widths (~ 1.5 km s^{-1}) at the location of the Hot Core millimeter/submillimeter peak, but broader lines (~3 km s^{-1}) in the region surrounding the peak. The fact that the millimeter/submillimeter peak is cospatial with a region of relatively narrow line widths and peaks in CH_3CN excitation temperature and column density, but that the elongated velocity structures are cospatial with broader lines, supports the conclusion that the elongated velocity structure to the north and south of this millimeter/submillimeter peak is the result of a low-velocity outflow.

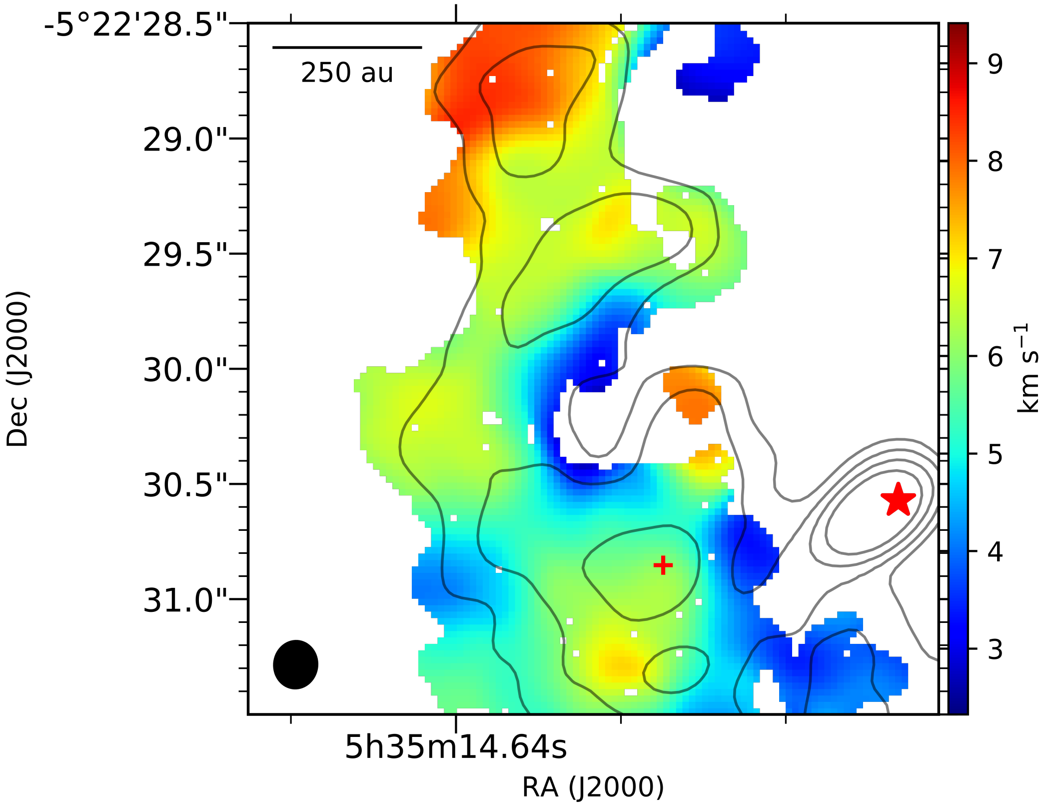

Figure 2.10: The same as the CH_3CN ν_8 = 1 V_{LSR} (top left) panel of Figure 2.6, but with a close-up view of the Hot Core region. The red cross shows the millimeter/submillimeter emission peak, and the red star denotes Source I. Contours show the 2 mm (~150 GHz) continuum from the left panel of Figure 2.5.

SMA1

SMA1 is a submillimeter source first identified by Beuther et al. (2004) at 346 GHz (865 μm). It has since been observed to have a 3 mm emission peak and a $HCOOCH_3$ emission peak (Friedel & Widicus Weaver, 2011; Favre et al., 2011). Beuther and Nissen (Beuther & Nissen, 2008) suggest that SMA1 hosts the driving source of the high-velocity outflow that runs northwest-southeast in Orion KL, but the nature of this object otherwise remains not well understood.

The structure surrounding SMA1 is particularly dynamic in our images. The velocity fields derived from the CH_3CN ν_8 = 1 emission line at both 0.″2 and 0.″9 angular resolution show a gradient that seems to emanate from just southeast of the SMA1 submillimeter emission center. As seen in Figure 2.6, the velocity peaks at around 8 km s^{-1}. The velocity gradient decreases gradually moving to the southeast (seen in the 0.″2 map only) and northwest but changes abruptly in the orthogonal direction.

This agrees with previous conclusions that SMA1 is the location of a driver of the northwest-southeast outflow.

Hot Core-SW

The Hot Core-SW, the region to the southwest of the Hot Core and east of the Compact Ridge, is distinct from, but shares characteristics with, both the Hot Core and the Compact Ridge. The velocity fields in this region, traced by $^{13}CH_3OH$, show a gradient from lower LSR velocity toward SMA1 (~6.5 km s^{-1}) to higher velocities (~7.8 km s^{-1}) toward the south near the Compact Ridge. This gradient can be explained by the interaction between gas emanating from the center of the explosion northwest of Source I with the clumps distributed throughout the nebula. As the gas travels away from the explosion center toward the east and south, it first interacts with the denser Hot Core and Source I regions, which act as a buffer to slow the gas. Toward the Compact Ridge in the south, there is less dust to act as a buffer, allowing the gas to pass through more easily and thus become more blue-shifted.

In this sense, the Hot Core-SW region is like the Hot Core and Source I in that it is denser than the Compact Ridge. Moreover, the Hot Core-SW contains higher column densities of $^{13}CH_3OH$ than the Compact Ridge, a characteristic that is evident in both the $0\farcs3$ and $0\farcs7$ maps. This region also has higher excitation temperatures than the Compact Ridge.

It is curious, then, that the Hot Core-SW region is not traced by nitrogen-bearing compounds, which is evident here from the lack of CH_3CN $\nu_8 = 1$ emission and from previous observations (e.g., Friedel & Snyder, 2008). Despite having velocity, density, and temperature profiles more akin to the Hot Core region, the Hot Core-SW region appears to be more chemically similar to the Compact Ridge.

Previous interferometric observations show strong emission in the Hot Core-SW from the oxygen-bearing species dimethyl ether ($(CH_3)_2O$, CARMA; Friedel & Snyder, 2008) and methyl formate ($HCOOCH_3$, IRAM PdBI; Favre et al., 2011). Friedel and Snyder (Friedel & Snyder, 2008) also found acetone ($(CH_3)_2CO$) emission toward the Hot Core-SW, part of which overlaps with ethyl cyanide (C_2H_5CN) emission near SMA1 and C22 in the north. In their observations, $(CH_3)_2CO$ was detected only toward the Hot Core-SW and IRc7, both of which have overlapping oxygen- and nitrogen-bearing chemistry. Subsequent observations of $(CH_3)_2CO$ show that this molecule is much more extended than reported by Friedel and Snyder and that it is an oxygen-bearing species that has a distribution similar to that of large nitrogen-bearing molecules (Peng et al., 2013).

It would appear then that the Hot Core-SW is a hybrid of the Hot Core and Compact Ridge regions, and thus the Hot Core-SW presents itself as a possible location for bridging the oxygen-bearing chemistry of the less dense, colder Compact Ridge and the nitrogen-bearing chemistry of the denser, warmer Hot Core region. Sutton et al. (1995) suggest that the chemical differentiation between the Hot Core and Compact regions is not so stark as originally thought and that the chemical emission from both nitrogen-bearing and oxygen-bearing species is spatially extended. Nevertheless, such chemical differentiation has also been observed in other sources, such as the ultracompact H II region W3(OH) (Wyrowski et al., 1997), the high-mass protostar AGAL 328.25 (Csengeri et al., 2019), and cluster-forming clumps in NGC 2264 (Taniguchi et al., 2020). In a sample of seven high-mass protostars, Bisschop et al. (2007) found that complex organics could be classified as either cold (<100 K) or hot (>100 K) based on their rotation temperatures, and that nitrogen-bearing species were exclusively "hot" molecules whereas different oxygen-bearing species were found in both categories. Fayolle et al. (2015) found chemical differentiation in a sample of three massive young stellar objects (YSOs); in their sample, CH_3CN and CH_3OCH_3 originated from the central cores, CH_3CHO and CH_3CCH emission came from the extended envelope, and CH_3OH (and sometimes HNCO) straddled both regimes. While the origin(s) of this chemical differentiation are not well understood, it may may be influenced by the precursor content (e.g., H_2O, NH_3, CH_4) in icy grain mantles (e.g., Fayolle et al., 2015) and prestellar core evolutionary time-scales (e.g., Laas et al., 2011; Sakai & Yamamoto, 2013). In Orion KL, this may translate to a scenario in which, on large spatial scales, the Hot Core-SW is analogous to the region between an embedded YSO core and its extended envelope, which would begin to explain the observed distribution of $^{13}CH_3OH$ in this work and $(CH_3)_2CO$ by Friedel and Snyder (Friedel & Snyder, 2008). However, a better understanding of complex organic formation—and of the initial conditions in Orion KL before the putative explosive event—is likely needed to explain the observed chemical and physical patterns.

2.6 Thermal Structure

In considering the thermal structure of Orion KL, we assume local thermodynamic equilibrium (LTE, see Appendix A) and that the kinetic temperature in the nebula is approximated by the excitation temperature of the molecular gas due to the nebula's high density. The derived temperature maps for $^{13}CH_3OH$ $\nu = 0$ and CH_3CN $\nu_8 = 1$ are shown in the middle right panels of each group of plots in Figures 2.6 and 2.9, respectively. Because we have temperature maps on two different angular scales, we can get information about possible sources of heating throughout the nebula. In particular, the higher-angular-resolution (~$0\farcs2$–$0\farcs3$) images probe spatial scales on the order of ~78−116 au, which is within the protostellar radius of 150 au where the gas-phase chemistry is expected to be driven by thermal submlimation from the young stellar object (e.g., Schöier et al., 2002). Conversely, the tapered angular resolution (~$0\farcs7$–$0\farcs9$) images correspond to spatial resolutions of ~272−350 au, which is greater than the typical radius of a protostellar core. That is, our angular resolutions enable us to look at possible heating sources on scales that straddle the boundary of whether thermal sublimation is expected to be driven by an embedded protostar.

We consider possible sources of heating in Orion KL by mapping the difference between the excitation temperatures derived in a larger versus smaller beam. That is, we subtract the excitation temperature derived within the smaller beam $T_{ex,S}$ from that derived within the larger beam $T_{ex,L}$ to give $\Delta T_{\rm ex} = T_{ex,L} - T_{ex,S}$ at each pixel. It follows then that $\Delta T_{\rm ex} > 0$ suggests an external source of heating whereas $\Delta T_{\rm ex} < 0$ suggests an internal source of heating. In other words, $\Delta T_{\rm ex} < 0$ indicates that the warmer temperature, potentially from a compact heating source, measured in a smaller beam is diluted by colder temperatures in the more extended larger beam. Similarly, $\Delta T_{\rm ex} > 0$ indicates that a colder region detected in a smaller beam is in the presence of nearby warmer gas.

We note that whether the sign of $\Delta T_{\rm ex}$ accurately reflects the source of heating depends on the assumed source radius and proximity to the source peak. As such, we ran simple Gaussian temperature distribution models for externally and internally heated material with approximate temperatures and radii of sources described in this section. In these toy models, briefly described in Appendix C, the sign of $\Delta T_{\rm ex}$ consistently reflected whether a modeled compact source was internally or externally heated. Furthermore, we note that, as mentioned in Section 2.2, we recover about the same amount of ^{13}CH$_3$OH flux in both the full and tapered image cubes, indicating that $\Delta T_{\rm ex}$ is not affected by flux recovery in the $0\farcs3$ and $0\farcs7$ synthesized beams.

The resulting maps for $\Delta T_{\rm ex}$ are presented in Figures 2.11 and 2.12 for ^{13}CH$_3$OH and CH$_3$CN $v_8 = 1$, respectively. In these maps, regions where $\Delta T_{\rm ex} > 0$, indicative of an external source of heating, are shaded red. Regions where $\Delta T_{\rm ex} < 0$, indicative of a possible internal heating source, are shaded blue.

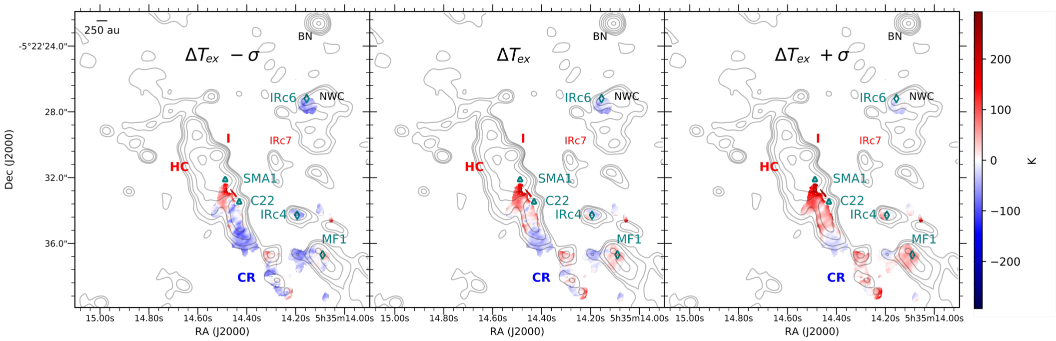

Figure 2.11: Maps showing $\Delta T_{\rm ex} = T_{ex,0''.7} - T_{ex,0''.3}$, i.e., the difference between the derived excitation temperature from a 0″.7 and 0″.3 beam for $^{13}CH_3OH$. From left to right, the panels show $\Delta T_{\rm ex} - \sigma$, $\Delta T_{\rm ex}$, and $\Delta T_{\rm ex} + \sigma$ where σ is the propagated uncertainty. Red represents an external source of heating, and blue represents internal heating. Contours show the 2 mm (~150 GHz) continuum.

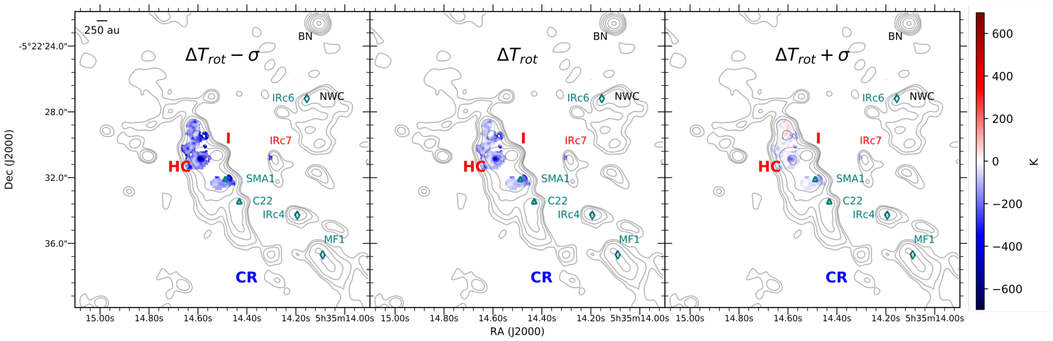

Figure 2.12: Maps showing $\Delta T_{\rm ex} = T_{ex,0''.9} - T_{ex,0''.2}$, i.e., the difference between the derived excitation temperature from a 0″.9 and 0″.2 beam, for CH_3CN $\nu_8 = 1$. From left to right, the panels show $\Delta T_{\rm ex} - \sigma$, $\Delta T_{\rm ex}$, and $\Delta T_{\rm ex} + \sigma$ where σ is the propagated uncertainty. Red represents a possible external source of heating, and blue represents possible internal heating. Contours show the 2 mm (~150 GHz) continuum.

Hot Core

Our analyses suggest possible internal sources of heating in the Hot Core. As seen in Figure 2.12, $\Delta T_{\text{ex}} < 0$ at the millimeter/submillimeter emission peak of the Hot Core. We also see $^{13}CH_3OH$ in the $0''.3$ images only and not in the $0''.7$ images, implying a highly compact methanol source, which would also be consistent with an internally heated core. This, along with a possibility of a low-velocity outflow, as discussed in Section 2.5, matches the profile of an embedded young star.

Sources of heating in the Hot Core region of Orion KL remain the topic of ongoing debate. In a more general sense, the term "hot core" describes a compact, molecule-rich region with temperatures between 100 and 300 K resulting from the warm-up of young massive stars (e.g., Evans, 1999; Kurtz et al., 2000; Herbst & van Dishoeck, 2009). Moreover, the nearly two dozen hot cores presented in the literature typically are characterized as being internally heated by embedded massive stars (Hernández-Hernández et al., 2014; Fayolle et al., 2015). However, there have been a couple of hot molecular cores—namely the Orion KL Hot Core and G34.26+0.15 (Mookerjea et al., 2007)—for which definitive evidence of an embedded heating source has eluded observations. Despite the expectation that a region of hot molecular gas would have an internal source of heating, the source of heating in Orion KL's Hot Core region is currently unknown.

The so-called Hot Core was first identified by Ho et al. (1979), who observed it as a compact source of hot NH_3 emission. Blake et al. (1996) found no evidence for a (strong) source of internal heating there, and since then, there have been multiple studies that support an externally heated "hot core" (e.g., Goddi et al., 2011; Zapata et al., 2011; Bally et al., 2017; Orozco-Aguilera et al., 2017; Peng et al., 2017). Zapata et al. (2011), for example, favor an externally heated Hot Core model (SMM3 in their work) because they do not find hot molecular gas emission associated with self-luminous submillimeter, radio, or infrared sources. Furthermore, they find that hot HC_3N gas seems to form a shell around the northeastern edge of the Hot Core, which suggests the Hot Core is illuminated from the edges—that is, externally heated, specifically by shockwaves.

Alternatively, Kaufman (Kaufman et al., 1998) show that large, warm columns of molecular gas are more easily produced in internally heated cores. They conclude that, while Source I may externally heat some of the material in the area surrounding the Hot Core, there are likely young embedded star(s) heating the core. de Vicente et al. (2002) further suggest that the Hot Core is internally heated by an embedded massive star obscured by an edge-on disk. Their speculation is based on vibrationally excited HC_3N observed in the Hot Core at energy levels that would require a heating source with too large a luminosity to come from nearby external sources. Furthermore, Crockett et al. (2014a) conclude that H_2S emission, which is pumped by far-IR radiation, in the Hot Core region signals the presence of a hidden source of luminosity. However, recent ALMA continuum observations of Orion KL by Otter et al. (2021) show an embedded edge-on disk (source 24 in their analysis) at the Hot Core millimeter/submillimeter emission peak that is much fainter than Source I and unlikely to be high-mass. Another hybrid hypothesis is that the Hot Core might have been a typical hot core around Source I prior to Orion's explosive event, and that, as a result of this, even the dense gas of the Hot Core were spatially separated from the protostars, especially Source I (Nickerson et al., 2021), giving us the enigmatic molecular core we observe today.

We stress that our evidence in support of an internal heating source does not preclude external heating in the Hot Core. Other studies that have looked at whether the Hot Core is externally or internally heated have made use of a range of angular resolutions. For example, Zapata et al. (2011) used Submillimeter Array (SMA) observations with an angular resolution of $3''.28\times3''.12$, which corresponds to spatial scales of >1200 au in Orion KL. They suggest that external heating of the Hot Core comes from energetic shocks from the Orion KL explosion that are now passing through the Hot Core region. Goddi et al. (2011) drew similar conclusions but with EVLA observations at subarcsecond angular resolutions.

Heating from a combination of shocks and embedded young stars may explain the line width profiles observed for CH_3CN $\nu_8 = 1$. At $0''.2$ angular resolution, the CH_3CN $\nu_8 = 1$ line widths are narrower, with $\Delta V \sim 1.5$ km s^{-1}, at the millimeter/submillimeter Hot Core peak and are surrounded by CH_3CN $\nu_8 = 1$ emission marked by slightly broader lines of $\Delta V \sim 2.0$ km s^{-1}. While this is only a modest difference, the fact that the line width field is not uniform, specifically at the millimeter/submillimeter peak, and that shocked material is marked by broader line widths are evidence that the conditions at this site are distinct from the surrounding region.

Crockett et al. (2014b) demonstrate that, relative to other components, the Hot Core is the most heterogeneous thermal structure in Orion KL given the spread of excitation temperatures derived for a spread of cyanides, sulphur-bearing molecules, and oxygen-bearing complex organics. Therefore, it is likely that the Hot Core region is heated by a multitude of sources, both internally and externally. Based on mass estimates of $1001 \pm 791\ M_\odot$ (Pattle et al., 2017) and a 10% star formation efficiency combined with a mean stellar mass of $\sim 2\ M_\odot$ (Hillenbrand & Hartmann, 1998), the Orion KL/BN region could be expected to have enough mass to form 50 ± 40 stars. In other words, Orion is a dense protostellar cluster in which additional protostellar sources beyond Source I are expected.

Compact Ridge

Figure 2.11 shows that the Compact Ridge, as traced by ^{13}CH$_3$OH emission, is externally heated. This conclusion agrees with past studies of ground-state methanol in Orion KL (Wang et al., 2011). The derived excitation temperature for a HCOOCH$_3$ emission peak in the Compact Ridge—denoted by the teal diamond labeled 'MF1' in Figure 2.11—was also measured to be higher in a larger beam than in a smaller one (Favre et al., 2011).

Hot Core-SW

As discussed in Section 2.5, the region southwest of the Hot Core is interesting because it seems to exhibit, broadly speaking, the physical parameters of the Hot Core but the chemical composition of the Compact Ridge. The thermal structure of this region is also interesting because of its heterogeneity.

The average ^{13}CH$_3$OH excitation temperature in the Hot Core-SW (i.e., the mean derived $T_{\rm ex}$ across all pixels in the range of $\alpha_{\rm J2000} = 05^{\rm h}35^{\rm m}14^{\rm s}\!.21-14^{\rm s}\!.64$ and $\delta_{\rm J2000} = -05°22'32''-38''$ in the $0''\!.3$ map) is 140 K, which agrees with methanol excitation temperatures toward the Compact Ridge reported by Crockett et al. (2014b). As seen in the full angular resolution ^{13}CH$_3$OH excitation temperature map, the Hot Core-SW exhibits pockets of higher temperature, with some areas having temperatures as warm as ~225 K. The sizes of these pockets range from $\sim 0''\!.15$ to $\sim 0''\!.50$ across, which corresponds to approximately 60 and 200 au, respectively, at Orion KL's distance. Thus, the pockets have the same spatial scales as embedded YSOs.

Furthermore, Figure 2.11 shows that the pockets of higher temperature align with regions where $\Delta T_{\rm ex} < 0$. This suggests that there could be internal sources of heating at these sites, and that these warm pockets could house embedded YSOs which are heating the gas.

However, these pockets are irregularly shaped and do not have temperature gradients resembling a localized "spot heating" effect, in which the gas temperature decreases radially outward from the center of an embedded YSO (e.g., van 't Hoff et al., 2018, 2020). As such, we cannot definitively say whether these anomalous temperature pockets in the Hot Core-SW can be attributed to embedded sources of heating. Determining the nature of these pockets may require detailed radiative transfer modeling or additional continuum observations to complement the existing data sets.

One of these pockets is cospatial with a strong $HCOOCH_3$ emission peak, reported as MF2 (α_{J2000} = $05^h35^m14\overset{s}{.}44$, δ_{J2000} = $-05°22'34\overset{''}{.}4$) by Favre et al. (2011). Favre et al. report T_{ex} ~ 130 K in both a $1\overset{''}{.}8\times0\overset{''}{.}8$ (T_{ex} = 128 ± 9 K) and a $3\overset{''}{.}6\times2\overset{''}{.}2$ (140 ± 14 K) beam. As such, their results at this site do not agree with ours; however, their observations use larger beam sizes than our analysis, which likely contributes to this discrepancy.

Like the Hot Core, the thermal structure of the Hot Core-SW region is likely affected by a mix of internal and external heating sources. At $0\overset{''}{.}7$ angular resolution, we see high temperatures of ~300 K typical of hot cores adjacent to SMA1 and C22 and along the western edge of the Hot Core-SW. This may show the edge of this region being heated by the shocks from the Orion KL explosion propagating through the gas. This part of the Hot Core-SW is also marked by $\Delta T_{ex} > 0$, further supporting some source of external heating.

IRc4

IRc4 is a compact emission region north of the Compact Ridge that is associated with a high-density core on the order of ~200-300 au (Hirota et al., 2015). The heating source of IRc4 remains uncertain. Okumura et al. (2011) propose that IRc4 is a simple, externally heated dust cloud, whereas de Buizer et al. (2012) suggests that it is self-luminous.

The $^{13}CH_3OH$ ΔT_{ex} profile is ambiguous toward IRc4. East of the emission peak center, $\Delta T_{ex} < 0$ K, including when accounting for uncertainty, suggesting a source of internal heating. However, just west of center, $\Delta T_{ex} > 0$ within radii where simple Gaussian models of an internally heated source predict $\Delta T_{ex} < 0$ K. These ambiguous results may indicate that IRc4 is indeed heated both internally close-in to the core and externally everywhere else. However, dedicated follow-up observations are necessary to confirm this hypothesis.

Northwest Clump

IRc6 is a mid-IR source toward the northwestern part of the Northwest Clump (NWC). In our observations, we do not detect vibrationally excited CH_3CN, which traces material pumped by far-IR radiation from massive stars, toward IRc6, and other studies have reported that there is no evidence of an embedded young star there (e.g., Shuping et al., 2004).

Curiously, we find $\Delta T_{\rm ex} < 0$ K from the $^{13}CH_3OH$ temperature measured toward IRc6. This signals that there is perhaps a source of internal heating in this region. Further evidence in support of IRc6 being internally heated can be seen in the $^{13}CH_3OH$ excitation temperature maps, particularly the tapered angular resolution map (Figure 2.9). The Northwest Clump exhibits a radial temperature gradient from ~95 K in the center to ~65 K near the edges of that region. This localized "spot heating" effect, in which the gas temperature decreases radially outward from the center of an embedded young stellar object, has been observed toward the warm embedded disk in L1527 (van 't Hoff et al., 2018) and the deeply embedded protostellar binary IRAS 16293-2422 (van 't Hoff et al., 2020). If there is, in fact, an internal heating source in the Northwest Clump, it likely does not play a dominant role in the thermal profile of the region (Li et al., 2020).

2.7 Summary

We have used ground-state $^{13}CH_3OH$ and vibrationally excited CH_3CN emission in ALMA Band 4 from Cycles 4 and 5 observations to map the velocity and thermal structure of Orion KL at angular resolutions of $\sim 0\farcs2-0\farcs3$ and $\sim 0\farcs7-0\farcs9$. Overall, our results agree with the previous work at lower angular resolutions (e.g.,by Wang et al., 2011; Friedel & Widicus Weaver, 2011; Feng et al., 2015). The angular resolution employed in this work probes spatial scales $\leq$350 au in Orion KL, giving us a more localized look at the nebula's physical structure, specifically that induced by YSOs.

1. We find evidence of possible sources of internal heating in the Hot Core. The velocity field exhibits an elongated structure centered on the Hot Core millimeter/submillimeter emission peak, which has also been reported to be the site of an embedded edge-on disk. This elongated structure, which is perpendicular to the edge-on disk, may be a low-velocity outflow with an LSR velocity of $\sim$ 7−8 km s^{-1}, which is slightly higher than the ambient velocity ($V_{\rm LSR} \sim 5$ km s^{-1}) of the Hot Core region. Furthermore, the derived CH_3CN

$v_8 = 1$ excitation temperature in the Hot Core is higher in a smaller beam than in a larger beam, suggesting an internal heating source. The thermal profile and apparent outflow structure emanating from the Hot Core may be evidence of an embedded protostar in the Hot Core.

2. The Hot Core-SW appears to have an exceptionally heterogeneous thermal structure. The average excitation temperature in the region is 140 K, and there are pockets of higher temperature as much as 225 K throughout. These pockets have higher temperatures in a smaller beam versus a larger beam, suggesting that they are internally heated. However, these pockets are not associated with compact millimeter/submillimeter emission sources. The Hot Core-SW is also externally heated on the northeastern edge, presumably by the Orion KL explosion that took place about 500 years ago northwest of Source I.

3. The thermal structure of IRc6 in the Northwest Clump suggests that this region has an internal heating source. Specifically, the temperature there is higher in a smaller beam, and the excitation temperature profile decreases radially from 95 K in the center to 65 K near the edges, resembling a spot heating effect found in embedded YSOs elsewhere. If there is an internal source of heating at IRc6, however, it does not play a dominant role in the Northwest Clump.

As we uncover more about Orion KL, it is becoming increasingly apparent that is a dynamic and heterogeneous region, and that each of its spatial components is not accurately described by one set of parameters. Furthermore, identifying the heating sources within Orion KL, and in particular the sources of internal heating, are critical to better understanding the nebula and its chemistry.

Acknowledgements

The work presented here makes use of the following ALMA data: ADS/JAO.ALMA #2017.1.01149, #2016.1.01019, and #2013.1.01034. ALMA is a partnership of ESO (representing its member states), NSF (USA), and NINS (Japan), together with NRC (Canada), MOST and ASIAA (Tawain), and KASI (Republic of Korea), in cooperation with the Republic of Chile. The Joint ALMA Observatory is operated by ESO, AUI/NRAO, and NAOJ. The National Radio Astronomy Observatory (NRAO) is a facility of the National Science Foundation (NSF) operated under Associated Universities, Inc. (AUI). This research made use of APLpy, an open-source plotting package for Python (Robitaille & Bressert, 2012; Robitaille, 2019).

This work has been supported by the NSF Graduate Research Fellowship Program under grant No. DGE-1144469 and NRAO Student Observing Support under Award No. SOSPA6-014. It was also funded by the NSF AAG (AST-1514918) and NASA Astrobiology (NNX15AT33A) and Exoplanet Research (XRP, NNX16AB48G) programs. This work benefited from discussions with Cam Buzard, Dana Anderson, Griffin Mead, Kyle Virgil, and Sadie Dutton. We thank Susanna Widicus Weaver and the anonymous referee for feedback on the prepared manuscript, as well as Adam Ginsburg and Justin Otter for comments related to the nature of the Hot Core. We also thank Erica Keller, Sarah Wood, and the NRAO North American ALMA Science Center (NAASC) for their assistance with the data reduction.

Facilities: ALMA
Software: CASA (McMullin et al., 2007), CDMS (Müller et al., 2001), LMFIT (Newville et al., 2019), APLpy (Robitaille & Bressert, 2012; Robitaille, 2019), Gaussian16 (Frisch et al., 2016)

References

ALMA Pipeline Team. 2016, ALMA Science Pipeline Reference Manual CASA 4.7.0, ALMA Doc 4.14v1.0

Andreani, P., Carpenter, J., Diaz Trigo, M., et al. 2018, ALMA Cycle 6 Proposer's Guide, ALMA Doc. 6.2 v1.0

Bally, J., Ginsburg, A., Arce, H., et al. 2017, *Astrophys. J.*, 837, 60, doi: `10.3847/1538-4357/aa5c8b`

Bally, J., Ginsburg, A., Silvia, D., & Youngblood, A. 2015, *Astron. Astrophys.*, 579, A130, doi: `10.1051/0004-6361/201425073`

Beuther, H., & Nissen, H. D. 2008, *Astrophys. J. Lett.*, 679, L121, doi: `10.1086/589330`

Beuther, H., Zhang, Q., Greenhill, L. J., et al. 2004, *Astrophys. J. Lett.*, 616, L31, doi: `10.1086/423670`

Beuther, H., Zhang, Q., Reid, M. J., et al. 2006, *Astrophys. J.*, 636, 323, doi: `10.1086/498015`

Bisschop, S. E., Jørgensen, J. K., van Dishoeck, E. F., & de Wachter, E. B. M. 2007, *Astron. Astrophys.*, 465, 913, doi: `10.1051/0004-6361:20065963`

Blake, G. A., Mundy, L. G., Carlstrom, J. E., et al. 1996, *Astrophys. J. Lett.*, 472, L49, doi: `10.1086/310347`

Blake, G. A., Sutton, E. C., Masson, C. R., & Phillips, T. G. 1987, *Astrophys. J.*, 315, 621, doi: `10.1086/165165`

Boonman, A. M. S., Stark, R., van der Tak, F. F. S., et al. 2001, *Astrophys. J. Lett.*, 553, L63, doi: `10.1086/320493`

Carroll, P. B. 2018, PhD thesis, California Institute of Technology, doi: `10.7907/8Y1M-6C76`

Cortes, P. C., Le Gouellec, V. J. M., Hull, C. L. H., et al. 2021, *Astrophys. J.*, 907, 94, doi: `10.3847/1538-4357/abcafb`

Crockett, N. R., Bergin, E. A., Neill, J. L., et al. 2014a, *Astrophys. J.*, 781, 114, doi: `10.1088/0004-637X/781/2/114`

—. 2014b, *Astrophys. J.*, 787, 112, doi: `10.1088/0004-637X/787/2/112`

Csengeri, T., Belloche, A., Bontemps, S., et al. 2019, *Astron. Astrophys.*, 632, A57, doi: `10.1051/0004-6361/201935226`

de Buizer, J. M., Morris, M. R., Becklin, E. E., et al. 2012, *Astrophys. J.*, 749, L23, doi: `10.1088/2041-8205/749/2/l23`

de Vicente, P., Martín-Pintado, J., Neri, R., & Rodríguez-Franco, A. 2002, *Astrophys. J. Lett.*, 574, L163, doi: `10.1086/342508`

Evans, Neal J., I. 1999, *Annu. Rev. Astron. Astrophys.*, 37, 311, doi: `10.1146/annurev.astro.37.1.311`

Favre, C., Despois, D., Brouillet, N., et al. 2011, *Astron. Astrophys.*, 532, A32, doi: `10.1051/0004-6361/201015345`

Favre, C., Pagani, L., Goldsmith, P. F., et al. 2017, *Astron. Astrophys.*, 604, L2, doi: `10.1051/0004-6361/201731327`

Fayolle, E. C., Öberg, K. I., Garrod, R. T., van Dishoeck, E. F., & Bisschop, S. E. 2015, *Astron. Astrophys.*, 576, A45, doi: `10.1051/0004-6361/201323114`

Feng, S., Beuther, H., Henning, T., et al. 2015, *Astron. Astrophys.*, 581, A71, doi: `10.1051/0004-6361/201322725`

Friedel, D. N., & Snyder, L. E. 2008, *Astrophys. J.*, 672, 962, doi: `10.1086/523896`

Friedel, D. N., & Widicus Weaver, S. L. 2011, *Astrophys. J.*, 742, 64, doi: `10.1088/0004-637X/742/2/64`

Frisch, M. J., Trucks, G. W., Schlegel, H. B., et al. 2016, Gaussian~16 Revision C.01

Genzel, R., & Stutzki, J. 1989, *Annu. Rev. Astron. Astrophys.*, 27, 41, doi: `10.1146/annurev.aa.27.090189.000353`

Gieser, C., Semenov, D., Beuther, H., et al. 2019, *Astron. Astrophys.*, 631, A142, doi: `10.1051/0004-6361/201935865`

Ginsburg, A., Bally, J., Goddi, C., Plambeck, R., & Wright, M. 2018, *Astrophys. J.*, 860, 119, doi: `10.3847/1538-4357/aac205`

Ginsburg, A., Goddi, C., Kruijssen, J. M. D., et al. 2017, *Astrophys. J.*, 842, 92, doi: `10.3847/1538-4357/aa6bfa`

Goddi, C., Greenhill, L. J., Humphreys, E. M. L., Chand ler, C. J., & Matthews, L. D. 2011, *Astrophys. J. Lett.*, 739, L13, doi: `10.1088/2041-8205/739/1/L13`

Hall, D. N. B., Kleinmann, S. G., Ridgway, S. T., & Gillett, F. C. 1978, *Astrophys. J. Lett.*, 223, L47, doi: `10.1086/182725`

Herbst, E., & van Dishoeck, E. F. 2009, *Annu. Rev. Astron. Astrophys.*, 47, 427, doi: `10.1146/annurev-astro-082708-101654`

Hernández-Hernández, V., Zapata, L., Kurtz, S., & Garay, G. 2014, *Astrophys. J.*, 786, 38, doi: `10.1088/0004-637X/786/1/38`

Hillenbrand, L. A., & Hartmann, L. W. 1998, *Astrophys. J.*, 492, 540, doi: `10.1086/305076`

Hirota, T., Kim, M. K., Kurono, Y., & Honma, M. 2015, *Astrophys. J.*, 801, 82, doi: `10.1088/0004-637X/801/2/82`

Ho, P. T. P., Barrett, A. H., Myers, P. C., et al. 1979, *Astrophys. J.*, 234, 912, doi: `10.1086/157575`

Kaufman, M. J., Hollenbach, D. J., & Tielens, A. G. G. M. 1998, *Astrophys. J.*, 497, 276, doi: `10.1086/305444`

Kepley, A. A., Tsutsumi, T., Brogan, C. L., et al. 2020, *Publ. Astron. Soc. Pac.*, 132, 024505, doi: `10.1088/1538-3873/ab5e14`

Kounkel, M., Hartmann, L., Loinard, L., et al. 2017, *Astrophys. J.*, 834, 142, doi: `10.3847/1538-4357/834/2/142`

Kurtz, S., Cesaroni, R., Churchwell, E., Hofner, P., & Walmsley, C. M. 2000, in Protostars and Planets IV, ed. V. Mannings, A. P. Boss, & S. S. Russell, 299–326

Laas, J. C., Garrod, R. T., Herbst, E., & Widicus Weaver, S. L. 2011, *Astrophys. J.*, 728, 71, doi: `10.1088/0004-637X/728/1/71`

Law, C. J., Zhang, Q., Öberg, K. I., et al. 2021, *Astrophys. J.*, 909, 214, doi: `10.3847/1538-4357/abdeb8`

Li, D., Tang, X., Henkel, C., et al. 2020, *Astrophys. J.*, 901, 62, doi: `10.3847/1538-4357/abae60`

Luo, G., Feng, S., Li, D., et al. 2019, *Astrophys. J.*, 885, 82, doi: `10.3847/1538-4357/ab45ef`

Masson, C. R., Claussen, M. J., Lo, K. Y., et al. 1985, *Astrophys. J. Lett.*, 295, L47, doi: `10.1086/184535`

McMullin, J. P., Waters, B., Schiebel, D., Young, W., & Golap, K. 2007, Astronomical Society of the Pacific Conference Series, Vol. 376, CASA Architecture and Applications, ed. R. A. Shaw, F. Hill, & D. J. Bell, 127

Mookerjea, B., Casper, E., Mundy, L. G., & Looney, L. W. 2007, *Astrophys. J.*, 659, 447, doi: `10.1086/512095`

Moscadelli, L., Rivilla, V. M., Cesaroni, R., et al. 2018, *Astron. Astrophys.*, 616, A66, doi: `10.1051/0004-6361/201832680`

Müller, H. S. P., Thorwirth, S., Roth, D. A., & Winnewisser, G. 2001, *Astron. Astrophys.*, 370, L49, doi: `10.1051/0004-6361:20010367`

Neill, J. L., Crockett, N. R., Bergin, E. A., Pearson, J. C., & Xu, L.-H. 2013, *Astrophys. J.*, 777, 85, doi: `10.1088/0004-637X/777/2/85`

Newville, M., Otten, R., Nelson, A., et al. 2019, lmfit/lmfit-py 0.9.15, 0.9.15, Zenodo, doi: `10.5281/zenodo.3567247`

Nickerson, S., Rangwala, N., Colgan, S. W. J., et al. 2021, *Astrophys. J.*, 907, 51, doi: `10.3847/1538-4357/abca36`

Nissen, H. D., Gustafsson, M., Lemaire, J. L., et al. 2007, *Astron. Astrophys.*, 466, 949, doi: `10.1051/0004-6361:20054304`

Okumura, S.-i., Yamashita, T., Sako, S., et al. 2011, Publications of the Astronomical Society of Japan, 63, 823, doi: `10.1093/pasj/63.4.823`

Orozco-Aguilera, M. T., Zapata, L. A., Hirota, T., Qin, S.-L., & Masqué, J. M. 2017, *Astrophys. J.*, 847, 66, doi: `10.3847/1538-4357/aa88cd`

Otter, J., Ginsburg, A., Ballering, N. P., et al. 2021, *Astrophys. J. (accepted)*, arXiv:2109.14592. `https://arxiv.org/abs/2109.14592`

Pagani, L., Favre, C., Goldsmith, P. F., et al. 2017, *Astron. Astrophys.*, 604, A32, doi: `10.1051/0004-6361/201730466`

Pattle, K., Ward-Thompson, D., Berry, D., et al. 2017, *Astrophys. J.*, 846, 122, doi: `10.3847/1538-4357/aa80e5`

Peng, T. C., Despois, D., Brouillet, N., et al. 2013, *Astron. Astrophys.*, 554, A78, doi: `10.1051/0004-6361/201220891`

Peng, Y., Qin, S.-L., Schilke, P., et al. 2017, *Astrophys. J.*, 837, 49, doi: `10.3847/1538-4357/aa5c81`

Pickett, H. M., Poynter, R. L., Cohen, E. A., et al. 1998, J. Quant. Spectrosc. Radiat. Transfer, 60, 883, doi: `10.1016/S0022-4073(98)00091-0`

Remijan, A., Snyder, L. E., Friedel, D. N., Liu, S. Y., & Shah, R. Y. 2003, *Astrophys. J.*, 590, 314, doi: `10.1086/374890`

Robitaille, T. 2019, APLpy v2.0: The Astronomical Plotting Library in Python, doi: `10.5281/zenodo.2567476`

Robitaille, T., & Bressert, E. 2012, APLpy: Astronomical Plotting Library in Python, Astrophysics Source Code Library. `http://ascl.net/1208.017`

Sakai, N., & Yamamoto, S. 2013, *Chem. Rev.*, 113, 8981, doi: `10.1021/cr4001308`

Schöier, F. L., Jørgensen, J. K., van Dishoeck, E. F., & Blake, G. A. 2002, *Astron. Astrophys.*, 390, 1001, doi: `10.1051/0004-6361:20020756`

Shuping, R. Y., Morris, M., & Bally, J. 2004, *Astron. J.*, 128, 363, doi: `10.1086/421373`

Sutton, E. C., Peng, R., Danchi, W. C., et al. 1995, *Astrophys. J. Supp.*, 97, 455, doi: `10.1086/192147`

Taniguchi, K., Plunkett, A., Herbst, E., et al. 2020, *Mon. Not. R. Astron. Soc.*, 493, 2395, doi: `10.1093/mnras/staa012`

Tercero, B., Cuadrado, S., López, A., et al. 2018, *Astron. Astrophys.*, 620, L6, doi: `10.1051/0004-6361/201834417`

van 't Hoff, M. L. R., Bergin, E. A., Jørgensen, J. K., & Blake, G. A. 2020, *Astrophys. J. Lett.*, 897, L38, doi: `10.3847/2041-8213/ab9f97`

van 't Hoff, M. L. R., Tobin, J. J., Harsono, D., & van Dishoeck, E. F. 2018, *Astron. Astrophys.*, 615, A83, doi: `10.1051/0004-6361/201732313`

Wang, S., Bergin, E. A., Crockett, N. R., et al. 2011, *Astron. Astrophys.*, 527, A95, doi: `10.1051/0004-6361/201015079`

Wilson, T. L., Johnston, K. J., Henkel, C., & Menten, K. M. 1989, *Astron. Astrophys.*, 214, 321

Wright, M., Plambeck, R., Hirota, T., et al. 2020, *Astrophys. J.*, 889, 155, doi: `10.3847/1538-4357/ab5864`

Wright, M. C. H., & Plambeck, R. L. 2017, *Astrophys. J.*, 843, 83, doi: `10.3847/1538-4357/aa72e6`

Wright, M. C. H., & Vogel, S. N. 1985, *Astrophys. J. Lett.*, 297, L11, doi: `10.1086/184547`

Wyrowski, F., Hofner, P., Schilke, P., et al. 1997, *Astron. Astrophys.*, 320, L17

Youngblood, A., Ginsburg, A., & Bally, J. 2016, *Astron. J.*, 151, 173, doi: `10.3847/0004-6256/151/6/173`

Zapata, L. A., Schmid-Burgk, J., & Menten, K. M. 2011, *Astron. Astrophys.*, 529, A24, doi: `10.1051/0004-6361/201014423`

“We’re never going to be able to model anything ever again.

—Eric Herbst”

—Susanna Widicus Weaver

Chapter 3

UNDERSTANDING METHANOL POST-FORMATION CHEMISTRY IN ORION KL

3.1 Introduction

Methanol (CH_3OH) is ubiquitous throughout the universe. It is detected in every stage and aspect of star formation, from cold cloud cores and hot cores and corinos, to outflows and circumstellar disks (e.g., Herbst & van Dishoeck, 2009; Drozdovskaya et al., 2014; Walsh et al., 2016). Because it is abundant in interstellar space, methanol is a common probe of physical structure in star-forming regions. Furthermore, methanol is one of the simplest complex organic molecules (COMs), which have six or more atoms, making it a commonly-used tracer of other, more complex organics.

It is widely accepted that methanol forms on the surfaces of icy grains, primarily through successive hydrogenation of frozen CO (e.g., Charnley et al., 1997; Nagaoka et al., 2005; Watanabe et al., 2006):

$$\mathrm{CO} \xrightarrow{H} \mathrm{HCO} \xrightarrow{H} \mathrm{H_2CO} \xrightarrow{H} \mathrm{H_3CO} \xrightarrow{H} \mathrm{CH_3OH} \tag{3.1}$$

However, the mechanism by which methanol desorbs off the grains is perhaps the least understood aspect of methanol formation (Garrod et al., 2006). Proposed mechanisms for methanol desorption include thermal desorption, liberation by shocks, ejection by cosmic rays, ultraviolet (UV) photodesorption, and desorption by formation energy (e.g., Turner, 1998; Hasegawa & Herbst, 1993; Katz et al., 1999). However, methanol has been found to dissociate to produce H_2CO, CH_3O, CH_2OH, and other fragments when leaving the grains via UV photodesorption, rendering it unlikely that this mechanism is the main driver behind gas-phase methanol abundances (Bertin et al., 2016). Similarly, desorption by formation energy has been shown to be an unlikely scenario for injection of CH_3OH into the gas phase (Katz et al., 1999).

We investigate the means of methanol desorption off the grains in the Orion Kleinmann-Low (Orion KL) nebula using subarcsecond observations with the Atacama Large Millimeter/submillimeter Array (ALMA). At a distance of ~388 pc, Orion KL is the closest region of high-mass star formation to Earth (Kounkel et al., 2017). The complex molecular aspect of the cloud consists of several spatial components, such as the Hot Core and the Compact Ridge, each of which have varying chemical and physical properties (e.g., Blake et al., 1987; Friedel & Widicus Weaver, 2011; Feng et al., 2015), making Orion KL an excellent laboratory for studying chemical patterns across different physical environments.

In this work, we use $^{13}CH_3OH$ as a proxy for the primary methanol isotopologue, which is often optically thick in star-forming regions and has been shown to be optically thick toward Orion KL specifically (Crockett et al., 2014). We suggest that thermal desorption is the primary mechanism by which methanol is liberated off the grains in Orion KL. The data used here are from the ALMA Cycle 5 data cubes used in Chapter 2 (Wilkins et al., 2022); the observations and analytical methods are described in Sections 2.2 and 2.3, respectively. In this chapter, Section 3.2 provides brief descriptions of the Orion KL components discussed in this work. Our findings are presented in Section 3.3, and this work is summarized in Section 3.4.

3.2 Descriptions of Regions Studied

Here, we focus on three emission regions in Orion KL: the Hot Core-SW, the Compact Ridge, and IRc4. These are briefly introduced in this section.

Hot Core-SW

The Hot Core-SW is an elongated region to the southwest of the Hot Core region, which is a warm, dense region typically associated with nitrogen chemistry (e.g., Blake et al., 1987; Friedel & Widicus Weaver, 2011; Crockett et al., 2014). The Hot Core-SW has not been as extensively reported on as other, more famous components of Orion KL, but it has a particularly heterogeneous thermal profile (Wilkins et al., 2022). Despite being adjacent to the Hot Core and being denser than the Compact Ridge, the Hot Core-SW does not seem to be characterized by nitrogen-bearing chemistry (Friedel & Snyder, 2008). Dedicated observations are needed to more fully characterize this region.

Compact Ridge

The Compact Ridge is a colder region in Orion KL characterized by its oxygen-bearing chemistry (e.g., Blake et al., 1987; Friedel & Widicus Weaver, 2011). Much of Orion KL is thought to be influenced by an explosion that took place in the nebula about 500 years ago (e.g., Bally & Zinnecker, 2005; Bally et al., 2015, 2017), but narrow line widths for molecular emission in the Compact Ridge suggest that the Compact Ridge is a quiescent region unaffected by the explosion (Pagani et al., 2017).

IRc4

IRc4 is a compact emission region north of the Compact Ridge. It is associated with a high-density core (Hirota et al., 2015), but its source of heating is presently unknown. Previous work has suggested that IRc4 is an externally heated dust cloud (e.g., Okumura et al., 2011), whereas other reports suggest the object is self-luminous (e.g., de Buizer et al., 2012).

3.3 Methanol Desorption

As discussed in Section 3.1, there are several possible mechanisms by which methanol molecules, which form on icy grains, are injected into the gas phase. However, several of these—namely, UV photodesorption and desorption by formation energy—are unlikely to be key drivers of methanol desorption. As such, the main contenders for desorption in the Orion KL are thermal desorption and liberation by shocks.

We conclude that the observed gas-phase $^{13}CH_3OH$ abundances in the Hot Core-SW and Compact Ridge of Orion KL are predominantly the result of thermal desorption in which material is liberated from the grains as they gradually warm. In this work, $^{13}CH_3OH$ is used as an optically thin proxy for the primary CH_3OH isotopologue, which is optically thick toward Orion KL (e.g., Crockett et al., 2014). Around massive protostars, methanol begins to sublimate as the environment approaches ~90-100 K (e.g., Green et al., 2009, for micron-sized grains), which explains why most of the methanol observed in our observations traces gas warmer than 90 K.

Thermal desorption by methanol in Orion KL is supported by the line width profiles and relative abundance enhancements in $^{13}CH_3OH$ across the nebula. A scenario in which molecules are liberated predominantly by shocks would produce wider lines and a velocity structure different from that observed in quiescent material (Schöier et al., 2002). However, as demonstrated in Figure 3.1, $^{13}CH_3OH$ line widths are consistently 1-2 km s^{-1} in most of the Hot Core-SW and the Compact Ridge. Furthermore, the velocity profiles for $^{13}CH_3OH$ in all regions across Orion KL exhibit smooth gradients (Wilkins et al., 2022), whereas we might expect a stark discontinuity in shocked material.

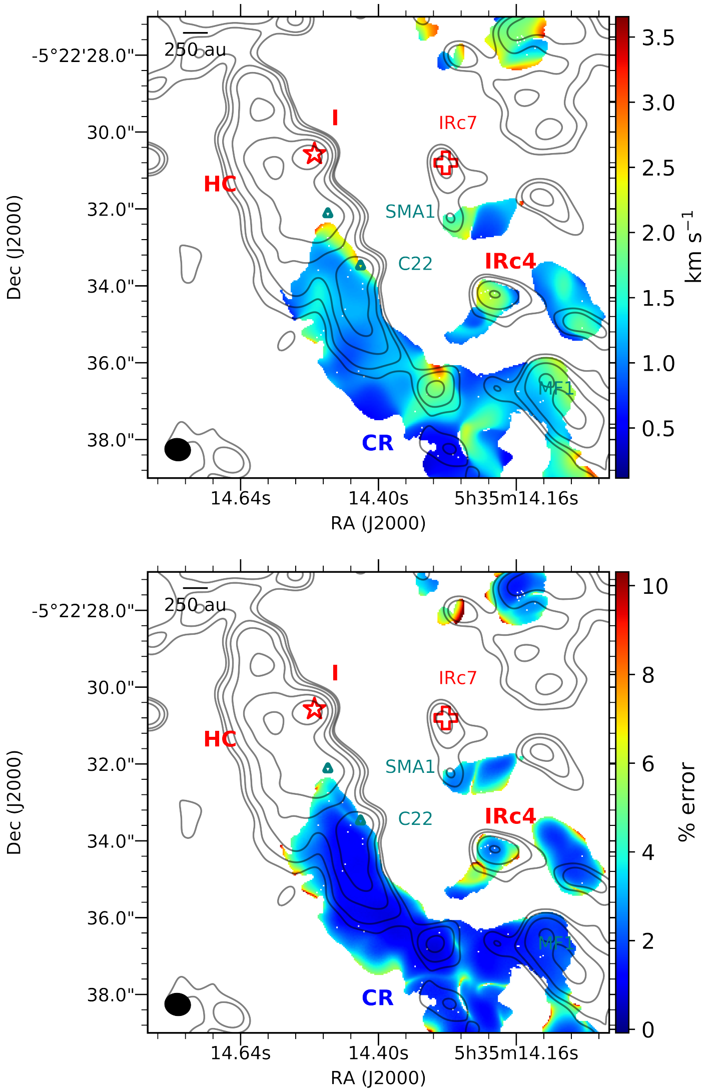

Figure 3.1: Derived ^{13}CH$_3$OH line width field and percent propagated uncertainty maps in a $\sim 0.''7$ beam shown by the color map. The continuum is shown by the grey contours at $2\sigma_{\rm rms}, 4\sigma_{\rm rms}, 8\sigma_{\rm rms}, 16\sigma_{\rm rms}, \ldots$ The synthesized beam is shown by the black ellipse in the bottom left corner. Adapted from Wilkins et al. (2022).

Another piece of evidence in favor of thermal desorption rather than liberation by shocks, even on small scales, is the range of column density measured. The derived $\sim 0.''7$ column density map is shown in Figure 3.2 and shows abundances on the order of 10^{16}-10^{17} cm^{-2}. Computational models of CH$_3$OH in shocked material suggest that the abundance of CH$_3$OH in shocked gas would be enhanced by several orders of magnitude relative to the ambient gas. For instance, models of the young shocks from the L1448-mm dark cloud molecular outflow show rapid enhancements of CH$_3$OH in shocked material on the order of 10^3-10^6 within as few as ten years of

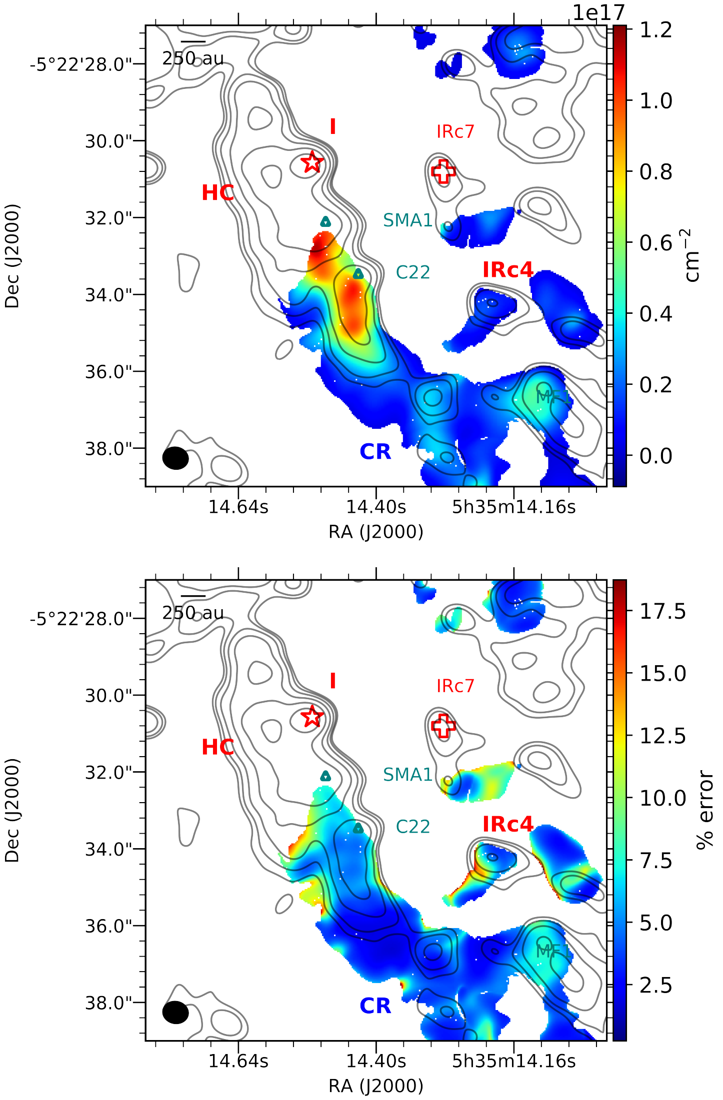

Figure 3.2: Derived ^{13}CH$_3$OH column density and percent propagated uncertainty maps in a $\sim 0''.7$ beam shown by the color map. The continuum is shown by the grey contours at $2\sigma_{\mathrm{rms}}, 4\sigma_{\mathrm{rms}}, 8\sigma_{\mathrm{rms}}, 16\sigma_{\mathrm{rms}}, \ldots$ The synthesized beam is shown by the black ellipse in the bottom left corner. Adapted from Wilkins et al. (2022).

the onset of the outflow (Jiménez-Serra et al., 2008). Any enhancements of CH$_3$OH that we see toward Orion KL are at most a factor of $\sim$6, which does not match the profile of steep enhancements in molecular abundances in shocked gas.

Finally, there appears to be a correlation between methanol abundances and temperature, as seen in Figure 3.3, which we conclude is further evidence in favor of thermal desorption. Although methanol desorption begins at temperatures of $\sim$100 K, complete methanol desorption occurs at higher temperatures of around 150 K

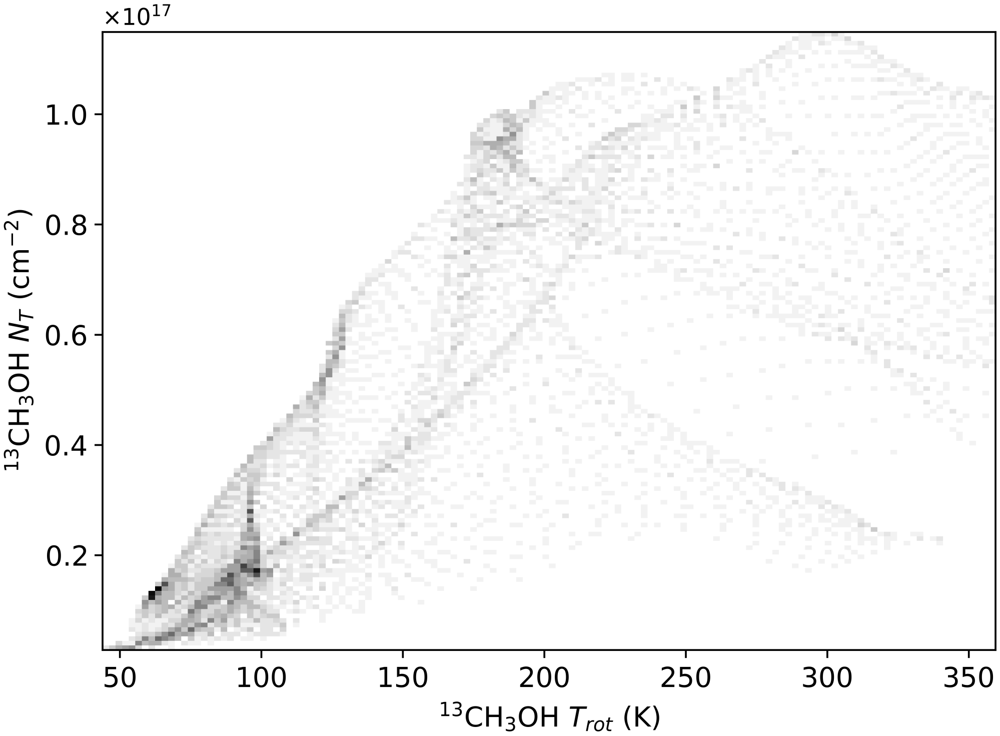

Figure 3.3: Two-dimensional histogram with 50 points per bin showing the derived $^{13}CH_3OH$ column density from Figure 3.2 against the rotation temperature $T_{\rm rot}$ derived by Wilkins et al. (2022).

(Müller et al., 2021). Similarly, water achieves its peak sublimation rate at around 180 K (Collings et al., 2015). It would appear then that warmer temperatures lead to higher methanol abundances in the gas. Laboratory experiments investigating the thermal desorption of interstellar ice analogues can explain this trend. Experiments have shown that the desorption of interstellar ices is not instantaneous but depends on ice morphology and that the rate of methanol desorption in ice mixtures increases with temperature (Burke & Brown, 2010). Furthermore, methanol formed on icy grain mantles is incorporated into the ice mixture and forms complexes with other molecules such as CO_2 prior to ice segregation and subsequent desorption (e.g., Skinner et al., 1992; Ehrenfreund et al., 1998; Vidali et al., 2004, 2006). Whether methanol also diffuses into (hence becomes trapped in) the porous ice—a phenomenon exhibited by smaller volatiles such as CO (Collings et al., 2003)—remains unclear. In either case, the gradual release of methanol alongside warming YSOs matches a thermal sublimation scenario in Orion KL.

For these reasons, it is likely that the gas-phase $^{13}CH_3OH$ observed is predominantly the result of thermal desorption accompanying the warming of grain mantles by young stellar objects (YSOs) and that liberation by shocks plays a minor role for the observed methanol gas in the Hot Core-SW and the Compact Ridge. This agrees with previous speculations that the Compact Ridge is a quiescent region unaffected by the putative Orion KL explosion (e.g., Pagani et al., 2017).

Abundance Enhancements from YSOs?

If molecules are thermally released by protostars warming the grains, abundance enhancements in the resulting gas should be located within a ~150 au radius of the central star (Schöier et al., 2002). This is not likely for the Compact Ridge, which has been repeatedly shown to be externally heated and shows no evidence of self-luminous YSOs (e.g., Wang et al., 2011; Favre et al., 2011). Furthermore, there do not appear to be compact regions of abundance enhancements in the Compact Ridge (Figure 3.2).

The Hot Core-SW, which lies to the southwest of the Hot Core with the compact SMA1 and C22 sources to the north, may have modest $^{13}CH_3OH$ abundance enhancements spurred by embedded YSOs. Wilkins et al. (2022) showed that this region exhibits pockets of higher temperature and $^{13}CH_3OH$ column density in which the temperature derived from a smaller beam (~0.″3) is greater than that in a larger beam (0.″7), indicative of a possible internal heating source (see also Section 2.6 of this thesis). Furthermore, the higher abundances in the higher resolution images reported by Wilkins et al. are confined to regions with radii <100 au at Orion KL's distance. Figure 3.2 shows abundance enhancements directly south of SMA1—thought to be an embedded massive protostar driving an outflow (Beuther et al., 2006)—and C22—a possible hot core (Friedel & Widicus Weaver, 2011). Such abundance enhancements driven by protostellar warming would be expected to envelop the central star whereas we see an elongated structure. We suspect that this profile is due to the relatively methanol-rich gas being pushed south away from an explosive event that took place north of Source I (and hence north of SMA1 and C22) in Orion KL about 500 years ago (e.g., Bally & Zinnecker, 2005).

Non-Thermal Desorption of $^{13}CH_3OH$

Indeed, non-thermal desorption must also be considered and is non-negligible for several gas-phase species, including methanol (e.g., Chang et al., 2007). Thermal desorption of CH_3OH ice in hot cores begins at temperatures of 95-108 K, and in environments where desorption is strictly due to thermal processes, gas-phase

CH_3OH would not be observed below 94 K (Luna et al., 2018).

In the temperature maps presented by Wilkins et al. (2022), there are regions in the observed $^{13}CH_3OH$ gas where the gas temperature falls below 94 K. Such profiles are found in relatively diffuse material away from any (candidate) YSOs. As previously noted, non-thermal desorption mechanisms such as UV photodesorption and desorption by formation energy have been shown to be inefficient for CH_3OH injection into the gas phase (e.g., Bertin et al., 2016; Katz et al., 1999), and we have already ruled out liberation by shocks as a primary driver of methanol desorption.

A more recently proposed mechanism is the rotational desorption of ice mantles. Most desorption mechanisms assume that grains are at rest, when in fact interstellar dust grains rotate rapidly because of collisions with neutral atoms and protons as well as interactions with passing ions (Draine & Lazarian, 1998). Hoang & Tram (2020) modeled the effect of suprathermal grain rotation driven by stellar radiation on icy grains in YSOs. This mechanism, in which ice mantles are disrupted off of rotating grains into small fragments prior to chemical desorption, was found to be efficient in hot cores at gas temperatures down to 40 K and densities down to 10^4 cm^{-3}. The derived rotational temperatures for $^{13}CH_3OH$ in Orion KL bottom out at ~50 K, and so some rotational desorption is plausible in the context of the physical conditions of Orion KL.

3.4 Summary

We address desorption mechanisms after methanol formation on icy dust grains. We used ALMA Band 4 observations of $^{13}CH_3OH$ at $\sim 0\farcs7$ angular resolution to map this compound's chemical abundances throughout the nebula, building on previous high-angular-resolution studies of Orion KL's structure via molecular probes by Wilkins et al. (2022). Through this work, we find the following:

1. The narrow line widths, limited abundance enhancements, and increasing abundance with temperature measured for $^{13}CH_3OH$ suggest that thermal desorption, and not shocks, is the primary driver of methanol injection into the gas in Orion KL above 94 K. At colder temperatures, we suspect methanol is present in the gas-phase due to suprathermal desorption, as proposed by Hoang & Tram (2020).

2. Abundance enhancements of as much as a factor of ~6 are observed for $^{13}CH_3OH$ south of SMA1 and C22. These moderate enhancements also sup-

> port thermal desorption over shock-induced desorption, which is associated with abundance enhancements of several orders of magnitude. Interestingly, the higher $^{13}CH_3OH$ abundance enhancements appear to extend south from these two (candidate) protostellar sources, which we suggest is due to the gas being pushed away from the putative explosion that took place in Orion KL ~500 years ago.

While the observed $^{13}CH_3OH$ profiles in Orion KL are consistent with thermal desorption as the primary driver of gas-phase abundances, this work would benefit from models to confirm that shocks would not produce similar profiles. Specifically, predictions of the column density and rotation temperature profiles that would result from continuous magnetohydrodynamic shocks are needed, and such models would need to consider different shock velocities and different initial methanol abundances.

Acknowledgements

This chapter makes use of the following data: ADS/JAO.ALMA#2017.1.01149 and ADS/JAO.ALMA#2013.1.01034. ALMA is a partnership of ESO (representing its member states), NSF (USA), and NINS (Japan), together with NRC (Canada), MOST and ASIAA (Tawain), and KASI (Republic of Korea), in cooperation with the Republic of Chile. The Joint ALMA Observatory is operated by ESO, AUI/NRAO, and NAOJ. The National Radio Astronomy Observatory (NRAO) is a facility of the National Science Foundation (NSF) operated under Associated Universities, Inc. (AUI). This research made use of APLpy, an open-source plotting package for Python (Robitaille & Bressert, 2012; Robitaille, 2019).

This work has been supported by the NSF Graduate Research Fellowship Program under grant No. DGE-1144469, NRAO Student Observing Support under Award No. SOSPA6-014, and the NSF AAG (AST-1514918) and NASA Astrobiology (NNX15AT33A) and Exoplanet Research (XRP, NNX16AB48G) programs. This work also benefited from discussions with Dana Anderson, Cam Buzard, Sadie Dutton, Griffin Mead, and Kyle Virgil. We thank Erica Keller, Sarah Wood, and the NRAO North American ALMA Science Center (NAASC) for their assistance with the data reduction.

Facilities: ALMA
Software: CASA (McMullin et al., 2007), CDMS (Müller et al., 2001), APLpy (Robitaille & Bressert, 2012; Robitaille, 2019)

References

Bally, J., Ginsburg, A., Arce, H., et al. 2017, *Astrophys. J.*, 837, 60, doi: `10.3847/1538-4357/aa5c8b`

Bally, J., Ginsburg, A., Silvia, D., & Youngblood, A. 2015, *Astron. Astrophys.*, 579, A130, doi: `10.1051/0004-6361/201425073`

Bally, J., & Zinnecker, H. 2005, *Astron. J.*, 129, 2281, doi: `10.1086/429098`

Bertin, M., Romanzin, C., Doronin, M., et al. 2016, *Astrophys. J. Lett.*, 817, L12, doi: `10.3847/2041-8205/817/2/L12`

Beuther, H., Zhang, Q., Reid, M. J., et al. 2006, *Astrophys. J.*, 636, 323, doi: `10.1086/498015`

Blake, G. A., Sutton, E. C., Masson, C. R., & Phillips, T. G. 1987, *Astrophys. J.*, 315, 621, doi: `10.1086/165165`

Burke, D. J., & Brown, W. A. 2010, *Phys. Chem. Chem. Phys.*, 12, 5947, doi: `10.1039/B917005G`

Chang, Q., Cuppen, H. M., & Herbst, E. 2007, *Astron. Astrophys.*, 469, 973, doi: `10.1051/0004-6361:20077423`

Charnley, S. B., Tielens, A. G. G. M., & Rodgers, S. D. 1997, *Astrophys. J. Lett.*, 482, L203, doi: `10.1086/310697`

Collings, M. P., Dever, J. W., Fraser, H. J., McCoustra, M. R. S., & Williams, D. A. 2003, *Astrophys. J.*, 583, 1058, doi: `10.1086/345389`

Collings, M. P., Frankland, V. L., Lasne, J., et al. 2015, *Mon. Not. R. Astron. Soc.*, 449, 1826, doi: `10.1093/mnras/stv425`

Crockett, N. R., Bergin, E. A., Neill, J. L., et al. 2014, *Astrophys. J.*, 787, 112, doi: `10.1088/0004-637X/787/2/112`

de Buizer, J. M., Morris, M. R., Becklin, E. E., et al. 2012, *Astrophys. J.*, 749, L23, doi: `10.1088/2041-8205/749/2/l23`

Draine, B. T., & Lazarian, A. 1998, *Astrophys. J. Lett.*, 494, L19, doi: `10.1086/311167`

Drozdovskaya, M. N., Walsh, C., Visser, R., Harsono, D., & van Dishoeck, E. F. 2014, *Mon. Not. R. Astron. Soc.*, 445, 913, doi: `10.1093/mnras/stu1789`

Ehrenfreund, P., Dartois, E., Demyk, K., & D'Hendecourt, L. 1998, *Astron. Astrophys.*, 339, L17

Favre, C., Despois, D., Brouillet, N., et al. 2011, *Astron. Astrophys.*, 532, A32, doi: `10.1051/0004-6361/201015345`

Feng, S., Beuther, H., Henning, T., et al. 2015, *Astron. Astrophys.*, 581, A71, doi: `10.1051/0004-6361/201322725`

Friedel, D. N., & Snyder, L. E. 2008, *Astrophys. J.*, 672, 962, doi: `10.1086/523896`

Friedel, D. N., & Widicus Weaver, S. L. 2011, *Astrophys. J.*, 742, 64, doi: `10.1088/0004-637X/742/2/64`

Garrod, R., Park, I. H., Caselli, P., & Herbst, E. 2006, *Faraday Discuss.*, 133, 51, doi: `10.1039/b516202e`

Green, S. D., Bolina, A. S., Chen, R., et al. 2009, *Mon. Not. R. Astron. Soc.*, 398, 357, doi: `10.1111/j.1365-2966.2009.15144.x`

Hasegawa, T. I., & Herbst, E. 1993, *Mon. Not. R. Astron. Soc.*, 261, 83, doi: `10.1093/mnras/261.1.83`

Herbst, E., & van Dishoeck, E. F. 2009, *Annu. Rev. Astron. Astrophys.*, 47, 427, doi: `10.1146/annurev-astro-082708-101654`

Hirota, T., Kim, M. K., Kurono, Y., & Honma, M. 2015, *Astrophys. J.*, 801, 82, doi: `10.1088/0004-637X/801/2/82`

Hoang, T., & Tram, L. N. 2020, *Astrophys. J.*, 891, 38, doi: `10.3847/1538-4357/ab6eff`

Jiménez-Serra, I., Caselli, P., Martín-Pintado, J., & Hartquist, T. W. 2008, *Astron. Astrophys.*, 482, 549, doi: `10.1051/0004-6361:20078054`

Katz, N., Furman, I., Biham, O., Pirronello, V., & Vidali, G. 1999, *Astrophys. J.*, 522, 305, doi: `10.1086/307642`

Kounkel, M., Hartmann, L., Loinard, L., et al. 2017, *Astrophys. J.*, 834, 142, doi: `10.3847/1538-4357/834/2/142`

Luna, R., Satorre, M. Á., Domingo, M., et al. 2018, *Mon. Not. R. Astron. Soc.*, 473, 1967, doi: `10.1093/mnras/stx2473`

McMullin, J. P., Waters, B., Schiebel, D., Young, W., & Golap, K. 2007, Astronomical Society of the Pacific Conference Series, Vol. 376, CASA Architecture and Applications, ed. R. A. Shaw, F. Hill, & D. J. Bell, 127

Müller, B., Giuliano, B. M., Goto, M., & Caselli, P. 2021, *Astron. Astrophys.*, 652, A126, doi: `10.1051/0004-6361/202039139`

Müller, H. S. P., Thorwirth, S., Roth, D. A., & Winnewisser, G. 2001, *Astron. Astrophys.*, 370, L49, doi: `10.1051/0004-6361:20010367`

Nagaoka, A., Watanabe, N., & Kouchi, A. 2005, *Astrophys. J. Lett.*, 624, L29, doi: `10.1086/430304`

Okumura, S.-i., Yamashita, T., Sako, S., et al. 2011, *Publ. Astron. Soc. Jpn.*, 63, 823, doi: `10.1093/pasj/63.4.823`

Pagani, L., Favre, C., Goldsmith, P. F., et al. 2017, *Astron. Astrophys.*, 604, A32, doi: `10.1051/0004-6361/201730466`

Robitaille, T. 2019, APLpy v2.0: The Astronomical Plotting Library in Python, doi: `10.5281/zenodo.2567476`

Robitaille, T., & Bressert, E. 2012, APLpy: Astronomical Plotting Library in Python, Astrophysics Source Code Library. `http://ascl.net/1208.017`

Schöier, F. L., Jørgensen, J. K., van Dishoeck, E. F., & Blake, G. A. 2002, *Astron. Astrophys.*, 390, 1001, doi: `10.1051/0004-6361:20020756`

Skinner, C. J., Tielens, A. G. G. M., Barlow, M. J., & Justtanont, K. 1992, *Astrophys. J. Lett.*, 399, L79, doi: `10.1086/186611`

Turner, B. E. 1998, *Astrophys. J.*, 501, 731, doi: `10.1086/305859`

Vidali, G., Roser, J. E., Ling, L., et al. 2006, *Faraday Discuss.*, 133, 125, doi: `10.1039/b517282a`

Vidali, G., Roser, J. E., Manicò, G., & Pirronello, V. 2004, *Adv. Space Res.*, 33, 6, doi: `10.1016/j.asr.2003.08.003`

Walsh, C., Loomis, R. A., Öberg, K. I., et al. 2016, *Astrophys. J. Lett.*, 823, L10, doi: `10.3847/2041-8205/823/1/L10`

Wang, S., Bergin, E. A., Crockett, N. R., et al. 2011, *Astron. Astrophys.*, 527, A95, doi: `10.1051/0004-6361/201015079`

Watanabe, N., Nagaoka, A., Hidaka, H., et al. 2006, *Planet. Space Sci.*, 54, 1107, doi: `10.1016/j.pss.2006.05.019`

Wilkins, O. H., Carroll, P. B., & Blake, G. A. 2022, *Astrophys. J.*, accepted.

Chapter 4

OBSERVING THE RELATIONSHIP BETWEEN CH_3OD AND TEMPERATURE IN ORION KL

4.1 Introduction

Deuterated compounds are powerful tools that can be used to trace chemical evolution. For example, relative abundances of heavy water in comets and meteorites can provide insights on the processing of water between the primordial molecular cloud and present-day Earth (e.g., Altwegg et al., 2017). In general, deuterated compounds have D/H ratios higher than the cosmic value of $\sim 10^{-5}$, and that ratio is a function of temperature, with higher D/H ratios signalling formation in colder environments (e.g., Fontani et al., 2015).

In many high-mass and low-mass protostars alike, the deuterium chemistry of methanol—namely, the relative abundances of the singly-deuterated isotopomers CH_2DOH and CH_3OD—has presented itself as a mystery. Methanol is one of the simplest complex (having ≥ 6 atoms) organic molecules, and it is found at every stage of star formation, from cold cloud cores and hot cores/corinos to outflows and circumstellar disks (e.g., Herbst & van Dishoeck, 2009; Walsh et al., 2016). As such, it is commonly used as a tracer of other complex organics. In prestellar and protostellar cores, methanol forms primarily via successive hydrogenation of frozen CO on grain mantles (Equation 4.1; e.g., Nagaoka et al., 2005; Watanabe et al., 2006).

$$\mathrm{CO} \xrightarrow{H} \mathrm{HCO} \xrightarrow{H} \mathrm{H_2CO} \xrightarrow{H} \mathrm{H_3CO} \xrightarrow{H} \mathrm{CH_3OH} \tag{4.1}$$

Statistically, we would expect the $[CH_2DOH]/[CH_3OD]$ ratio to be 3 since there are three methyl ($-CH_3$) hydrogen sites compared to a single hydroxyl (-OH) site. This statistical ratio has been observed in the massive star-forming region NGC 7538-IRS1 (Ospina-Zamudio et al., 2019) but not toward many other star-forming regions, with low-mass cores exhibiting ratios >3 and as much as $\gtrsim 10$ (Bizzocchi et al., 2014; Taquet et al., 2019). Conversely, high-mass stars tend to have $[CH_2DOH]/[CH_3OD]$ ratios of <3 (e.g., Ratajczak et al., 2011; Belloche et al., 2016; Bøgelund et al., 2018).

The Orion Kleinmann-Low (Orion KL) nebula is a high-mass star-forming region infamous for its peculiar methanol deuteration. Jacq et al. (1993) reported the first definitive detection of CH_2DOH toward Orion KL and combined their measurements with past CH_3OD measurements to report a $[CH_2DOH]/[CH_3OD]$ ratio in the range of 1.1-1.5. Neill et al. (2013a) similarly reported a ratio of 1.2 ± 0.3. Peng et al. (2012) reported an even lower ratio of 0.7 ± 0.3 toward the central part of Orion KL.

There has been extensive debate about whether the apparent CH_3OD enhancements are the result of grain-surface or gas-phase processes. Early on, Jacq et al. (1993) concluded that their observed ratio was evidence of grain surface processing followed by injection into the gas phase. Shortly after, chemical models of gas-phase exchange rejected the grain-surface hypothesis on the premise that such chemistry would require unrealistically high $[HDO]/[H_2O]$ ratios (Charnley et al., 1997). Rodgers & Charnley (2002) criticized the assumed statistical $[CH_2DOH]/[CH_3OD]$ ratio since D and H react with species other than CO and H_2CO, which could affect the relative abundances of the singly-deuterated methanol isotopologues. Osamura et al. (2004) used models to suggest that ion-molecule reactions in the gas phase lead to the destruction of CH_3OD, which they conclude accounts for high $[CH_2DOH]/[CH_3OD]$ ratios in low-mass star-forming regions. They also find that D/H exchange on the methyl ($-CH_3$) site is inefficient.

Nevertheless, D/H exchange on the hydroxyl (-OH) group of methanol on icy grain mantles has emerged as a favored explanation for the $[CH_2DOH]/[CH_3OD]$ ratios observed in massive star-forming regions (e.g., Nagaoka et al., 2005; Ratajczak et al., 2009; Peng et al., 2012). In this mechanism, deuterated water in the ice reacts with CH_3OH to produce CH_3OD.

$$CH_3OH + HDO \rightleftharpoons CH_3OD + H_2O \tag{4.2}$$

$$CH_3OH + D_2O \rightleftharpoons CH_3OD + HDO \tag{4.3}$$

However, the intricacies of this exchange are still being investigated.

This work provides a new observational perspective of possible D/H exchange at the methanol hydroxyl site by mapping gas-phase CH_3OD abundances in Orion KL at sub-arcsecond ($\sim 0\overset{''}{.}7$) angular resolution using the Atacama Large Millimeter/submillimeter Array (ALMA). At Orion KL's distance of ~388 pc (Kounkel et al., 2017), this corresponds to linear scales of ~270 au. This allows us to plot gas-phase CH_3OD as a function of temperature across relatively small scales within the nebula. A description of the observations is presented in Section 4.2. Derived CH_3OD abundances are presented in Section 4.3, and their implications for CH_3OD

chemistry are presented in Section 4.4. The findings are compared to previous work in Section 4.5 and summarized in Section 4.6.

4.2 Observations

Observations of Orion KL were taken in ALMA Band 4 during Cycle 5 (project code: ADS/JAO.ALMA#2017.1.01149, PI: Wilkins) on 2017 December 14, completely on the main 12-m array. The pointing center was set to $\alpha_{\mathrm{J2000}} = 05^{\mathrm{h}}35^{\mathrm{m}}14\overset{\mathrm{s}}{.}50$, $\delta_{\mathrm{J2000}} = -05°22'30\overset{''}{.}9$. These observations consisted of a maximum baseline of 3.3 km using 49 antennas during one execution block. All spectra were obtained in a single set-up consisting of 10 spectral windows; as such, the uncertainties for quantities derived from these spectra are dominated by thermal noise and mostly unaffected by calibration uncertainty. Of these spectral windows, the targeted CH_3OD lines were contained in three spectral windows with spectral resolutions of 244 kHz (~0.5 km s^{-1}) covering 143.51-143.97 GHz, 153.16-153.40 GHz, and 154.84-155.07 GHz. Projected baselines were between 15.1 m and 3.3 km (7.6kλ and 1650kλ), and the primary beam was 39.1″. The on-source integration time was 2062 s. Precipitable water vapor was 3.7 mm, and typical system temperatures were around 75-125 K.

Calibration was completed using standard `CASA` (version 5.1.1-5) calibration pipeline scripts. The source J0423−0120 was used as a calibrator for amplitude, atmosphere, bandpass, pointing, and WVR (Water Vapor Radiometer) variations, and J0541−0211 was used as the phase and WVR calibrator.

The CH_3OD data introduced here were prepared in the same way as the $^{13}CH_3OH$ images presented by Wilkins et al. (2022). In brief, the data cubes were created from measurement sets split to include only baselines of ≤500 m, resulting in a synthesized beam of $0\overset{''}{.}74 \times 0\overset{''}{.}63$. Cubes were reduced with continuum emission estimated from line-free channels subtracted using the `uvcontsub` function followed by imaging using the `tclean` algorithm with robust weighting, a Briggs parameter of 1.5 (i.e., semi-natural weighting) for deconvolution, and the ‘auto-multithresh’ masking algorithm (Kepley et al., 2020) in conjunction with interactive `tclean`. The images have a noise-level of $\sigma_{\mathrm{RMS}} \lesssim 1.3$ mJy beam^{-1}.

4.3 CH_3OD Abundances

The CH_3OD column density as a function of position was derived by a pixel-by-pixel fit of the data assuming optically thin lines at local thermodynamic equilibrium

Table 4.1: Transitions of CH_3OD used for line fits.*

Transition	ν (GHz)	E_u (K)	$S_{ij}\mu^2$ (Debye^2)	g_u
$5_{(1,4)} - 5_{(0,5)}$	143.7417	39.48	11.2	11
$7_{(1,6)} - 7_{(0,7)}$	153.3240	68.05	14.7	15
$3_{(-1,2)} - 2_{(0,1)}$	154.9628	17.71	2.2	7

*From Anderson et al. (1988).

(LTE) in a similar manner to $^{13}CH_3OH$ by Wilkins et al. (2022).[1] In brief, spectra in a single synthesized beam centered on each pixel were extracted in succession. The CH_3OD rotation temperature T_{rot} profile was assumed to be the same as that derived from $^{13}CH_3OH$ by Wilkins et al. since the transitions of both isotopologues (Tables 2.1 and 4.1) have similar upper energy states E_u. Column density, line width, and local standard of rest (LSR) velocity were determined by simultaneous fits using `LMFIT`, a least-squares fitting software package.[2] Because all lines used in the fit were observed simultaneously, the uncertainties in excitation, which are derived from relative fluxes, should be dominated by thermal noise rather than by multiple sources of calibration uncertainty.

As shown in Figure 4.1, the derived CH_3OD column density is generally on the order of 10^{17} cm^{-2} and peaks to the south of SMA1 and south of C22. The relationship between CH_3OD and $^{13}CH_3OH$ abundances (column density, N_{tot}) and rotation temperature (T_{rot}) is illustrated by Figure 4.2. In general, $[CH_3OD]/[^{13}CH_3OH]$ falls between 1 and 5. Assuming an interstellar $^{12}C/^{13}C$ ratio of 77 (Wilson & Rood, 1994), this suggests $[CH_3OD]/[CH_3OH] \approx 0.013$-$0.065$, which agrees well with the range of 0.01-0.06 observed in Orion KL by Mauersberger et al. (1988).

4.4 Chemical Processes

As introduced in Section 4.1, observed $[CH_2DOH/CH_3OD]$ ratios in Orion KL are much less than the statistically expected ratio of 3 (e.g., Jacq et al., 1993; Peng et al., 2012), suggesting tsome form of chemical processing is taking place, either on grain surfaces (as suggested by Jacq et al., 1993) or predominantly in thee gas (as speculated by Charnley et al., 1997), to cause H/D exchange on the hydroxyl group. In either case, processing is not expected to take place at the methyl H/D site (Osamura et al., 2004; Ratajczak et al., 2009). As such, this work focuses specifically

---

[1] Python script available at https://github.com/oliviaharperwilkins/LTE-fit.

[2] https://doi.org/10.5281/zenodo.11813

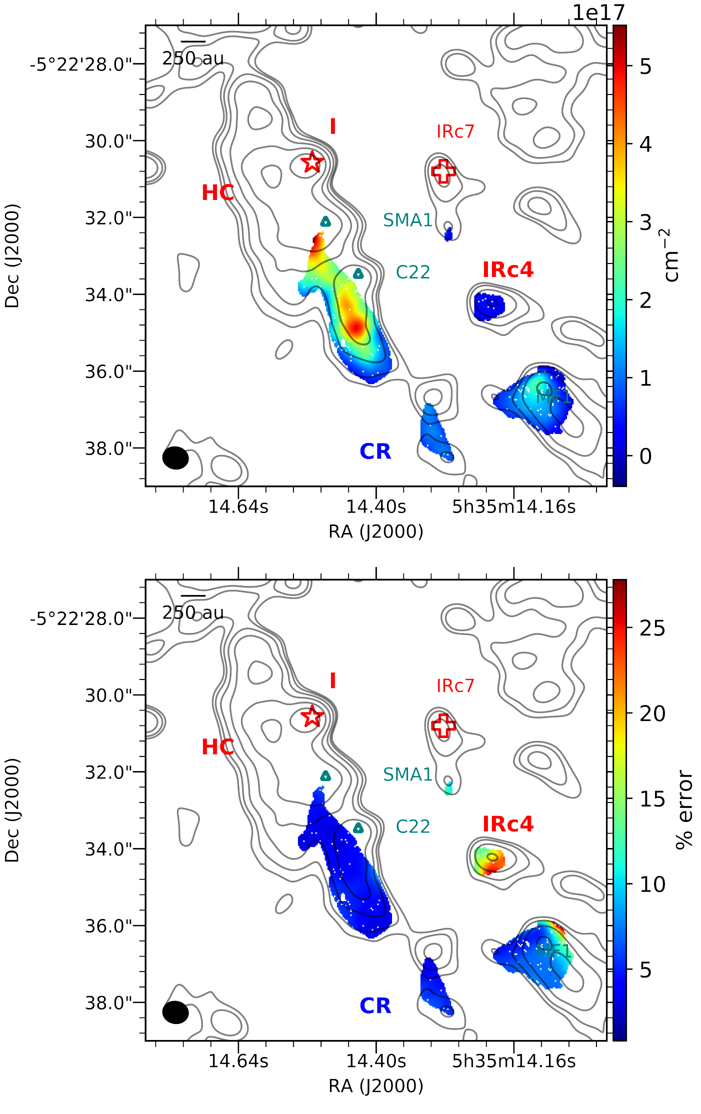

Figure 4.1: Derived CH_3OD column density and percent propagated uncertainty shown by the color maps. The continuum is shown by the grey contours at $2\sigma_{RMS}, 4\sigma_{RMS}, 8\sigma_{RMS}, 16\sigma_{RMS}, \ldots$ The $0\farcs7$ synthesized beam is shown by the black ellipse in the bottom left corner.

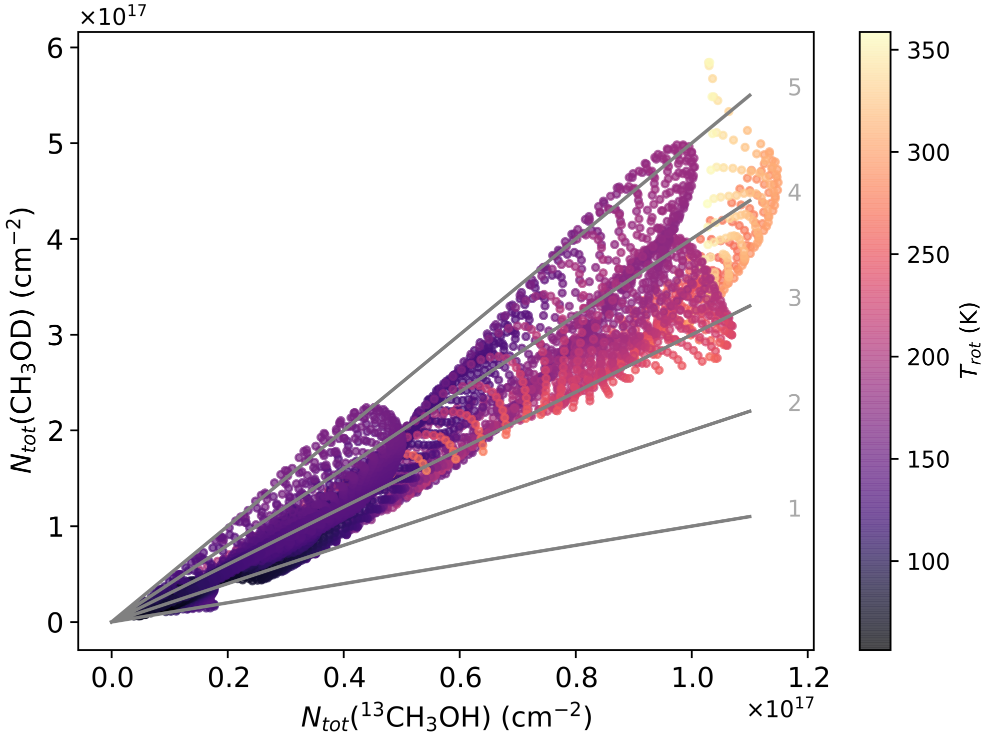

Figure 4.2: Column densities N_{tot} of $^{13}CH_3OH$ (horizontal axis, from Wilkins et al., 2022) and CH_3OD (vertical axis, this work) with each point representing a single pixel in Figure 4.1. Each pixel is colored by its rotation temperature. The grey lines are labeled by the methanol D/^{13}C ratios (1 to 5) they represent.

on what may cause CH_3OD enhancements in high-mass star-forming regions and Orion KL in particular. In this section, we analyze the relationship between CH_3OD abundance and temperature and offer support in favor of the hypothesis that the observed CH_3OD abundance patterns are the result of D/H exchange with water on the surfaces of icy grains.

Figure 4.3a shows the CH_3OD column density increasing with rotation temperature, which is characteristic of thermal desorption by which material gradually comes off the grains as its environment warms (Burke & Brown, 2010). However, the profile also contains a “shark-tooth” feature where the column density starts to rise more rapidly at ~110 K before peaking close to 185 K. At temperatures higher than 185 K, there is a sharp decrease in the CH_3OD column density.

Power-law distributions are commonly used to characterize the temperature and density profiles of star-forming regions and young stellar objects (e.g., Carney et al., 2017; Gieser et al., 2021); a brief demonstration of this is given in Appendix D. The

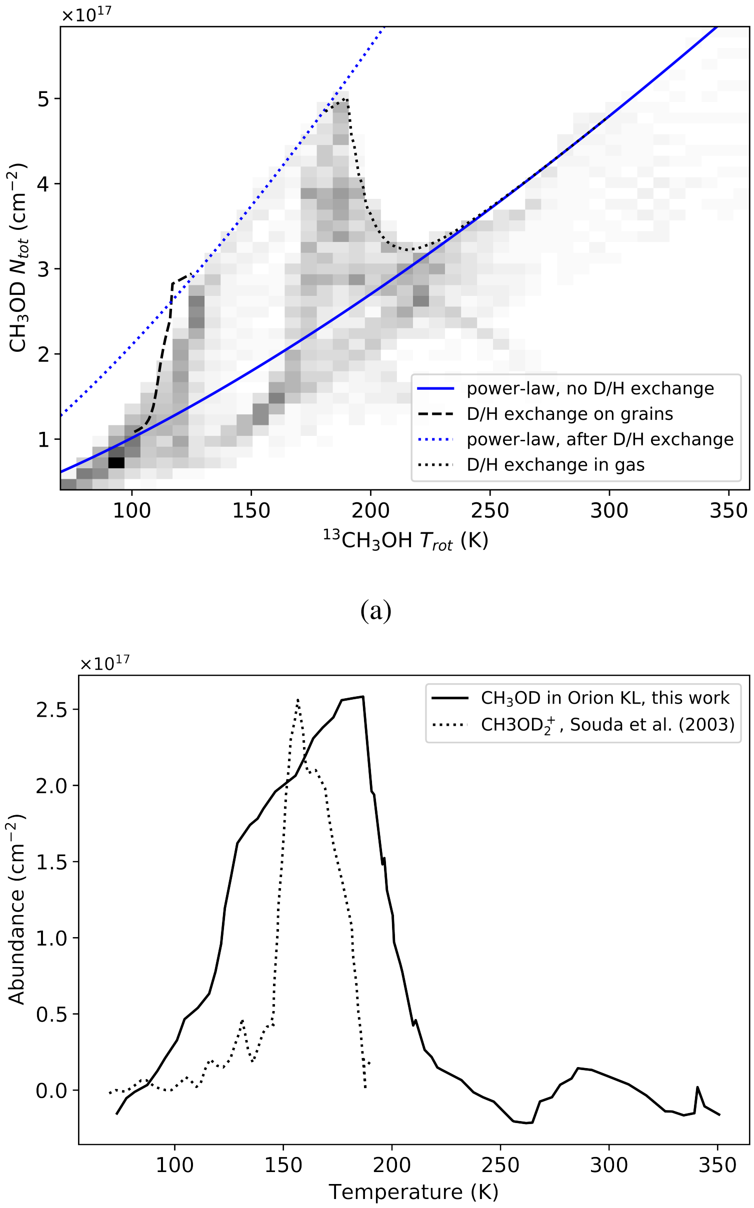

(a)

(b)

Figure 4.3: (a) Two-dimensional histogram with 50 points per bin showing the derived CH_3OD column densities N_{tot} from Figure 4.1 against rotation temperature T_{rot}. The blue solid line shows the power-law fit to the data if there were no D/H exchange. The black dashed line shows the modeled D/H exchange followed by desorption based on ice experiments by Souda et al. (2003) and assumptions by Faure et al. (2015). The blue dotted curve is the power-law fit after the CH_3OD enhanced by D/H exchange desorbs off the grains. The black dashed line shows the modeled protonation of CH_3OD, which is followed by rapid dissociative recombination to form CH_3OH. (b) The solid curve shows the data from panel (a) but with the underlying power-law (blue curve in a) subtracted. The dotted curve shows the relative intensity of the sputtered $CH_3OD_2{}^+$ reported by Souda et al. (2003).

solid line in Figure 4.3b shows the "shark-tooth" from Figure 4.3a with the fitted underlying power-law relationship (Equation 4.4) between T_{rot} and N_{tot} subtracted.

$$N_{tot} = 1.5 \times 10^{14} T_{rot}^{1.4148} \tag{4.4}$$

Grain Surface Processes

The rapid rise in gas-phase CH_3OD column density between ∼110 K and ∼120 K is consistent with D/H exchange between methanol and heavy water (HDO, D_2O) on the ices at ∼100 K. Souda et al. (2003) experimentally investigated hydrogen bonding between water and methanol in low-temperature ices warmed from 15 K to 200 K under ultrahigh vacuum. They observed that, when CH_3OH was adsorbed onto D_2O ice, secondary $CH_3OD_2{}^+$ ions—evidence of D/H exchange at the hydroxyl site—sputtered off the ice analogue surfaces predominantly between 140 and 175 K. Follow-up analyses by Kawanowa et al. (2004) describes this as a "rapid and almost complete H/D exchange" to yield the sputtered $CH_3OD_2{}^+$ species. The fact that we see a similar sudden increase in CH_3OD abundances at similar temperatures (Figure 4.3b, dotted line), with discrepancies owing to the differences in pressure between ultrahigh vacuum and the interstellar medium, supports a similar rapid exchange in Orion KL.

Models of D/H exchange between water and methanol in ices by Faure et al. (2015) successfully produced gas-phase CH_3OH deuterium fractionation in Orion KL using initial ice abundances of $n_S(CH_3OH) = 2.0 \times 10^{-6} n_H$, $n_S(HDO) = 3.0 \times 10^{-7} n_H$, and $n_S(CH_3OD) = 6.0 \times 10^{-9} n_H$. Assuming an initial ice column density of $N_S(CH_3OD) = 6.0 \times 10^{-9} N_H = 6.0 \times 10^{14}$ cm^{-2}, since $N_H \sim 10^{23}$ cm^{-2} in Orion KL (Neill et al., 2013b; Crockett et al., 2014), and an initial gas-phase column density of $N(CH_3OD) = 1 \times 10^{16}$ cm^{-2} (based on the abundances measured at 100 K in this work), we modeled the desorption of CH_3OD following rapid D/H exchange.

The D/H exchange introducing additional CH_3OD from the reaction of CH_3OH + HDO was modeled, in the absence of temperature-programmed desorption measurements, by fitting a line to the $CH_3OD_2{}^+$ curve of Souda et al. (2003) (Figure 4.3b, dotted line) between 110 K and 145 K, normalizing the relative intensity amplitude to the column densities observed for CH_3OD in our data. This results in a relationship of

$$N'_S(CH_3OD) = 6.2 \times 10^{14} T - 6.0 \times 10^{16} \tag{4.5}$$

that is used to calculate the additional CH_3OD available for desorption at a given temperature.

The desorption rate coefficient is expressed as

$$k_{des} = \nu_{des} e^{(-E_d/T)} \tag{4.6}$$

where the pre-exponential factor ν_{des} and the binding energy E_d are taken to be approximately the values for annealed amorphous solid water—2.0×10^{12} s^{-1} and 5200 K, respectively—under the assumption that the methanol desorbs with water (Sandford & Allamandola, 1988; Faure et al., 2015).

It follows that the change in gas-phase $N(\mathrm{CH_3OD})$ is approximated by combining Equations 4.5 and 4.6 to give a rate of

$$\frac{d}{dt} N(\mathrm{CH_3OD}) = -k_{des} N_S(\mathrm{CH_3OD}) + N'_S(\mathrm{CH_3OD}) \tag{4.7}$$

using temperature steps of 1 K between 100 and 150 K, the time steps for which were determined by

$$\Delta t = \left(\frac{T - T_0}{T_{max} - T_0} \right)^{1/n} t_h \tag{4.8}$$

where Δt is the time elapsed since $t = 0$; T_0 and T_{max} are the initial (10 K) and maximum (200 K) temperatures, respectively; t_h is the heating timescale; and n is the order of heating, which is assumed to be 2 following previous work (e.g., Taniguchi et al., 2019). The resulting desorption model from Equation 4.7 with $t_h = 10^3$ yr is shown by the black dashed line in Figure 4.3a. Longer timescales (i.e., $t_h \geq 10^4$ yr) characterstic of massive YSOs do not follow the increasing $\mathrm{CH_3OD}$ profile as closely. Although Wilkins et al. (2022) suggest potential internal heating within the Hot Core-SW, Li et al. (2020) conclude that this region, part of the "elongated ridge" comprising the Hot Core and Source I, is predominantly heated externally by shocks induced by the Orion KL explosion, which took place about 500 years ago. Furthermore, the models by Faure et al. (2015) suggest the D/H exchange in Orion KL reaches steady-state in $<10^3$ yr. After D/H exchange, the power-law relationship from Equation 4.4 applies but with a coefficient of 3.2×10^{14}.

The hypothesis that the $\mathrm{CH_3OD}$ abundance profile in Figure 4.3 is the result of rapid H/D exchange on the grains relies on two assumptions regarding temperature. First, we assume that the rotation temperature T_{rot} is an appropriate estimate for the kinetic temperature T_{kin}. This assumption is based on the fact that the Compact Ridge has a high density of $\sim 10^6$ cm^{-3} (Blake et al., 1987; Genzel & Stutzki, 1989), implying that LTE is a reasonable assumption. Second, we assume that the dust and gas are thermally coupled. Li et al. (2003) found that other quiescent regions (no IR sources, no evident outflows) in the Orion Molecular Cloud are thermally coupled. Models by Garrod & Herbst (2006) also support coupling between dust and gas temperature at high densities; their models were fit to several massive star-forming regions, including the Orion KL Compact Ridge. As such, it is reasonable to assume that the gas temperatures shown in Figure 4.3 are also representative of the temperatures of the dust on which methanol forms and that any decoupling between the dust and gas is negligible for the purposes of this discussion.

Gas Chemistry

Above ~200 K, the profile in Figure 4.3a drops sharply. One avenue for CH_3OD depletion is gas-phase D/H exchange via protonation of the hydroxyl group (e.g., Equation 4.9) followed by dissociative recombination (Equations 4.10 and 4.11).

$$\mathrm{CH_3OD + H_3O^+ \longrightarrow CH_3ODH^+ + H_2O} \tag{4.9}$$

$$\mathrm{CH_3ODH^+ + e^- \longrightarrow CH_3OH + D, CH_3OD + H} \tag{4.10}$$

$$\mathrm{CH_2DOH_2{}^+ + e^- \longrightarrow CH_2DOH + H} \tag{4.11}$$

The methyl H/D site is not exchangeable; therefore, in this model, only CH_3OD can be depleted while CH_2DOH cannot, which has been suggested as an explanation for the depleted CH_3OD relative abundances in low-mass star-forming regions (Osamura et al., 2004). This may also account for the decrease in gas-phase CH_3OD at high temperatures in the Orion KL Hot Core-SW following enrichment on grain surfaces.

The dissociative recombination shown in Equation 4.10 is faster than protonation, for example by $CH_3OD + H_3O^+$ (Wakelam et al., 2012; Woon & Herbst, 2009). Thus, we modeled the approximate gas-phase D/H exchange and accompanying CH_3OD depletion using the rate constant for the reaction of $CH_3OH + H_3O^+$. The resulting model is shown by the black dotted line in Figure 4.3a. The rate constant, obtained from the KInetic Database for Astrochemistry (KIDA), used in this model is expressed as

$$k = 1.06 \times 10^{-9} \left(0.62 + 0.4767(3.32) \left(\frac{300}{T}\right)^{0.5}\right). \tag{4.12}$$

Typically, ion-neutral reaction rate coefficients are calculated using Langevin cross-sections, assuming a nonpolar neutral species, and are temperature-independent. The rate constant expressed in Equation 4.12, however, is based on high-level quantum chemical calculations by Woon & Herbst (2009), who invoked capture theory to obtain temperature-dependent rate coefficients.

Because Equation 4.10 is faster than Equation 4.9, we assume that all protonated CH_3OD rapidly undergoes dissociative recombination. As seen in Figure 4.3a, the simple model of this process—when turned on at 190 K and using the same warm-up model as for the grain-surface D/H exchange—replicates the observed data well. Another mechanism considered was the neutral-radical reaction with the hydroxyl radical (OH); however, this reaction is too slow at ~200 K to account for the observed patterns (see Appendix E for an explanation).

Methyl Group Chemistry

If the hump observed in the CH_3OD column density versus temperature profile is indeed evidence of surface D/H exchange at the hydroxyl site, then we would expect a smooth profile (i.e., without a similar hump) in the profile of CH_2DOH. Unfortunately, we do not have sufficient CH_2DOH transitions in our data to test this directly. However, Carroll (2018) mapped the physical parameters of CH_2DCN toward Orion KL using data from ALMA (project: ADS/JAO.ALMA#2013.1.01034). Figure 4.4 shows a histogram of the CH_2DCN column density and rotation temperature using these data where they overlap with CH_3OD emission in the current observations. In this plot, we see consistent power-law relationship between temperature and abundance, which supports the assumption that the methyl groups of complex organics would not undergo D/H exchange as concluded by Osamura et al. (2004). In other words, the hump visible in Figure 4.3a is indeed likely the result of chemistry on the hydroxyl site and not the methyl site.

4.5 Comparison to Past Studies

The evidence presented here adds to the growing list of observational and theoretical evidence in favor of a grain-surface mechanism for CH_3OD enrichment in massive star-forming regions. A key difference between this work and that of past observations is that here, we map CH_3OD column density across much of Orion KL, including the Compact Ridge, whereas past work derives one abundance for the Compact Ridge as a whole. Furthermore, resolving the small-scale structure of CH_3OD abundances (and temperature) allows us to look at how abundance is related to temperature, something that has not yet been investigated through observations.

Computational models to assess D/H exchange generally have investigated temporal variations in relative CH_3OD abundances at a single temperature (~100 K; e.g.,

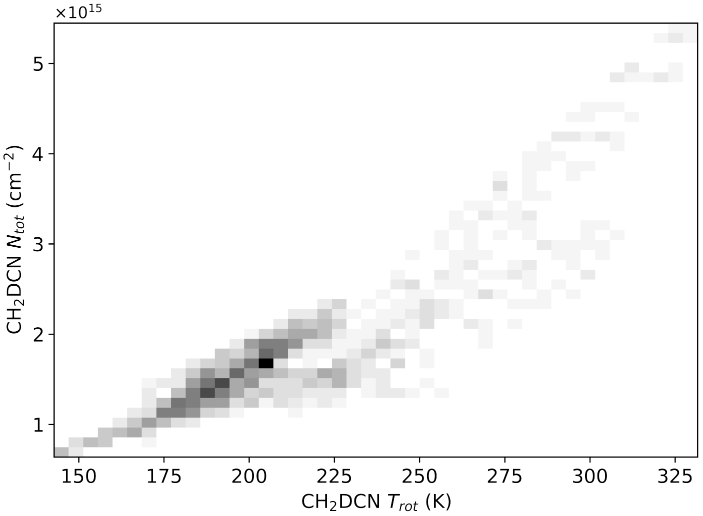

Figure 4.4: Two-dimensional histogram with 20 points per bin showing the derived CH_2DCN column density against rotation temperature.

Osamura et al., 2004) or have looked at singly-deuterated methanol chemistry across a range of temperatures but less than 140 K (e.g., Faure et al., 2015; Bøgelund et al., 2018). As such, the observations presented here probe a temperature regime beyond that of existing astrochemical models and call for revised models to investigate D/H chemistry at higher temperatures.

Perhaps the leading criticism of proposed grain-surface chemistry prompting the enhancement of CH_3OD abundances relative to CH_2DOH is that such processes would require a large initial [HDO]/[H_2O] of ~0.1 (Charnley et al., 1997), which is a couple of orders of magnitude larger than the ratio of ~0.003 reported by Neill et al. (2013b) for compact regions of Orion KL. However, Thi et al. (2010) suggest that the [HDO]/[H_2O] ratio can exceed 0.01 in dense ($\geq 10^6$ cm^{-3}), warm ($T > 100$ K) regions (such as those observed here) via photodissociation and neutral-neutral reactions, which may be promising for the hypothesis of a grain-surface CH_3OD enhancement. Even more promising is a model presented by Faure et al. (2015), who reproduced observed [CH_2DOH]/[CH_3OD] ratios in the Compact Ridge assuming a primitive [HDO]/[H_2O] fractionation of 0.006, only a factor of 2 larger than the observed ratio reported by Neill et al. (2013b)

A remaining question, then, is what makes methanol deuteration in low-mass star-forming regions so different from that in high-mass star-forming regions? Ratajczak et al. (2011) suggest observational biases, namely that, since high-mass objects tend to be further away than those low-mass objects were deuterium chemistry has been studied, measurements of the [CH_2DOH]/[CH_3OD] ratio may be affected, particularly if the spatial distributions of the two isotopomers are different. High-angular-resolution mapping, like that presented in Figure 4.1, would address this by comparing the CH_2DOH and CH_3OD abundances only where their emission overlapped. As stated in Section 4.4, we do not have sufficient CH_2DOH lines available to test this. Dedicated high-angular-resolution observations targeting low-energy CH_2DOH lines are necessary to further address the spatial distribution of the singly-deuterated methanol isotopomers and their overall relative abundance patterns.

Another conjecture for the different deuterium fractionation patterns in massive YSOs compared to low-mass star-forming regions is that there is simply less deuteration in massive protostars because of the warmer environments (Bøgelund et al., 2018). Faure et al. (2015) reproduced relative singly-deuterated methanol abundances for Orion KL (a high-mass source) and IRAS 16293-2422 (a low-mass object) using kinetic models that were identical except for the initial deuterium fractionation ratios. They reported that the Orion KL Compact Ridge's gas-phase deuterium chemistry could be modeled assuming similar primitive deuteration of water and methanol ices (~0.2-0.3%), whereas IRAS 16293's gas-phase deuterated methanol chemistry required a significantly higher deuterium fractionation in methanol (12%) than water (1%). Their model shows complete methanol desorption by ~110 K. As seen in Figure 4.3a, this desorption model (dashed line) matches where we see the CH_3OD column density rise between 100 and 110 K; however, the CH_3OD in our data increases at temperatures up to ~125 K. This slight discrepancy might be addressed by temperature-programmed desorption experiments, for example, studying the release of CH_3OD directly rather than via sputtered $CH_3OD_2^+$ detected by Souda et al. (2003).

Such questions require more robust chemical networks for deuterium chemistry as well as a better understanding of the initial chemical conditions of both high-mass and low-mass star-forming regions.

4.6 Summary

We provide observational evidence in support of rapid D/H exchange in methanol, specifically at the hydroxyl site, between ~100 K and 125 K in Orion KL. Using ALMA Band 4 observations of CH_3OD at ~$0.''7$ angular resolution, we mapped the small-scale variations in CH_3OD abundance and compare that to temperatures mapped at the same angular resolution (and derived from $^{13}CH_3OH$) by Wilkins et al. (2022).

We fit power-law relationships and toy models of D/H exchange at methanol's hydroxyl (-OH) site followed by CH_3OD desorption to the observed CH_3OD abundance profile in Orion KL. These analyses suggest that D/H exchange and rapid CH_3OD desorption rapidly increase the gas-phase CH_3OD column density between 100 and 125 K. Between 125 and 185 K, the abundance profile follows a power-law relationship with temperature. At higher temperatures, the CH_3OD rapidly decreases, perhaps through gas-phase D/H exchange at the hydroxyl site.

Future investigations—through observations, experiments, and computational models—are still needed to further constrain the peculiar D-methanol chemistry in Orion KL and other star-forming regions. The work presented here would be aided by dedicated high-resolution observations of CH_2DOH and HDO, experiments measuring the kinetics of CH_3OD formation via D/H exchange in heavy water ice and subsequent desorption, and temperature-dependent astrochemical models of possible CH_3OD loss at higher temperatures (185-225 K).

Acknowledgements

This work makes use of the following ALMA data: ADS/JAO.ALMA#2017.1.01149 and ADS/JAO.ALMA#2013.1.01034.ALMA is a partnership of ESO (representing its member states), NSF (USA), and NINS (Japan), together with NRC (Canada), MOST and ASIAA (Tawain), and KASI (Republic of Korea), in cooperation with the Republic of Chile. The Joint ALMA Observatory is operated by ESO, AUI/NRAO, and NAOJ. The National Radio Astronomy Observatory (NRAO) is a facility of the National Science Foundation (NSF) operated under Associated Universities, Inc. (AUI). This research made use of APLpy, an open-source plotting package for Python (Robitaille, 2019), and the KInetic Database for Astrochemistry (KIDA), an online database of kinetic data (Wakelam et al., 2012).

This work has been supported by the NSF Graduate Research Fellowship Program under grant No. DGE-1144469 and NRAO Student Observing Support under Award No. SOSPA6-014. OHW is additionally supported by an ARCS Los Angeles Founder Chapter scholarship. GAB gratefully acknowledges support from the NSF AAG (AST-1514918) and NASA Astrobiology (NNX15AT33A) and Exoplanet Research (XRP, NNX16AB48G) programs. This work benefited from discussions with Brandon Carroll, Dana Anderson, Aida Behmard, and Cam Buzard. OHW thanks Erica Keller, Sarah Wood, and the NRAO North American ALMA Science Center (NAASC) for their assistance with the data reduction.

Facilities: ALMA

Software: CASA (McMullin et al., 2007), CDMS (Müller et al., 2001), KIDA (Wakelam et al., 2012), APLpy (Robitaille & Bressert, 2012; Robitaille, 2019), WebPlotDigitizer (Rohatgi, 2021)

References

Altwegg, K., Balsiger, H., Berthelier, J. J., et al. 2017, *Philos. Trans. R. Soc., A*, 375, 20160253, doi: `10.1098/rsta.2016.0253`

Anderson, T., Crownover, R. L., Herbst, E., & De Lucia, F. C. 1988, *Astrophys. J. Supp.*, 67, 135, doi: `10.1086/191269`

Belloche, A., Müller, H. S. P., Garrod, R. T., & Menten, K. M. 2016, *Astron. Astrophys.*, 587, A91, doi: `10.1051/0004-6361/201527268`

Bizzocchi, L., Caselli, P., Spezzano, S., & Leonardo, E. 2014, *Astron. Astrophys.*, 569, A27, doi: `10.1051/0004-6361/201423858`

Blake, G. A., Sutton, E. C., Masson, C. R., & Phillips, T. G. 1987, *Astrophys. J.*, 315, 621, doi: `10.1086/165165`

Bøgelund, E. G., McGuire, B. A., Ligterink, N. F. W., et al. 2018, *Astron. Astrophys.*, 615, A88, doi: `10.1051/0004-6361/201832757`

Burke, D. J., & Brown, W. A. 2010, *Phys. Chem. Chem. Phys.*, 12, 5947, doi: `10.1039/B917005G`

Carney, M. T., Hogerheijde, M. R., Loomis, R. A., et al. 2017, *Astron. Astrophys.*, 605, A21, doi: `10.1051/0004-6361/201629342`

Carroll, P. B. 2018, PhD thesis, California Institute of Technology, doi: `10.7907/8Y1M-6C76`

Charnley, S. B., Tielens, A. G. G. M., & Rodgers, S. D. 1997, *Astrophys. J. Lett.*, 482, L203, doi: `10.1086/310697`

Crockett, N. R., Bergin, E. A., Neill, J. L., et al. 2014, *Astrophys. J.*, 787, 112, doi: `10.1088/0004-637X/787/2/112`

Faure, A., Faure, M., Theulé, P., Quirico, E., & Schmitt, B. 2015, *Astron. Astrophys.*, 584, A98, doi: `10.1051/0004-6361/201526499`

Fontani, F., Busquet, G., Palau, A., et al. 2015, *Astron. Astrophys.*, 575, A87, doi: `10.1051/0004-6361/201424753`

Garrod, R. T., & Herbst, E. 2006, *Astron. Astrophys.*, 457, 927, doi: `10.1051/0004-6361:20065560`

Genzel, R., & Stutzki, J. 1989, *Annu. Rev. Astron. Astrophys.*, 27, 41, doi: `10.1146/annurev.aa.27.090189.000353`

Gieser, C., Beuther, H., Semenov, D., et al. 2021, *Astron. Astrophys.*, 648, A66, doi: `10.1051/0004-6361/202039670`

Herbst, E., & van Dishoeck, E. F. 2009, *Annu. Rev. Astron. Astrophys.*, 47, 427, doi: `10.1146/annurev-astro-082708-101654`

Jacq, T., Walmsley, C. M., Mauersberger, R., et al. 1993, *Astron. Astrophys.*, 271, 276

Kawanowa, H., Kondo, M., Gotoh, Y., & Souda, R. 2004, *Surf. Sci.*, 566, 1190, doi: `10.1016/j.susc.2004.06.086`

Kepley, A. A., Tsutsumi, T., Brogan, C. L., et al. 2020, *Publ. Astron. Soc. Pac.*, 132, 024505, doi: `10.1088/1538-3873/ab5e14`

Kounkel, M., Hartmann, L., Loinard, L., et al. 2017, *Astrophys. J.*, 834, 142, doi: `10.3847/1538-4357/834/2/142`

Li, D., Goldsmith, P. F., & Menten, K. 2003, *Astrophys. J.*, 587, 262, doi: `10.1086/368078`

Li, D., Tang, X., Henkel, C., et al. 2020, *Astrophys. J.*, 901, 62, doi: `10.3847/1538-4357/abae60`

Mauersberger, R., Henkel, C., Jacq, T., & Walmsley, C. M. 1988, *Astron. Astrophys.*, 194, L1

McMullin, J. P., Waters, B., Schiebel, D., Young, W., & Golap, K. 2007, Astronomical Society of the Pacific Conference Series, Vol. 376, CASA Architecture and Applications, ed. R. A. Shaw, F. Hill, & D. J. Bell, 127

Müller, H. S. P., Thorwirth, S., Roth, D. A., & Winnewisser, G. 2001, *Astron. Astrophys.*, 370, L49, doi: `10.1051/0004-6361:20010367`

Nagaoka, A., Watanabe, N., & Kouchi, A. 2005, *Astrophys. J. Lett.*, 624, L29, doi: `10.1086/430304`

Neill, J. L., Crockett, N. R., Bergin, E. A., Pearson, J. C., & Xu, L.-H. 2013a, *Astrophys. J.*, 777, 85, doi: `10.1088/0004-637X/777/2/85`

Neill, J. L., Wang, S., Bergin, E. A., et al. 2013b, *Astrophys. J.*, 770, 142, doi: `10.1088/0004-637X/770/2/142`

Osamura, Y., Roberts, H., & Herbst, E. 2004, *Astron. Astrophys.*, 421, 1101, doi: `10.1051/0004-6361:20035762`

Ospina-Zamudio, J., Favre, C., Kounkel, M., et al. 2019, *Astron. Astrophys.*, 627, A80, doi: `10.1051/0004-6361/201834948`

Peng, T. C., Despois, D., Brouillet, N., Parise, B., & Baudry, A. 2012, *Astron. Astrophys.*, 543, A152, doi: `10.1051/0004-6361/201118310`

Ratajczak, A., Quirico, E., Faure, A., Schmitt, B., & Ceccarelli, C. 2009, *Astron. Astrophys.*, 496, L21, doi: `10.1051/0004-6361/200911679`

Ratajczak, A., Taquet, V., Kahane, C., et al. 2011, *Astron. Astrophys.*, 528, L13, doi: `10.1051/0004-6361/201016402`

Robitaille, T. 2019, APLpy v2.0: The Astronomical Plotting Library in Python, doi: `10.5281/zenodo.2567476`

Robitaille, T., & Bressert, E. 2012, APLpy: Astronomical Plotting Library in Python, Astrophysics Source Code Library. `http://ascl.net/1208.017`

Rodgers, S. D., & Charnley, S. B. 2002, *Planet. Space Sci.*, 50, 1125, doi: `10.1016/S0032-0633(02)00073-9`

Rohatgi, A. 2021, WebPlotDigitizer, 4.3. `https://automeris.io/WebPlotDigitizer`

Sandford, S. A., & Allamandola, L. J. 1988, *Icarus*, 76, 201, doi: `10.1016/0019-1035(88)90069-3`

Souda, R., Kawanowa, H., Kondo, M., & Gotoh, Y. 2003, *J. Chem. Phys.*, 119, 6194, doi: `10.1063/1.1602055`

Taniguchi, K., Herbst, E., Caselli, P., et al. 2019, *Astrophys. J.*, 881, 57, doi: `10.3847/1538-4357/ab2d9e`

Taquet, V., Bianchi, E., Codella, C., et al. 2019, *Astron. Astrophys.*, 632, A19, doi: `10.1051/0004-6361/201936044`

Thi, W. F., Woitke, P., & Kamp, I. 2010, *Mon. Not. R. Astron. Soc.*, 407, 232, doi: `10.1111/j.1365-2966.2009.16162.x`

Wakelam, V., Herbst, E., Loison, J. C., et al. 2012, *Astrophys. J. Supp.*, 199, 21, doi: `10.1088/0067-0049/199/1/21`

Walsh, C., Loomis, R. A., Öberg, K. I., et al. 2016, *Astrophys. J. Lett.*, 823, L10, doi: `10.3847/2041-8205/823/1/L10`

Watanabe, N., Nagaoka, A., Hidaka, H., et al. 2006, *Planet. Space Sci.*, 54, 1107, doi: `10.1016/j.pss.2006.05.019`

Wilkins, O. H., Carroll, P. B., & Blake, G. A. 2022, *Astrophys. J.*, accepted.

Wilson, T. L., & Rood, R. 1994, *Annu. Rev. Astron. Astrophys.*, 32, 191, doi: `10.1146/annurev.aa.32.090194.001203`

Woon, D. E., & Herbst, E. 2009, Astrophysical Journal Supplement Series, 185, 273, doi: `10.1088/0067-0049/185/2/273`

Chapter 5

SEARCHING FOR NEW INTERSTELLAR LABORATORIES IN THE MOLECULAR RING

5.1 Introduction

Molecules are widespread throughout the universe and can be useful tools for understanding astronomical phenomena. Their utility includes acting as chemical tracers for different environments, with HCN, HCO^+, and CS being tracers of dense gas (Nguyen-Q-Rieu et al., 1989) and CH_3CN tracing hot cores (Pankonin et al., 2001; Araya et al., 2005), for example. Chemical tracers can also be used as a constraint on a star-forming region's evolutionary state, such as class II methanol masers being signposts of high-mass protostars (Jones et al., 2020). Molecules can additionally be used to derive kinetic temperatures under the assumption of local thermodynamic equilibrium (LTE, e.g., Goldsmith & Langer, 1999; Teng & Hirano, 2020). Furthermore, understanding chemical processes through star formation are interesting in the context of astrobiology and linking solar system chemistry to the presolar nebula through comets and meteorites.

Much of our understanding of the chemistry that occurs alongside star formation has come from observations of nearby low-mass star-forming regions. These observations have shown that low-mass stars form in the coldest ($T \sim 10$ K), densest ($\rho \sim n(\mathrm{H}) + 2n(\mathrm{H_2}) \sim 10^4$ cm^{-3}) cores, and that such regions host a wide range of molecules (e.g., van Dishoeck & Blake, 1998; Herbst & van Dishoeck, 2009; Öberg et al., 2011b, 2014).

Similarly, astrochemical studies of intermediate- and high-mass star-forming regions can enhance our understanding of stellar evolution in these environments. Whereas there is an evolutionary sequence for low-mass star formation, there is no such firmly established sequence for intermediate- and high-mass stars (Motte et al., 2018). Attempts at constructing an evolutionary sequence have thus far included diagnostics that are based in chemical studies of star-forming regions, including the detection of class II methanol masers. Another diagnostic is the chemical enrichment of hot cores, particularly with complex organic molecules (COMs) which have six or more atoms (Herbst & van Dishoeck, 2009). Thus, tighter chemical constraints on intermediate- and high-mass star-forming regions will provide insight into their evolutionary stages.

Despite the potential for chemistry to shed light on the evolution of high-mass stars, the evolution of intermediate- and high-mass star formation has faced many observational challenges. A plethora of studies—including those in Chapters 2-4 of this thesis—have focused on the nearby Orion KL region, which is often used as an archetype for high-mass star formation (Murata et al., 1992; Blake et al., 1996). Several more distant, exceptionally bright molecular sources such as Sgr B2(N) ($d \sim 8$ kpc), W33A ($d \sim 4$ kpc), and W3(H_2O) ($d \sim 2$ kpc) have also been the subjects of repeated observations (van der Tak et al., 2000a,b; Bisschop et al., 2007) but with concomitantly poorer linear spatial resolution.

Here, we present the 1.2 mm continuum (detected using the Atacama Compact Array, or ACA) of a sample of 11 giant molecular clouds (GMCs). These results establish a catalogue of candidate intermediate- and high-mass young stellar objects (YSOs) for future chemical studies. The sample observed in this pilot survey is presented in this chapter, and preliminary chemical results from simultaneous molecular line emission observations are presented in Chapter 6.

The aim of this ongoing survey is to complement the existing literature on high-mass star formation in the context of astrochemistry by focusing on the so-called molecular ring at distances from the galactic center of ~4−8 kpc where the bulk of molecular matter in the Milky Way is thought to reside (Figure 5.1. Unbiased astrochemical studies of the 11 GMCs observed here have been fairly limited despite their potential to enhance our understanding of the physical and chemical processes present during star formation. These observations will be used to inform future astrochemical observations at high spatial resolution.

The observations, including the strategy for source selection, are summarized in Section 5.2. The analysis methods are described in Section 5.3. Section 5.4 presents the 1.2 mm continuum emission of the 11 targeted GMCs; this section also includes an overview of a thorough literature search to understand what types of objects were observed in the pilot survey. These results are combined with far-infrared (far-IR) images from Herschel in Section 5.5. Section 5.6 discusses the implications of these findings, and the project is summarized in Section 5.7.

5.2 Observations

Source Selection

The regions observed in this study were selected from a sample of 437 GMCs with gas masses reported by Battisti & Heyer (2014). The GMCs were detected by the

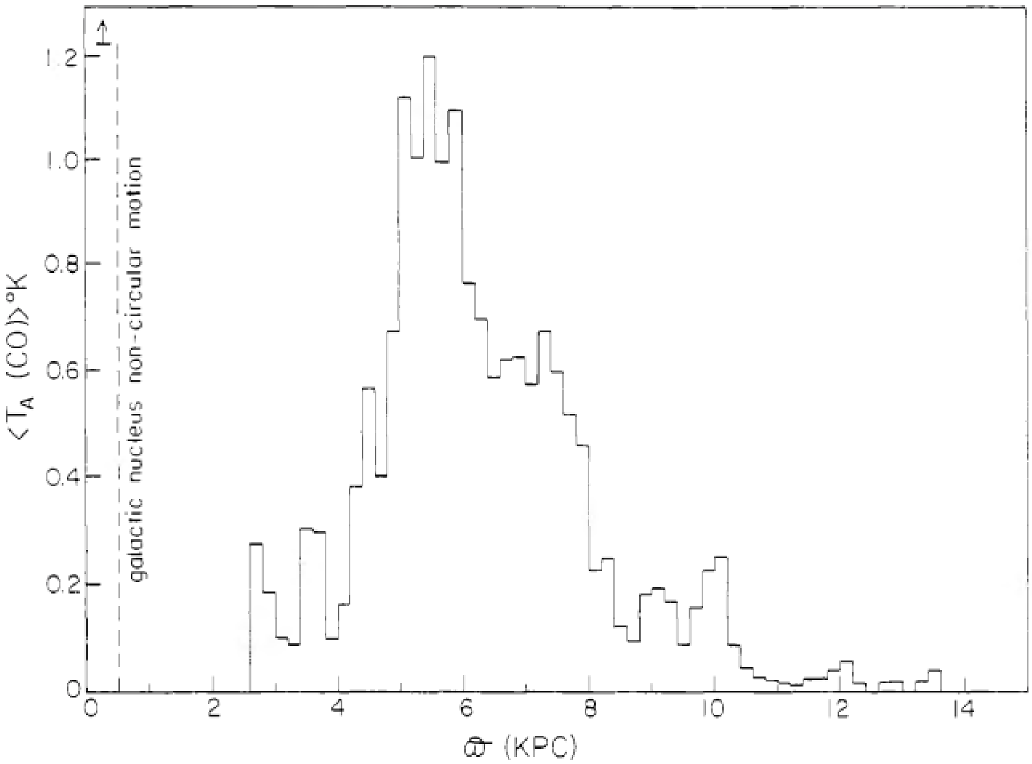

Figure 5.1: The mean CO antenna temperature T_A as a function of radius in the Milky Way ω (x-axis) as presented by Scoville & Solomon (1975)

Bolocam Galactic Plane Survey (BGPS) of 1.1 mm dust continuum emission, and gas masses were derived from optically thin ^{13}CO $J = 1{-}0$ emission from the Five College Radio Astronomy Observatory (FCRAO) Galactic Plane Surveys.

The *Spitzer* c2d (Cores to Disks) survey confirmed a linear relationship between a cloud's mass surface density and the star formation rate therein, and further that star-forming regions are clustered about the densest cores (Evans et al., 2009). As such, the GMCs were first screened for mass surface density $\Sigma_{\rm GMC}$

$$\Sigma_{\rm GMC} = \frac{M_{\rm GMC}}{\pi R^2_{\rm GMC}} \tag{5.1}$$

where $M_{\rm GMC}$ is the mass and $R_{\rm GMC}$ is the effective radius of the cloud. A mass surface density of 200 $M_\odot$ pc^{-2} approximately corresponds to the 10^3 cm^{-3} density threshold for "dense" molecular clouds and was therefore used as the cut-off for selecting targets.

We then considered GMCs with radii $\leq 2.0'$ such that they could be observed with the Atacama Compact Array in a single session (i.e., with ≤ 150 pointings). Based on their coordinates on the sky, targeted GMCs fall at kinematic distances of $d \sim 4$

Table 5.1: Properties of the 11 targeted GMCs

BGPS^a ID	Name^a	$\alpha^a_{\mathrm{J2000}}$	$\delta^a_{\mathrm{J2000}}$	V^a_{LSR} (km s^{-1})
3053	G023.368−00.290	$18^{\mathrm{h}}34^{\mathrm{m}}53\overset{\mathrm{s}}{.}0$	$-08^\circ37'43''$	78.1
3474	G025.227+00.289	$18^{\mathrm{h}}36^{\mathrm{m}}15\overset{\mathrm{s}}{.}1$	$-06^\circ42'50''$	47.1
4449	G030.536+00.021	$18^{\mathrm{h}}46^{\mathrm{m}}53\overset{\mathrm{s}}{.}2$	$-02^\circ07'22''$	47.8
5623	G030.952−00.389	$18^{\mathrm{h}}57^{\mathrm{m}}05\overset{\mathrm{s}}{.}5$	$+02^\circ06'44''$	55.3
6029	G040.622−00.139	$19^{\mathrm{h}}06^{\mathrm{m}}01\overset{\mathrm{s}}{.}3$	$+06^\circ47'01''$	32.8
6082	G041.741+00.095	$19^{\mathrm{h}}07^{\mathrm{m}}15\overset{\mathrm{s}}{.}1$	$+07^\circ53'09''$	13.7
6112	G043.079−00.005	$19^{\mathrm{h}}10^{\mathrm{m}}05\overset{\mathrm{s}}{.}7$	$+09^\circ01'06''$	14.2
6120	G043.237−00.047	$19^{\mathrm{h}}10^{\mathrm{m}}33\overset{\mathrm{s}}{.}0$	$+09^\circ08'12''$	7.5
6299	G049.070−00.350	$19^{\mathrm{h}}22^{\mathrm{m}}46\overset{\mathrm{s}}{.}3$	$+14^\circ09'25''$	66.0
6310	G049.170−00.208	$19^{\mathrm{h}}22^{\mathrm{m}}26\overset{\mathrm{s}}{.}3$	$+14^\circ19'26''$	63.1
6318	G049.255−00.412	$19^{\mathrm{h}}23^{\mathrm{m}}21\overset{\mathrm{s}}{.}0$	$+14^\circ17'54''$	66.3

BGPS^a ID	Name^a	$d_{kin}{}^{a,b}$ (kpc)	$R_{\mathrm{GMC}}{}^a$ (pc)	$\Sigma_{\mathrm{GMC}}{}^c$ ($'$)
3053	G023.368−00.290	10.67 ± 2.50	5.17	352.50
3474	G025.227+00.289	3.16 ± 0.73	1.61	233.32
4449	G030.536+00.021	3.03 ± 0.14	1.53	258.36
5623	G030.952−00.389	$10.49^{+1.32}_{-1.23}$	5.11	308.41
6029	G040.622−00.139	11.01 ± 2.79	4.94	341.74
6082	G041.741+00.095	11.91 ± 5.85	2.63	271.51
6112	G043.079−00.005	11.65 ± 1.61	3.64	394.00
6120	G043.237−00.047	12.04 ± 2.72	5.28	682.78
6299	G049.070−00.350	5.57 ± 1.25	1.66	323.44
6310	G049.170−00.208	5.56 ± 0.86	2.67	589.39
6318	G049.255−00.412	5.55 ± 1.06	1.48	508.62

Targeted GMCs were chosen such that they have densities $\Sigma_{\mathrm{GMC}} \geq 200\ M_\odot$ pc^{-2} and $R_{\mathrm{GMC}} \leq 2.0'$.

[a] Values taken from Battisti & Heyer.

[b] The uncertainties for d_{kin} were not reported by Battisti & Heyer but were calculated for use in this work following the procedure in Appendix G.

[c] Calculated using Equation 5.1.

kpc or $d \sim 11$ kpc and are within the "molecular ring," which spans radii between 4 and 8 kpc from the galactic center and is where the bulk of molecular matter in the Milky Way is thought to exist (e.g., Scoville & Solomon, 1975; Sanders et al., 1984). This ultimately yielded 11 target BGPS objects, the observations of which are described below. The properties of the observed targets are given in Table 5.1. For simplicity, we refer to these objects by their BGPS IDs throughout this paper; their official names are listed in column (2) of Table 5.1 for reference.

Table 5.2: GMC image properties

BGPS ID	σ_{rms} (mJy beam^{-1})	θ_{syn}	ACA Field of View
3053	1.7	$5''.9 \times 3''.8$	$210'' \times 210''$
3474	1.6	$6''.3 \times 4''.0$	$216'' \times 216''$
4449	1.6	$6''.7 \times 3''.9$	$210'' \times 210''$
5623	2.2	$9''.4 \times 4''.1$	$210'' \times 210''$
6029	1.9	$7''.1 \times 4''.2$	$180'' \times 180''$
6082	1.4	$6''.4 \times 3''.8$	$145'' \times 145''$
6112	1.2	$7''.5 \times 4''.7$	$163'' \times 163''$
6120	1.4	$7''.2 \times 4''.7$	$186'' \times 186''$
6299	1.8	$7''.4 \times 4''.4$	$165'' \times 165''$
6310	1.2	$6''.3 \times 4''.7$	$254'' \times 254''$
6318	1.5	$8''.2 \times 2''.5$	$145'' \times 145''$

1.2 mm ALMA Observations

Observations of the 11 GMCs were carried out using the Atacama Compact Array (ACA), which is a subset of antennas from the Atacama Large Millimeter/submillimeter Array (ALMA) and uses up to twelve 7-meter antennas. For each source, there were two local oscillator (LO) settings in ALMA Band 6: the “lower” LO setting centered at ~226 GHz and the “upper” centered at ~251 GHz. These LO settings were chosen to target tracer and otherwise astrochemically-interesting compounds and also included a continuum window in each. Continuum windows had bandwidths of 2 GHz with 2048 channels. The passband was examined for excess line emission, and line-free channels across all spectral windows were used to measure the continuum flux. The ACA has an angular resolution of $5''.5-6''.2$ in the lower LO and $5''.2-5''.9$ in the upper LO setting. The mosaic fields of view were chosen based on GMC angular sizes reported by Battisti & Heyer (2014).

Calibration was completed using standard `CASA` (version 5.4.0-70) calibration pipeline scripts. The images presented here were created with continuum emission estimated from line-free channels and subtracted using the `tclean` algorithm with robust weighting and a Briggs parameter of 0.5 for deconvolution. The image noise-levels and synthesized beams are presented in Table 5.2. In general, the noise-level is $\sigma_{\mathrm{rms}} \leq 2.2$ mJy beam^{-1}.

A detailed description of the observations—including calibrators, number of antennas, and dates—for each source can be found in Appendix F.

5.3 Methods

Identifying Substructures

Compact dust emission within each of the targeted GMCs was identified from continuum images made from both the lower and upper LO settings. Features are designated as detected millimeter structures if (a) they have a peak flux of $\geq 3\sigma_{\mathrm{rms}}$ and (b) are present in both the upper and lower Band 6 continuum images. We also consulted the existing literature for previously-reported objects within the field-of-view of our observations using the SIMBAD astronomical database (Wenger et al., 2000) and incorporated these results to further characterize the objects found in our survey, where possible.

Flux Density and Peak Flux

Our initial assessment of the identified millimeter substructures within the sample includes measurements of peak flux S_{peak} taken from the `CASA` *viewer* command. The peak flux was determined by drawing an area around each millimeter source and taking the reported statistical flux density.

We attempted Gaussian fits to constrain the flux measurements and sizes of the identified millimeter sources (via the *gaussfit* function in the `CASA` *viewer*), but the fits often came with high uncertainty; i.e., many of our sources are not well fit by a Gaussian profile, either because of irregular shape or low flux. For consistency, we use the aforementioned "statistical" method of measuring flux density and peak flux for all sources. We do, however, adopt the coordinates from the Gaussian fit attempts since they well constrain the location of peak flux, even if not the magnitude of the peak flux itself.

Recovered Flux

The original 1.1 mm BGPS total power data were acquired with a $33''$ beam using the 10.4m Caltech Submillimeter Observatory. This primary beam is much larger than the ACA synthesized beam of $\sim 5-6''$ at 1.2 mm, and thus much of the smooth, larger-scale structures toward these sources is resolved out in our observations. Table 5.3 gives the percentage of flux recovered in our observations compared to that of the BGPS observations compiled by Rosolowsky et al. (2010), who report recovered flux density with aperture diameters of $40''$ and $120''$ centered on the coordinates listed in Table 5.1 (the coordinates of maximum intensity reported by Battisti & Heyer and the pointing centers used here). The values we recover in each of those apertures were calculated by drawing a circular region with the appropriate

Table 5.3: Recovered flux density at 245 GHz (1.2 mm) in apertures of diameter 40″ and 120″

BGPS ID	$F_{40,R10}$[a] (Jy)	F_{40}[b] (Jy)	Recovered Flux	$F_{120,R10}$[a] (Jy)	F_{120}[b] (Jy)	Recovered Flux
3053	0.710	0.008	1%	1.916	0.361	19%
3474	0.769	0.003	<1%	2.202	0.616	28%
4449	0.803	-0.002	<1%	2.262	0.090	4%
5623	0.228	0.180	79%	0.642	0.195	30%
6029	0.834	0.043	5%	2.546	0.801	31%
6082	0.330	0.018	5%	0.735	0.414	56%
6112	0.324	0.042	11%	1.542	0.219	14%
6120	1.385	1.436	104%	4.754	1.984	42%
6299	0.455	0.078	17%	2.243	0.243	11%
6310	0.880	0.057	6%	4.321	0.446	10%
6318	0.383	0.003	1%	1.663	0.148	9%

[a] Rosolowsky et al. (2010)
[b] This work.

diameter in the `CASA` viewer tool and reading out the reported flux density.

The percentage of flux recovery in these observations is highly variable among the observed BGPS objects. Some have low flux recovery at all apertures, such as BGPS 4449 with ≤4% in all apertures, whereas others have relatively high flux recovery, like BGPS 6120 with ≥42% recovery. Others still have low flux recovery in one aperture but high flux recovery in another, e.g., BGPS 6082 with 5% recovery in a 40″ aperture but 61% in an 80″ aperture (not listed in Table 5.3).

5.4 1.2 mm Continuum Emission

In this preliminary look at an unbiased sample of 11 molecular-ring GMCs, we detect a total of 96 millimeter emission sources, listed in Table H.1 (Appendix H), across the 11 target GMCs. We refer to these sources by their BGPS ID and number them mm1, mm2, ..., mm*N* in decreasing order of peak flux for *N* detected objects. All of the detected objects have a peak flux of $\geq 3\sigma_{\rm rms}$, and 52 have peak fluxes of $\geq 10\sigma_{\rm rms}$, where $\sigma_{\rm rms}$ is the noise level for each BGPS source listed in Table 5.2.

Our target BGPS sources exhibit a wide range of characteristics within the field of view of our observations, with some (BGPS 6029, BGPS 6082) having only one resolved object with 1.2 mm emission with the ACA and others (BGPS 6299, BGPS 6310) having 20 or more 1.2 mm emission features, many of which overlap or form complex groupings. We considered a relationship between mass surface density in

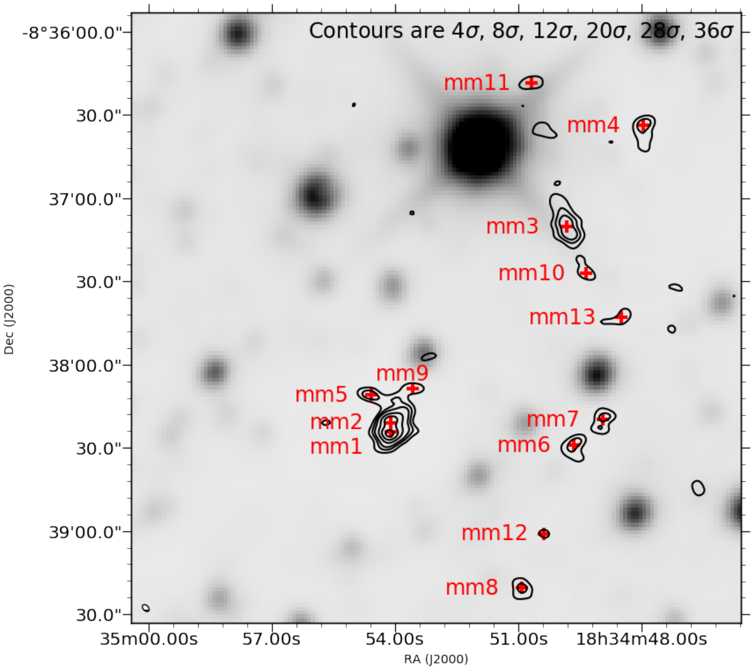

Figure 5.2: BGPS 3053 continuum at 245 GHz (1.2 mm) contour image over the WISE Band 1 (3.35 μm) data in greyscale. Red crosses show the peak flux for each of the detected mm-wave objects. The synthesized beam is shown by the oval in the bottom left corner. The contour levels with respect to $\sigma_{\rm rms}$ are listed in the top right corner of each image. The synthesized beam and $\sigma_{\rm rms}$ are listed in Table 5.2.

these GMCs and the number and profile of objects therein but found no correlation suggestive of the level of mm-continuum complexity being determined by a cloud's overall evolution, as represented by mass surface density.

In the following sections, we present an overview of the emission sources detected toward each GMC, including brief reviews of corresponding objects in past literature. We also present the 1.2 mm upper Band 6 continuum images acquired using the ACA. All images give the continuum in black contours over a WISE Band 1 (3.35 μm) image obtained from the NASA/IPAC Infrared Science Archive (IRSA).[1] Observed properties—namely coordinates, peak flux S_{peak}, and detection significance—are listed in Table H.1.

BGPS 3053

BGPS 3053 has 13 detected continuum emission objects that seem to be part of two distinct regional structures (Figure 5.2): a conglomerate of four partially-resolved sources in the southeast quadrant of our field of view and a possible filament

---

[1] https://irsa.ipac.caltech.edu/applications/wise/

extending vertically in the west. The grouping to the southeast contains the two brightest sources in BGPS 3053, which are separated by 3.3″, or a linear distance of 0.075 pc (1.5×10^4 au) at the adopted distance of 4.70 kpc for mm1+2. Extending from these to the northeast and northwest are mm5 and mm9. As far as we know, this work is the first account of mm5 and mm9 as distinctly resolved structures.

The remaining sources seem to follow a filament from mm11 in the north to mm8 in the south. Several of the sources along this filament potentially harbor additional substructures that are not resolved in these data. For instance, mm3 appears to be a cluster of at least three individual substructures. One is centered on the peak flux marked by the cross labeled mm3 in Figure 5.2, the others flank this source to either side. The emission source mm7 also appears to have at least two substructures present, both of which can be easily seen in Figure 5.2.

The field of view in which we observe BGPS 3053 hosts a variety of astronomical objects. This includes an embedded protostar, a class I[2] protostar, a class II pre-main-sequence star, and multiple faint objects that have not been characterized previously. There are are also two known bright stars (HD171390 and BD-08 4635) and an X-ray source; however, these objects are ≤500 pc from the Earth and extragalactic, respectively, and thus do not affect the objects in our survey (Gaia Collaboration, 2018; Lansbury et al., 2017).

BGPS 3053 mm1 and mm2 constitute a complex made up of two partially-resolved sources that have been identified as part of several past surveys. The grouping was included in the ATLASGAL survey (Csengeri et al., 2014; Wienen et al., 2015; Urquhart et al., 2018), and Su et al. (2015) note that this region is a fragmentation point within dense filamentary molecular gas interacting with the supernova remnant W41. Ragan et al. (2009) identify an embedded protostar centered on mm1 within the mm1+2 complex using *Spitzer*, which is supported by Merello et al. (2015) who identify a compact substructure (which they designate as source 223) toward mm1.

To the north of the mm1+2 complex are mm5 and mm9. These sources, along with

---

[2] Young stellar objects are commonly classified by their spectral index α, which is the slope of an object's spectral energy distribution in the mid-IR. The spectral index is defined as $\alpha = d\log(\lambda F_\lambda)/d\log(\lambda)$ where F_λ is the flux density at wavelength λ. Class 0 objects are deeply embedded protostars that are undetectable at $\lambda < 20$ μm. Class I objects have $\alpha > 0.3$ and are embedded protostars whose envelopes have begun to dissipate. Class II and Class III young stellar objects are more evolved and constitute protoplanetary disks. Class II stars have gas-rich protoplantary disks whereas Class III stars do not; Class III stars are typically referred to as classical T Tauri stars, named for the protostype low-mass stars in the Taurus Molecular Cloud that have only just become visible at optical wavelengths.

mm1+2, are located in the dark cloud SDC G23.367-0.288 reported by Peretto & Fuller (2009), whose *Spitzer* observations at 8 μm and 24 μm did not detect any fragmentation within the cloud. No previously reported individual objects seem to be associated with either mm5 or mm9.

The northernmost "filament" sources, mm11 and mm4, are both included in the SCUBA Legacy Catalogues presented by Di Francesco et al. (2008) as submillimeter (850 μm) continuum sources.

The source mm3 has been reported as a faint substructure by Merello et al. (2015). In our ACA observations, mm3 appears to be a cluster of at least three individual sources. Just to the southwest of mm3 is the object mm10, which has been reported as a faint substructure by Merello et al. (2015) and as a class I protostar by Ragan et al. (2009). Even further to the southwest, mm13 forms a line with mm3 and mm10. As far as we know, there are no known sources centered on mm13. However, Merello et al. (2015) report three submillimeter objects—which they label 219, 220, and 222—centered to the southwest of mm13 with separations of at least 6.3″.

The sources mm6 and mm7 are the only objects in our observations toward BGPS 3053 that have no previously observed objects nearby, within 25″ and 11″, respectively. Nevertheless, their fluxes are larger than some of the previously identified objects (e.g., mm10, mm11, mm13), so it is likely that mm6 and mm7 are indeed real.

Finally, there are no known sources centered on either mm8 or mm12, but Ragan et al. (2009) report a class II pre-main-sequence star (namely G023.37-0.29 27) roughly between these two millimeter sources. Therefore mm8 and mm12 may be associated with an outflow or fragment from the outer envelope, or they may be distinct sources altogether. Nevertheless, it is possible that they are influenced by their apparent close proximity to the pre-main-sequence star.

The distance to objects in BGPS 3053 is ambiguous, with both far and near distances being adopted in the literature. Battisti & Heyer report a distance of 10.67 ± 2.50 kpc, which we tentatively adopt as the distance for the filamentary structure to the west. For the mm1+2 complex, however, we adopt a nearer distance. Ragan et al. (2006) report a distance of $4.70^{+0.90}_{-0.88}$ kpc toward mm1 from 8 μm observations. Similarly, Wienen et al. (2015) report a distance of $4.93^{+0.28}_{-0.29}$ kpc based on ATLASGAL observations at 870 μm but for a group of five objects centered about 6″ west of the mm1 peak flux. As such, we adopt the Ragan et al. distance since it better matches

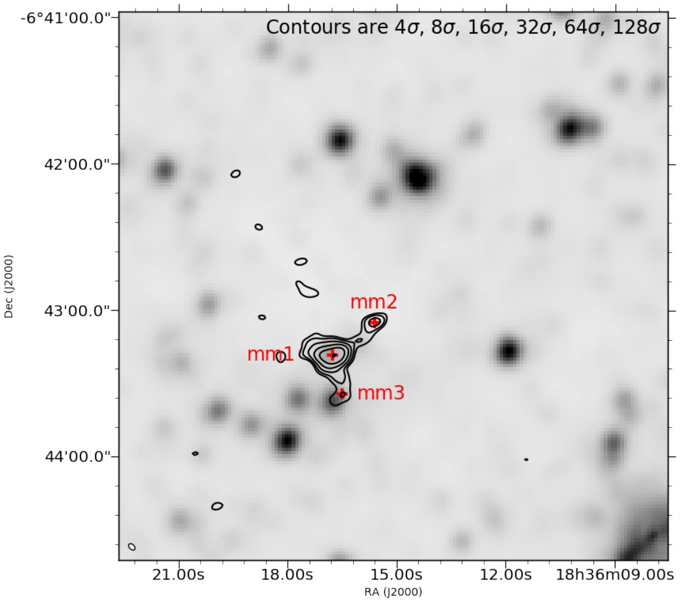

Figure 5.3: BGPS 3474 continuum at 245 GHz (1.2 mm, contours) over a WISE Band 1 (3.35 μm) image. Red crosses show the peak flux for each of the detected millimeter-wave (mm) emission objects. The synthesized beam is shown by the oval in the bottom left corner. The contour levels with respect to $\sigma_{\rm rms}$ are listed in the top right corner of each image. The synthesized beam and $\sigma_{\rm rms}$ are listed in Table 5.2.

our observations spatially. We also adopt this distance for mm5 and mm9 because of their proximity and apparent intimate connection with mm1+2.

Toward the filament-like band of millimeter objects to the west, there have not been additional reports on distance beyond that by Battisti & Heyer. Future work includes looking at molecular line data, which could potentially be used to help further constrain the distances to the string of objects stretching from mm11 to mm8 by comparing velocity shifts of molecular lines in these sources to those in the mm1+2 complex. In the meantime, we tentatively assume all of these objects reside at the same distance since they may be regions of higher density along the same filament.

BGPS 3474

We resolve three millimeter sources within BGPS 3474, all of which constitute one larger complex. As seen in Figure 5.3, mm2 and mm3 appear to be related to mm1.

There are several other regions with emission $>4\sigma_{\rm rms}$, however they do not meet our criteria outlined in Section 5.3 in that they are not clearly detected in the lower band continuum image.

BGPS 3474 is one of three sources (the others being BGPS 6029 and BGPS 6082) for which we recover $\leq$5% of the flux in a 40″-diameter aperture only, which is attributed to the emission features in our data being off of the pointing center. With the larger apertures, we recover much more of the flux, specifically 26–28%.

Our detected BGPS 3474 sources are associated with a dense core thought to be the site of high-mass star formation (Wienen et al., 2012). There has also been γ-ray emission detected towards these mm sources, possibly associated with star-formation being driven by a nearby OB cluster about 4′ (~3.7 pc at the adopted distance of 3.16 kpc) to the south (Katsuta et al., 2017). While this OB cluster is likely too far away to have a large effect on the detected mm objects, the established literature nevertheless points to BGPS 3474 mm1, mm2, and mm3 as a high-mass star-forming region with influence from local stellar activity.

The BGPS 3474 source mm1 has been previously identified as a YSO. Kanarek et al. (2015) report it as a "likely YSO" with a distance of 2.596 ± 0.194 kpc, which falls within the margin of error of Battisti & Heyer's reported distance. Baug et al. (2016) also report mm1 as a component of the C1 clump in the C25.29+0.31 molecular cloud from mid-IR observations, classifying mm1 as a "flat spectrum" YSO, which have near-IR spectra strongly veiled by continuum emission from hot circumstellar dust (Greene et al., 1994). There has also been submillimeter emission detected to be centered on mm1 (Wienen et al., 2015).

Centered toward mm2 is a dark cloud in which no fragments have been previously reported (Peretto & Fuller, 2009; Peretto et al., 2016). This dark cloud has an equivalent radius of 8.″5; this is extended beyond mm2, which we measure to have a radius of <6″. However, the area assigned to this dark cloud is not large enough to encompass mm1 and thus is limited to mm2.

Centered ~5″ to the southeast of mm3 is an IR source identified by Baug et al. (2016) as a class II YSO. Thus, this may be the first report of mm3 as a distinct emission source. Whether it is material coming off of mm1 or related to this other YSO, or a separate object altogether, is presently unknown.

Battisti & Heyer report a distance of 3.16 ± 0.73 kpc, which we adopt for all BGPS 3474 objects in our analyses. Two other values have been published—2.596 ± 0.194

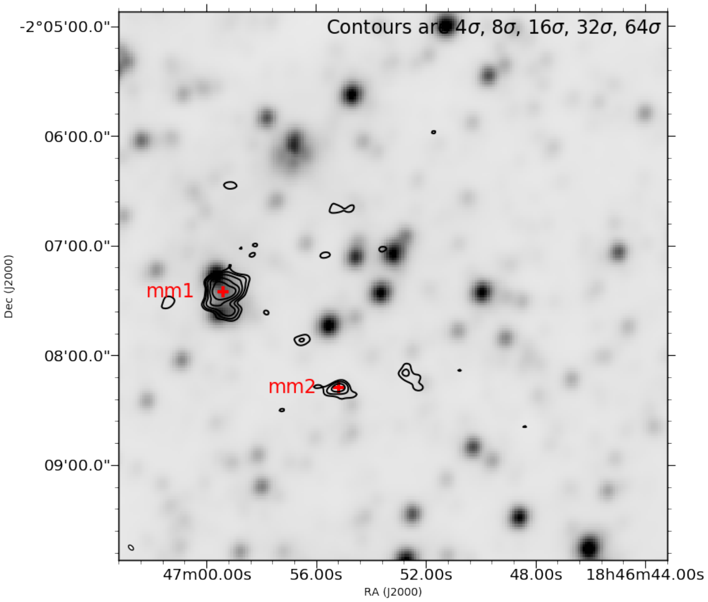

Figure 5.4: BGPS 4449 continuum at 245 GHz (1.2 mm, contours) over a WISE Band 1 (3.35 μm) image. Red crosses show the peak flux for each of the detected millimeter-wave (mm) emission objects. The synthesized beam is shown by the oval in the bottom left corner. The contour levels with respect to σ_{rms} are listed in the top right corner of each image. The synthesized beam and σ_{rms} are listed in Table 5.2.

kpc by Kanarek et al. (2015) and 3.30 kpc by Wienen et al. (2015)—both of which agree with Battisti & Heyer's reported distance.

BGPS 4449

We detect millimeter emission regions in BGPS 4449 as seen in Figure 5.4. The object mm1 appears to have some structure, with emission extending to the southwest. There are several other possible distinct objects, for instance to the west of mm2 and between mm1 and mm2, however these are not clearly visible in both the upper and lower Band 6 continuum images.

We recover particularly low relative flux toward BGPS 4449, with <5% flux recovery compared to Rosolowsky et al. at all apertures. However, this is not surprising given that most of the flux we observe is toward the eastern (left) edge of our field of view as seen in Figure 5.4.

In the literature, previous observations toward BGPS 4449 mm1 have been associated with a molecular cloud (Carlhoff et al., 2013), H II regions (e.g., Wood & Churchwell, 1989; Kolpak et al., 2003; Urquhart et al., 2009), a dense core (e.g., Ellsworth-Bowers et al., 2015), YSO and YSO candidates (e.g., Saral et al., 2017), and submillimeter (e.g., Merello et al., 2015; Urquhart et al., 2018; Yang et al., 2018), millimeter (Hill et al., 2005, 2006, 2009), and radio sources (e.g., Wood et al., 1988; Zoonematkermani et al., 1990; Becker et al., 1994). Yang et al. (2018) report an area of submillimeter emission with an effective radius of 41″ toward mm1's southwestern region, which they designate as the site of a massive outflow. Despite its inclusion in a multitude of surveys, detailed characterization of mm1 remains limited. BGPS 4449 mm2 has also been identified as the site of a YSO (Veneziani et al., 2013; Urquhart et al., 2018).

We adopt the Battisti & Heyer distance of 3.03 ± 0.14 kpc. Other estimates include both near and far distances. Ellsworth-Bowers et al. (2015) report a distance of 11.24 ± 0.44 kpc toward a dense core in our field of view, and Urquhart et al. (2018) estimate a distance of ~2.7 kpc toward a submillimeter emission source. The measurement by Ellsworth-Bowers et al. is over a radius of ~72″ thus incorporates material extended beyond the scope of either mm1 or mm2, and so it may not be the best source to compare to our own observations. The Urquhart et al. distance is lower than our adopted distance but at submillimeter wavelengths. As such, the Battisti & Heyer value, which was derived from millimeter-wave observations, offers the best option for our data at present.

BGPS 5623

The continuum for BGPS 5623 (Figure 5.5) is relatively complex, in particular to the northeast where there are fairly weak filamentary structures, making it difficult to meaningfully constrain millimeter-wave-emitting sources there. BGPS 5623 mm1 and mm2 are strong (peak fluxes of $55\sigma_{\rm rms}$ and $29\sigma_{\rm rms}$) isolated sources in the center and to the southwest in our field of view, respectively. The remaining six sources comprise the apparent filamentary structure. While mm3 and mm4 have fairly elliptical shapes, mm5 and mm6 are irregularly shaped, potentially indicative of substructures within these objects.

BGPS 5623 has 79% of the flux recovered in a 40″-diameter aperture, which is where the the brightest emission object, mm1, resides. Except for the very edges of the field of view, there is virtually no other millimeter-wave emission near the

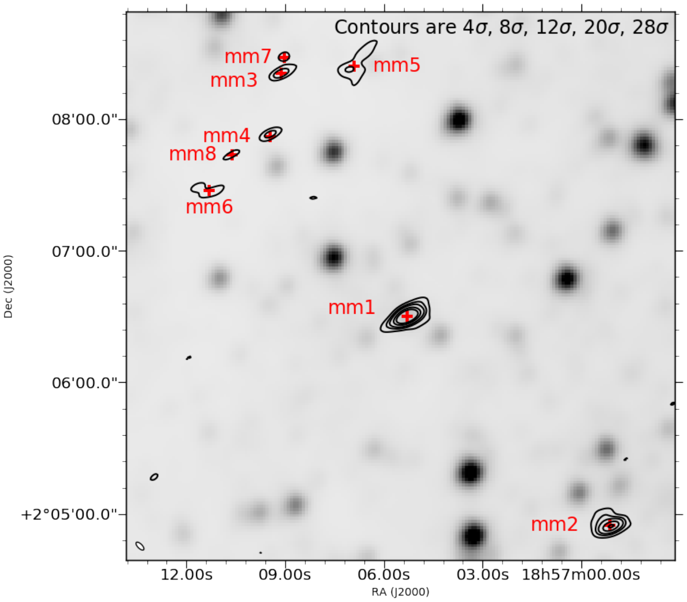

Figure 5.5: BGPS 5623 continuum at 245 GHz (1.2 mm, contours) over a WISE Band 1 (3.35 μm) image. Red crosses show the peak flux for each of the detected millimeter-wave (mm) emission objects. The synthesized beam is shown by the oval in the bottom left corner. The contour levels with respect to $\sigma_{\rm rms}$ are listed in the top right corner of each image. The synthesized beam and $\sigma_{\rm rms}$ are listed in Table 5.2.

center of the image. Thus it is not surprising that the recovered flux drops to 40% and then 30% in the 80″ and 120″ apertures where large-scale extended emission is not detected.

There have been several observations toward this region, but the previously published literature has high variance with respect to how objects therein, especially mm1, are characterized. Nevertheless, most reports agree that the objects detected toward BGPS 5623 are indeed related to high-mass star formation.

Both mm1 and mm2 have been designated as sites of high-mass YSOs in multiple surveys (Rathborne et al., 2006; Nguyen Luong et al., 2011; Urquhart et al., 2018). The remaining six objects that we detect constitute a cluster of relatively faint objects in the northeastern part of our field of view.

We go through the group of faint objects from northwest (top right) to southeast (bottom left), beginning with mm5. BGPS 5623 mm5 has been identified as the site of a YSO (Urquhart et al., 2018) and dense cores (e.g., Rygl et al., 2010; Kong et al., 2017; Liu et al., 2018b). Using relatively high spatial resolution ($1\farcs5 \times 1\farcs0$) with the ALMA 12m array, Kong et al. (2017) report 6 individual cores toward this region alone at 1.1 mm, supporting the hypothesis that mm5's irregular shape is attributed to multiple objects. The brightest source in this portion of our field of view is mm3, which is closely neighbored by mm7. Despite its low flux, cross-referencing the previously published literature with mm7 supports this faint source being a real, but low-mass, source and the site of a dense core (Kong et al., 2017; Liu et al., 2018a,b). BGPS 5623 mm3 is also associated with dense cores but with much higher mass estimates in the existing literature.

Both mm4 and mm6 have been identified as the site of dense cores, and mm6 is also associated with a YSO (Nguyen Luong et al., 2011; Kong et al., 2017; Urquhart et al., 2018). About halfway between mm4 and mm6 is mm8, for which there are no objects listed in SIMBAD within a $10''$ radius of its center. Thus mm8, with a detection significance of only $4.7\sigma_{\rm rms}$, may in fact be an artifact.

There have been multiple distance measurements, both near and far, in the direction of BGPS 5623. Battisti & Heyer report high uncertainties on the mass and radius toward this GMC (192% and 106%, respectively), yielding an exceptionally high uncertainty on their BGPS distance measurement using the error propagation outlined in Appendix G with $d \sim 10.49 \pm 25.83$ kpc. Nevertheless, Urquhart et al. (2018) also adopt a far distance of 10.29 kpc toward mm1. As such, we adopt a distance to BGPS 5623 mm1 of $10.49^{+1.32}_{-1.23}$ kpc with the uncertainties calculated to correspond to the near and far boundaries of the molecular ring. Conversely, Rathborne et al. (2010) and Rygl et al. (2010) assume near distances of 3.0 kpc and 3.6 kpc. Indeed, there may be emission coming from both near and far distances. However, since we recover 79% of the BGPS flux (see Table 5.3) within a $20''$-radius aperture of the pointing center of BGPS 5623, where mm1 is located, we tentatively adopt the BGPS distance of 10.49 kpc in these analyses.

The remaining millimeter emission sources in BGPS 5623 appear to have a near distance of ~3 kpc based on the existing literature. Because these remaining structures are toward the southwest and northeast corners of our field of view, it is not reasonable to automatically assume the reported BGPS value. As far as we know, the only distance measurement reported toward mm2 (to the southwest) alone is a near measurement of 3.24 kpc by Urquhart et al. (2018), which we adopt as our mm2 distance. The group of emission sources to the northeast have multiple distance constraints reported, specifically 2.74 kpc, 2.9 kpc, and 3.0 kpc toward both

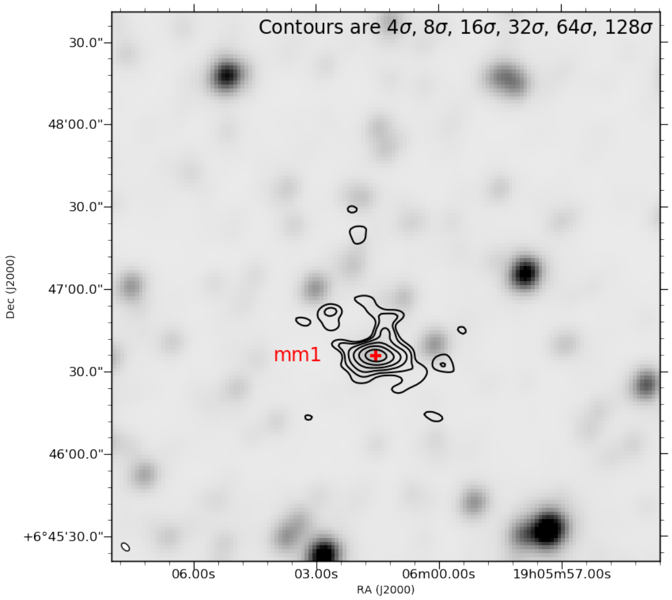

Figure 5.6: BGPS 6029 continuum at 245 GHz (1.2 mm, contours) over a WISE Band 1 (3.35 μm) image. Red crosses show the peak flux for each of the detected millimeter-wave (mm) emission objects. The synthesized beam is shown by the oval in the bottom left corner. The contour levels with respect to $\sigma_{\rm rms}$ are listed in the top right corner of each image. The synthesized beam and $\sigma_{\rm rms}$ are listed in Table 5.2.

mm5 and mm3 (Urquhart et al., 2018; Zhang et al., 2017; Rygl et al., 2010); 2.9 kpc toward mm7 (Liu et al., 2018a); and 2.74 kpc and 2.90 kpc toward mm6 (Urquhart et al., 2018; Zhang et al., 2017). We adopt the median value of 2.90 kpc for all northeast objects.

BGPS 6029

We detect one source toward BGPS 6029, which is rather bright with a peak flux of $204\sigma_{\rm rms}$. As seen in Figure 5.6, there is structure coming off of this source to the northern and southwestern edges, but between the upper and lower band continua, we are unable to resolve whether these are filamentary structures associated with mm1 or distinct structures that are only partially resolved.

Like BGPS 3474 (Section 5.4), BGPS 6029 has ≤5% of the flux in a 40″ aperture but higher relative flux recover in the larger apertures. This source's sole emission object—mm1—is located south of the image center. Thus when it is included in the 80″-diameter aperture, the recovered flux jumps to 43%. The recovered flux then decreases to 31% in the 120″ aperture, signaling that there is perhaps more extended emission that we do not detect toward the south of mm1.

There are a number of objects in SIMBAD reported toward the single source in BGPS 6029, including an H II region (Urquhart et al., 2009), dense cores (e.g., Beuther et al., 2002; Lu et al., 2014), OH and CH_3OH masers (e.g., Argon et al., 2000; Caswell et al., 1995), and a YSO (e.g., Svoboda et al., 2016; Areal et al., 2018). Lu et al. (2014) report three distinct dense cores toward mm1 from VLA ammonia observations with a synthesized beam of ∼3″ × 3″. They constrain these cores to have radii of 0.03 pc, which corresponds to 2.″7 in their observations.

BGPS 6029 mm1 has also been the site of multiple astrochemical studies, for example toward understanding the nature of deuterium chemistry in high-mass star-forming regions (e.g., Fontani et al., 2014). Even so, the existing astrochemical literature for BGPS 6029 mm1 is limited to the gas-phase. Fontani et al. (2015) searched for deuterated methanol—using it as a tracer of high-mass protostellar objects in which molecules formed through grain-surface chemistry is sputtered from icy grain mantles—toward mm1 but did not detect any. They conclude the region toward mm1, which they refer to as an H II region, is too evolved for such grain-surface chemistry to be observed. Nevertheless, the reports of dense cores by Lu et al. provide hope that ice chemistry, as well as gas chemistry, could be studied toward BGPS 6029 mm1. Moreover, as will be briefly discussed in Section 5.5, the millimeter emission toward mm1 correlates well with far-IR emission, an indicator for possible presence of ices. Thus, despite the work done toward characterizing this source thus far, there is still much more to uncover.

We adopt the BGPS distance of 11.01 ± 2.79 kpc toward mm1 (Battisti & Heyer, 2014). This source is south of the pointing center, but our observations recover ∼43% of the Bolocam survey flux within an 80″-diameter aperture. As such, we find that our observations of mm1 likely constitute a significant portion of the material for which the BGPS distance was calculated. Furthermore, Urquhart et al. (2018) report a distance of 10.63 kpc toward mm1. Only one near distance (of 2.3 kpc) has been adopted in analyses of this region as far as we know (Lu et al., 2014).

BGPS 6082

There is one source detected toward BGPS 6082, which we refer to as mm1. This object has extended emission, particularly to the southwest and southeast, as can be seen in Figure 5.7.

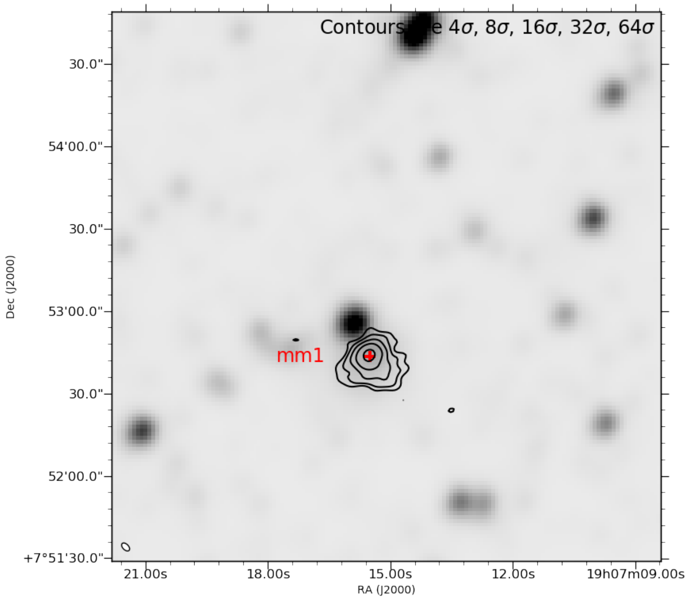

Figure 5.7: BGPS 6082 continuum at 245 GHz (1.2 mm, contours) over a WISE Band 1 (3.35 μm) image. Red crosses show the peak flux for each of the detected millimeter-wave (mm) emission objects. The synthesized beam is shown by the oval in the bottom left corner. The contour levels with respect to σ_{rms} are listed in the top right corner of each image. The synthesized beam and σ_{rms} are listed in Table 5.2.

BGPS 6082 follows a similar flux recovery pattern as BGPS 6029 in that we recover $\leq$5% of the flux in a 40″ aperture but substantially more (61%) in the 80″-diameter aperture before decreasing slightly with the 120″ aperture (56%). Like BGPS 6029, the sole millimeter emission source in BGPS 6082 is south of the pointing center. With a 40″ aperture, it is mostly excluded, and the loss of recovered flux from the 80″- to the 120″-diameter aperture is perhaps the result of unrecovered extended emission toward the south of BGPS 6082 mm1.

Objects toward BGPS 6082 mm1 have been reported in surveys by more than 30 articles. This region has been associated with an H II region (e.g., Urquhart et al., 2009), a molecular cloud (e.g., Anderson et al., 2009), submillimeter sources (e.g., Thompson et al., 2006; Ellsworth-Bowers et al., 2015; Urquhart et al., 2014, 2018), and a YSO (e.g., Areal et al., 2018). Centered to the east of mm1 is IRAS 19048+0748, a composite object that is the site of a H_2O maser (Codella et al., 1995); a search for CH_3OH masers yielded a non-detection toward this object (van der Walt et al., 1995).

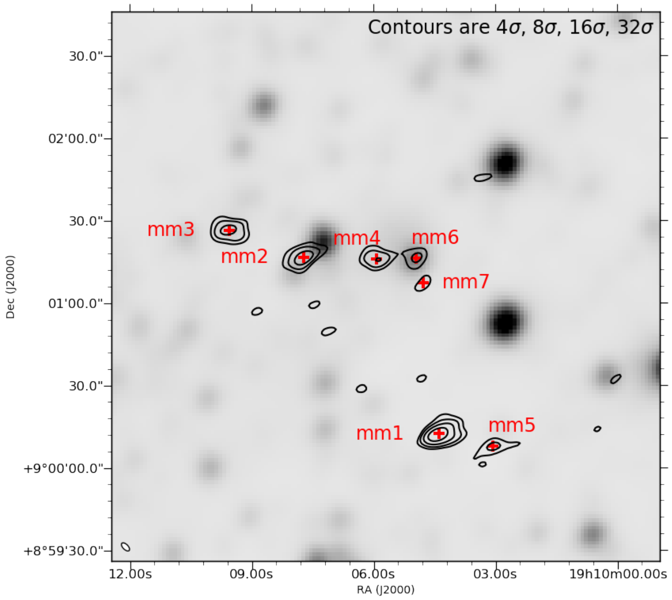

Figure 5.8: BGPS 6112 continuum at 245 GHz (1.2 mm, contours) over a WISE Band 1 (3.35 μm) image. Red crosses show the peak flux for each of the detected millimeter-wave (mm) emission objects. The synthesized beam is shown by the oval in the bottom left corner. The contour levels with respect to σ_{rms} are listed in the top right corner of each image. The synthesized beam and σ_{rms} are listed in Table 5.2.

Battisti & Heyer report a distance of 11.91 ± 5.85 kpc. This value is supported by measurements by Ellsworth-Bowers et al. (2015), who report a distance of 11.36 ± 0.54 kpc with a max-likelihood probability of 0.94. Similarly, Urquhart et al. (2018) adopt a distance of 11.68 kpc. Within a 80″-diameter aperture that encompasses mm1 (which is south of the pointing center), we recover 56% of the BGPS flux. Therefore, the Battisti & Heyer BGPS distance is a reasonable choice for mm1.

BGPS 6112

BGPS 6112, shown in Figure 5.8, contains seven millimeter emission objects. The brightest, mm1, is located to the southwest with mm5 as a neighbor. The remaining objects appear to follow a filamentary structure north of center, but our observations do not recover any such large-scale structure.

We recover <15% of the flux at all apertures for BGPS 6112, for which most of the 1.2 mm emission is separated from the pointing center, accounting for low recovered flux at smaller apertures. The absence of large-scale structure related to the sources that may be part of a filament may account for the small proportion of flux recovered toward this source.

Centered toward mm1, a YSO (Urquhart et al., 2014, 2018) has been identified in the established literature. Centered nearby to the northwest is a molecular cloud observed at submillimeter wavelengths (Matthews et al., 2009), as well as a dark nebula centered to the north (Peretto & Fuller, 2009; Peretto et al., 2016). BGPS 6112 mm5, which neighbors mm1, does not seem to be associated with any individual objects reported in the literature.

The remaining sources, which seem to trace a filament, also correspond to a number of previously reported objects. BGPS 6112 mm3 corresponds to a class I YSO candidate, and mm4 is the site of a class II YSO (Saral et al., 2015). Centered toward mm2 is a molecular cloud with an effective radius of $25\overset{''}{.}8$ (Matthews et al., 2009). BGPS 6112 mm6 has been detected at multiple wavelengths, including submillimeter (Urquhart et al., 2014, 2018) and infrared (e.g., Urquhart et al., 2011; Saral et al., 2015). Saral et al. (2015) identify two candidate YSOs toward mm6, a class I massive YSO candidate centered on the flux peak and a class II YSO centered on the edge. As far as we know, mm7, like mm5, is not associated with any individual object discussed in the literature.

We adopt the Bolocam survey distance of 11.65 ± 1.61 kpc (Battisti & Heyer, 2014) for all detected emission objects in BGPS 6112. Toward mm1, Urquhart et al. (2018) assume a distance of 11.11 kpc, which supports a far distance for this source.

Urquhart et al. (2018) also adopt the far distance of 11.11 kpc toward mm6. Because we are not aware of any other distance constraints toward the filamentary millimeter emission sources, we adopt a far distance for them as well.

BGPS 6120

We detect 11 millimeter emission sources toward BGPS 6120, with the exceptionally bright mm1 ($364\sigma_{\rm rms}$) to the center of our field of view (Figure 5.9). Because of its size ($\geq 13''$ across) and its irregular shape with multiple bulges, mm1 could be a cluster of multiple objects. North of mm1's peak flux is mm2, a partially-resolved object whose dust emission is extended from mm1. To the east, mm8 is a faint but distinct source that may also be associated with this group of objects.

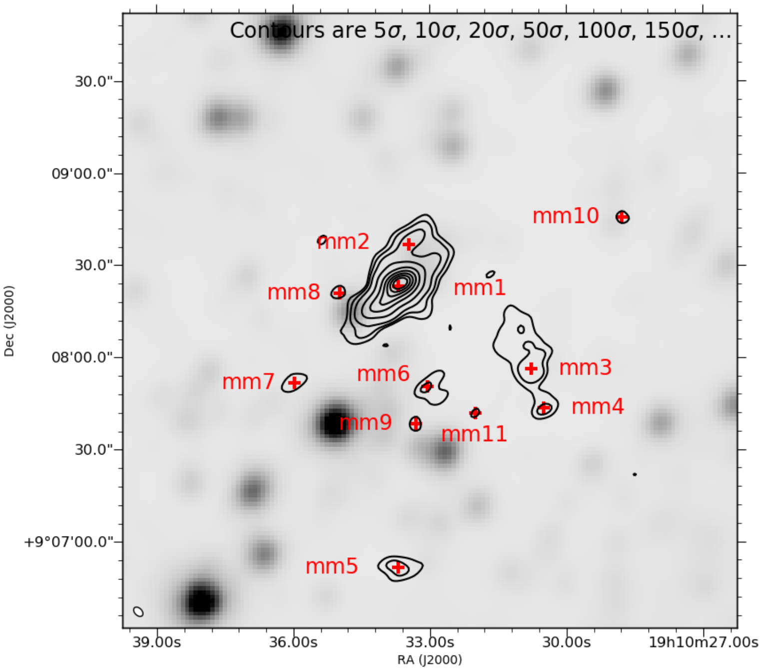

Figure 5.9: BGPS 6120 continuum at 245 GHz (1.2 mm, contours) over a WISE Band 1 (3.35 μm) image. Red crosses show the peak flux for each of the detected millimeter-wave (mm) emission objects. The synthesized beam is shown by the oval in the bottom left corner. The contour levels with respect to $\sigma_{\rm rms}$ are listed in the top right corner of each image. The synthesized beam and $\sigma_{\rm rms}$ are listed in Table 5.2.

To the southwest of the group encompassing mm1 is another emission source seeming to contain multiple substructures. In it, mm3 and mm4 are distinct, and there appear to be two more continuum sources in the northern part of this feature.

BGPS 6120 sees a sharp decline in recovered flux from 104% in a 40″-diameter aperture to 42% in a 120″ aperture. The bulk of the emission in BGPS 6120 comes from mm1, which has a detection significance of $364\sigma_{\rm rms}$ and is within 20″ of the pointing center. With a larger aperture, the next most extensive source of emission is the mm3 and mm4 conglomerate, which contribute significantly less flux and have peak fluxes that are $20\sigma_{\rm rms}$ and $13\sigma_{\rm rms}$, respectively, accounting for the steep decrease in recovered flux and pointing to large-scale structure enveloping these two groups of emission objects.

BGPS 6120 corresponds to a partially embedded cluster about 66″ across preliminarily characterized by Morales et al. (2013). There are also multiple reported YSOs and YSO candidates (Saral et al., 2015; Urquhart et al., 2018), among other types of emission, reported in this region. Saral et al. (2015) report a candidate asymptotic giant branch star (centered at $1^{\mathrm{h}}10^{\mathrm{m}}35\overset{\mathrm{s}}{.}06$ $+09°07'38\overset{\prime\prime}{.}8$), for which a distance has not been reported to our knowledge; thus it is not clear whether it is part of the partially embedded cluster reported by Morales et al. and in turn whether it would affect the objects in our survey.

The possibility of mm1 harboring multiple objects, as well as being related to mm2 and mm8, is best supported by the identification of five YSO candidates by Saral et al. (2015) that overlap with the mm1+2 complex. Two YSO candidates, a class I and a class II, are reported within $\sim 3''$ of the peak emission in mm1, and another class II candidate corresponds to mm2. The remaining YSO candidates are on opposite edges of the mm1 complex: one toward the southeastern edge and the other toward the northwest. Furthermore, Urquhart et al. (2011) report a YSO—also the site of a H_2O maser detection—centered northwest of mm1 and southwest of mm2 in what appears to be a partially-resolved continuum source. This possible source is not substantially distinguishable from mm1, and so we do not consider it a distinct source here.

In addition to (candidate) YSOs, the region surrounding mm1 is associated with submillimeter emission (e.g., Thompson et al., 2006; Urquhart et al., 2018), radio sources (e.g., Kurtz et al., 1994), and an H II region (e.g., Anderson et al., 2009).

Despite the complexity of the extended emission region encompassing mm3 and mm4, only one known object—a YSO reported toward mm3—has been reported toward this region (Urquhart et al., 2018). BGPS 6120 mm6 also possibly corresponds to a YSO, specifically a class I YSO candidate (Saral et al., 2015). Because they are faint and not associated with any known individual objects, we only tentatively identify mm9 and mm11 as millimeter sources.

The remaining BGPS 6120 objects are fairly isolated, with mm5 to the south, mm7 to the east of mm6 and southeast of mm1, and mm10 to the northwest. None of these sources are associated with any known objects, specifically within $50''$ for mm5 and mm10. Because mm5 is stronger than YSO candidate mm6, we are confident that it is in fact a real emission source. We only tentatively identify mm7 and mm10 as millimeter sources because they are are also faint objects without any known analogues in the literature.

We assume the detected objects toward BGPS 6120 lie at the Battisti & Heyer distance of 12.04 ± 2.72 kpc. This distance agrees with that of the partially embedded cluster detected in the direction of BGPS 6120, with Morales et al. reporting an

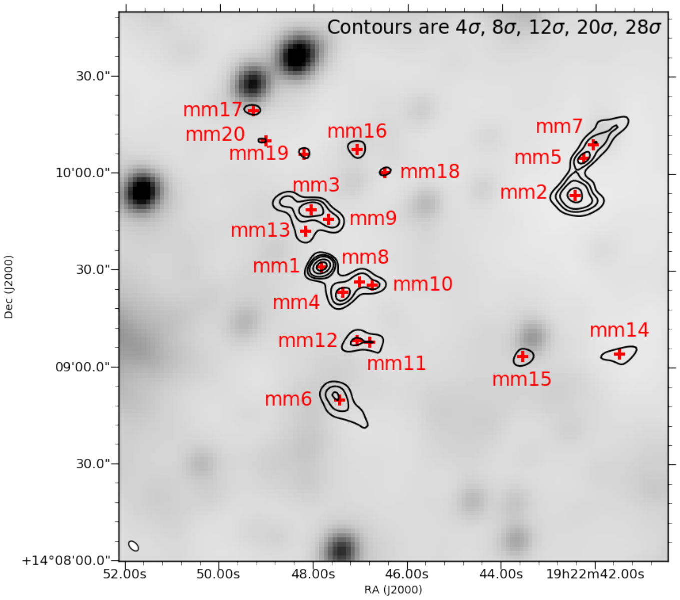

Figure 5.10: BGPS 6299 continuum at 245 GHz (1.2 mm, contours) over a WISE Band 1 (3.35 μm) image. Red crosses show the peak flux for each of the detected millimeter-wave (mm) emission objects. The synthesized beam is shown by the oval in the bottom left corner. The contour levels with respect to $\sigma_{\rm rms}$ are listed in the top right corner of each image. The synthesized beam and $\sigma_{\rm rms}$ are listed in Table 5.2.

unambiguous far distance of 11.40 ± 1.20 kpc. Similarly, Urquhart et al. (2018) report a YSO toward mm3 with a distance of 11.11 kpc. As far as we know, no near distances have been reported for objects detected in this region.

BGPS 6299

BGPS 6299 is a particularly complex target, with 20 millimeter sources detected in our field of view. The brightest sources are all grouped with at least two other distinguishable sources of millimeter emission. Near the center of our field of view are mm1, mm4, mm8, and mm10. North of this, mm9 and mm13, as well as another possible source (which we do not consider distinct in these data), surround mm3. Both of these groupings, along with mm6, mm11, and mm12, appear to follow a larger filamentary structure. To the northwest in our field of view is a third clump containing mm2, mm5, and mm7 following a linear structure that seems to be isolated from the other sources.

BGPS 6299 has decreasing flux recovery with larger aperture, meaning that most of the flux in our observations is concentrated on the same area as the peak flux listed in the BGPS catalogue. The recovered flux density in BGPS 6299 is still fairly low, decreasing from 17% to 11% flux recovery from a $40''$ to a $120''$ aperture. As seen in Figure 5.10, most of the brighter objects in this source are off-center and even toward the edges of the field of view (specifically mm2, mm5, and mm7), which perhaps explains the relatively low recovered fluxes. Nevertheless, mm1 and mm4 are still relatively close to the center of the image. The bulk of the emission in this source appears to follow a filament from mm17 in the north to mm6 in the south, which is supported by the significant amount of large-scale flux not recovered in these observations.

The brightest sources in BGPS 6299 all appear to be associated with previously reported YSOs or YSO candidates. Toward the mm1 group including mm4, mm8, and mm10, a YSO with a radius of $24''$ is reported to be centered about $6.4''$ to the northwest of mm1 (Urquhart et al., 2018), and just to the south of mm4 is a flat-spectrum YSO candidate (Saral et al., 2017). This area is also encompassed by a dense core of radius $55.3''$ that is centered just north of mm8 and mm10 and contains a H_2O maser detection (Svoboda et al., 2016). To the north of the mm1 grouping, a YSO candidate is centered on mm3 (Saral et al., 2017), and Kang et al. (2009) designate this as a “high-reliability” stage 0/I source.

Five YSOs or YSO candidates are associated with the group toward the northwest of our field of view, with one centered on mm2 and two centered in the emission extending to the northwest of mm7. Another YSO candidate has been reported to the south of mm2 (Saral et al., 2017), and the final YSO is centered to the northwest of mm2 and southwest of mm5 (Urquhart et al., 2014). This region also overlaps with a dense core of radius $71.3''$ reported to have a 1.00 probability of star formation and be the site of a H_2O maser (Urquhart et al., 2014; Svoboda et al., 2016).

The sources mm14 and mm15 are not associated with any known individual objects, however Saral et al. (2017) report a YSO candidate near mm14 to the northeast. The remaining sources—mm11, mm12, and mm6—are also not associated with any known individual sources but seem to be a part of a larger filamentary structure that encompasses the groups surrounding mm1 and mm3.

There are several YSO candidates near the the faint sources to the north—mm16, mm17, mm18, mm19, and mm20—but none of these millimeter sources are associated with any known individual objects in the literature.

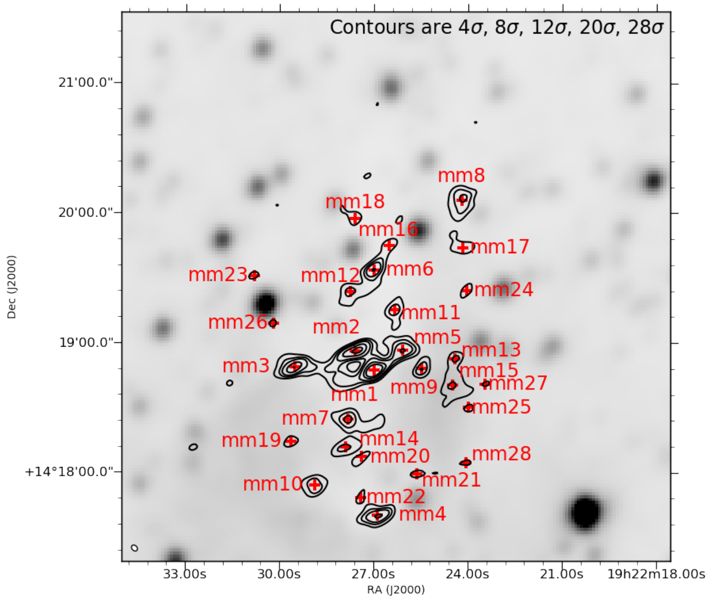

Figure 5.11: BGPS 6310 continuum at 245 GHz (1.2 mm, contours) over a WISE Band 1 (3.35 μm) image. Red crosses show the peak flux for each of the detected millimeter-wave (mm) emission objects. The synthesized beam is shown by the oval in the bottom left corner. The contour levels with respect to σ_{rms} are listed in the top right corner of each image. The synthesized beam and σ_{rms} are listed in Table 5.2.

Only near distances have been reported toward BGPS 6299, and so we adopt the Battisti & Heyer distance of 5.57 ± 1.25 kpc. This is on par with distances adopted by Urquhart et al. (2018, 5.3 kpc) and Ellsworth-Bowers et al. (2015, 4.72 kpc).

BGPS 6310

BGPS 6310, like BGPS 6299, is exceedingly complex with 28 millimeter emission sources detected. The most noteworthy of these are mm1, mm2, mm3, and mm5, all of which appear to be a part of an emission clump near the center of our field of view. In particular, mm1 and mm2 are part of a ring of emission surrounding a non-emitting bowl.

We recover relatively low flux toward BGPS 6310, with $\leq$10% of the flux recovered with all apertures. This is surprising because BGPS 6310 is perhaps our most complicated source, with 28 millimeter-wave emission objects detected, all of which are clustered fairly close together and not far off-center in the field of view. The five brightest sources are all south of center, but even in the larger-diameter apertures, only a small fraction of the flux is recovered. However, because of the close proximity of the BGPS 6310 objects, many of which are grouped together (e.g., mm1+mm2+mm3+mm5, mm6+mm12+mm16, mm13+mm15), it is likely that there is large-scale structure encompassing all of these objects that we are unable to recover with the ACA.

As shown in Figure 5.11, mm1 and mm2 are part of a ring of millimeter emission from which mm3 and mm5 appear to be extended. In the vicinity of this group, a YSO-bearing clump has been identified with a radius of 1.79 pc ($69\farcs6$ at a distance of 5.28 kpc, Urquhart et al. 2018). There is also a dense core associated with the region, for which Svoboda et al. (2016) report a 1.00 star formation probability for an object of radius $\sim 105''$ from 1.1 mm observations. Ellsworth-Bowers et al. (2015) also report a dense core approximately centered on mm1 with a similar radius of 2.64 pc, or $100''$ at their adopted distance of 5.37 kpc. These observations encompass much of the region in BGPS 6310 in which we detect 1.2 mm emission.

South of this region, a class I YSO has been reported to be centered on mm14 (Kang et al., 2009). Toward the center of mm12, another YSO has been reported (Saral et al., 2017). Northeast of mm6 is a class II YSO, however this YSO is reportedly in the foreground of W51 (Kang et al., 2009).

There are also a number of YSO candidates corresponding to our detections of millimeter sources in BGPS 6310 by Saral et al. (2017). These YSO candidates are northwest of mm4, east of mm7, east and north of mm8, and centered on mm24. There is also a YSO candidate that does not appear to be associated with any of our BGPS 6310 sources but is situated in the middle of mm12, mm23, and mm26.

The remaining sources, as far as we can tell, have no known individual counterparts in the literature. These sources are mm9, mm10, mm11, mm13, mm15 through mm22, mm25, mm27, and mm28.

We adopt the distance of 5.56 ± 0.86 kpc reported by Battisti & Heyer (2014). This distance is supported by Wienen et al. (2015) who resolve the distance ambiguity toward this region with a tangent solution, meaning there is only one solution instead of both a near and far distance, of 5.28 kpc. Urquhart et al. (2018) also adopt a distance of 5.28 kpc for the YSO-bearing clump detected in the vicinity of mm1+2+3+5, and Ellsworth-Bowers et al. (2015) assume a similar distance of 5.37 kpc.

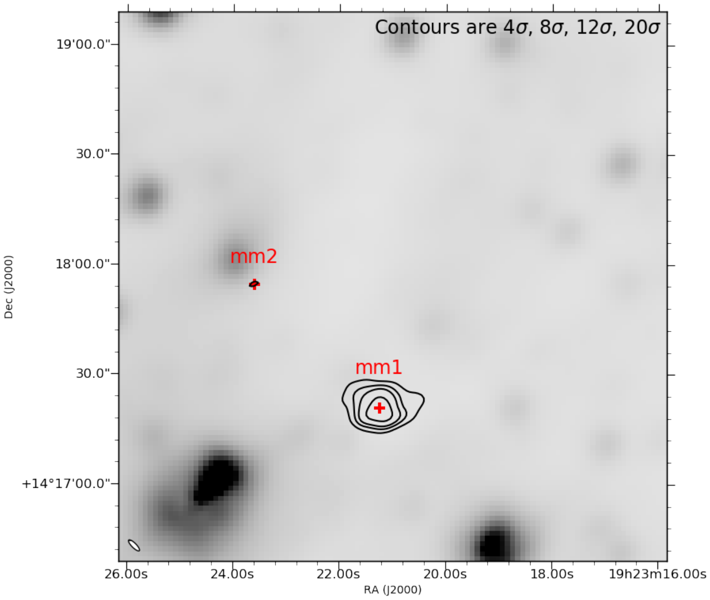

Figure 5.12: BGPS 6318 continuum at 245 GHz (1.2 mm, contours) over a WISE Band 1 (3.35 μm) image. Red crosses show the peak flux for each of the detected millimeter-wave (mm) emission objects. The synthesized beam is shown by the oval in the bottom left corner. The contour levels with respect to σ_{rms} are listed in the top right corner of each image. The synthesized beam and σ_{rms} are listed in Table 5.2.

BGPS 6318

BGPS 6318 has two detected millimeter emission sources shown in Figure 5.12. Most of the emission comes from mm1 which is in the southern half of our field of view. BGPS 6318 mm1 has some extended emission to the west but otherwise lacks evidence pointing toward it having unresolved substructure.

We recover <15% of the flux at all apertures for BGPS 6318. Virtually all of the flux we recover comes from mm1 to the south. Thus because the emission in these sources in our observations is concentrated away from the pointing center—i.e., the location of peak flux intensity in the BGPS catalogue—it is evident we have resolved out much of the large-scale structure in these ACA survey observations.

The extended mm1 source toward BGPS 6318 is associated with multiple objects in the literature, including a dark cloud (Peretto & Fuller, 2009; Peretto et al., 2016), a dense core (e.g., Ellsworth-Bowers et al., 2015; Svoboda et al., 2016), and a YSO (e.g., Urquhart et al., 2014, 2018; Wienen et al., 2015) and YSO candidate (Saral et al., 2017). Svoboda et al. (2016) report a 0.00 star-formation probability toward this region but with a radius of 63.8″; we detect emission toward mm1 over a diameter of only ∼20″ and so this zero-probability could be moot.

There have not been reports of any objects within 13″ of mm2.

Battisti & Heyer report a distance of 5.55 ± 1.06 kpc toward BGPS 6318, which we adopt. This is supported by Wienen et al. (2015), who also report a distance of 5.55 kpc (as a tangent, i.e., unambiguous, solution) for a YSO corresponding to mm1.

5.5 Far-infrared Images from Herschel

While this work focuses on millimeter (mm) emission toward the GMC targets, far-infrared data can also be telling about the nature of YSOs. In the context of astrochemistry, millimeter-wave (i.e., rotational) spectroscopy probes the molecular gas within YSOs whereas infrared (IR, i.e., vibrational) spectroscopy provides a glimpse into dust grains. As such, both millimeter-wave and IR observations are necessary for a holistic understanding of the chemistry in the early stages of star formation.

Figure 5.13 shows the continuum emission from Figures 5.2-5.12 plotted over images taken with the Herschel Photoconductor Array Camera and Spectrometer (PACS) at 70 μm. The Herschel images used had been processed with the `JScanam` map-maker code (Graciá-Carpio et al., 2017) and were acquired from the PACS Highly Processed Data Products (PHPDP) cutouts library in the NASA/IPAC Infrared Science Archive (IRSA).[3]

Table 5.4 lists the 14 ACA objects that overlap with 70 μm emission in Herschel PACS images. All of these correspond to YSOs or YSO candidates reported in the literature, representing about one-third of the total objects in this survey that are associated with YSOs.

The ice ($T \sim 20$ K) found on grain mantles radiates at near 100 μm (e.g., Boogert et al., 2000), and so the background PACS images in Figure 5.13 can provide clues to which objects presented here have observable ices for coupling observations of gas-phase and surface chemistry. Indeed, 70 μm emission has been used to trace cold dust in massive star-forming regions (e.g., Barlow et al., 2010; Whelan et al., 2011), as well as in the outer regions of debris disks (Morales et al., 2016). However, it has also been found that 70 μm does not necessarily trace cold dust exclusively;

---

[3] https://irsa.ipac.caltech.edu/data/Herschel/PHPDP/index_cutouts.html

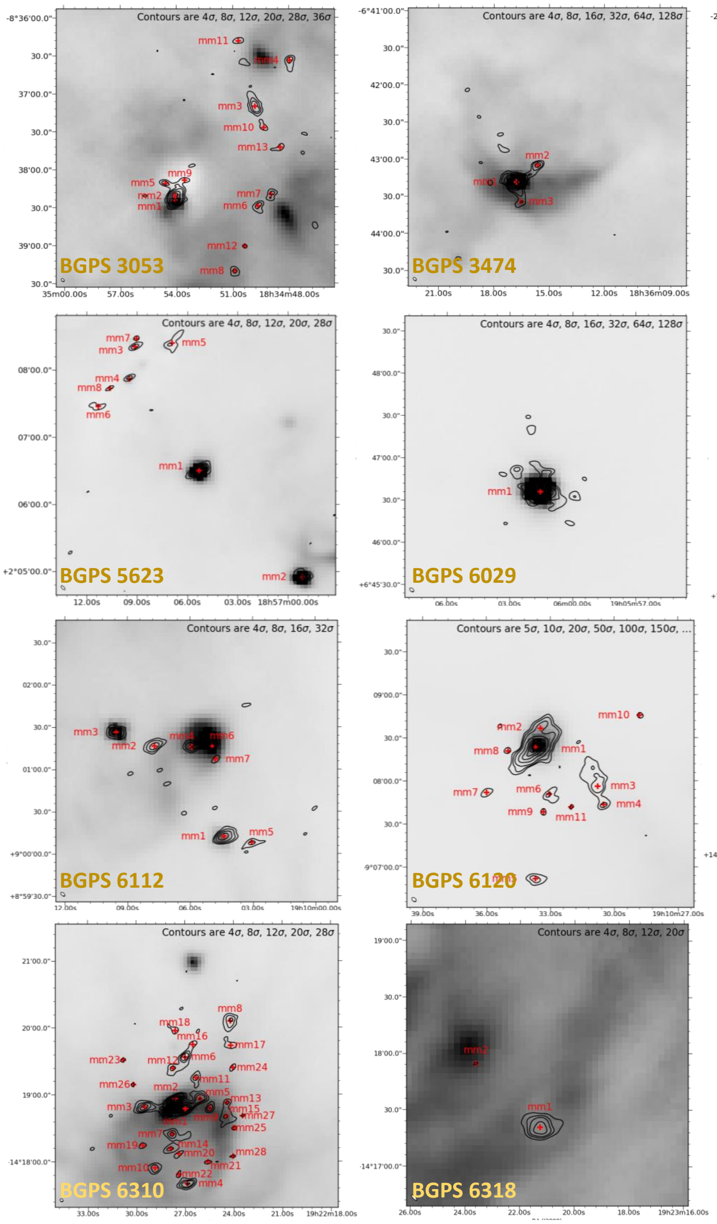

Figure 5.13: 1.2 mm ACA continuum emission of targeted GMCs plotted over Herschel PACS 70 μm images. The BGPS ID is in the bottom left corner of each image.

Table 5.4: Objects with overlapping 70 μm emission

Identifier	Corresponding YSO(s)
BGPS 3053 mm1	Embedded protostar[a]
BGPS 3474 mm1	Flat-spectrum YSO[b]
BGPS 4449 mm1	YSO[c,d]
BGPS 5623 mm1	High-mass YSO[e,f]
BGPS 5623 mm2	High-mass YSO[g]
BGPS 6029 mm1	YSO[h,i]
BGPS 6082 mm1	YSO[c,i]
BGPS 6112 mm1	YSO[g,j]
BGPS 6112 mm3	Class I YSO candidate[k]
BGPS 6112 mm4	Class II YSO[k]
BGPS 6112 mm6	2 YSO candidates[k]
BGPS 6120 mm1	5 YSO candidates[k]
BGPS 6299 mm7	2 YSO candidates[d]
BGPS 6310 mm1+2	YSO-bearing clump[g]

[a]Ragan et al. (2009); [b]Baug et al. (2016); [c]Urquhart et al. (2009); [d]Saral et al. (2017); [e]Rathborne et al. (2006); [f] Nguyen Luong et al. (2011); [g]Urquhart et al. (2018); [h]Svoboda et al. (2016); [i]Areal et al. (2018); [j]Urquhart et al. (2014); [k]Saral et al. (2015)

rather, 70 μm emission also traces the hot dust close-in to a protostar (e.g., Barlow et al., 2010; Hill et al., 2011). Toward BGPS 5623 mm1, for example, this emission has been attributed to hot dust close to the corresponding protostar (Nguyen Luong et al., 2011). In some observations of massive star-forming regions, it has also been used to differentiate between starless cores and YSOs, with 70 μm emission indicative of the latter (e.g., Bontemps et al., 2010; Könyves et al., 2010). Whether tracing icy dust grains or YSOs, 70 μm emission is a useful tool in identifying regions of star formation for further investigation.

5.6 Discussion

Many of the mm-emitting sources we detect correspond to objects included in previous large surveys, but to date, none of these sources have been studied in detail as far as we can tell. Of the 96 objects we resolve in this pilot survey, 41 are associated with known YSOs or YSO candidates.

Indeed, the level of complexity in the detected mm-emitting objects is generally unknown at present, but it is still nevertheless possible that these objects harbor multiple YSOs and other substructures. If we consider the Orion Kleinmann-Low (Orion KL) nebula, which is the archetype of high-mass star-forming regions at a

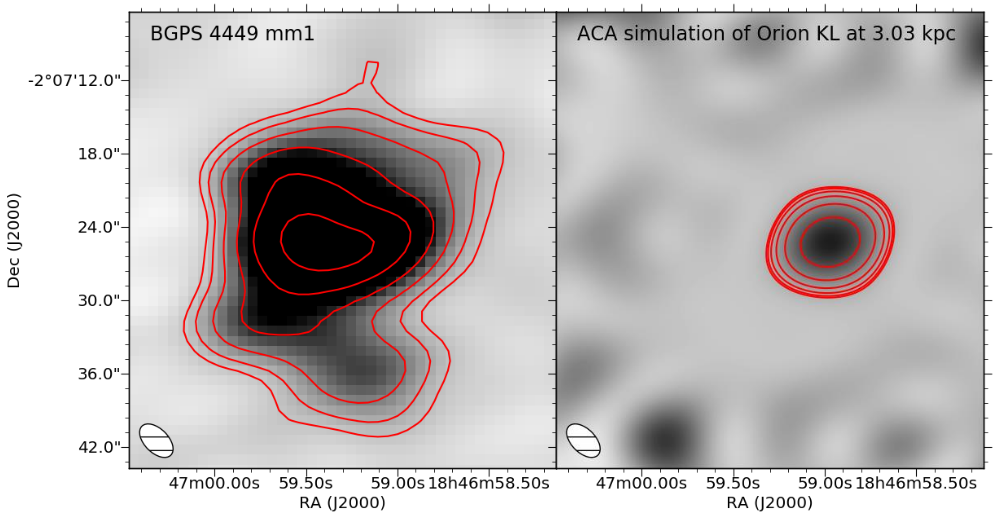

Figure 5.14: Continuum emission at 1.2 mm observed toward BGPS 4449 mm1 (left panel) with simulated observations of Orion KL but at $d \sim 3$ kpc with the ACA (right panel). The red contours are $4\sigma, 8\sigma, 16\sigma, 32\sigma, \ldots$ where $\sigma = 1.6$ mJy beam^{-1}. The ACA synthesized beam at 1.2 mm is shown in the bottom left of each panel.

distance of 388 ± 5 pc (Kounkel et al., 2017), we can get a sense of what types of complexity could be lurking in our sample. At 1.3 mm, the Orion KL continuum has a peak flux of 1.2 Jy beam^{-1} as observed by Pagani et al. (2017). If Orion KL were in fact ~3 kpc away, for instance toward BGPS 4449, and observed with the ACA, it would have an expected peak flux of about 300 mJy beam^{-1}, similar to that of BGPS 4449 mm1 (273.6 mJy beam^{-1}).

Moreover, even at 3 kpc away, Orion KL can still be detected if not resolved by the ACA. Figure 5.14 shows the resulting image of simulated ACA observations[4] toward Orion KL (right panel) but if it were located ~3 kpc away, toward BGPS 4449 mm1 (left panel). When observed normally, the substructures of Orion KL that make it notoriously complex—such as the hot core, the compact ridge, source I, source BN, and the northwest clump (e.g., Blake et al., 1987) shown if Figure 2.1—can be detected. In the simulated image, Orion KL has a diameter of ~10″, about half that of BGPS 4449 mm1, and individual emission features are smoothed out.

The existing literature on observations toward the vicinity of BGPS 4449 mm1

---

[4] ACA observations were simulated in `CASA` using the tasks *simobserve* and *simanalyze*. The model Orion KL FITS file used is from a ~2″ ALMA image (Project Code: 2013.1.01034.S).

supports the potential for this region to be complex, not unlike Orion KL. Like Orion KL, BGPS 4449 mm1 corresponds to the site of a massive outflow, and it potentially contains multiple young stellar objects. Specifically, Saral et al. (2017) report four YSO candidates, one of which was definitively labeled a YSO by Urquhart et al. (2009).

We can also consider regions like NGC 7538, an H II region at a distance of $d \sim 2.8$ kpc capable of producing high- and intermediate-mass stars (Blitz et al., 1982; Fallscheer et al., 2013). Imaging the 1.4 mm continuum emission toward NGC 7538 S with CARMA showed that the dust emission is dominated by an elliptical source of size $\sim 8'' \times 3''$ (Wright et al., 2012). Within this elliptical emission region, Wright et al. report three compact sources, a high-mass protostar and two YSOs in the early protostellar phase that are probable high-mass candidates. BGPS 4449 mm1 ($d \sim 3.0$ kpc) covers a larger area than NGC 7538 S with an approximate angular size of $20'' \times 20''$ at approximately the same distance. As such, it is reasonable to suspect that BGPS 4449 mm1 and other objects in our sample could have multiple YSOs at different evolutionary stages, which can only be divulged with future high-spatial-resolution studies.

By coupling the observations presented here with previous large surveys, we can begin to hone in on promising regions for future studies of the chemistry that takes place alongside high-mass star formation. For instance, this data set also includes molecular line data, which will be discussed in Chapter 6. As an example, we detect methanol in all but one of the GMCs presented here. Methanol is considered a tracer of complex organic molecules, and so it may help us identify which objects would be interesting subjects in future high-spatial-resolution observations of gas chemistry in high-mass YSOs.

Gas chemistry is thought to be intimately connected to the surface chemistry on grains, and so having a picture of the chemistry in ices is imperative for investigating this relationship observationally. However, studies that couple observations of gas and ice chemistry have been limited. While much of our understanding of the relationship between gas and grain chemistry comes from laboratory interstellar ice experiments and computational modeling, observations—specifically of isotopologues—can be used to test theories of chemical formation pathways in ice mantles (e.g., Charnley et al., 2004). Gibb et al. (2004) constrained the ice abundances for a number of simple molecules, including both CO_2 and $^{13}CO_2$, and more complex species, such as CH_3OH and CH_3CHO, in a range of embedded young stellar objects using near-IR spectra using the *Infrared Space Observatory* (ISO), and Öberg et al. (2011a) determined standard relative ice abundances of simple molecules in both low- and high-mass star-forming regions.

Far-IR emission can also provide clues about the presence of non-heated ice or hot dust in YSOs, which emits around 100 μm. We compare the 1.2 mm continuum emission observed by the ACA with 70 μm images obtained with Herschel PACS, in Figure 5.13. From these images, we find 14 places where reported YSOs or YSO candidates overlap with 70 μm emission, pointing to the presence of either icy mantles on the dust grains therein and, in turn, candidates for future studies of coupled gas and grain chemistry, or heated dust in towards a more evolved YSO.

We intend to couple these survey data and subsequent millimeter-wave observations of the gas-phase chemistry with infrared studies, e.g., with the JWST to constrain the ice compositions of the objects presented here and investigate the relationship between grain and gas chemistry in the molecular ring. Multi-wavelength studies will better divulge the source of far-IR emission as well as the nature of the objects from which such emission is observed.

5.7 Summary

We presented 96 millimeter (mm) sources detected toward 11 giant molecular clouds (GMCs) in 1.2 mm continuum emission using the Atacama Compact Array (ACA). The targeted GMCs were taken from the Bolocam Galactic Plane Survey (BGPS, Battisti & Heyer 2014) and screened for their potential to harbor regions of high-mass star formation for pilot 1.2 mm continuum observations of the Chemistry Alongside Massive Protostellar Objects (CAMPO) survey. The detected millimeter sources toward each GMC are presented in Table H.1 (Appendix H). For each millimeter source, we conducted a thorough literature search via SIMBAD to learn about corresponding objects in the literature.

In these pilot survey results, we find several gaps in our understanding of the targeted GMCs and the millimeter sources therein. First, there is uncertainty as to whether objects are located at near or far distances, or whether there are multiple objects at the same coordinates but different distances. Nevertheless, we (in some cases, tentatively) adopt the BGPS distances for all objects in 9 of our 11 target GMCs. The distance to millimeter sources in BGPS 3053 and BGPS 5623 is particularly ambiguous.

Second, H II regions and methanol masers are tracers of high-mass star formation, but low-frequency observations that target these types of emission have been limited. The 6.7 GHz methanol maser has been detected toward one source in our sample, BGPS 6029 mm1, indicative of a high-mass protostar early on in its evolution. H II regions have been identified toward several of our objects as well. Therefore, more complete characterization at multiple wavelengths is needed to better constrain the nature of the detected mm-emitting regions.

These pilot results are the first step toward increasing the sample size in which we observe the chemistry happening throughout high-mass star formation. Despite the gaps in our knowledge of the GMCs explored here, we can begin to identify candidates for future observational studies of intermediate- and high-mass star formation. By coupling these data with higher-spatial-resolution observations, e.g., with ALMA and JWST, we can begin to better understand the chemical processes in intermediate- and high-mass star-forming regions in the molecular ring.

Acknowledgements

This work makes use of the following ALMA data: ADS/JAO.ALMA#2018.1.01259. ALMA is a partnership of ESO (representing its member states), NSF (USA), and NINS (Japan), together with NRC (Canada), MOST and ASIAA (Tawain), and KASI (Republic of Korea), in cooperation with the Republic of Chile. The Joint ALMA Observatory is operated by ESO, AUI/NRAO, and NAOJ. The National Radio Astronomy Observatory (NRAO) is a facility of the National Science Foundation (NSF) operated under Associated Universities, Inc. (AUI). This publication also uses data products from the Wide-field Infrared Survey Explorer (WISE), which is a joint project of the University of California, Los Angeles, and the Jet Propulsion Laboratory / California Institute of Technology, funded by the National Aeronautics and Space Administration (NASA), as well as images from the ESA *Herschel Space Observatory*. WISE and Herschel images were obtained from the NASA/IPAC Infrared Science Archive, which is funded by the National Aeronautics and Space Administration and operated by the California Institute of Technology. This research has made use of the SIMBAD database, operated at CDS, Strasbourg, France (Wenger et al., 2000) and APLpy, an open-source plotting package for Python (Robitaille & Bressert, 2012; Robitaille, 2019).

Financial support for this work was provided through a National Science Foundation Graduate Research Fellowship under grant No. DGE-1144469 and through the NSF AAG (AST-1514918) and NASA Astrobiology (NNX15AT33A) and Exoplanet

Research (XRP, NNX16AB48G) programs. This work benefited from discussions with Klaus Pontoppidan, Cam Buzard, Nicole Wallack, and Sadie Dutton. We thank Sarah Wood, Melissa Hoffman, and the NRAO North American ALMA Science Center (NAASC) for their assistance with the data reduction.

Facilities: ALMA, IRSA, WISE, Herschel
Software: CASA (McMullin et al., 2007), CDMS (Müller et al., 2001), SIMBAD (Wenger et al., 2000), APLpy (Robitaille & Bressert, 2012; Robitaille, 2019)

References

Anderson, L. D., Bania, T. M., Jackson, J. M., et al. 2009, *Astrophys. J. Supp.*, 181, 255, doi: `10.1088/0067-0049/181/1/255`

Araya, E., Hofner, P., Kurtz, S., Bronfman, L., & DeDeo, S. 2005, *Astrophys. J. Supp.*, 157, 279, doi: `10.1086/427187`

Areal, M. B., Paron, S., Celis Peña, M., & Ortega, M. E. 2018, *Astron. Astrophys.*, 612, A117, doi: `10.1051/0004-6361/201732067`

Argon, A. L., Reid, M. J., & Menten, K. M. 2000, *Astrophys. J. Supp.*, 129, 159, doi: `10.1086/313406`

Barlow, M. J., Krause, O., Swinyard, B. M., et al. 2010, *Astron. Astrophys.*, 518, L138, doi: `10.1051/0004-6361/201014585`

Battisti, A. J., & Heyer, M. H. 2014, *Astrophys. J.*, 780, 173, doi: `10.1088/0004-637X/780/2/173`

Baug, T., Dewangan, L. K., Ojha, D. K., & Ninan, J. P. 2016, *Astrophys. J.*, 833, 85, doi: `10.3847/1538-4357/833/1/85`

Becker, R. H., White, R. L., Helfand, D. J., & Zoonematkermani, S. 1994, *Astrophys. J. Supp.*, 91, 347, doi: `10.1086/191941`

Beuther, H., Schilke, P., Menten, K. M., et al. 2002, *Astrophys. J.*, 566, 945, doi: `10.1086/338334`

Blake, G. A., Sutton, E. C., Masson, C. R., & Phillips, T. G. 1987, *Astrophys. J.*, 315, 621, doi: `10.1086/165165`

Blitz, L., Fich, M., & Stark, A. A. 1982, *Astrophys. J. Supp.*, 49, 183, doi: `10.1086/190795`

Bontemps, S., André, P., Könyves, V., et al. 2010, *Astron. Astrophys.*, 518, L85, doi: `10.1051/0004-6361/201014661`

Boogert, A. C. A., Ehrenfreund, P., Gerakines, P. A., et al. 2000, *Astron. Astrophys.*, 353, 349. `https://arxiv.org/abs/astro-ph/9909477`

Carlhoff, P., Nguyen Luong, Q., Schilke, P., et al. 2013, *Astron. Astrophys.*, 560, A24, doi: `10.1051/0004-6361/201321592`

Caswell, J. L., Vaile, R. A., Ellingsen, S. P., Whiteoak, J. B., & Norris, R. P. 1995, *Mon. Not. R. Astron. Soc.*, 272, 96, doi: `10.1093/mnras/272.1.96`

Charnley, S. B., Ehrenfreund, P., Millar, T. J., et al. 2004, *Mon. Not. R. Astron. Soc.*, 347, 157, doi: `10.1111/j.1365-2966.2004.07188.x`

Codella, C., Palumbo, G. G. C., Pareschi, G., et al. 1995, *Mon. Not. R. Astron. Soc.*, 276, 57, doi: `10.1093/mnras/276.1.57`

Csengeri, T., Urquhart, J. S., Schuller, F., et al. 2014, *Astron. Astrophys.*, 565, A75, doi: `10.1051/0004-6361/201322434`

Di Francesco, J., Johnstone, D., Kirk, H., MacKenzie, T., & Ledwosinska, E. 2008, *Astrophys. J. Supp.*, 175, 277, doi: `10.1086/523645`

Ellsworth-Bowers, T. P., Glenn, J., Riley, A., et al. 2015, *Astrophys. J.*, 805, 157, doi: `10.1088/0004-637X/805/2/157`

Evans, Neal J., I., Dunham, M. M., Jørgensen, J. K., et al. 2009, *Astrophys. J. Supp.*, 181, 321, doi: `10.1088/0067-0049/181/2/321`

Fallscheer, C., Reid, M. A., Di Francesco, J., et al. 2013, *Astrophys. J.*, 773, 102, doi: `10.1088/0004-637X/773/2/102`

Fontani, F., Busquet, G., Palau, A., et al. 2015, *Astron. Astrophys.*, 575, A87, doi: `10.1051/0004-6361/201424753`

Fontani, F., Sakai, T., Furuya, K., et al. 2014, *Mon. Not. R. Astron. Soc.*, 440, 448, doi: `10.1093/mnras/stu298`

Gaia Collaboration. 2018, *VizieR Online Data Catalog*, I/345

Gibb, E. L., Whittet, D. C. B., Boogert, A. C. A., & Tielens, A. G. G. M. 2004, *Astrophys. J. Supp.*, 151, 35, doi: `10.1086/381182`

Goldsmith, P. F., & Langer, W. D. 1999, *Astrophys. J.*, 517, 209, doi: `10.1086/307195`

Graciá-Carpio, J., Wetzstein, M., Roussel, H., & PACS Instrument Control Centre Team. 2017, in Astronomical Society of the Pacific Conference Series, Vol. 512, Astronomical Data Analysis Software and Systems XXV, ed. N. P. F. Lorente, K. Shortridge, & R. Wayth, 379

Greene, T. P., Wilking, B. A., Andre, P., Young, E. T., & Lada, C. J. 1994, *Astrophys. J.*, 434, 614, doi: `10.1086/174763`

Herbst, E., & van Dishoeck, E. F. 2009, *Annu. Rev. Astron. Astrophys.*, 47, 427, doi: `10.1146/annurev-astro-082708-101654`

Hill, T., Burton, M. G., Minier, V., et al. 2005, *Mon. Not. R. Astron. Soc.*, 363, 405, doi: `10.1111/j.1365-2966.2005.09347.x`

Hill, T., Pinte, C., Minier, V., Burton, M. G., & Cunningham, M. R. 2009, *Mon. Not. R. Astron. Soc.*, 392, 768, doi: `10.1111/j.1365-2966.2008.14103.x`

Hill, T., Thompson, M. A., Burton, M. G., et al. 2006, *Mon. Not. R. Astron. Soc.*, 368, 1223, doi: `10.1111/j.1365-2966.2006.10220.x`

Hill, T., Motte, F., Didelon, P., et al. 2011, *Astron. Astrophys.*, 533, A94, doi: `10.1051/0004-6361/201117315`

Jones, B. M., Fuller, G. A., Breen, S. L., et al. 2020, *Mon. Not. R. Astron. Soc.*, 493, 2015, doi: `10.1093/mnras/staa233`

Kanarek, G., Shara, M., Faherty, J., Zurek, D., & Moffat, A. 2015, *Mon. Not. R. Astron. Soc.*, 452, 2858, doi: `10.1093/mnras/stv1342`

Kang, M., Bieging, J. H., Povich, M. S., & Lee, Y. 2009, *Astrophys. J.*, 706, 83, doi: `10.1088/0004-637X/706/1/83`

Katsuta, J., Uchiyama, Y., & Funk, S. 2017, *Astrophys. J.*, 839, 129, doi: `10.3847/1538-4357/aa6aa3`

Kolpak, M. A., Jackson, J. M., Bania, T. M., Clemens, D. P., & Dickey, J. M. 2003, *Astrophys. J.*, 582, 756, doi: `10.1086/344752`

Kong, S., Tan, J. C., Caselli, P., et al. 2017, *Astrophys. J.*, 834, 193, doi: `10.3847/1538-4357/834/2/193`

Könyves, V., André, P., Men'shchikov, A., et al. 2010, *Astron. Astrophys.*, 518, L106, doi: `10.1051/0004-6361/201014689`

Kounkel, M., Hartmann, L., Loinard, L., et al. 2017, *Astrophys. J.*, 834, 142, doi: `10.3847/1538-4357/834/2/142`

Kurtz, S., Churchwell, E., & Wood, D. O. S. 1994, *Astrophys. J. Supp.*, 91, 659, doi: `10.1086/191952`

Lansbury, G. B., Stern, D., Aird, J., et al. 2017, *Astrophys. J.*, 836, 99, doi: `10.3847/1538-4357/836/1/99`

Liu, M., Tan, J. C., Cheng, Y., & Kong, S. 2018a, *Astrophys. J.*, 862, 105, doi: `10.3847/1538-4357/aacb7c`

Liu, T., Li, P. S., Juvela, M., et al. 2018b, *Astrophys. J.*, 859, 151, doi: `10.3847/1538-4357/aac025`

Lu, X., Zhang, Q., Liu, H. B., Wang, J., & Gu, Q. 2014, *Astrophys. J.*, 790, 84, doi: `10.1088/0004-637X/790/2/84`

Matthews, H., Kirk, H., Johnstone, D., et al. 2009, *Astron. J.*, 138, 1380, doi: `10.1088/0004-6256/138/5/1380`

McMullin, J. P., Waters, B., Schiebel, D., Young, W., & Golap, K. 2007, Astronomical Society of the Pacific Conference Series, Vol. 376, CASA Architecture and Applications, ed. R. A. Shaw, F. Hill, & D. J. Bell, 127

Merello, M., Evans, Neal J., I., Shirley, Y. L., et al. 2015, *Astrophys. J. Supp.*, 218, 1, doi: `10.1088/0067-0049/218/1/1`

Morales, E. F. E., Wyrowski, F., Schuller, F., & Menten, K. M. 2013, *Astron. Astrophys.*, 560, A76, doi: `10.1051/0004-6361/201321626`

Morales, F. Y., Bryden, G., Werner, M. W., & Stapelfeldt, K. R. 2016, *Astrophys. J.*, 831, 97, doi: `10.3847/0004-637X/831/1/97`

Motte, F., Bontemps, S., & Louvet, F. 2018, *Annu. Rev. Astron. Astrophys.*, 56, 41, doi: `10.1146/annurev-astro-091916-055235`

Müller, H. S. P., Thorwirth, S., Roth, D. A., & Winnewisser, G. 2001, *Astron. Astrophys.*, 370, L49, doi: `10.1051/0004-6361:20010367`

Murata, Y., Kawabe, R., Ishiguro, M., et al. 1992, *Publ. Astron. Soc. Jpn.*, 44, 381

Nguyen Luong, Q., Motte, F., Hennemann, M., et al. 2011, *Astron. Astrophys.*, 535, A76, doi: `10.1051/0004-6361/201117831`

Nguyen-Q-Rieu, Nakai, N., & Jackson, J. M. 1989, *Astron. Astrophys.*, 220, 57

Öberg, K. I., Boogert, A. C. A., Pontoppidan, K. M., et al. 2011a, *Astrophys. J.*, 740, 109, doi: `10.1088/0004-637x/740/2/109`

Öberg, K. I., Lauck, T., & Graninger, D. 2014, *Astrophys. J.*, 788, 68, doi: `10.1088/0004-637X/788/1/68`

Öberg, K. I., van der Marel, N., Kristensen, L. E., & van Dishoeck, E. F. 2011b, *Astrophys. J.*, 740, 14, doi: `10.1088/0004-637X/740/1/14`

Pagani, L., Favre, C., Goldsmith, P. F., et al. 2017, *Astron. Astrophys.*, 604, A32, doi: `10.1051/0004-6361/201730466`

Pankonin, V., Churchwell, E., Watson, C., & Bieging, J. H. 2001, *Astrophys. J.*, 558, 194, doi: `10.1086/322249`

Peretto, N., & Fuller, G. A. 2009, *Astron. Astrophys.*, 505, 405, doi: `10.1051/0004-6361/200912127`

Peretto, N., Lenfestey, C., Fuller, G. A., et al. 2016, *Astron. Astrophys.*, 590, A72, doi: `10.1051/0004-6361/201527064`

Ragan, S. E., Bergin, E. A., & Gutermuth, R. A. 2009, *Astrophys. J.*, 698, 324, doi: `10.1088/0004-637X/698/1/324`

Ragan, S. E., Bergin, E. A., Plume, R., et al. 2006, *Astrophys. J. Supp.*, 166, 567, doi: `10.1086/506594`

Rathborne, J. M., Jackson, J. M., Chambers, E. T., et al. 2010, *Astrophys. J.*, 715, 310, doi: `10.1088/0004-637X/715/1/310`

Rathborne, J. M., Jackson, J. M., & Simon, R. 2006, *Astrophys. J.*, 641, 389, doi: `10.1086/500423`

Robitaille, T. 2019, APLpy v2.0: The Astronomical Plotting Library in Python, doi: `10.5281/zenodo.2567476`

Robitaille, T., & Bressert, E. 2012, APLpy: Astronomical Plotting Library in Python, Astrophysics Source Code Library. `http://ascl.net/1208.017`

Rosolowsky, E., Dunham, M. K., Ginsburg, A., et al. 2010, *Astrophys. J. Supp.*, 188, 123, doi: `10.1088/0067-0049/188/1/123`

Rygl, K. L. J., Wyrowski, F., Schuller, F., & Menten, K. M. 2010, *Astron. Astrophys.*, 515, A42, doi: `10.1051/0004-6361/200913510`

Sanders, D. B., Solomon, P. M., & Scoville, N. Z. 1984, *Astrophys. J.*, 276, 182, doi: `10.1086/161602`

Saral, G., Hora, J. L., Willis, S. E., et al. 2015, *Astrophys. J.*, 813, 25, doi: `10.1088/0004-637X/813/1/25`

Saral, G., Hora, J. L., Audard, M., et al. 2017, *Astrophys. J.*, 839, 108, doi: `10.3847/1538-4357/aa6575`

Scoville, N. Z., & Solomon, P. M. 1975, *Astrophys. J. Lett.*, 199, L105, doi: `10.1086/181859`

Su, Y., Zhang, S., Shao, X., & Yang, J. 2015, *Astrophys. J.*, 811, 134, doi: `10.1088/0004-637X/811/2/134`

Svoboda, B. E., Shirley, Y. L., Battersby, C., et al. 2016, *Astrophys. J.*, 822, 59, doi: `10.3847/0004-637X/822/2/59`

Teng, Y.-H., & Hirano, N. 2020, *Astrophys. J.*, 893, 63, doi: `10.3847/1538-4357/ab7cca`

Thompson, M. A., Hatchell, J., Walsh, A. J., MacDonald, G. H., & Millar, T. J. 2006, *Astron. Astrophys.*, 453, 1003, doi: `10.1051/0004-6361:20054383`

Urquhart, J. S., Hoare, M. G., Purcell, C. R., et al. 2009, *Astron. Astrophys.*, 501, 539, doi: `10.1051/0004-6361/200912108`

Urquhart, J. S., Morgan, L. K., Figura, C. C., et al. 2011, *Mon. Not. R. Astron. Soc.*, 418, 1689, doi: `10.1111/j.1365-2966.2011.19594.x`

Urquhart, J. S., Csengeri, T., Wyrowski, F., et al. 2014, *Astron. Astrophys.*, 568, A41, doi: `10.1051/0004-6361/201424126`

Urquhart, J. S., König, C., Giannetti, A., et al. 2018, *Mon. Not. R. Astron. Soc.*, 473, 1059, doi: `10.1093/mnras/stx2258`

van der Tak, F. F. S., van Dishoeck, E. F., & Caselli, P. 2000a, *Astron. Astrophys.*, 361, 327. `https://arxiv.org/abs/astro-ph/0008010`

van der Tak, F. F. S., van Dishoeck, E. F., Evans, Neal J., I., & Blake, G. A. 2000b, *Astrophys. J.*, 537, 283, doi: `10.1086/309011`

van der Walt, D. J., Gaylard, M. J., & MacLeod, G. C. 1995, *Astron. Astrophys. Supp.*, 110, 81

van Dishoeck, E. F., & Blake, G. A. 1998, *Annu. Rev. Astron. Astrophys.*, 36, 317, doi: `10.1146/annurev.astro.36.1.317`

Veneziani, M., Elia, D., Noriega-Crespo, A., et al. 2013, *Astron. Astrophys.*, 549, A130, doi: `10.1051/0004-6361/201219570`

Wenger, M., Ochsenbein, F., Egret, D., et al. 2000, *Astron. Astrophys. Supp.*, 143, 9, doi: `10.1051/aas:2000332`

Whelan, D. G., Johnson, K. E., Whitney, B. A., Indebetouw, R., & Wood, K. 2011, *Astrophys. J.*, 729, 111, doi: `10.1088/0004-637X/729/2/111`

Wienen, M., Wyrowski, F., Schuller, F., et al. 2012, *Astron. Astrophys.*, 544, A146, doi: `10.1051/0004-6361/201118107`

Wienen, M., Wyrowski, F., Menten, K. M., et al. 2015, *Astron. Astrophys.*, 579, A91, doi: `10.1051/0004-6361/201424802`

Wood, D. O. S., & Churchwell, E. 1989, *Astrophys. J. Supp.*, 69, 831, doi: `10.1086/191329`

Wood, D. O. S., Churchwell, E., & Salter, C. J. 1988, *Astrophys. J.*, 325, 694, doi: `10.1086/166040`

Wright, M., Zhao, J.-H., Sandell, G., et al. 2012, *Astrophys. J.*, 746, 187, doi: `10.1088/0004-637X/746/2/187`

Yang, A. Y., Thompson, M. A., Urquhart, J. S., & Tian, W. W. 2018, *Astrophys. J. Supp.*, 235, 3, doi: `10.3847/1538-4365/aaa297`

Zhang, C.-P., Yuan, J.-H., Li, G.-X., Zhou, J.-J., & Wang, J.-J. 2017, *Astron. Astrophys.*, 598, A76, doi: `10.1051/0004-6361/201629771`

Zoonematkermani, S., Helfand, D. J., Becker, R. H., White, R. L., & Perley, R. A. 1990, *Astrophys. J. Supp.*, 74, 181, doi: `10.1086/191496`

Chapter 6

CHEMISTRY ALONGSIDE MASSIVE PROTOSTELLAR OBJECTS: PILOT SURVEY RESULTS

6.1 Introduction

Much of what is known about chemistry in star-forming regions comes from observations of nearby low-mass objects and a handful of more distant, exceptionally bright molecular sources. The so-called molecular ring, which falls at radii of ~4-8 kpc from the galactic center, has been mostly absent from astrochemical observations thus far despite containing the bulk of molecular matter in the Milky Way. Scoville & Solomon (1975) found that the surface density of giant H II regions along the galactic equator is highest between 4 and 8 kpc and that it peaks at ~6 kpc. Within this molecular ring, an estimated 85% of the gas is molecular (Sanders et al., 1984). This suggests that much of our understanding of interstellar chemistry neglects the regions of our galaxy where a substantial portion of molecular chemistry proceeds.

Here, we present the pilot results of a molecular line survey carried out toward an unbiased sample of 11 giant molecular clouds (GMCs) in the molecular ring using the Atacama Compact Array (ACA). This work addresses a subset of the continuum emission regions presented in Chapter 5; the sample and observations are presented in Sections 5.2 and 5.2, respectively. Section 6.2 describes the chemical inventory identified from the ACA spectra. Derived methanol (CH_3OH) abundances and temperatures are presented in Section 6.3, and Section 6.4 discusses the assumptions made for these calculations. The results of this pilot survey are discussed in Section 6.6; specifically, the chemistry in the molecular-ring GMCs is discussed in the context of previous studies and open questions in astrochemistry. The work and the implications for future observations are briefly summarized in Section 6.7.

6.2 Spectral Analysis

The spectra of each GMC target were inspected to compile a preliminary census of molecular compounds present in each source. Figure 6.1 shows an example spectrum for BGPS 6120, which is one of the most chemically rich targets in our sample. A variety of compounds were detected across the sample, including carbon monoxide (CO, $C^{18}O$), complex (having ≥6 atoms) organic compounds (CH_3OH, CH_3CCH), ionized species ($H^{13}CO^+$, $HC^{18}O^+$, HCS^+), nitrogen-bearing

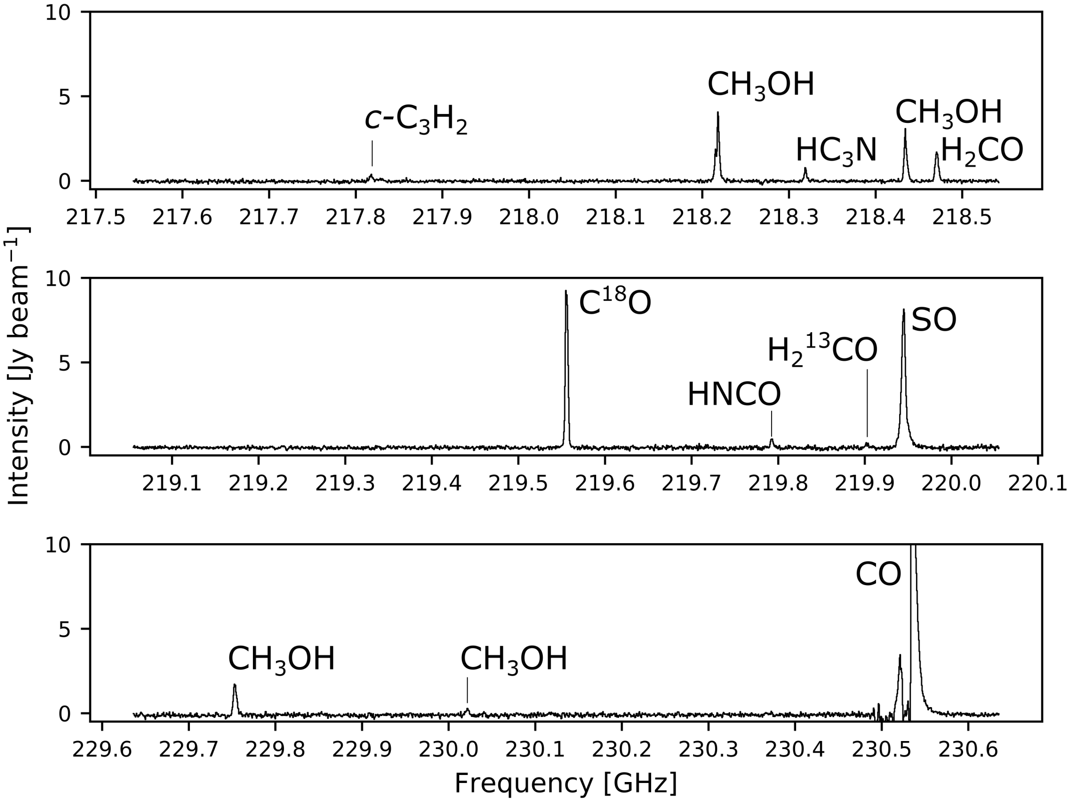

Figure 6.1: ACA “lower” Band 6 spectra for BGPS 6120.

species (HC_3N), oxygen-bearing species (H_2CO, $H_2{}^{13}CO$), low gas density tracers (c-C_3H_2), grain chemistry tracers (HNCO), and compounds formed in outflows (SO, ^{33}SO, ^{34}SO, SO_2, SiO). Table 6.1 summarizes the GMCs where these compounds are detected.

As seen in Table 6.1, BGPS 6029 and BGPS 6120 are particularly molecule-rich from this limited spectral line survey. BGPS 6318 is particularly molecule-poor, containing detectable CO and $C^{18}O$ emission only. For most compounds, only one line was present in our data. Several GMCs (BGPS 6029 and BGPS 6120) contain two lines of SO.

All sources except BGPS 6318 contain detectable CH_3OH and $C^{18}O$ emission concentrated around regions of continuum emission. These sources also contain H_2CO, $H^{13}CO^+$, and SO. In this work, we focus on CH_3OH because multiple CH_3OH transitions are present in our data, allowing us to get a preliminary look at the gas temperature via line fitting. Furthermore, CH_3OH is a hallmark of hot

Table 6.1: Compounds with at least one line detected toward the target GMCs

	BGPS ID										
Compound	3053	3474	4449	5623	6029	6082	6112	6120	6299	6310	6318
CO	X	X	X	X	X	X	X	X	X	X	X
$C^{18}O$	X	X	X	X	X	X	X	X	X	X	X
SiO				X	X		X	X			
SO	X	X	X	X	X	X	X	X	X	X	
^{33}SO								X			
^{34}SO					X						
SO_2					X			X			
HCS^+					X			X			
$H^{13}CO^+$	X	X	X	X	X	X	X	X	X	X	
$HC^{18}O^+$					X			X			
H_2CO	X	X	X	X	X	X	X	X	X	X	
$H_2{}^{13}CO$		X			X		X				
c-C_3H_2	X	X	X	X	X				X		
CH_3CCH			X					X			
CH_3OH	X	X	X	X	X	X	X	X	X	X	
HNCO		X			X			X			
HC_3N		X			X						

Table 6.2: Molecular emission regions and their corresponding mm-emitting objects

BGPS ID	ACA# ID	mm# ID
3053	ACA1	mm1+2
	ACA2	mm6+7
3474	ACA1	mm1
4449	ACA1	mm1
	ACA2	mm2
5623	ACA1	mm1
6029	ACA1	mm1
6112	ACA1	mm1
	ACA2	mm2
	ACA3	mm4
6120	ACA1	mm1
6299	ACA1	mm2+5+7
6310	ACA1	mm1
6310	ACA2	mm4

molecular cores, signalling places where there may be new molecular-ring organic chemistry laboratories.

Figure 6.2 shows the regions where we see both $C^{18}O$ (a tracer of dense regions, such as dense cores) and CH_3OH (a tracer of other complex organics). In the figure, each panel is labeled by its BGPS ID and an ACA# ID. For GMCs with multiple millimeter-emitting regions shown, the # was assigned by decreasing peak continuum flux. The corresponding mm# IDs used in Chapter 5 are given in Table 6.2 for each ACA# ID.

6.3 CH_3OH Abundances and Temperatures

Figures 6.3-6.11 show the derived rotation temperature $T_{\rm rot}$ and column density $N_{\rm tot}$ maps for CH_3OH toward nine of the 11 target GMCs. Each map shows the entire ACA field of view (listed in Table 5.2) for each target. As mentioned in Section 6.2, BGPS 6318 did not contain CH_3OH emission. BGPS 6082 is also not represented in the figures because the lines in those spectra were too noisy to be fit successfully. Percent propagated uncertainty maps are presented in Appendix I and show that most fitted objects have fit uncertainties of $\leq$10% near the cospatial continuum emission peak.

The rotation temperature and column density were derived using a pixel-by-pixel fit of the spectra extracted within a single synthesized beam centered on each pixel. This follows the same procedure as Wilkins et al. (2022), which is also

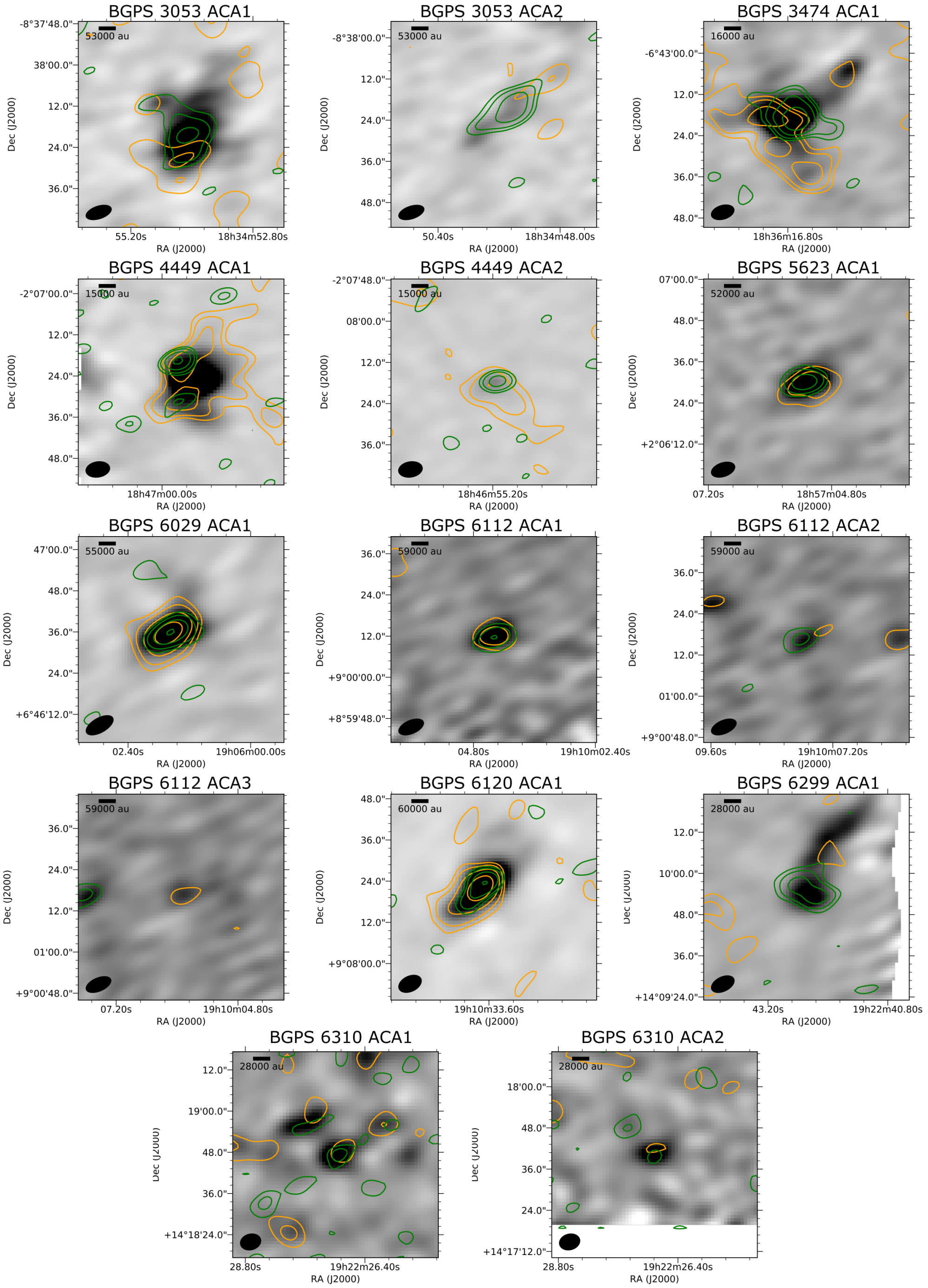

Figure 6.2: Contours showing the distribution of $C^{18}O$ (orange) and CH_3OH (green) emission in the millimeter sources. The greyscale images show the Band 6 (~240 GHz) continuum.

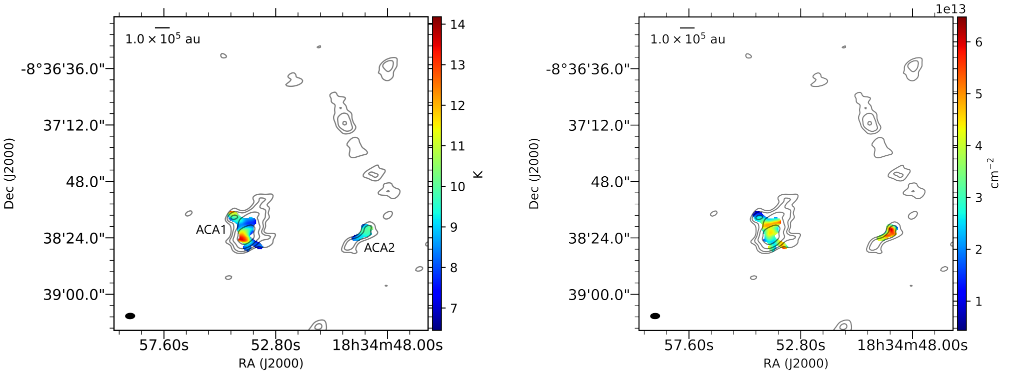

Figure 6.3: Derived rotation temperature (left) and column density (right) for CH_3OH in BGPS 3053. Contours show the continuum from Figure 5.2.

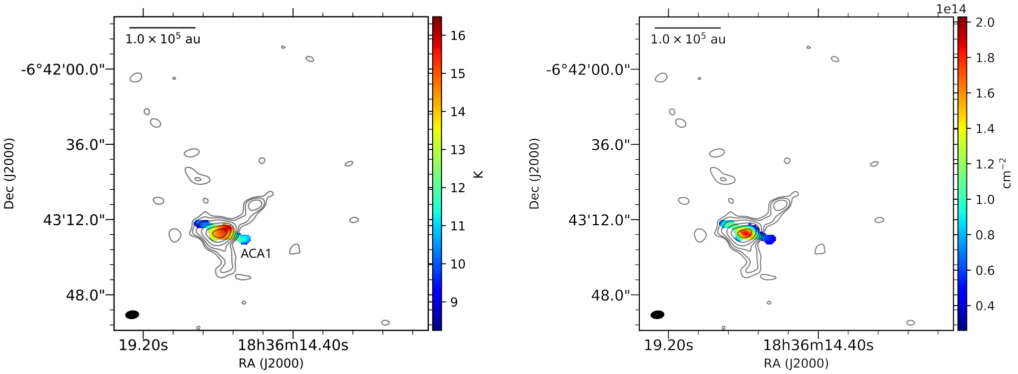

Figure 6.4: Derived rotation temperature (left) and column density (right) for CH_3OH in BGPS 3474. Contours show the continuum from Figure 5.3.

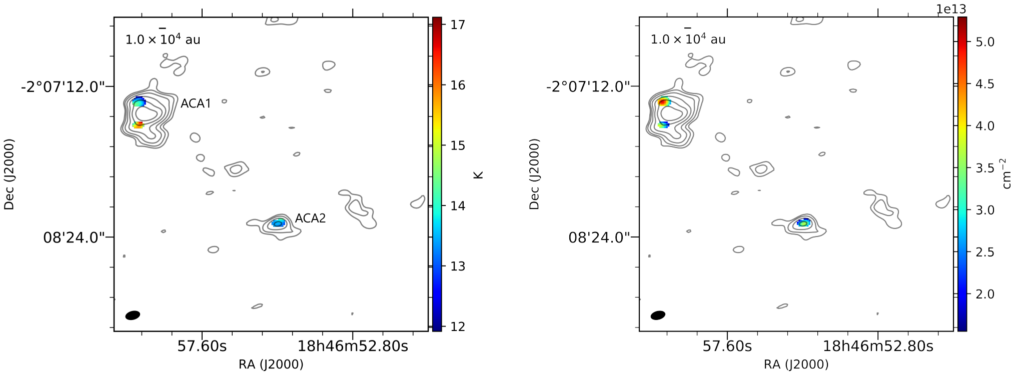

Figure 6.5: Derived rotation temperature (left) and column density (right) for CH_3OH in BGPS 4449. Contours show the continuum from Figure 5.4.

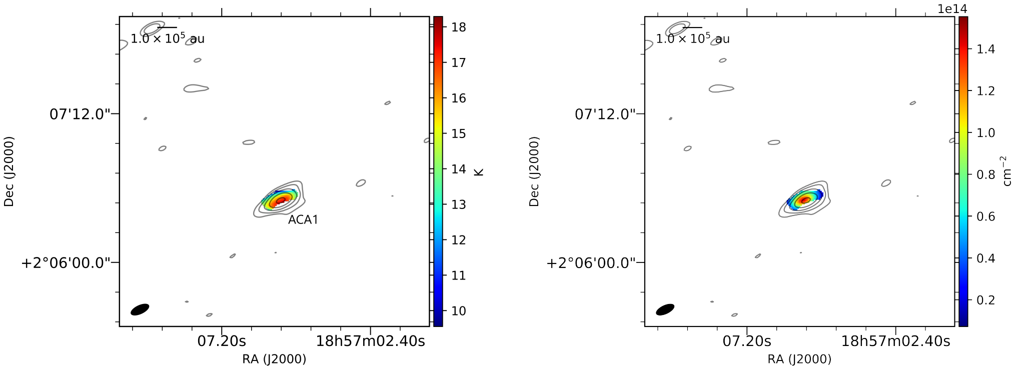

Figure 6.6: Derived rotation temperature (left) and column density (right) for CH_3OH in BGPS 5623. Contours show the continuum from Figure 5.5.

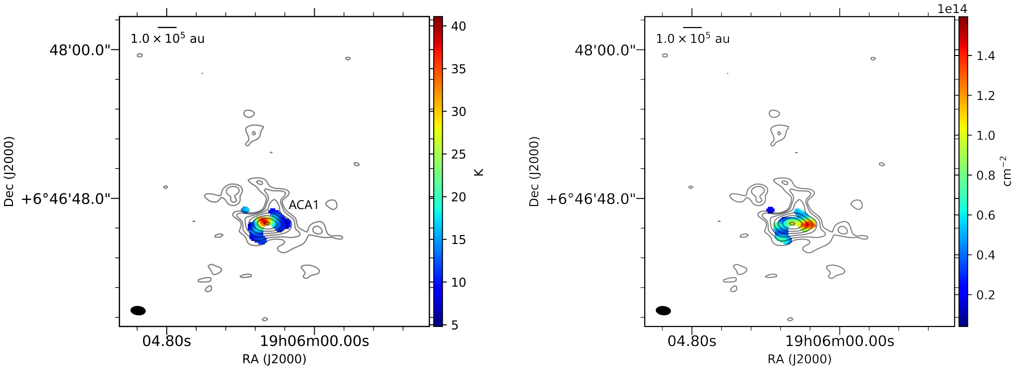

Figure 6.7: Derived rotation temperature (left) and column density (right) for CH_3OH in BGPS 6029. Contours show the continuum from Figure 5.6.

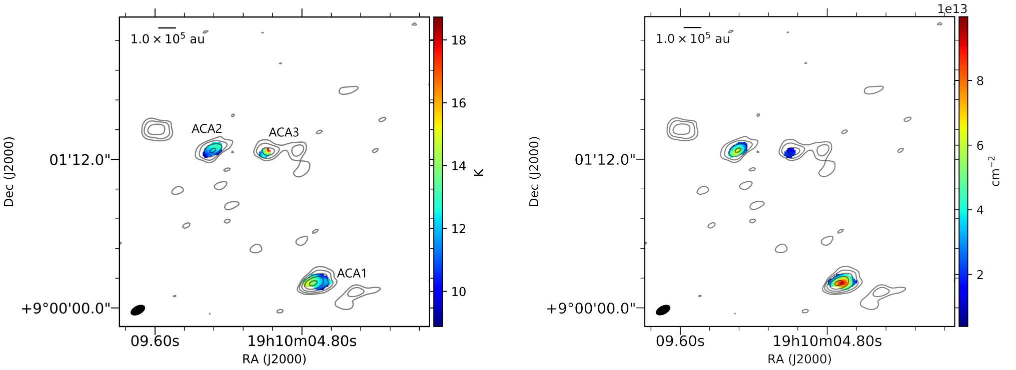

Figure 6.8: Derived rotation temperature (left) and column density (right) for CH_3OH in BGPS 6112. Contours show the continuum from Figure 5.8.

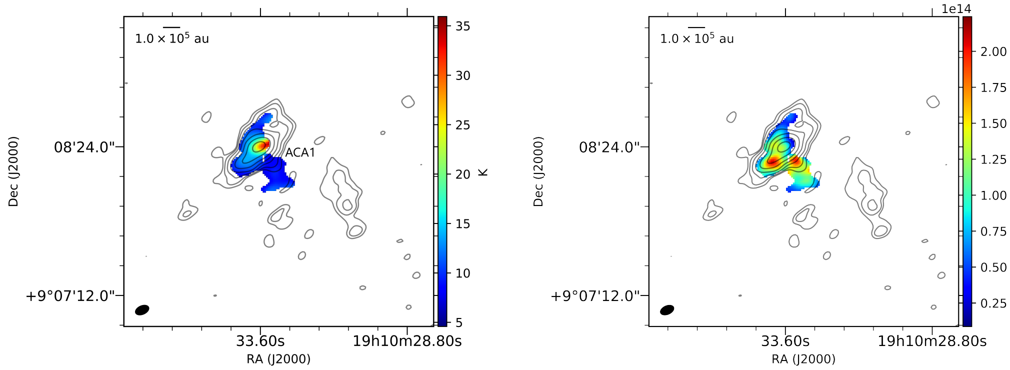

Figure 6.9: Derived rotation temperature (left) and column density (right) for CH_3OH in BGPS 6120. Contours show the continuum from Figure 5.9.

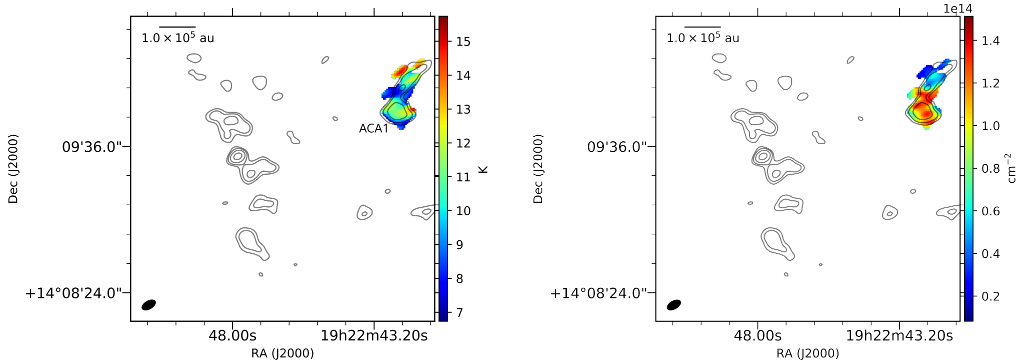

Figure 6.10: Derived rotation temperature (left) and column density (right) for CH_3OH in BGPS 6299. Contours show the continuum from Figure 5.10.

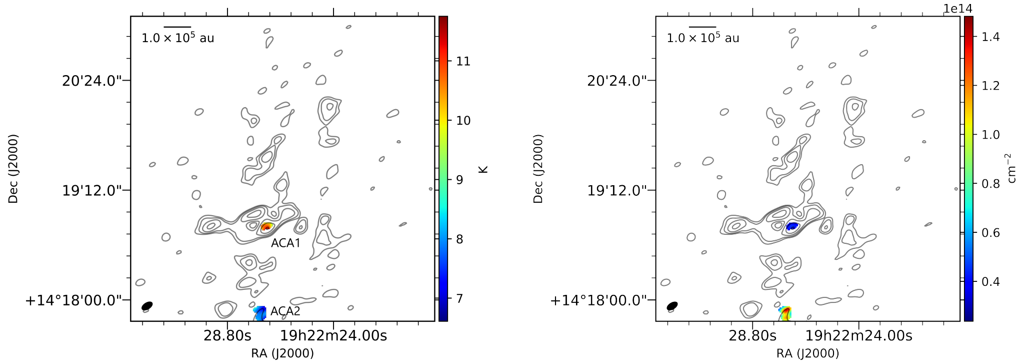

Figure 6.11: Derived rotation temperature (left) and column density (right) for CH_3OH in BGPS 6310. Contours show the continuum from Figure 5.11.

Table 6.3: CH_3OH lines fit to derive column density and rotation temperature

Transition	ν (GHz)	E_u (K)	g_u	A_{ul} (s^{-1})	$S_{ij}\mu^2$ (Debye^2)
$5_{(-0,5)} - 4_{(-0,4)}$	241.7002	47.93	44	6.03×10^{-5}	16.16
$5_{(1,5)} - 4_{(1,4)}$	241.7672	40.39	44	5.81×10^{-5}	15.53
$5_{(0,5)} - 4_{(0,4)}$	241.7914	34.82	44	6.04×10^{-5}	16.17
$5_{(-1,4)} - 4_{(-1,3)}$	241.8790	55.87	44	5.96×10^{-5}	15.92
$5_{(-2,4)} - 4_{(-2,3)}$	241.9046	57.07	44	5.03×10^{-5}	13.43

described in Chapter 2. To avoid erroneous fits, only lines with peak amplitudes of $\geq 3\sigma_{\rm rms}$ were considered; the $\sigma_{\rm rms}$ values for each GMC are given in Table 5.2. Rotation temperature $T_{\rm rot}$ [K] and column density $N_{\rm tot}$ [cm^{-2}], along with line width and velocity shift, were determined simultaneously by least-squares fitting with `LMFIT`[1] (version 0.9.15) to model the spectra assuming optically thin lines at local thermodynamic equilibrium (LTE); commentary on the robustness of the LTE assumption is given in Section 6.4 The spectra were modeled using Equation 1 (adapted from Remijan et al., 2003)

$$N_{\rm tot} = 2.04 \times 10^{20} C_\tau \frac{1}{\Omega_S(\Omega_S + \Omega_B)} \frac{\int I_\nu d\nu}{\theta_a \theta_b} \frac{Q(T_{\rm rot}) e^{E_u/T_{\rm rot}}}{\nu^3 S_{ij}\mu^2} \ \mathrm{cm}^{-2} \tag{6.1}$$

where the $\int I_\nu d\nu$ is the integrated intensity of the line [Jy beam^{-1} km s^{-1}], the optical depth correction factor $C_\tau = \tau/(1 - e^{-\tau})$ is assumed to be unity (since we assume the optical depth τ is small), Ω_S and Ω_B are the solid angles of the source and beam respectively, θ_a and θ_b are the synthesized beam sizes [$''$], Q is the partition function, E_u is the upper-state energy level [K], ν is the rest frequency of the transition [GHz], and $S_{ij}\mu^2$ is the product of the transition line strength and the square of the electric dipole moment [Debye^2]. The lines fit in this analysis are listed in Table 6.3. All lines come from a single spectral window but exhibit a range of line strengths and have similar excitation energies, as shown in Figure 6.12, which allows us to make robust measurements within our assumptions of LTE and small optical depth.

We assume that the source fills the beam at all positions and that $\Omega \approx \pi\theta^2$ since θ is small ($\sim 5''$), with the caveat that, because the objects targeted are overall not well characterized in the existing literature, this may not be a robust assumption; if

---

[1] `LMFIT` (Newville et al., 2019) is a nonlinear least-squares minimization and curve-fitting algorithm for Python that can be accessed at https://doi.org/10.5281/zenodo.598352.

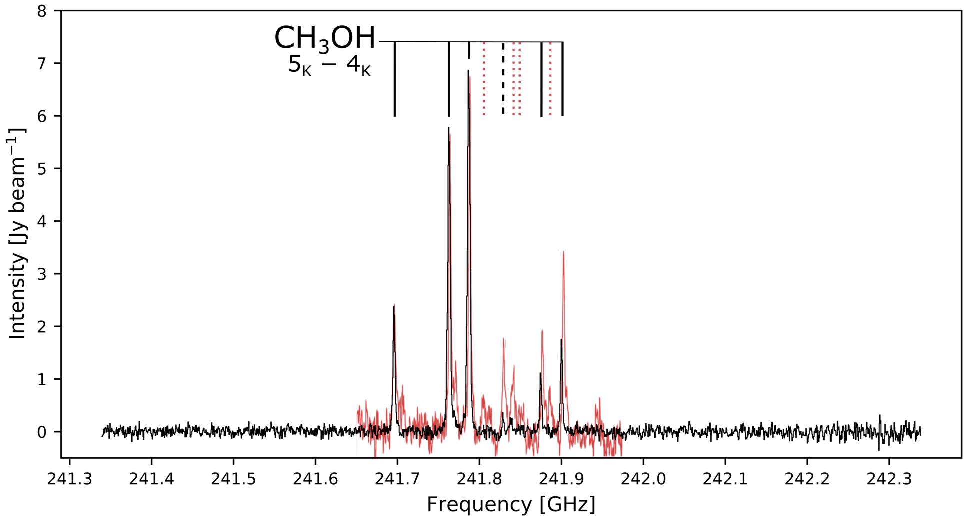

Figure 6.12: Spectrum from ACA “upper” Band 6 for BGPS 6120 showing the CH_3OH lines used to derive parameters, designated by the solid black lines. The CH_3OH line identified with the black dashed line was too weak to use in the fits and was excluded. The red spectrum shows JCMT observations of IRAS 16293-2422 by van Dishoeck et al. (1995), with CH_3OH lines detected toward IRAS 16293 but not toward our molecular-ring samples identified by the red dotted lines.

there are objects in the sample where the source does not fill the beam, this means that some emission may be diluted in our beam and some information may be lost. However, since the work described here is part of a pilot survey, the goal is to identify regions for more robust follow-up high-resolution observations.

As seen in Figures 6.3-6.11, the derived rotation temperature is less than 20 K for most objects. Under the assumptions of LTE, we can approximate the kinetic temperature of the objects by the rotation temperature. At the relatively low angular resolution of the ACA, we resolve the structure within the target sample GMCs on linear scales of $\sim 10^4$-10^5 au. These large scales correspond to the spatial scales of dense clumps but are too large to resolve individual protostars or hot cores; as such, these low temperatures are expected since the warmer temperatures of any hot cores would be diluted by the more extended colder emission within the ACA beam.

Two sources—BGPS 6029 (Figure 6.7) and BGPS 6120 (Figure 6.9)—have higher temperatures of up to 40 K and 35 K, respectively. These are still sub-hot-core temperatures but are warmer than the ~10 K of the gas in which the seeds of infant stars are planted. This may indicate that the objects in these sources are more evolved and contain cores that are undergoing warm-up. As seen in Table 6.1, BGPS 6029 and BGPS 6120 are also the most chemically rich in our sample, which is a further sign that these regions may be more evolved than other regions identified in the sample.

Comparing the BGPS 6120 spectrum in Figure 6.12 to that of the low-mass protobinary IRAS 16293-2422 at the same frequencies confirms that the molecular-ring sources are indeed cold and that the low temperatures derived are not the result of fitting errors. van Dishoeck et al. (1995) report a methanol rotation temperature of 85 ± 6 K in IRAS 16293, which is more than two times the highest temperatures derived for our molecular-ring targets. As seen by the red spectrum in Figure 6.12, van Dishoeck et al. detect several CH_3OH emission lines that are absent in our observations; these lines are all higher excitation lines with $E_u > 70$ K, whereas the lines we fit (Table 6.3) all have $E_u < 60$ K.

CH_3OH column densities N_{tot} were derived to be on the order of 10^{13}-10^{14} cm^{-2}, which is similar to abundances derived in prestellar cores (e.g., Scibelli & Shirley, 2020). For the most part, the sources exhibit a single peak in column density that is cospatial with the millimeter continuum emission peak. This is the case for BGPS 3474 ACA1 (Figure 6.4), BGPS 4449 ACA2 (Figure 6.5), BGPS 5623 ACA1 (Figure 6.6), BGPS 6112 ACA1, BGPS 6112 ACA2, BGPS 6112 ACA3 (Figure 6.8), BGPS 6310 ACA1, and BGPS 6310 ACA2 (Figure 6.11). The remaining sources—BGPS 4449 ACA1 (Figure 6.5), BGPS 6029 ACA1 (Figure 6.7), BGPS6120 ACA1 (Figure 6.9), and BGPS 6299 ACA1 (Figure 6.10)—have more peculiar $N_{\text{tot}}(CH_3OH)$ profiles.

BGPS 4449 ACA1 (Figure 6.5) shows two fittable CH_3OH emission regions, indicating that this object may contain not one but two molecular cores. Ellsworth-Bowers et al. (2015) reported a dense core in this region, and Saral et al. (2015) identified this location as the site of a YSO and YSO candidates. The two candidate cores have different temperature and abundance profiles. The northern source is slightly colder (13-14 K) but with a higher CH_3OH column density of $\lesssim 5.0 \times 10^{13}$ cm^{-2}. The southern source has temperature approaching 17 K but column densities about a factor of two lower than the northern source.

The peak column density ($\sim 1.4 \times 10^{14}$ cm^{-2}) in BGPS 6029 ACA1 is off-center to the west of the continuum emission peak. This is particularly curious because the maximum temperature ($\sim$40 K) in that object is nonetheless cospatial with the continuum peak. The peaks in the measured parameters have uncertainties of $\leq$10% (Figure I.5), so this profile is not the result of poor spectral line fits. Instead, we may be seeing the blended profiles of multiple objects early in stellar evolution. For instance, BGPS 6029 ACA1 corresponds to the location of dense cores (e.g., Beuther et al., 2002; Lu et al., 2014) and a YSO (Svoboda et al., 2016; Areal et al., 2018). Lu et al. (2014) report three distinct cores with radii of ~0.03 pc (~6000 au) from VLA ammonia observations. Fontani et al. (2014) observed BGPS 6029 ACA1 as part of an astrochemical study to understand the nature of deuterium chemistry in high-mass star-forming regions. However, Fontani et al. (2015) could not find deuterated methanol, which they used as a tracer of high-mass protostellar objects in which molecules formed through grain-surface chemistry are sputtered from the icy grain mantles, and concluded that the region is too evolved for grain-surface chemistry to be observed.

Like BGPS 4449 ACA1, the millimeter continuum region BGPS 6120 ACA1 (Figure 6.9) contains multiple methanol abundance peaks. There are two column density peaks of $\sim 2.0 \times 10^{14}$ cm^{-2} to the southeast and southwest of the continuum emission peak. There is potentially another peak with $N_{\rm tot} \sim 1.5 \times 10^{14}$ cm^{-2} just to the east of the continuum peak. This agrees with past large surveys that reveal structures related to the early stages of star formation. For example, Morales et al. (2013) characterized a partially embedded cluster about 66″ across in BGPS 6120. There are multiple YSOs and YSO candidates reported there as well (Saral et al., 2015; Urquhart et al., 2018). Saral et al. (2015) specifically report five YSO candidates. Our map of CH_3OH column density supports 2-3 of these being molecular cores.

BGPS 6299 ACA1 (Figure 6.10) is the most abnormal fitted region in our data. It appears to be a complex comprising multiple millimeter continuum peaks. There are two regions of ~12-15 K separated by a band of 7-8 K. Surprisingly, the cold band coincides with a region where $N_{\rm tot}(CH_3OH) \sim 1.4 \times 10^{14}$ cm^{-2} that stretches south. North of the cold band, $N_{\rm tot} \sim 6 \times 10^{13}$ cm^{-2}. The northern aspect of BGPS 6299 ACA1 has higher uncertainties of ~20% whereas the cold band and the region south of it are fit well with uncertainties of ≤5%. The higher uncertainty to the north may be because the emission falls at the edge of the ACA's field of view. In the south, the high-density region is broken up into several smaller regions, which may be indicative of a young stellar cluster. This is consistent with the existing literature, which reports five YSOs or YSO candidates in the vicinity of BGPS 6299 ACA1 (Urquhart et al., 2014; Saral et al., 2017). This region has also been reported to contain a dense core with a 1.00 probability of star formation as well as a H_2O maser (Urquhart et al., 2014; Svoboda et al., 2016).

In summary, across the nine GMCs that contain fittable CH_3OH emission, there are $\geq$15 apparent molecular cores with column densities of 10^{13}-10^{14} cm^{-2}. Typical temperatures are $\leq$20 K, but a couple of regions have higher temperatures of $\sim$40 K.

6.4 Optical Depth and LTE Assumptions

The analysis in the previous section assumes that all observed CH_3OH emission is optically thin. However, CH_3OH is notoriously optically thick toward protostars (e.g., Bisschop et al., 2007; Crockett et al., 2014). Given the apparent colder temperatures detected here, optically thin CH_3OH may be a valid assumption, as is the case toward low-mass YSOs and cold prestellar cores (Öberg et al., 2014; Scibelli & Shirley, 2020).

We tested this assumption by comparing the fitted parameters (N_{tot}, T_{rot}) to the CH_3OH spectrum for a pixel near the center of each emission region. The optical depth τ of a line can be calculated as

$$\tau = \frac{g_u}{\Delta V} \frac{N_{\text{tot}}}{Q(T_{\text{rot}})} \frac{A_{ul} c^3}{8 \pi \nu^3} e^{-E_u/T_{\text{rot}}} \left(e^{h\nu/kT_{\text{rot}}} - 1 \right) \tag{6.2}$$

where g_u is the degeneracy of the upper state, ΔV is the fitted line width, A_{ul} is the Einstein A coefficient, h is the Planck constant, and k is the Boltzmann constant. Other terms are the same as in Equation 6.1. Optical depth was calculated for each of the five lines listed in Table 6.3. From this, the optical depth correction factor $C_\tau = \tau/(1 - e^{-\tau})$ was calculated. Both τ and C_τ were averaged for each target and are summarized in Table 6.4.

Most sources in our sample have $\tau \ll 1$ or $C_\tau \sim 1$, confirming that the emission is indeed optically thin. A few sources, notably BGPS 3474 ACA1 ($C_\tau = 1.18$) and BGPS 6299 ACA1 ($C_\tau = 1.10$), have higher optical depth factors, hence optically thin lines may not be the most robust assumption for these data. However, since the goal of this work is to gain a preliminarly look at the chemistry in previously unexplored interstellar laboratories, the assumption that the analyzed lines are optically thin is sufficient.

Another consideration is the degree to which excitation, specifically rotation, temperatures T_{rot} reflect the kinetic temperatures T_{kin} in the targeted regions. This assumption typically holds in dense star-forming regions where $n_H \sim 10^5$-10^6 cm^{-3}. However, because these regions are not well characterized, making such an assumption is difficult.

Table 6.4: Optical depth test results

Source	τ	C_τ
BGPS 3053 ACA1	0.06	1.03
BGPS 3053 ACA2	0.04	1.02
BGPS 3474 ACA1	0.34	1.18
BGPS 4449 ACA1(N)	0.04	1.02
BGPS 4449 ACA1(S)	0.06	1.03
BGPS 4449 ACA2	0.04	1.02
BGPS 5623 ACA1	0.13	1.07
BGPS 6029 ACA1	0.04	1.02
BGPS 6112 ACA1	0.08	1.04
BGPS 6112 ACA2	0.05	1.02
BGPS 6112 ACA3	0.02	1.01
BGPS 6120 ACA1	0.03	1.02
BGPS 6299 ACA1	0.18	1.10
BGPS 6310 ACA1	0.16	1.08
BGPS 6310 ACA2	0.08	1.04

As discussed in Section 5.2, the target GMCs were screened to have mass surface densities $\geq$200 $M_\odot$ pc^{-2}, which approximately corresponds to $n_H \geq 10^3$ cm^{-3}. The mass surface density threshold is averaged over the entire field of view observed with the ACA, meaning that the continuum emission regions in which we fit the CH_3OH spectra are even denser. Many of these objects are associated with known YSOs or YSO candidates (e.g., from large surveys by Urquhart et al., 2014; Saral et al., 2017; Areal et al., 2018), meaning that a high density assumption is reasonable. Again, we stress that the purpose of this work is to survey the target GMCs for follow-up high-angular resolution studies, so the assumptions made here are sufficient.

6.5 SiO Distribution

Silicon monoxide (SiO) is a reliable tracer of shock chemistry, particularly that associated with protostellar outflows (Martin-Pintado et al., 1992, e.g.,). SiO is produced in the gas phase from Si-bearing material sputtered off of dust grains, either from the grain mantles or the cores (Schilke et al., 1997); the rate of SiO production has been further shown to be influenced by the sputtering of other simple compounds, such as CO (Jiménez-Serra et al., 2008).

As indicated in Table 6.1, we detected SiO toward only a few sources in our sample: BGPS 5623, BGPS 6029, BGPS 6112, and BGPS 6120. The distribution of SiO toward 1.2 mm continuum objects in these GMCs is illustrated in Figure 6.13. Of

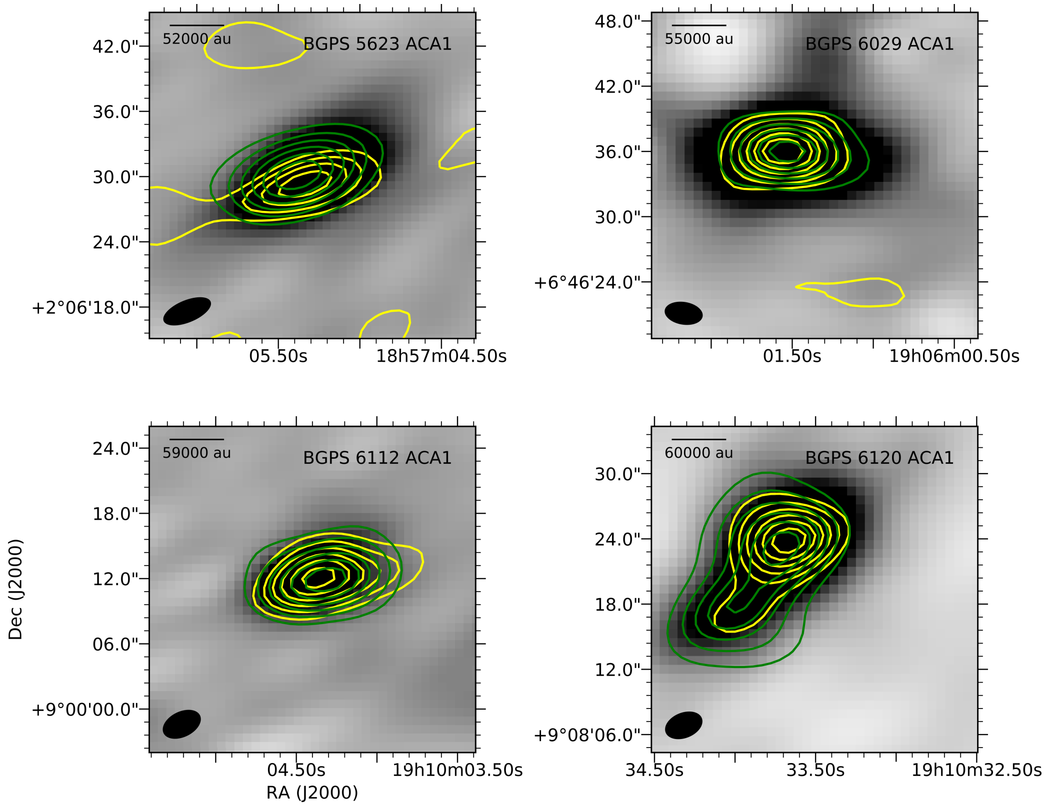

Figure 6.13: Contours showing the distribution of SiO (yellow) and CH_3OH (green) toward the four sources where SiO emission was confidently detected. The greyscale images show the Band 6 (∼240 GHz) continuum.

these, BGPS 6029 and BGPS 6120 were identified as being the most chemical-rich, as well as the warmest, sources in the sample, which may indicate that these objects are further along in the stellar evolutionary sequence. Thus, the presence of SiO emission, which has significantly enhanced abundances in protostellar outflows (Jiménez-Serra et al., 2005, 2008, 2009, e.g.,), is to be expected. This supports the conjecture that BGPS 6029 ACA1 and BGPS 6120 ACA1 are indeed sites of active star formation.

Compared to other sources in our sample, BGPS 5623 ACA1 and BGPS 6112 ACA1 are not exceptional in terms of molecular diversity (Table 6.1) and temperature profile (Figures 6.6 and 6.8, respectively). However, the presence of detectable SiO emission overlapping with the complex organic material traced by CH_3OH, as seen in the left column of Figure 6.13, suggests that these two objects harbor YSOs. This agrees with previous finding (Table 6.5). This may also indicate that the YSOs therein are more evolved than other sources in the sample. However, the absence of a detection of SiO toward other sources does not definitively preclude its presence.

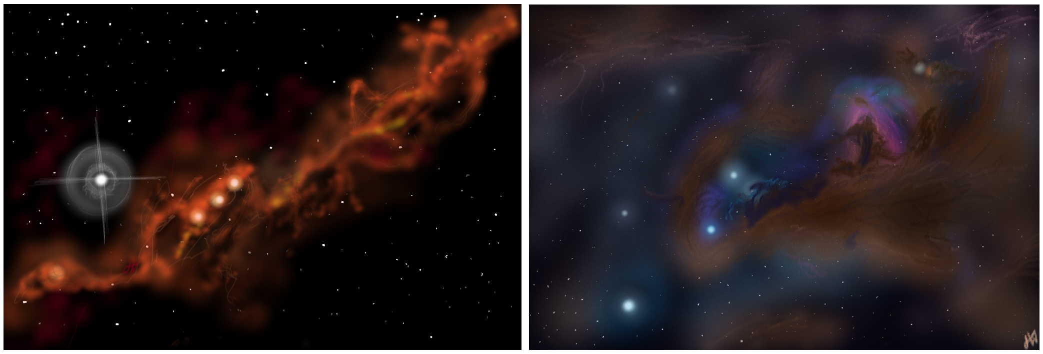

Figure 6.14: Illustrations of Taurus Molecular Cloud (left) and Perseus Molecular Cloud (right). These illustrations, digitally hand-drawn in Microsoft Paint by O. H. W., appeared in Wilkins & Blake (2021).

Nevertheless, the likelihood that BGPS 5623 ACA1 and BGPS 6112 ACA1 contain YSOs with accompanying protostellar outflows is interesting given their molecule-poor nature when compared to the other two SiO-containing sources. One possible explanation is that these regions are simply not as chemically diverse as their counterparts in BGPS 6029 and BGPS 6120. A more likely explanation, given the colder nature of these objects, is that they are in an evolutionary state between those of BGPS 6029 ACA1 and BGPS 6120 ACA1 and of the CH_3OH-containing objects for which SiO was not detected. If this is the case, the sample provides several snapshots along the evolutionary sequence of YSOs in molecular-ring star-forming regions, which could be used to better understand how chemistry progresses temporally alongside star formation.

6.6 Discussion

The maps presented in Sections 6.3 and 6.5 reveal a number of new astrochemical laboratories in the molecular ring. Except for BGPS 6029 (in which NH_3 was observed), the objects targeted in this pilot survey have not been observed in terms of molecular emission, as is evident from the extensive literature search conducted in Chapter 5. From this first look at the organic chemistry in these molecular-ring GMCs, we see a rich display of chemistry, including complex organics, ionized species, nitrogen-bearing species, and tracers of protostellar outflows. From the fitted CH_3OH parameter maps, we see that we may even have objects at different stages of stellar evolution (i.e., the warmer and more chemically-rich BGPS 6029 and BGPS 6120); this is further demonstrated by the distribution of SiO.

Table 6.5: Objects corresponding to previously identified YSOs*

Identifier	Corresponding YSO(c)
BGPS 3053 ACA1	Embedded protostar[a]
BGPS 3474 ACA1	Flat-spectrum YSO[b]
BGPS 4449 ACA1	YSO[c,d]
BGPS 5623 ACA1	High-mass YSO[e,f]
BGPS 6029 ACA1	YSO[g,h]
BGPS 6112 ACA1	YSO[i,j]
BGPS 6112 ACA2	Class I YSO candidate[k]
BGPS 6112 ACA3	Class II YSO[k]
BGPS 6120 ACA1	5 YSO candidates[k]
BGPS 6299 ACA1	2 YSO candidates[d]
BGPS 6310 ACA1	YSO-bearing clump[i]

* Modified from Table 5.4 to include only regions with fittable CH_3OH molecular line emission.
[a] Ragan et al. (2009); [b] Baug et al. (2016); [c] Urquhart et al. (2009); [d] Saral et al. (2017); [e] Rathborne et al. (2006); [f] Nguyen Luong et al. (2011); [g] Svoboda et al. (2016); [h] Areal et al. (2018); [i] Urquhart et al. (2018); [j] Urquhart et al. (2014); [k] Saral et al. (2015).

The number of molecular-ring objects that have been studied in the context of astrochemistry is limited. The massive star-forming region W33A ($d \sim 4$ kpc) is one such region that falls within the molecular ring at a radius of 4.2 kpc from the galactic center based on its celestial coordinates ($\alpha_{\mathrm{J2000}} = 18^{\mathrm{h}}14^{\mathrm{m}}39\overset{\mathrm{s}}{.}4$ $\delta_{\mathrm{J2000}} = -17^\circ 52' 01''$). For example, McCall et al. (1999) reported on gas-phase H_3^+, Dartois et al. (1999) observed CH_3OH ice, and Gibb et al. (2000) presented the overall ice inventory of this region.

One of the big questions in astrochemistry is whether the chemical inventories and processes observed are universal across the galaxy. As discussed in Section 6.1, most of our understanding of chemical processes in star-forming regions comes from the local ISM. However, whether chemistry in the molecular ring is different remains to be seen despite there being some key differences between star-forming regions in the molecular ring versus the local ISM. One difference is that the typical astrochemical laboratories—including Taurus Molecular Cloud and Perseus Molecular Cloud (Figure 6.14)—are low-mass star-forming regions. However, high-mass stars, such as those that form in GMCs perhaps like the ones observed in this pilot study, can severely affect the formation, and thus accompanying chemistry, of neighboring YSOs (Lada & Lada, 2003).

Even if the chemistry in the molecular ring is ultimately the same as what is observed in the local ISM, our current understanding of chemical evolution in the galaxy is limited by small sample sizes. This is especially true for the high-mass star-forming regions, our knowledge of which is observationally biased toward the shortest and rarest evolutionary stages located up to $d \sim 3$ kpc (Motte et al., 2018). Therefore, broader surveys are necessary to fully investigate the physical and chemical evolutionary sequences of such stars.

Fortunately, the chemical emission for many of the objects presented here corresponds to previously identified YSOs and YSO candidates. Some of these were already discussed in Section 6.3. A comprehensive list, based on a thorough literature search using the SIMBAD database, is given in Table 6.5. The fact that many of the CH_3OH emission regions presented here correspond to objects that have been, at least preliminarily, characterized in terms of their physical aspects emphasizes the potential for these objects to provide new insights about the chemistry alongside (massive) star formation.

6.7 Summary

We present pilot survey results of the chemistry in a sample of 11 GMCs. Of these, nine target GMCs contain fittable CH_3OH emission, from which rotation temperatures and column density abundances are derived. In general, the objects, many of which correspond to previously identified YSOs or YSO candidates, have temperatures of $\leq$40 K and column densities on the order of 10^{13}-10^{14} cm^{-2}.

In addition to CH_3OH, we detect a number of chemical compounds. All 11 GMCs contain CO and $C^{18}O$. Like CH_3OH, SO, $H^{13}CO^+$, and H_2CO are present in all but BGPS 6318. Isotopologues of these species are also found; ^{33}SO and ^{34}SO are each found in one GMC, $HC^{18}O^+$ is detected in two GMCs, and $H_2{}^{13}CO$ is found in three GMCs. The remaining species detected are c-C_3H_2 (6 GMCs), SiO (4 GMCs), HNCO (3 GMCs), and SO_2, HCS^+, CH_3CCH, and HC_3N (2 GMCs each).

The work presented here lays the foundation for follow-up high-angular-resolution studies of the gas-phase chemistry with ALMA. The variety of tracers identified in the spectra of these sources indicates that these objects contain a rich chemical inventory in which different chemical environments—from shocks propagated by outflows (via and SiO, SO, SO_2) to cold, more diffuse gas (via c-C_3H_2)—can be investigated. Furthermore, investigations of ices in these objects (e.g., with JWST), will help to constrain the coupling between gas and grain chemistry.

References

Areal, M. B., Paron, S., Celis Peña, M., & Ortega, M. E. 2018, *Astron. Astrophys.*, 612, A117, doi: `10.1051/0004-6361/201732067`

Baug, T., Dewangan, L. K., Ojha, D. K., & Ninan, J. P. 2016, *Astrophys. J.*, 833, 85, doi: `10.3847/1538-4357/833/1/85`

Beuther, H., Schilke, P., Menten, K. M., et al. 2002, *Astrophys. J.*, 566, 945, doi: `10.1086/338334`

Crockett, N. R., Bergin, E. A., Neill, J. L., et al. 2014, *Astrophys. J.*, 787, 112, doi: `10.1088/0004-637X/787/2/112`

Dartois, E., Schutte, W., Geballe, T. R., et al. 1999, *Astron. Astrophys.*, 342, L32

Ellsworth-Bowers, T. P., Glenn, J., Riley, A., et al. 2015, *Astrophys. J.*, 805, 157, doi: `10.1088/0004-637X/805/2/157`

Fontani, F., Busquet, G., Palau, A., et al. 2015, *Astron. Astrophys.*, 575, A87, doi: `10.1051/0004-6361/201424753`

Fontani, F., Sakai, T., Furuya, K., et al. 2014, *Mon. Not. R. Astron. Soc.*, 440, 448, doi: `10.1093/mnras/stu298`

Gibb, E. L., Whittet, D. C. B., Schutte, W. A., et al. 2000, *Astrophys. J.*, 536, 347, doi: `10.1086/308940`

Jiménez-Serra, I., Caselli, P., Martín-Pintado, J., & Hartquist, T. W. 2008, *Astron. Astrophys.*, 482, 549, doi: `10.1051/0004-6361:20078054`

Jiménez-Serra, I., Martín-Pintado, J., Caselli, P., Viti, S., & Rodríguez-Franco, A. 2009, *Astrophys. J.*, 695, 149, doi: `10.1088/0004-637X/695/1/149`

Jiménez-Serra, I., Martín-Pintado, J., Rodríguez-Franco, A., & Martín, S. 2005, *Astrophys. J. Lett.*, 627, L121, doi: `10.1086/432467`

Kanarek, G., Shara, M., Faherty, J., Zurek, D., & Moffat, A. 2015, *Mon. Not. R. Astron. Soc.*, 452, 2858, doi: `10.1093/mnras/stv1342`

Lada, C. J., & Lada, E. A. 2003, *Annu. Rev. Astron. Astrophys.*, 41, 57, doi: `10.1146/annurev.astro.41.011802.094844`

Lu, X., Zhang, Q., Liu, H. B., Wang, J., & Gu, Q. 2014, *Astrophys. J.*, 790, 84, doi: `10.1088/0004-637X/790/2/84`

Martin-Pintado, J., Bachiller, R., & Fuente, A. 1992, *Astron. Astrophys.*, 254, 315

McCall, B. J., Geballe, T. R., Hinkle, K. H., & Oka, T. 1999, *Astrophys. J.*, 522, 338, doi: `10.1086/307637`

Morales, E. F. E., Wyrowski, F., Schuller, F., & Menten, K. M. 2013, *Astron. Astrophys.*, 560, A76, doi: `10.1051/0004-6361/201321626`

Motte, F., Bontemps, S., & Louvet, F. 2018, *Annu. Rev. Astron. Astrophys.*, 56, 41, doi: `10.1146/annurev-astro-091916-055235`

Nguyen Luong, Q., Motte, F., Hennemann, M., et al. 2011, *Astron. Astrophys.*, 535, A76, doi: `10.1051/0004-6361/201117831`

Öberg, K. I., Lauck, T., & Graninger, D. 2014, *Astrophys. J.*, 788, 68, doi: `10.1088/0004-637X/788/1/68`

Ragan, S. E., Bergin, E. A., & Gutermuth, R. A. 2009, *Astrophys. J.*, 698, 324, doi: `10.1088/0004-637X/698/1/324`

Rathborne, J. M., Jackson, J. M., & Simon, R. 2006, *Astrophys. J.*, 641, 389, doi: `10.1086/500423`

Remijan, A., Snyder, L. E., Friedel, D. N., Liu, S. Y., & Shah, R. Y. 2003, *Astrophys. J.*, 590, 314, doi: `10.1086/374890`

Sanders, D. B., Solomon, P. M., & Scoville, N. Z. 1984, *Astrophys. J.*, 276, 182, doi: `10.1086/161602`

Saral, G., Hora, J. L., Willis, S. E., et al. 2015, *Astrophys. J.*, 813, 25, doi: `10.1088/0004-637X/813/1/25`

Saral, G., Hora, J. L., Audard, M., et al. 2017, *Astrophys. J.*, 839, 108, doi: `10.3847/1538-4357/aa6575`

Schilke, P., Walmsley, C. M., Pineau des Forets, G., & Flower, D. R. 1997, *Astron. Astrophys.*, 321, 293

Scibelli, S., & Shirley, Y. 2020, *Astrophys. J.*, 891, 73, doi: `10.3847/1538-4357/ab7375`

Scoville, N. Z., & Solomon, P. M. 1975, *Astrophys. J. Lett.*, 199, L105, doi: `10.1086/181859`

Svoboda, B. E., Shirley, Y. L., Battersby, C., et al. 2016, *Astrophys. J.*, 822, 59, doi: `10.3847/0004-637X/822/2/59`

Urquhart, J. S., Hoare, M. G., Purcell, C. R., et al. 2009, *Astron. Astrophys.*, 501, 539, doi: `10.1051/0004-6361/200912108`

Urquhart, J. S., Csengeri, T., Wyrowski, F., et al. 2014, *Astron. Astrophys.*, 568, A41, doi: `10.1051/0004-6361/201424126`

Urquhart, J. S., König, C., Giannetti, A., et al. 2018, *Mon. Not. R. Astron. Soc.*, 473, 1059, doi: `10.1093/mnras/stx2258` van Dishoeck, E. F., Blake, G. A., Jansen, D. J., & Groesbeck, T. D. 1995, *Astrophys. J.*, 447, 760, doi: `10.1086/175915`

Wilkins, O. H., & Blake, G. A. 2021, Astrochemistry (Washington, DC, USA: American Chemical Society), doi: `10.1021/acsinfocus.7e5004`

Wilkins, O. H., Carroll, P. B., & Blake, G. A. 2022, *Astrophys. J.*, accepted.

Chapter 7

SUMMARY AND OUTLOOK

While we have made strides in understanding chemistry that evolves along star formation over the last half-century or so, there is still much to learn, especially in the context of high-mass star formation. Our knowledge within the realm of astrochemistry is continually evolving, and some mysteries have persisted for several decades. For example, early hypotheses suggested that complex organics such as methanol form predominantly through gas-phase formation routes, but subsequent computational and laboratory work pointed to a primarily grain-surface formation (e.g., Charnley et al., 1997; Nagaoka et al., 2005; Watanabe et al., 2006). Even so, how methanol comes off the grains to be observed in the gas phase with radio telescopes has been less well understood (Garrod et al., 2006), and this injection of methanol into the gas-phase can be the result of a variety of chemical processes (e.g., Turner, 1998; Hasegawa & Herbst, 1993; Katz et al., 1999; Bertin et al., 2016). In Chapter 3, we addressed the transition of methanol into the gas-phase in Orion KL specifically, the closest region of high-mass star-formation to Earth that is often treated as the archetype for such regions. We suggested that thermal desorption, rather than other processes like injection by shocks, is the primary route to observed methanol via observations with ALMA. Based on the presence of methanol with relatively low temperatures, we also suggested that non-thermal rotational desorption of quickly rotating dust grains is also at play (Hoang & Tram, 2020).

Another chemical mystery, also centered on methanol, is the deuteration fractionation of methanol's singly-deuterated isotopomers: CH_2DOH and CH_3OD. Statistically, the ratio between these two species is expected to be ~3 since there are three hydrogen sites on the methyl (-CH_3) group but only one on the hydroxyl (-OH) group. While such a ratio has been observed in the massive star-forming region NGC 7538-IRS1 (Ospina-Zamudio et al., 2019), other high-mass star-forming regions, including Orion KL, appear to have relatively enriched abundances of CH_3OD (Jacq et al., 1993; Ratajczak et al., 2011; Peng et al., 2012; Neill et al., 2013; Belloche et al., 2016; Bøgelund et al., 2018). Conversely, CH_3OD appears to be depleted in many low-mass star-forming regions (Bizzocchi et al., 2014; Taquet et al., 2019). One hypothesis is that this distinction is driven by the initial deuterium fractionation in methanol and water (Faure et al., 2015), and that grain-surface exchange between deuterium and hydrogen at the hydroxyl site on methanol is the cause of the peculiar deuteration patterns. In Chapter 4, we looked at the relationship between measured CH_3OD abundances and temperatures mapped across Orion KL. Our observations support a rapid increase in CH_3OD resulting from D/H exchange with HDO and D_2O as the dust grains warm. While this has been studied computationally, our ability to resolve the small-scale temperature and density structure of Orion KL provides the first observations to show how CH_3OD abundance varies with temperature, in contrast with previous work that gives only one $[CH_2DOH]/[CH_3OD]$ value for the entire region.

The observations of methanol isotopologues in which we look at small-scale variations can also provide clues about temporal changes as well. In the ISM, the chemistry studied typically takes place over tens of thousands up to millions of years, far too long to be studied from start to finish during a doctoral thesis (even though it might sometimes feel like the path to a Ph.D. takes that long). By looking at small-scale variations in temperature and abundance, we are able to probe slightly different stages during the warm-up of protostellar and other material. In other words, instead of watching one point evolve directly, we collect snapshots across different stages of evolution, thereby observing how chemistry within a region evolves with gas warm-up and, indirectly, time.

In addition to studying chemical processes, this thesis uses molecules to understand physical environments as well. Chapter 2 looked at Orion KL at unprecedentedly high angular resolution and maps the nebula's heterogeneous thermal structure in a new way, providing a never-before-seen look at potential sources of heating that could be hidden sources of luminosity buried in Orion KL.

While Orion KL is certainly interesting and is considered the archetypal massive star-forming region of our galaxy, it is only one source and is not necessarily representative of interstellar laboratories distributed across the Milky Way. Furthermore, other commonly studied high-mass regions are especially molecule-rich, such as Sagittarius B2(N) near the galactic center. In Chapter 5, we searched for potential sites of star formation in the so-called molecular ring, which lies at radii of 4-8 kpc from the galactic center and is where the bulk of molecular matter in the galaxy is thought to reside. We found a number of millimeterwave-emitting objects. Some of these have been identified as part of large surveys, typically at lower angular resolutions than what we used with the ACA, but other emission objects were detected for the first time based on an extensive literature search. For all but one of nearly 100 continuum emission objects across the 11 giant molecular clouds targeted, astrochemical observations have not previously been conducted.

Chapter 6 looked at the chemistry of the 11 giant molecular clouds. This work identified 15 regions with fittable CH_3OH emission within nine of the target clouds, providing a first look at the physical conditions therein. We mapped the temperature and derived column densities on spatial scales of $\sim10^4$-10^5 au. This revealed a few preliminary results. For instance, the warmer regions are also the most chemically-rich, suggesting that they may be more evolved than other objects found in our survey. Furthermore, even on such large scales, we were able to partially resolve multiple abundance and temperature peaks within some of the objects. This work provides a catalogue of interstellar laboratories for future higher-angular-resolution observations.

Moving forward, there are several paths this work could take. Like virtually every other study of CH_3OD in Orion KL, the work in Chapter 4 calls for additional experimental and computational work. Experimental work showing rapid D/H exchange between CH_3OH and D_2O was based on the detection of the secondary ion $CH_3OD_2^+$ sputtered off a substrate at temperatures of $\sim$140 K in the lab rather than gas-phase CH_3OD itself (Souda et al., 2003). Follow-up work looking at CH_3OD directly via rotational spectroscopy, along with constraints on reaction rates, would be helpful in shaping models of D/H exchange in methanol. Currently, computational models in this area have been isothermal, with temperatures of typically $<$140 K (e.g., Faure et al., 2015). Better understanding of temperature-dependence of this exchange, then, would be useful. Furthermore, more work needs to be done to understand how the initial conditions of an environment affect the prevalence of D/H exchange on ices to enhance relative CH_3OD abundances in high-mass star-forming regions, as well as to constrain the physical and chemical differences that give rise to discrepancies in relative singly-deuterated methanol isotopomer abundances between low-mass and high-mass regions.

The goal of the pilot survey of molecular-ring giant molecular clouds has been to identify sources for follow-up high-angular-resolution observations of the gas with ALMA. Increasing the resolution to probe subarcsecond angular would be enough to resolve individual molecular cores within the clumps from the pilot survey. The ALMA main array will hopefully be used to do just this in future observing cycles to look at the gas chemistry in the molecular-ring laboratories, and facilities such as JWST could be used to understand the ice chemistry. Such investigations would allow us to look at the coupled gas-grain chemistry in the molecular ring. Even ALMA observations of the gas-phase alone would be useful in expanding the current sample of star-forming regions used for astrochemical observations. Furthermore, we could compare the molecular-ring chemistry to that of other well-studied regions to try to get a sense of how interstellar chemistry varies across the galaxy, if at all, and what conditions could prompt such variations.

We have presented several investigations using high-resolution imaging of the chemistry in extreme (by terrestrial standards) interstellar environments, from the well-studied Orion Kleinmann-Low nebula 1,300 light-years away to more distant and less-well-characterized regions of the molecular ring. Our findings reveal new perspectives of the chemical and physical environments related to high-mass star-forming regions, in particular through the use of methanol as a molecular probe. This work, like many other astrochemical investigations before it, calls for a combination of more observations, laboratory work, and computational modeling to better understand the chemistry observed. Our understanding of the wider chemical universe is rapidly changing, and I'm honored that this thesis could be a part of that.

References

Belloche, A., Müller, H. S. P., Garrod, R. T., & Menten, K. M. 2016, *Astron. Astrophys.*, 587, A91, doi: `10.1051/0004-6361/201527268`

Bertin, M., Romanzin, C., Doronin, M., et al. 2016, *Astrophys. J. Lett.*, 817, L12, doi: `10.3847/2041-8205/817/2/L12`

Bizzocchi, L., Caselli, P., Spezzano, S., & Leonardo, E. 2014, *Astron. Astrophys.*, 569, A27, doi: `10.1051/0004-6361/201423858`

Bøgelund, E. G., McGuire, B. A., Ligterink, N. F. W., et al. 2018, *Astron. Astrophys.*, 615, A88, doi: `10.1051/0004-6361/201832757`

Charnley, S. B., Tielens, A. G. G. M., & Rodgers, S. D. 1997, *Astrophys. J. Lett.*, 482, L203, doi: `10.1086/310697`

Faure, A., Faure, M., Theulé, P., Quirico, E., & Schmitt, B. 2015, *Astron. Astrophys.*, 584, A98, doi: `10.1051/0004-6361/201526499`

Garrod, R., Park, I. H., Caselli, P., & Herbst, E. 2006, *Faraday Discuss.*, 133, 51, doi: `10.1039/b516202e`

Hasegawa, T. I., & Herbst, E. 1993, *Mon. Not. R. Astron. Soc.*, 261, 83, doi: `10.1093/mnras/261.1.83`

Hoang, T., & Tram, L. N. 2020, *Astrophys. J.*, 891, 38, doi: `10.3847/1538-4357/ab6eff`

Jacq, T., Walmsley, C. M., Mauersberger, R., et al. 1993, *Astron. Astrophys.*, 271, 276

Katz, N., Furman, I., Biham, O., Pirronello, V., & Vidali, G. 1999, *Astrophys. J.*, 522, 305, doi: `10.1086/307642`

Nagaoka, A., Watanabe, N., & Kouchi, A. 2005, *Astrophys. J. Lett.*, 624, L29, doi: `10.1086/430304`

Neill, J. L., Crockett, N. R., Bergin, E. A., Pearson, J. C., & Xu, L.-H. 2013, *Astrophys. J.*, 777, 85, doi: `10.1088/0004-637X/777/2/85`

Ospina-Zamudio, J., Favre, C., Kounkel, M., et al. 2019, *Astron. Astrophys.*, 627, A80, doi: `10.1051/0004-6361/201834948`

Peng, T. C., Despois, D., Brouillet, N., Parise, B., & Baudry, A. 2012, *Astron. Astrophys.*, 543, A152, doi: `10.1051/0004-6361/201118310`

Ratajczak, A., Taquet, V., Kahane, C., et al. 2011, *Astron. Astrophys.*, 528, L13, doi: `10.1051/0004-6361/201016402`

Souda, R., Kawanowa, H., Kondo, M., & Gotoh, Y. 2003, *J. Chem. Phys.*, 119, 6194, doi: `10.1063/1.1602055`

Taquet, V., Bianchi, E., Codella, C., et al. 2019, *Astron. Astrophys.*, 632, A19, doi: `10.1051/0004-6361/201936044`

Turner, B. E. 1998, *Astrophys. J.*, 501, 731, doi: `10.1086/305859`

Watanabe, N., Nagaoka, A., Hidaka, H., et al. 2006, *Planet. Space Sci.*, 54, 1107, doi: `10.1016/j.pss.2006.05.019`

Appendix A

ASSUMING OPTICALLY THIN LINES AT LOCAL THERMODYNAMIC EQUILIBRIUM

The $^{13}CH_3OH$ $v = 0$ and CH_3CN $v_8 = 1$ transitions used in the analyses in Chapter 2 should be well-described by a local thermodynamic equilibrium (LTE). A rough collisional cross-section based on molecular geometry and van der Waals radii (2.096 Å for $^{13}CH_3OH$ and 2.408 Å for CH_3CN, based on geometry optimization conducted through density functional theory (DFT) with the B3LYP level of theory and 6-31G basis set available in the `Gaussian` 16 computational chemistry software program) give critical densities on the order of 10^4–10^5 cm^{-3} for both compounds. The reported densities toward Orion KL are $\geq 10^5$ cm^{-3}, suggesting that an LTE assumption is appropriate for these data. Moreover, LTE has been assumed in previous observations of complex organics toward Orion KL due to the high density of Orion KL's substructures (e.g., Feng et al., 2015).

We assume optically thin lines at LTE following guidelines set forth by Goldsmith and Langer (Goldsmith & Langer, 1999). They write the optical depth τ of a transition as

$$\tau = \frac{h}{\Delta V} N_u B_{ul} (e^{h\nu/kT} - 1) \tag{A.1}$$

where ΔV is the full-width at half-maximum line width in velocity units, N_u is the column density in the upper state, B_{ul} is the Einstein B coefficient for the transition, ν is the frequency of the transition, and T is the excitation temperature for the molecule (Goldsmith & Langer, 1999, Eqn. 6). This can be rewritten in terms of the Einstein A coefficient, which is related to B_{ul} by

$$B_{ul} = \frac{A_{ul} c^3}{8\pi h \nu^3}. \tag{A.2}$$

Moreover, N_u can be written in terms of the total column density N_{tot} as

$$N_u = \frac{N_{\text{tot}}}{Q(T)} g_u e^{-E_u/T} \tag{A.3}$$

where $Q(T)$ is the excitation partition function, g_u is the upper-state degeneracy, and E_u is the energy level of the upper state (Goldsmith & Langer, 1999, adapted from Eqn. 19). Substituting Eqns. A.2 and A.3 into Eqn. A.1, the optical depth can be expressed as

$$\tau = \frac{g_u}{\Delta V} \frac{N_{\text{tot}}}{Q(T)} \frac{A_{ul} c^3}{8\pi \nu^3} e^{-E_u/T} (e^{h\nu/kT} - 1). \tag{A.4}$$

To test whether each transition of each molecular tracer is optically thin in our data, we calculated τ at each transition using the constants from Splatalogue listed in Table 4.1. For $^{13}CH_3OH$, we selected a spectrum extracted from a single beam area near the center of the Compact Ridge, which has a total column density $N_{\rm tot}$ of 2.4×10^{16} cm^{-2}, a temperature of 196 K, and line width of 1.2 km s^{-1}; for CH_3CN, we selected a spectrum extracted from a single beam area near the center of the Hot Core, where $\Delta V = 2.9$ km s^{-1}, $N_{\rm tot} = 3.9 \times 10^{16}$ cm^{-2}, and $T_{\rm ex} = 275$ K. All lines have $\tau \leq 0.02 \ll 1$ thus are optically thin.

Furthermore, we ran χ^2 tests as an additional check for whether the LTE model is appropriate for the data presented in this work. The average χ^2 values for the $^{13}CH_3OH$ fits are 1.02 and 1.85 for the $0\farcs3$ and $0\farcs7$ data, respectively. For CH_3CN $v_8 = 1$, χ^2 is 3.60 and 0.15 for the $0\farcs2$ and $0\farcs9$ maps, respectively. These are slightly better than the χ^2 calculations for these molecules by Crockett et al. (2014), who calculated 1.9 for $^{13}CH_3OH$ and 4.0 for CH_3CN $v_8 = 1$.

References

Crockett, N. R., Bergin, E. A., Neill, J. L., et al. 2014, *Astrophys. J.*, 787, 112, doi: `10.1088/0004-637X/787/2/112`

Feng, S., Beuther, H., Henning, T., et al. 2015, *Astron. Astrophys.*, 581, A71, doi: `10.1051/0004-6361/201322725`

Goldsmith, P. F., & Langer, W. D. 1999, *Astrophys. J.*, 517, 209, doi: `10.1086/307195`

Appendix B

ORION KL DERIVED PARAMETER UNCERTAINTY MAPS

Percent uncertainty maps for the $^{13}CH_3OH$ $v = 0$ and CH_3CN $v_8 = 1$ parameter maps derived in Chapter 2 were calculated from the derived `LMFIT` standard errors. These maps are presented in Figures B.1 (p. 156) and B.2 (p. 157) for the full and tapered-angular-resolution images, respectively.

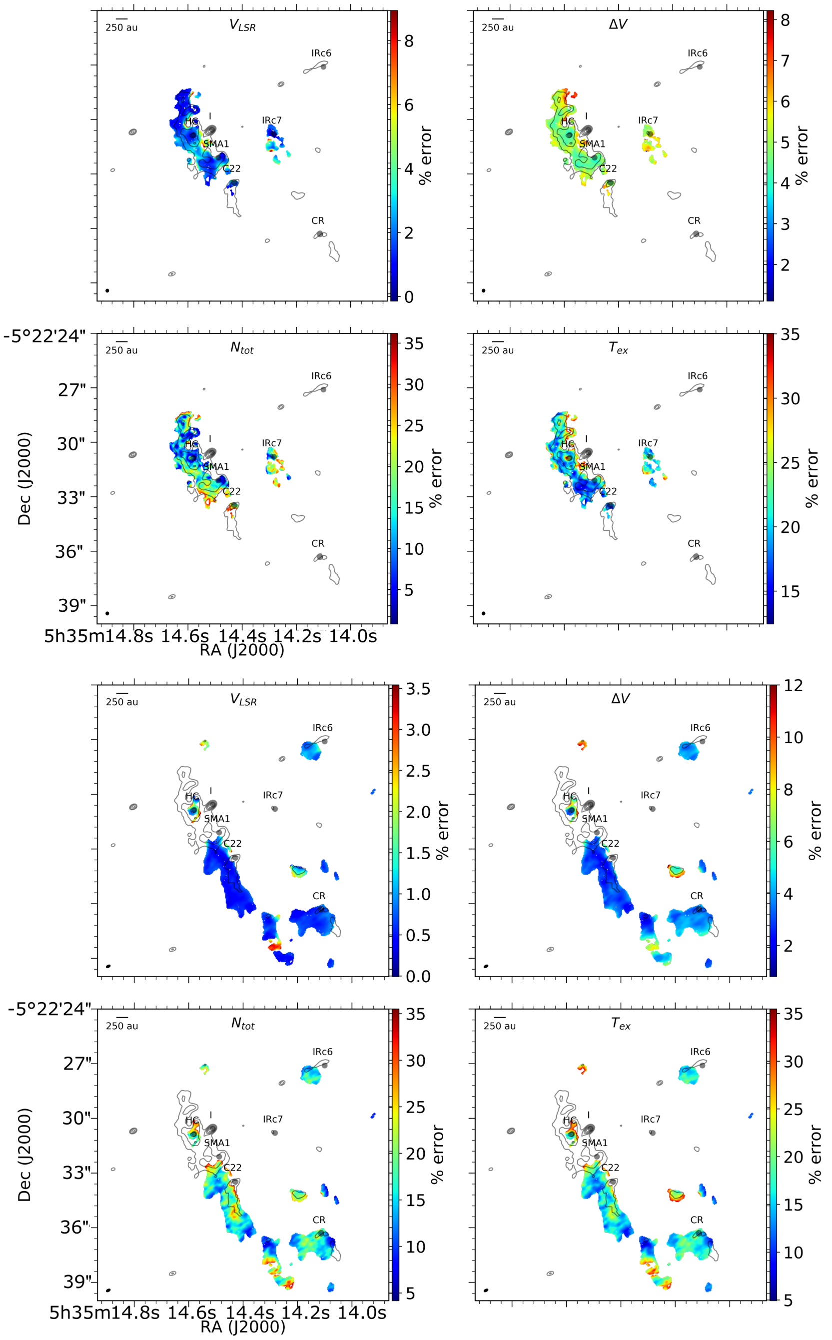

Figure B.1: Propagated percent error uncertainty maps for Figures 2.6 and 2.7, showing uncertainties for full resolution (first row) CH_3CN $v_8 = 1$ velocity field and line width field; (second row) CH_3CN $v_8 = 1$ total column density and excitation temperature; (third row) $^{13}CH_3OH$ velocity field and line width field; and (fourth row) $^{13}CH_3OH$ total column density and excitation temperature. Contours show the 2 mm (~150 GHz) continuum from the left panel of Figure 2.5.

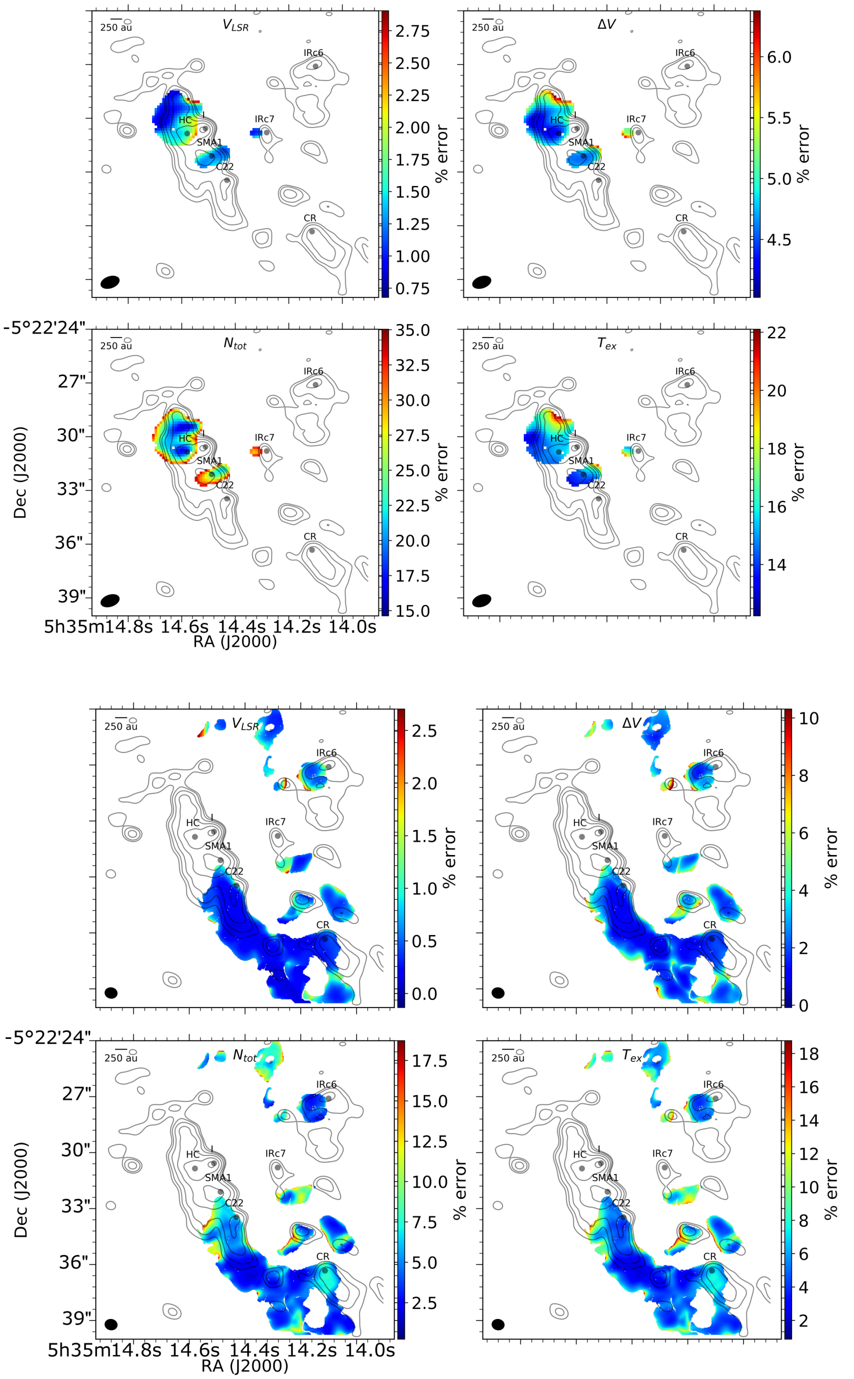

Figure B.2: Propagated percent error uncertainty maps for Figures 2.8 and 2.9, showing uncertainties for tapered resolution (first row) CH_3CN $\nu_8 = 1$ velocity field and line width field; (second row) CH_3CN $\nu_8 = 1$ total column density and excitation temperature; (third row) $^{13}CH_3OH$ velocity field and line width field; and (fourth row) $^{13}CH_3OH$ total column density and excitation temperature. Contours show the 2 mm (~150 GHz) continuum from the right panel of Figure 2.5.

Appendix C

INTERNAL VERSUS INTERNAL HEATING PROFILE MODELS

We ran simple models for different source sizes (with radii between 100 and 1000 au) and temperature gradients to test whether internally and externally heated sources are consistently characterized by $\Delta T_{\text{ex}} < 0$ and $\Delta T_{\text{ex}} > 0$, respectively, for the analyses presented in Chapter 2. The models calculated the temperature inside a full and tapered synthesized beam at various radii across two-dimensional Gaussian temperature profiles (both circular and elliptical). The models were run assuming both a smooth (unchanging) temperature background and a linear temperature gradient background. In all models, the sign of ΔT_{ex} accurately reflected whether a source of radius r_{src} was internally or externally heated at radii within $0.67r_{src}$ of the source center, with "higher contrast" source profiles (i.e., sources that have either much higher peak temperatures than their surroundings or particularly steep temperature gradients) being more likely to deviate from the predicted sign of ΔT_{ex} toward their outer radii. Smaller sources (e.g., with radii of 100 au) consistently had ΔT_{ex} values in agreement with their source of heating regardless of temperature contrast. In other words, within 100 au or more of a source's center (e.g., millimeter emission peak), the ΔT_{ex} sign is expected to accurately reflect whether that source is internally or externally heated. An example of the simple models used to test the sign of ΔT_{ex} is shown in Fig. C.1.

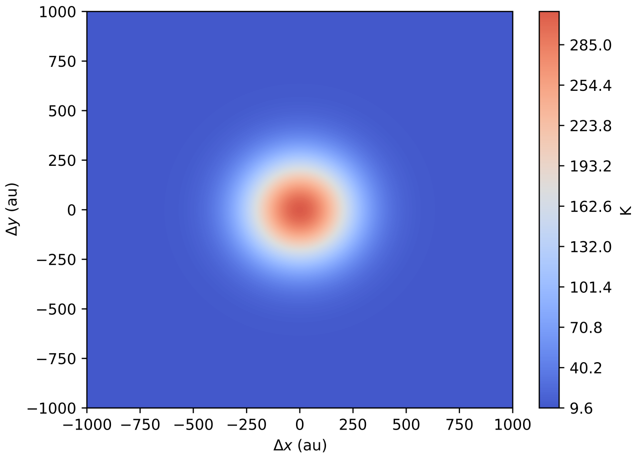

(a) Internal heating model

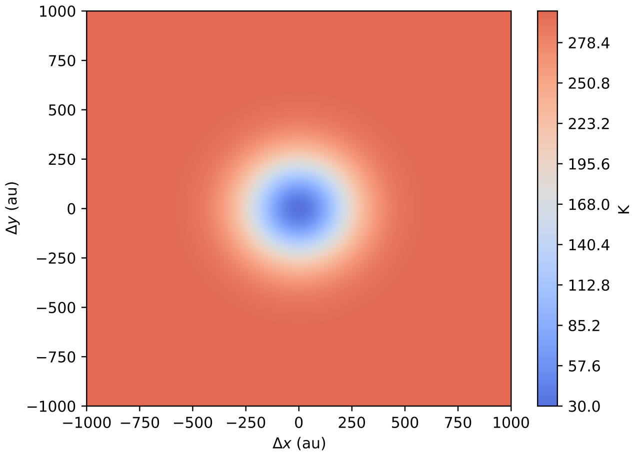

(b) External heating model

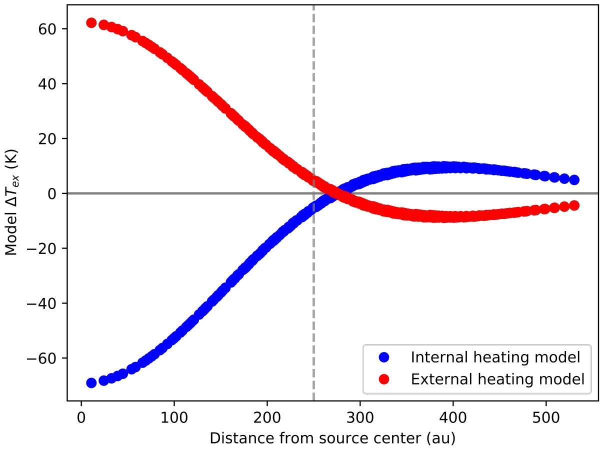

(c) ΔT_{ex}

Figure C.1: Example of the simple models used to test the sign of ΔT_{ex}. These plots show the temperature T_{ex} profile for an internally (a) and an externally (b) heated source with a radius of 250 au. The value of ΔT_{ex} (c) for each profile was measured at different radii from the source center. Here, the plot shows ΔT_{ex} with a small beam of $0\farcs2$ and a large beam of $0\farcs9$ (same used in the CH_3CN $v_8 = 1$ images).

Appendix D

POWER-LAW RELATIONSHIP BETWEEN ABUNDANCE AND TEMPERATURE

The radial temperature $T(r)$ and radial abundance $n(r)$ profiles for YSO envelopes can be described by the power-law functions

$$T(r) = T_{in} \left(\frac{r}{r_{in}} \right)^{-q} \tag{D.1}$$

and

$$n(r) = n_{in} \left(\frac{r}{r_{in}} \right)^{-p} \tag{D.2}$$

where T_{in} and n_{in} are the temperature and abundance at an arbitrary radius r_{in}. The power-law indices are q and p for the temperature and density profiles, respectively (Gieser et al., 2021).

Solving for radius r, Equations D.1 and D.2 can be transformed into

$$r = r_{in} \left(\frac{T}{T_{in}} \right)^{-1/q} \tag{D.3}$$

and

$$r = r_{in} \left(\frac{n}{n_{in}} \right)^{-1/p}. \tag{D.4}$$

Setting Equations D.3 and D.4 equal to each other and solving for density n yields

$$n = n_{in} \left(\frac{T}{T_{in}} \right)^{p/q} \tag{D.5}$$

which is always increasing for $p, q > 0$. This explains the general increase in column density with increasing rotation temperature seen, for example, in Figure 4.3.

References

Gieser, C., Beuther, H., Semenov, D., et al. 2021, *Astron. Astrophys.*, 648, A66, doi: `10.1051/0004-6361/202039670`

Appendix E

LOSS CALCULATIONS OF CH_3OD BY REACTIONS WITH OH

We considered the possible loss of gas-phase CH_3OD by the neutral-radical reaction with the hydroxyl radical (OH),

$$CH_3OH + OH \longrightarrow CH_3O + H_2O \tag{E.1}$$

$$CH_3OH + OH \longrightarrow CH_2OH + H_2O \tag{E.2}$$

which has been well studied by both theorists and experimentalists (e.g., Shannon et al., 2013; Acharyya et al., 2015; Gao et al., 2018; Heard, 2018). However, the rate coefficient of this reaction is about two orders of magnitude larger at 60 K, where the methyoxy radical (CH_3O, Equation E.1) is the dominant product, than at 200 K, where the hydroxymethyl radical (CH_2OH, Equation E.2) dominates (Shannon et al., 2013). At 200 K, the combined rate constant for Equations E.1 and E.2 is reported to be $k = 3.94 \times 10^{-13}$ cm^3 s^{-1} for CH_3OH + OH (Gao et al., 2018). Because of kinetic isotope effects, the actual rate constant is lower (and thus the reaction even slower) for the heavier CH_3OD isotopologue.

We estimate that the reactions in Equations E.1 and E.2 alone would require $\sim 10^5$ years to deplete the observed CH_3OD abundances in the Orion KL Hot Core-SW. The combined rate constant k for these two reactions gradually increases with temperature. For simplicity, we make temporal estimates using the value for 200 K, $k = 3.94 \times 10^{-13}$ cm^3 s^{-1}, reported by Gao et al. (2018).

Between 185 and 240 K in Figure 4.3b, there is a decrease in $N(CH_3OD)$ by about 2.5×10^{17} cm^{-2}, or—assuming an object depth of 2.9×10^{16} cm—$n(CH_3OD) \approx 8.7$ cm^{-3} from a maximum of 2.6×10^{17} cm^{-2} ≈ 9.0 cm^{-3}. The time for this decrease can be approximated as

$$dt = \frac{dn(CH_3OD)}{-k\ n(CH_3OD)} \tag{E.3}$$

where $n(CH_3OD)$ and $dn(CH_3OD)$ are 9.0 cm^{-3} and -8.7 cm^{-3}, respectively. The rate constant of $= 3.94 \times 10^{-13}$ cm^3 s^{-1} then suggests this reaction would take nearly 2.5×10^{12} seconds, or $\sim 10^5$ years, to deplete CH_3OD above 185 K, which is much longer than the assumed warm-up time of 10^3 yr that seems to explain the CH_3OD enrichment at temperatures of ~100-120 K.

References

Acharyya, K., Herbst, E., Caravan, R. L., et al. 2015, *Mol. Phys.*, 113, 2243, doi: `10.1080/00268976.2015.1021729`

Gao, L. G., Zheng, J., Fernández-Ramos, A., Truhlar, D. G., & Xu, X. 2018, *J. Am. Chem. Soc.*, 140, 2906, doi: `10.1021/jacs.7b12773`

Heard, D. E. 2018, *Acc. Chem. Res.*, 51, 2620, doi: `10.1021/acs.accounts.8b00304`

Shannon, R. J., Blitz, M. A., Goddard, A., & Heard, D. E. 2013, *Nat. Chem.*, 5, 745, doi: `10.1038/nchem.1692`

Appendix F

ACA SURVEY OBSERVATION DETAILS

An overview of the 1.2 mm ALMA observations analyzed in Chapters 5 and 6 is provided in Section 5.2. This work focuses on data from 7-meter Atacama Compact Array (ACA) Band 6 observations at ~251 GHz, which we refer to as the “upper” local oscillator (LO) setting. This data set also incorporates observations with the Total Power (TP) Array, which uses up to four 12-meter antennas; TP observations are outlined here for reference in future work. Here, we detail the ACA and the Total Power (TP) array observations toward each source in both the “lower” (~226 GHz) and “upper” (~251 GHz) LO settings, by BGPS ID, to complement the target and image properties listed in Tables 5.1 and 5.2 as well as to introduce the complete data set for ALMA project #2018.1.01259.

F.1 BGPS 3053

ACA observations toward BGPS 3053 consisted of 105 pointings. From the lower Band 6 observations, two executed observing blocks were used for imaging, with 10 antennas on 2019 April 28 and 9 antennas on 2019 April 29, both with a time on source of ~4000 seconds. A third execution block with 9 antennas on 2019 April 29 was disregarded in data imaging because it was terminated early after ~2210 seconds and thus does not incorporate all pointings over BGPS 3053. Upper Band 6 ACA data were taken from two execution blocks with 10 antennas each on 2019 May 05. These observations use J1832-1035 as a phase and WVR calibrator and J1924-2914 as an atmospheric, bandpass, flux, pointing, and WVR calibrator.

TP observations in lower Band 6 were taken over four execution blocks using 3 antennas on 2019 March 12, 3 antennas on 2019 March 17, and two blocks of 4 antennas on 2019 May 03 (one of which was at low elevation). In upper Band 6, there were three TP execution blocks of 4 antennas on 2019 May 06 and May 25 and 3 antennas on 2019 June 01.

F.2 BGPS 3474

ACA observations toward BGPS 3474 consisted of 115 pointings. The lower Band 6 observations were carried out in two execution blocks of ten antennas each on 2019 May 22. Upper Band 6 observations were made in two execution blocks of 11 antennas on 2019 May 25 and 10 antennas on 2019 May 29. J1832-1035 was used as a phase and WVR calibrator, J1924-2914 was used as an atmospheric, bandpass, flux, pointing, and WVR calibrator.

Lower Band 6 TP observations were taken over four execution blocks, three with 3 antennas on 2019 June 02 and one with 3 antennas on 2019 June 03. The upper band 6 TP observations were taken using 2 antennas on 2019 August 21 and 3 antennas on 2019 September 25; these data have baseline residuals due to precipitable water vapor (0.5 and 1.8 mm, respectively).

F.3 BGPS 4449

ACA observations toward BGPS 4449 consisted of 105 pointings. In the lower Band 6 observations, two execution blocks were carried out on 2019 May 20 with 11 antennas each. Upper Band 6 observations were made with 11 antennas on 2019 May 25 and 10 antennas on 2019 May 29. J1851+0035 was used as a phase, pointing, and WVR calibrator, and J1907+0127 was used as an atmospheric, phase, and WVR calibrator.

TP observations in lower Band 6 were made over four execution blocks of 2 antennas each between 2019 August 20 and 2019 August 27. Three execution blocks of 2 antennas each on 2019 August 19-20 for upper Band 6. To avoid galactic contamination, the off-pointing positions for calibrating the TP observations were made about 3.5° away, which is not ideal for calibration and results in noisy baselines in some of the spectral windows.

F.4 BGPS 5623

ACA observations toward BGPS 5623 were made with 105 pointings. Lower Band 6 ACA observations were carried out with two execution blocks of 10 antennas on 2019 May 05. This was the same for upper Band 6 but on 2019 May 22 and 29. J1924-2914 was used as an atmospheric, bandpass, flux, pointing, and WVR calibrator, and J1851+0035 was used as a phase, pointing, and WVR calibrator.

Lower Band 6 TP observations were carried out with three execution blocks of 4 antennas each on 2019 May 04, 05, and 06. Upper Band 6 observations were carried out in three execution blocks of 2 antennas each on 2019 August 15 and 17.

F.5 BGPS 6029

ACA observations toward BGPS 6029 were made with 85 pointings. Lower Band 6 observations were carried out in two execution blocks of 11 antennas each on 2019 May 12 and 18. Upper Band 6 ACA observations were carried out in two execution blocks of 10 antennas each on 2019 May 21-22. J1851+0035 was used as an atmospheric, phase, and WVR calibrator, and J1924-2914 was used as an atmospheric, bandpass, flux, pointing, and WVR calibrator.

TP observations in lower Band 6 were carried out in two execution blocks of 3 antennas each on 2019 June 04. Upper Band 6 TP observations were carried out in two execution blocks with 3 antennas on 2019 June 04 and 2 antennas on 2019 August 07.

F.6 BGPS 6082, BGPS 6112, BGPS 6299, and BGPS 6318

BGPS 6082, BGPS 6112, BGPS 6299, and BGPS 6318 were all observed during the same execution blocks. ACA lower Band 6 observations were taken during two execution blocks of 9 antennas each on 2019 April 29 and 2019 May 01. Upper band 6 observations were taking in two execution blocks of 9 antennas each on 2019 May 02-03. J1935+2031 was used as an atmospheric, phase, and WVR calibrator, and J1924-2914 was an atmospheric, bandpass, flux, pointing, and WVR calibrator.

There were five TP execution blocks in lower Band 6 of 4 antennas on 2018 October 28, 4 antennas on 2019 March 22, 3 antennas on 2019 April 09, 4 antennas on 2019 April 17, and 4 antennas on 2019 April 22. In upper Band 6, there were four execution blocks of 3 antennas on 2019 April 30, 3 antennas on 2019 May 01, and two blocks of 4 antennas on 2019 May 04.

F.7 BGPS 6120

ACA observations of BGPS 6120 were carried out in 105 pointings. In the lower band, there were two execution blocks of 9 antennas on 2019 May 03 and 11 antennas on 2019 May 04. Upper Band 6 observations were carried out in two execution blocks of 11 antennas on 2019 May 11 and 18. J1924-2914 was used as an atmospheric, bandpass, flux, pointing, and WVR calibrator; J1935+2031 was used as an atmospheric, phase, and WVR calibrator.

TP observations in lower Band 6 consisted of three execution blocks of 3 antennas on 2019 May 29, 4 antennas on 2019 June 02, and 3 antennas on 2019 June 04. Two executions of upper Band 6 TP observations were attempted but did not pass quality assurance. Therefore, there are not TP data for the upper Band 6 toward BGPS 6120.

F.8 BGPS 6310

ACA observations toward BGPS 6310 were carried out with 105 pointings. Lower Band 6 observations were carried out in two execution blocks of 9 antennas on 2019 May 02-03. Upper Band 6 ACA observations were taken with 11 antennas during two execution blocks on 2019 May 04. Calibrators were J1924-2914 for atmosphere, bandpass, flux, pointing, and WVR; J1924+1540 for pointing and WVR; and J1935+2031 for atmosphere, phase, and WVR.

TP observations in the lower band were carried out in three execution blocks with 3 antennas each on 2019 April 27-28 and 2019 May 02. Upper Band 6 TP observations were taken in three execution blocks of 4 antennas on 2019 May 25, 2 antennas on 2019 May 31, and 3 antennas on 2019 June 01.

Appendix G

CALCULATING DISTANCE UNCERTAINTY

The kinematic distances d_{kin} reported by Battisti & Heyer (2014) were calculated using the size-velocity dispersion relationship for molecular clouds

$$D_{svd} = \frac{1}{\theta}\left({\frac{\Sigma_{GMC}}{100\ M_\odot\ \mathrm{pc}^{-2}}}^{-1}\right)\left(\frac{\sigma_v}{v_o}\right)^2\ \mathrm{pc} \tag{G.1}$$

where θ is the angular radius of the cloud in radians, Σ_{GMC} is the surface density of the cloud in $M_\odot$ pc^{-2}, σ_v is the velocity dispersion, and $v_o = 0.7 \pm 0.07$ km s^{-1} pc$^{-1/2}$ (Heyer et al., 2009) is defined by

$$v_o = {\frac{\sigma_v}{\Sigma_{GMC} R}}^{1/2} \tag{G.2}$$

for cloud size R and is nearly constant for clouds within the disk of the Milky Way.

The propagation for uncertainty in the distance $\sigma(d_{kin})$ then follows Equation G.3.

$$\sigma(d_{kin}) = |d_{kin}|\sqrt{\left(\frac{\sigma(\Sigma_{GMC})}{|\Sigma_{GMC}|}\right)^2 + 2\left(\frac{\sigma(\sigma_v)}{|\sigma_v|}\right)^2 + 2\left(\frac{\sigma(v_o)}{|v_o|}\right)^2} \tag{G.3}$$

The uncertainty in surface density (Equation 5.1) is derived from uncertainty in GMC mass M_{GMC} and radius R_{GMC} reported by Battisti & Heyer such that

$$\sigma(\Sigma_{GMC}) = |\Sigma_{GMC}|\sqrt{\left(\frac{\sigma(M_{GMC})}{M_{GMC}}\right)^2 + 2\left(\frac{\sigma(R_{GMC})}{R_{GMC}}\right)^2}. \tag{G.4}$$

The velocity dispersion σ_v and associated uncertainty for reach GMC are also taken from Battisti & Heyer, and the third term in Equation G.3 is 0.02 for all GMCs. Rearranging Equation G.4 and substituting that and 0.02 for the first and third terms in Equation G.3, we propagate the distance uncertainty by

$$\sigma(d_{kin}) = |d_{kin}|\sqrt{\left(\frac{\sigma(M_{GMC})}{|M_{GMC}|}\right)^2 + 2\left(\frac{\sigma(R_{GMC}}{|R_{GMC}|})\right)^2 + 2\left(\frac{\sigma(\sigma_v)}{|\sigma_v|}\right)^2 + 0.02}. \tag{G.5}$$

References

Battisti, A. J., & Heyer, M. H. 2014, *Astrophys. J.*, 780, 173, doi: `10.1088/0004-637X/780/2/173`

Heyer, M., Krawczyk, C., Duval, J., & Jackson, J. M. 2009, *Astrophys. J.*, 699, 1092, doi: `10.1088/0004-637X/699/2/1092`

Appendix H

SUMMARY OF DETECTED MOLECULAR-RING OBJECTS

A summary of objects detected in the pilot ACA survey presented in Chapter 5 is given in Table H.1. Objects are separated by their respective GMCs, for which there are subheadings including the BGPS ID followed by the BGPS name in parentheses. All millimeter objects are numbered mm1, mm2, ... in order of decreasing peak flux S_{peak}. Detection significance is given with respect to σ_{rms} listed in Table 5.2.

Table H.1: Detected objects in molecular-ring GMCs at 245 GHz (1.2 mm)

ID	$\alpha_{\rm J2000}$	$\delta_{\rm J2000}$	S_{peak} (mJy beam^{-1})	Detection Significance
BGPS 3053 (G023.368−00.290)				
mm1	$18^{\rm h}34^{\rm m}54^{\rm s}.10$	$-08^\circ38'24''.1$	67.3	39.6σ
mm2	$18^{\rm h}34^{\rm m}54^{\rm s}.09$	$-08^\circ38'20''.8$	58.9	34.6σ
mm3	$18^{\rm h}34^{\rm m}49^{\rm s}.81$	$-08^\circ37'10''.3$	29.9	17.6σ
mm4	$18^{\rm h}34^{\rm m}47^{\rm s}.96$	$-08^\circ36'33''.8$	20.3	11.9σ
mm5	$18^{\rm h}34^{\rm m}54^{\rm s}.57$	$-08^\circ38'10''.9$	19.4	11.4σ
mm6	$18^{\rm h}34^{\rm m}49^{\rm s}.66$	$-08^\circ38'28''.9$	18.1	10.6σ
mm7	$18^{\rm h}34^{\rm m}48^{\rm s}.94$	$-08^\circ38'19''.7$	17.8	10.5σ
mm8	$18^{\rm h}34^{\rm m}50^{\rm s}.91$	$-08^\circ39'20''.4$	16.9	9.9σ
mm9	$18^{\rm h}34^{\rm m}34^{\rm s}.56$	$-08^\circ38'08''.5$	13.0	7.6σ
mm10	$18^{\rm h}34^{\rm m}49^{\rm s}.35$	$-08^\circ38'19''.7$	12.3	7.2σ
mm11	$18^{\rm h}34^{\rm m}47^{\rm s}.96$	$-08^\circ36'18''.5$	12.0	7.1σ
mm12	$18^{\rm h}34^{\rm m}50^{\rm s}.37$	$-08^\circ39'00''.8$	8.9	5.2σ
mm13	$18^{\rm h}34^{\rm m}48^{\rm s}.48$	$-08^\circ37'42''.9$	8.5	5.0σ
BGPS 3474 (G025.227+00.289)				
mm1	$18^{\rm h}36^{\rm m}16^{\rm s}.76$	$-06^\circ43'18''.5$	206.9	129.3σ
mm2	$18^{\rm h}36^{\rm m}15^{\rm s}.62$	$-06^\circ43'05''.0$	35.9	22.4σ
mm3	$18^{\rm h}36^{\rm m}16^{\rm s}.50$	$-06^\circ43'34''.4$	13.6	8.5σ
BGPS 4449 (G030.536+00.021)				
mm1	$18^{\rm h}46^{\rm m}59^{\rm s}.39$	$-02^\circ07'25''.1$	273.6	171.0σ
mm2	$18^{\rm h}46^{\rm m}55^{\rm s}.18$	$-02^\circ08'17''.7$	44.2	27.6σ
BGPS 5623 (G030.952−00.389)				
mm1	$18^{\rm h}57^{\rm m}05^{\rm s}.29$	$+02^\circ06'30''.1$	121.2	55.1σ
mm2	$18^{\rm h}56^{\rm m}59^{\rm s}.13$	$+02^\circ04'54''.9$	64.6	29.4σ
mm3	$18^{\rm h}57^{\rm m}09^{\rm s}.11$	$+02^\circ08'20''.8$	26.2	11.9σ
mm4	$18^{\rm h}57^{\rm m}09^{\rm s}.45$	$+02^\circ07'52''.9$	23.1	10.5σ
mm5	$18^{\rm h}57^{\rm m}06^{\rm s}.91$	$+02^\circ08'24''.1$	19.6	8.9σ
mm6	$18^{\rm h}57^{\rm m}11^{\rm s}.30$	$+02^\circ07'27''.6$	14.8	6.7σ
mm7	$18^{\rm h}57^{\rm m}09^{\rm s}.03$	$+02^\circ08'28''.0$	10.7	4.9σ
mm8	$18^{\rm h}57^{\rm m}10^{\rm s}.61$	$+02^\circ07'43''.6$	10.4	4.7σ
BGPS 6029 (G040.622−00.139)				
mm1	$1^{\rm h}06^{\rm m}01^{\rm s}.54$	$06^\circ46'35''.2$	386.6	203.5σ
BGPS 6082 (G041.741+00.095)				
mm1	$1^{\rm h}07^{\rm m}15^{\rm s}.51$	$07^\circ52'43''.5$	108.5	77.5σ
BGPS 6112 (G043.079−00.005)				
mm1	$1^{\rm h}10^{\rm m}04^{\rm s}.40$	$+09^\circ01'12''.3$	68.3	56.9σ
mm2	$1^{\rm h}10^{\rm m}07^{\rm s}.72$	$+09^\circ01'16''.5$	32.0	26.7σ
mm3	$1^{\rm h}10^{\rm m}09^{\rm s}.54$	$+09^\circ01'26''.4$	25.7	21.4σ
mm4	$1^{\rm h}10^{\rm m}05^{\rm s}.92$	$+09^\circ01'16''.0$	19.9	16.6σ
mm5	$1^{\rm h}10^{\rm m}03^{\rm s}.06$	$+09^\circ00'07''.9$	12.0	10.0σ
mm6	$1^{\rm h}10^{\rm m}04^{\rm s}.95$	$+09^\circ01'16''.3$	13.7	11.4σ
mm7	$1^{\rm h}10^{\rm m}04^{\rm s}.78$	$+09^\circ01'07''.2$	7.9	6.6σ

Table H.1: Detected objects in molecular-ring GMCs *(continued)*

ID	$\alpha_{\rm J2000}$	$\delta_{\rm J2000}$	S_{peak} (mJy beam^{-1})	Detection Significance
BGPS 6120 (G043.237−00.047)				
mm1	$1^{\rm h}10^{\rm m}33^{\rm s}.69$	$+09^{\circ}08'23''.3$	509.1	363.6σ
mm2	$1^{\rm h}10^{\rm m}33^{\rm s}.45$	$+09^{\circ}08'36''.6$	39.8	28.4σ
mm3	$1^{\rm h}10^{\rm m}30^{\rm s}.77$	$+09^{\circ}07'56''.2$	27.4	19.6σ
mm4	$1^{\rm h}10^{\rm m}30^{\rm s}.49$	$+09^{\circ}07'43''.5$	18.4	13.1σ
mm5	$1^{\rm h}10^{\rm m}33^{\rm s}.70$	$+09^{\circ}06'51''.8$	18.0	12.9σ
mm6	$1^{\rm h}10^{\rm m}33^{\rm s}.04$	$+09^{\circ}07'50''.6$	16.5	11.8σ
mm7	$1^{\rm h}10^{\rm m}35^{\rm s}.98$	$+09^{\circ}07'51''.8$	13.7	9.6σ
mm8	$1^{\rm h}10^{\rm m}34^{\rm s}.98$	$+09^{\circ}08'20''.8$	10.1	7.2σ
mm9	$1^{\rm h}10^{\rm m}33^{\rm s}.31$	$+09^{\circ}07'38''.3$	9.1	6.5σ
mm10	$1^{\rm h}10^{\rm m}28^{\rm s}.79$	$+09^{\circ}08'45''.6$	8.6	6.1σ
mm11	$1^{\rm h}10^{\rm m}32^{\rm s}.00$	$+09^{\circ}07'41''.7$	8.1	5.8σ
BGPS 6299 (G049.070−00.350)				
mm1	$1^{\rm h}22^{\rm m}47^{\rm s}.82$	$+14^{\circ}09'30''.9$	61.7	34.3σ
mm2	$1^{\rm h}22^{\rm m}42^{\rm s}.43$	$+14^{\circ}09'53''.1$	43.3	24.1σ
mm3	$1^{\rm h}22^{\rm m}48^{\rm s}.05$	$+14^{\circ}09'48''.5$	33.5	18.6σ
mm4	$1^{\rm h}22^{\rm m}47^{\rm s}.37$	$+14^{\circ}09'23''.2$	27.8	15.4σ
mm5	$1^{\rm h}22^{\rm m}42^{\rm s}.25$	$+14^{\circ}10'04''.8$	26.7	14.8σ
mm6	$1^{\rm h}22^{\rm m}47^{\rm s}.44$	$+14^{\circ}08'49''.8$	22.6	12.5σ
mm7	$1^{\rm h}22^{\rm m}42^{\rm s}.04$	$+14^{\circ}10'08''.9$	21.9	12.2σ
mm8	$1^{\rm h}22^{\rm m}47^{\rm s}.01$	$+14^{\circ}09'26''.4$	21.4	11.9σ
mm9	$1^{\rm h}22^{\rm m}47^{\rm s}.68$	$+14^{\circ}09'45''.7$	21.2	11.8σ
mm10	$1^{\rm h}22^{\rm m}46^{\rm s}.74$	$+14^{\circ}09'25''.4$	17.3	34.3σ
mm11	$1^{\rm h}22^{\rm m}47^{\rm s}.68$	$+14^{\circ}09'08''.1$	16.3	9.1σ
mm12	$1^{\rm h}22^{\rm m}46^{\rm s}.79$	$+14^{\circ}09'07''.8$	14.7	8.2σ
mm13	$1^{\rm h}22^{\rm m}48^{\rm s}.16$	$+14^{\circ}09'42''.0$	13.6	7.6σ
mm14	$1^{\rm h}22^{\rm m}41^{\rm s}.48$	$+14^{\circ}09'04''.1$	13.6	7.5σ
mm15	$1^{\rm h}22^{\rm m}43^{\rm s}.54$	$+14^{\circ}09'03''.3$	12.4	6.9σ
mm16	$1^{\rm h}22^{\rm m}47^{\rm s}.07$	$+14^{\circ}10'07''.3$	10.5	5.8σ
mm17	$1^{\rm h}22^{\rm m}49^{\rm s}.29$	$+14^{\circ}10'19''.2$	9.3	5.2σ
mm18	$1^{\rm h}22^{\rm m}46^{\rm s}.48$	$+14^{\circ}10'00''.3$	8.6	4.8σ
mm19	$1^{\rm h}22^{\rm m}48^{\rm s}.20$	$+14^{\circ}10'05''.8$	8.4	4.7σ
mm20	$1^{\rm h}22^{\rm m}49^{\rm s}.01$	$+14^{\circ}10'09''.9$	7.6	4.2σ

Table H.1: Detected objects in molecular-ring GMCs *(continued)*

ID	$\alpha_{\rm J2000}$	$\delta_{\rm J2000}$	S_{peak} (mJy beam^{-1})	Detection Significance
BGPS 6310 (G049.170−00.208)				
mm1	$1^{\rm h}22^{\rm m}26^{\rm s}.99$	$+14^\circ18'47''.3$	60.5	50.4σ
mm2	$1^{\rm h}22^{\rm m}27^{\rm s}.58$	$+14^\circ18'56''.0$	39.4	32.8σ
mm3	$1^{\rm h}22^{\rm m}29^{\rm s}.52$	$+14^\circ18'48''.7$	35.4	29.5σ
mm4	$1^{\rm h}22^{\rm m}26^{\rm s}.87$	$+14^\circ17'40''.2$	26.7	22.3σ
mm5	$1^{\rm h}22^{\rm m}26^{\rm s}.09$	$+14^\circ18'56''.5$	26.2	21.8σ
mm6	$1^{\rm h}22^{\rm m}27^{\rm s}.00$	$+14^\circ19'33''.6$	25.6	21.4σ
mm7	$1^{\rm h}22^{\rm m}27^{\rm s}.81$	$+14^\circ18'24''.5$	17.1	14.3σ
mm8	$1^{\rm h}22^{\rm m}24^{\rm s}.20$	$+14^\circ20'05''.9$	16.6	13.8σ
mm9	$1^{\rm h}22^{\rm m}25^{\rm s}.47$	$+14^\circ18'48''.1$	15.4	12.8σ
mm10	$1^{\rm h}22^{\rm m}28^{\rm s}.87$	$+14^\circ17'54''.1$	14.2	11.9σ
mm11	$1^{\rm h}22^{\rm m}26^{\rm s}.33$	$+14^\circ19'15''.1$	14.2	11.8σ
mm12	$1^{\rm h}22^{\rm m}27^{\rm s}.74$	$+14^\circ19'23''.6$	12.1	10.1σ
mm13	$1^{\rm h}22^{\rm m}24^{\rm s}.41$	$+14^\circ18'52''.6$	11.7	9.7σ
mm14	$1^{\rm h}22^{\rm m}27^{\rm s}.89$	$+14^\circ18'11''.6$	11.5	9.6σ
mm15	$1^{\rm h}22^{\rm m}24^{\rm s}.48$	$+14^\circ18'40''.5$	11.2	9.3σ
mm16	$1^{\rm h}22^{\rm m}26^{\rm s}.52$	$+14^\circ19'44''.8$	9.4	7.9σ
mm17	$1^{\rm h}22^{\rm m}24^{\rm s}.17$	$+14^\circ19'44''.0$	9.1	7.6σ
mm18	$1^{\rm h}22^{\rm m}27^{\rm s}.61$	$+14^\circ19'57''.4$	8.9	7.4σ
mm19	$1^{\rm h}22^{\rm m}29^{\rm s}.63$	$+14^\circ18'14''.4$	8.0	6.7σ
mm20	$1^{\rm h}22^{\rm m}27^{\rm s}.39$	$+14^\circ18'07''.2$	7.5	6.2σ
mm21	$1^{\rm h}22^{\rm m}25^{\rm s}.62$	$+14^\circ17'59''.5$	6.4	5.4σ
mm22	$1^{\rm h}22^{\rm m}27^{\rm s}.41$	$+14^\circ17'48''.5$	6.4	5.4σ
mm23	$1^{\rm h}22^{\rm m}30^{\rm s}.81$	$+14^\circ19'31''.0$	6.3	5.3σ
mm24	$1^{\rm h}22^{\rm m}24^{\rm s}.05$	$+14^\circ19'24''.2$	6.3	5.3σ
mm25	$1^{\rm h}22^{\rm m}23^{\rm s}.99$	$+14^\circ18'30''.0$	6.1	5.1σ
mm26	$1^{\rm h}22^{\rm m}30^{\rm s}.20$	$+14^\circ19'08''.9$	5.8	4.8σ
mm27	$1^{\rm h}22^{\rm m}26^{\rm s}.46$	$+14^\circ18'40''.9$	5.5	4.6σ
mm28	$1^{\rm h}22^{\rm m}24^{\rm s}.05$	$+14^\circ18'04''.5$	5.5	4.6σ
BGPS 6318 (G049.255−00.412)				
mm1	$1^{\rm h}23^{\rm m}21^{\rm s}.25$	$+14^\circ17'20''.8$	41.9	27.9σ
mm2	$1^{\rm h}23^{\rm m}23^{\rm s}.60$	$+14^\circ17'54''.5$	6.4	4.3σ

Appendix I

MOLECULAR RING GMCS DERIVED PARAMETER UNCERTAINTY MAPS

Percent uncertainty maps were calculated from the derived `LMFIT` standard errors for the rotation temperature and column density maps presented in Chapter 6. These uncertainty maps are presented in Figures I.1-I.9. For most objects, the rotation temperature and column density uncertainties are ≤10% near the millimeter continuum emission peak for each fitted region. Higher uncertainty is seen toward the edges of the fitted regions, which is expected since the emission falls off and noiser and hence more difficult to fit robustly.

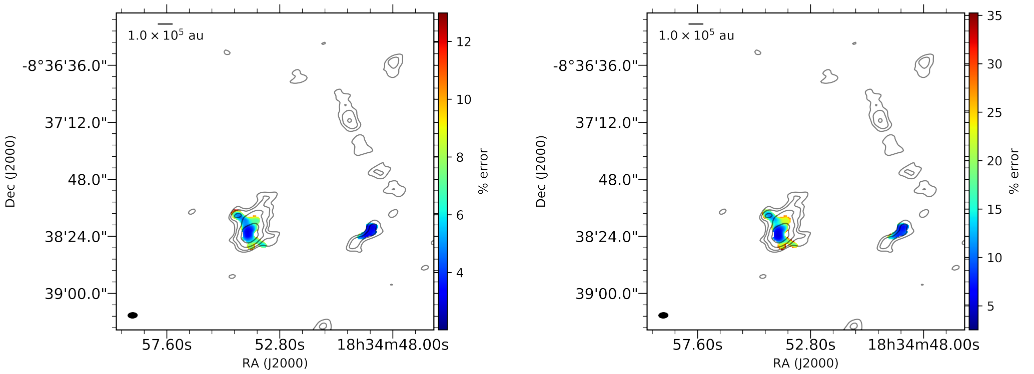

Figure I.1: Percent uncertainty maps for the derived CH_3OH rotation temperature (left) and column density (right) in BGPS 3053.

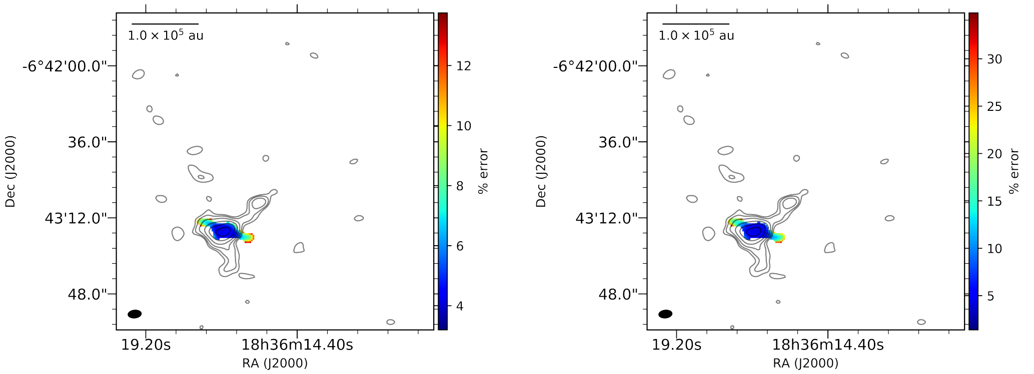

Figure I.2: Percent uncertainty maps for the derived CH_3OH rotation temperature (left) and column density (right) in BGPS 3474.

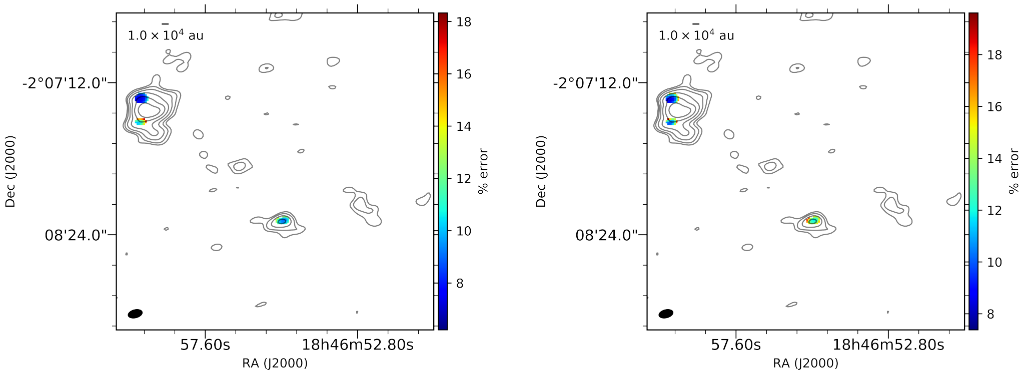

Figure I.3: Percent uncertainty maps for the derived CH_3OH rotation temperature (left) and column density (right) in BGPS 4449.

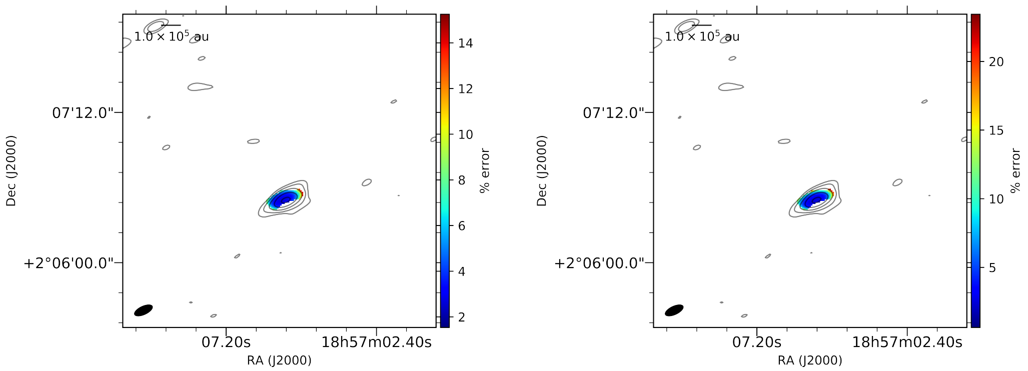

Figure I.4: Percent uncertainty maps for the derived CH_3OH rotation temperature (left) and column density (right) in BGPS 5623.

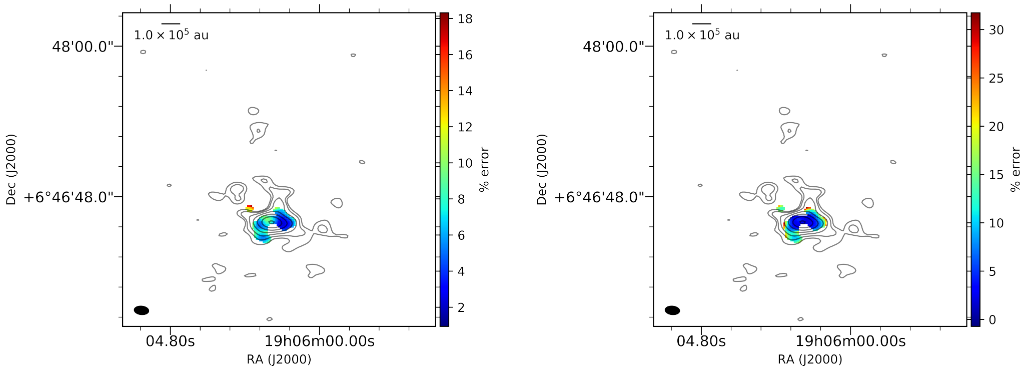

Figure I.5: Percent uncertainty maps for the derived CH_3OH rotation temperature (left) and column density (right) in BGPS 6029.

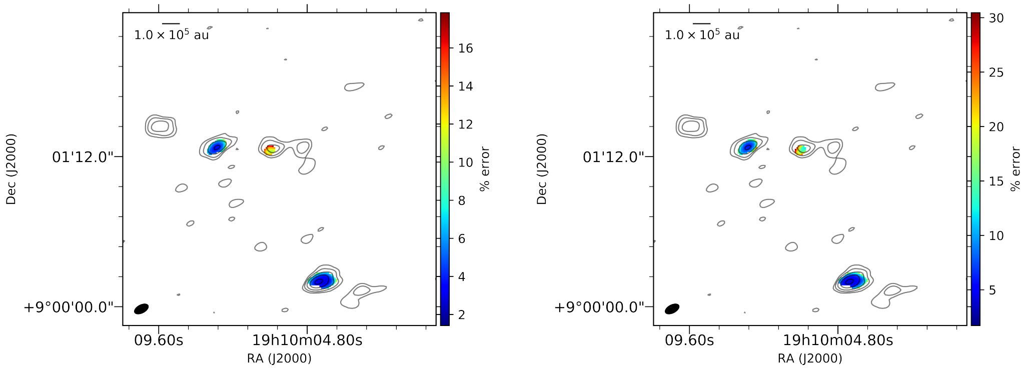

Figure I.6: Percent uncertainty maps for the derived CH_3OH rotation temperature (left) and column density (right) in BGPS 6112.

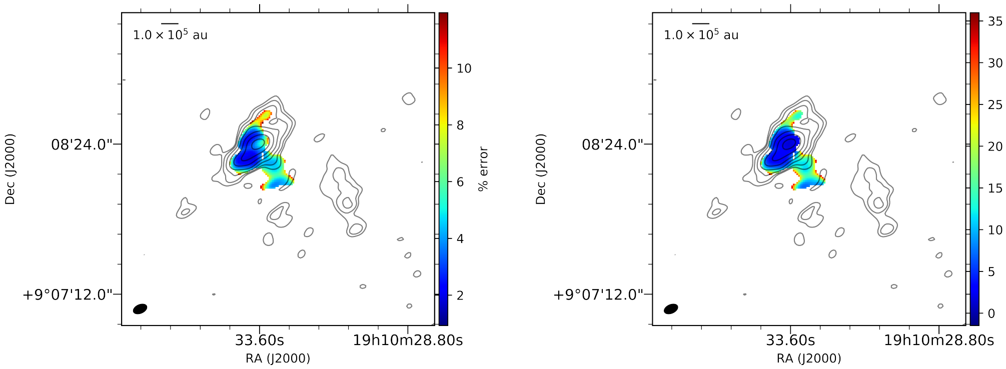

Figure I.7: Percent uncertainty maps for the derived CH_3OH rotation temperature (left) and column density (right) in BGPS 6120.

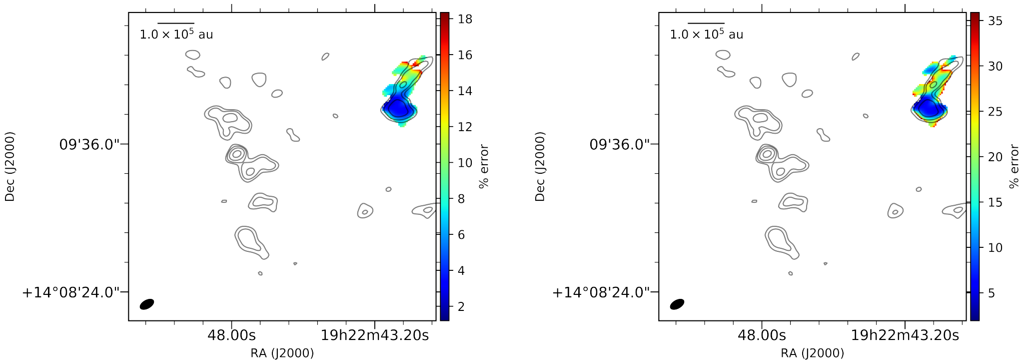

Figure I.8: Percent uncertainty maps for the derived CH_3OH rotation temperature (left) and column density (right) in BGPS 6299.

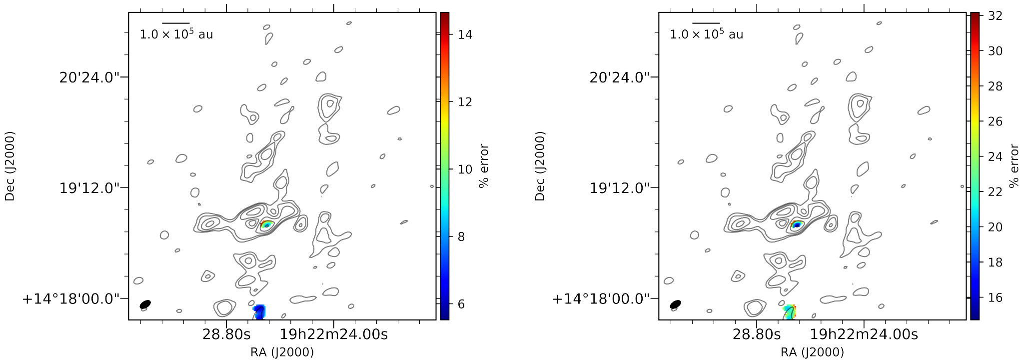

Figure I.9: Percent uncertainty maps for the derived CH_3OH rotation temperature (left) and column density (right) in BGPS 6310.

Appendix J

SUMMARY OF GRADUATE TEACHING

My graduate experience at Caltech has given me the opportunity to grow not only as a researcher but as an educator. While this is not the primary goal of the chemistry Ph.D. program at Caltech, developing my teaching has nonetheless been one of the most rewarding aspects of my graduate tenure. As such, a summary of my graduate teaching deserves a place in my thesis because it has shaped who I am as a scientist.

When I arrived on campus in Fall 2016, teaching was not required to complete a chemistry Ph.D. I requested to be the teaching assistant (TA) for Ch/ChE 91: Scientific Writing because of my passion for working in the Eberly Writing Center at Dickinson College as an undergraduate. I began teaching with Prof. Carl Parker that term, and I have taught the course with him every fall and winter term since then for a total of 11 terms. Carl referred to and treated me as his co-instructor, and he gave me the agency to test out different pedagogical practices. Along the way, I transformed the assignment prompts following a model of transparency in which skills learned and criteria for success are explicitly communicated with students; such approaches to teaching have been shown to help all and especially under-served students (Winkelmes, 2013). More transparent assignment prompts can also lessen the workload for instructors by making implicit expectations explicit, meaning I could provide more meaningful feedback on student writing while lessening the frequency of needing to make comments reminding students to include references. Carl also let me write the grading policy for the course. He gradually transferred more responsibilities with each term, allowing me to lead class meetings after a couple of years of observing him in this role.

In addition to being the Scientific Writing TA for 11 terms, I was a TA for Ge 128: Cosmochemistry (Fall 2019) taught by Prof. Geoff Blake. In this course, I provided additional insights during the lecture sections and co-led a lecture with my fellow TA, Cam Buzard. This course gave me the opportunity to grade assignments and practice fair grading practices; Cam and I were thoughtful in how we split up problem sets when grading, and we worked together to make sure that we had similar expectations. Cam and I also hosted office hours, which often turned into recitation sections where we helped students understand lecture concepts and bridge the concepts learned in the classroom to their application in the problem sets.

Cam and I also co-designed and co-taught two chemistry tutorial courses: Ch 101: Astrochemistry—Spectroscopy in Space (Spring 2017) and Ch 101: Chemistry throughout the Universe (Spring 2018). In these courses, we designed a progressive writing assignment that broke down a final term paper into smaller regularly-spaced assignments and a proposal writing assignment that gave students the opportunity to practice writing and defending a scientific justification. An overview and review of the first assignment was published in the *Prompt* journal (Wilkins & Buzard, 2018). In both of these courses, we also wrote the syllabus and prepared class meetings, including lecture and active learning components.

I designed and taught Ch 101: Communicating Chemistry (Spring 2019) in addition to the two astrochemistry-focused tutorials. For this course, I designed a series of assignments aimed at giving students exposure to a variety of science communication media in a low-stakes environment. These included Tweeting, popular writing, science sketching, presenting a lightning talk, and teaching the rest of the class about a type of science communication in a weekly SciComm Showcase.

In addition to developing my teaching as an instructor, I pursued formal training through the Center for Teaching, Learning, and Outreach (CTLO) and the Caltech Project for Effective Teaching (CPET). I completed both a Certificate of Interest in University Teaching and a Certificate of Practice in University Teaching, and I participated in E 110: Principles of University Teaching in STEM and Dr. Jenn Weaver's ABCs of Course Design short course. I also served as (co-)director of CPET between July 2017 and September 2019. During this time, I presented posters about CPET at several regional conferences and co-led a round-table discussion at the Professional Organizational Development (POD) Network conference with Jenn (Weaver & Wilkins, 2018). In addition, I facilitated one or two sessions at each of the five Caltech teaching conferences following my first year.

References

Weaver, J. E., & Wilkins, O. H. 2018, Successful Models of Graduate Student Teaching Certificates and Pedagogy Courses, POD Network Conference Portland

Wilkins, O. H., & Buzard, C. F. 2018, *Prompt*, 2, doi: `10.31719/pjaw.v2i1.18`

Winkelmes, M. 2013, *NEA Higher Education Advocate*, 30, 6

Appendix K

SUMMARY OF GRADUATE SERVICE

In addition to research and teaching, I have explored other ways to be an active member of the Caltech and broader scientific community.

On campus, I joined the Chemistry Graduate Studies Committee (CGSC) in 2017. As a member of CGSC, I reviewed the chemistry web pages with the aim of making the processes of being admitted to Ph.D. candidacy more transparent. I also took care to update information that was outdated by several years. I did similar work to update information about the end stages of the chemistry Ph.D. program as well. In CGSC, I also managed the chemistry T-shirts for two years and was part of the diversity, equity, and inclusion working group. I was one of the chemistry tutorial program facilitators beginning in 2018. As a facilitator, I reviewed chemistry tutorial course proposals and helped manage the program. I also designed and implemented training for graduate and postdoctoral instructors. I am most proud of my work successfully advocating to remove the GRE[1] from the chemistry graduate program application. I was quoted in *Chemical & Engineering News* (C&EN) about my experiences taking the GRE and a spreadsheet I set up for prospective students showing which chemistry programs require the GRE.[2]

I was involved in other parts of campus as well. I was a member of the Graduate Honor Council (GHC) between 2016 and 2019. I was also a graduate orientation leader three times, in 2017, 2019, and 2020. I joined with other graduate students to form the Graduate Student-Parent Advocacy Committee; as a student-parent, I advocated for increases in the dependent healthcare reimbursement and started a clothing bank for other student-parents. In 2019, I joined the inaugural cohort of the Caltech Diversity & Inclusion Ambassador (CDIA) program, and I regularly attended events and trainings hosted by the Center for Inclusion and Diversity, including Safezone training. Outside of these areas, I advocated for mental health, having written a viewpoint for *Caltech Letters* about my own struggles with mental health and some of the issues surrounding mental health in academia, both on- and off-campus. Prof. Scott Cushing and I addressed stigmatization of mental

---

[1] Graduate Requisite Exam

[2] Halford, B. (2019). Is there a future for the GRE? *Chemical & Engineering News*, 97(5), https://cen.acs.org/education/graduate-education/future-GRE/97/i5

health on campus by starting a monthly lunch centered around mental well-being and community-building, especially in chemistry.

One of my favorite activities has been to be a panelist in a variety of areas to share my experiences and answer questions from other people. At Caltech, I have been on panels about applying to the NSF GRFP[3] (2016) and Fulbright research fellowships (2017); graduate life at Caltech for orientation (2017, 2019, 2020); reading, writing, and research (2018) through the Hixon Writing Center; support structures in graduate school for the FUTURE of Physics conference for undergraduate women at Caltech (2019-2021); parenting dynamics (2019) through the Center for Inclusion and Diversity; and the student experience in Geological and Planetary Sciences for the FUTURE Ignited conference at Caltech (2021). I also was part of a career panel for the Goldwater Scholar Community Symposium (2021).

Other off-campus service has included virtually mentoring several undergraduate women through the Goldwater Scholar Community and through Camp Talaria. I also conducted liquid nitrogen demonstrations at Pasadena elementary and middle school science nights (2017-2018), and I was a judge at the Sierra Madre Middle School Science Fair in 2019. I participated in outreach initiatives such as Skype a Scientist (2018-2020), and I have especially loved being a scientist pen pal to middle school students through Letters to a Pre-Scientist, which I started doing in 2018. Finally, I have been especially active in Project Scientist, an organization that puts on programming for girls between 4 and 12 years old. Specifically, I have been a STEM Superstar visiting scientist speaker for Project Scientist's science academy for five summers, every summer since coming to Caltech. I also designed and organized a Project Scientist Expedition during which a group of 30 girls visited South Mudd and rotated through sessions on star and planet formation (which I presented), meteorites, and comets; the expedition included a "research notebook" assembled by me that contained activities, including drawing a meteorite sample observed through a microscope.

All of these activities have been an enjoyable and fulfilling part of my graduate school experience. I am sincerely grateful for the opportunity to have grown through these ventures, not only as a scientist and science communicator but as a more thoughtful and engaged community member.

---

[3] National Science Foundation Graduate Research Fellowship Program

INDEX

COMMON ABBREVIATIONS

BGPS	Bolocam Galactic Plane Survey
COMs	complex organic molecules
GMC	giant molecular cloud
ISM	interstellar medium
YSO	young stellar object

TELESCOPES & OBSERVATORIES

ACA	Atacama Compact Array (Chile)
ALMA	Atacama Large Millimeter/submillimeter Array (Chile)
GBT	Green Bank Telescope (West Virginia, USA)
JCMT	James Clerk Maxwell Telescope (Hawaii, USA)
JWST	“Just Wait” Space Telescope (space)
IRAM	Institute de Radioastronomie Millimétrique (France)
NRAO	National Radio Astronomy Observatory (Virginia, USA)

UNIT CONVERSIONS

Constants

c	speed of light	2.99×10^{8} m s^{-1}
h	Planck constant	6.626×10^{-34} J s
k	Boltzmann constant	1.381×10^{-23} J K^{-1}

Distance

1 au = 149 597 871 km

1 pc = 3.0857×10^{13} km

1 ly = 9.46×10^{12} km

linear size [au] = angular size [″] · distance [pc]

Electric Dipole Moment

1 Debye = 10^{-18} cm$^{5/2}$ g$^{1/2}$ s^{-1}

Flux

1 Jy = 10^{-26} W m^{-2} Hz^{-1}

Frequency ν and Wavelength λ

$\nu = c\lambda^{-1}$

$\lambda = c\nu^{-1}$

1 Hz = 1 s^{-1}

Mass

$1M_{\odot} = 1.989 \times 10^{30}$ kg

Temperature

1 K= $T/^{\circ}\mathrm{C} + 273.15$ K

$$1^{\circ}\mathrm{C} = (T/^{\circ}\mathrm{F} - 32\,^{\circ}\mathrm{F})\left(\frac{5\,^{\circ}\mathrm{C}}{9\,^{\circ}\mathrm{F}}\right)$$

Unit Abbreviations

$''$	arcsecond
μm	micron, micrometer (10^{-6} m)
au	astronomical unit
cm	centimeter (10^{-2} m)
GHz	gigahertz (10^{9} Hz)
Hz	hertz
J	Joule
Jy	jansky
K	kelvin
kg	kilograms (10^{3} g)
km	kilometer (10^{3} m)
kpc	kiloparsec (10^{3} pc)
m	meter
$M_\odot$	solar mass
MHz	megahertz (10^{6} Hz)
pc	parsec
s	second
W	Watt
ly	light-year